

ELF/VLF PHASED ARRAY GENERATION VIA  
FREQUENCY-MATCHED STEERING OF A CONTINUOUS HF  
IONOSPHERIC HEATING BEAM

A DISSERTATION  
SUBMITTED TO THE DEPARTMENT OF  
ELECTRICAL ENGINEERING  
AND THE COMMITTEE ON GRADUATE STUDIES  
OF STANFORD UNIVERSITY  
IN PARTIAL FULFILLMENT OF THE REQUIREMENTS  
FOR THE DEGREE OF  
DOCTOR OF PHILOSOPHY

Morris Bernard Cohen

October 2009

© Copyright by Morris Bernard Cohen 2010  
All Rights Reserved

I certify that I have read this dissertation and that, in my opinion, it is fully adequate in scope and quality as a dissertation for the degree of Doctor of Philosophy.

---

(Umran S. Inan) Principal Adviser

I certify that I have read this dissertation and that, in my opinion, it is fully adequate in scope and quality as a dissertation for the degree of Doctor of Philosophy.

---

(Timothy F. Bell)

I certify that I have read this dissertation and that, in my opinion, it is fully adequate in scope and quality as a dissertation for the degree of Doctor of Philosophy.

---

(Butrus T. Khuri-Yakub)

Approved for the University Committee on Graduate Studies.

.

*To life, to life, l'chaim!*

*L'chaim, l'chaim, to life!*

# Abstract

The radio spectrum between 300 Hz and 10 kHz (ELF/VLF) has broad applications to global communication, remote sensing of the ionosphere and magnetosphere, and subterranean prospecting. While lightning is a dominant source of these radio waves, artificial generation of these waves has posed an enduring challenge to scientists and engineers, due to the extremely long wavelengths (30-1000 km) and the lossiness of the Earth's surface at these frequencies.

Recently, ELF/VLF waves have been successfully generated by high frequency (HF, 3-10 MHz) heating of the lower ionosphere (60-100 km altitude), which changes the atmospheric plasma conductivity. In the presence of natural currents such as the auroral electrojet, ON-OFF modulation of this HF energy can impose an ELF/VLF alternating current onto those natural currents. This technique turns the lower atmosphere into a large antenna, which radiates energy downward into the Earth-ionosphere waveguide and upward into the magnetosphere.

While this technique remains one of the few means of reliable ELF/VLF wave generation, HF to ELF/VLF conversion efficiencies remain quite low. Utilizing the 3.6 MW HAARP HF heating facility in Alaska, we show that proper utilization of motion of the HF beam can boost the generated ELF/VLF wave power by as much as tenfold. Furthermore, as a result of having effectively created the world's first controllable large-element ELF/VLF phased array, directional launching of this energy becomes possible. We utilize theoretical models of the HF heating and cooling process, and of ELF/VLF wave propagation, to illuminate the observations and identify the physical mechanisms underlying the wave generation, particularly as it relates to motion of the HF beam.

# Acknowledgements

I begin with a slightly paraphrased quote from the ancient Jewish law book *Talmud*, Pirkei Avot, Chapter 3, attributed to Rabbi Yochanan Ben Zakai.

*If you have learned much (scholarly wisdom), do not take credit for yourself; it is for this reason that you have been formed.*

Indeed, it may be my name printed on the front of this thesis, but really none of it would have happened without the support of a lot of other people.

First and foremost, I’ve been blessed with a fantastic family. My parents have truly been role models to me for my entire life. I say with no qualification that I have the best parents I possibly could have. My brothers, Sam and Dave, have always been terrific and very supportive, and I’m delighted that both of them have grown the family, with my sisters-in-law Fern and Audria, and their children Josh, Ian, Rachel, and Ethan.

I thank my teachers and friends from Beth Tfiloh School in Pikesville, Maryland, where a great general education was complemented with a firm grounding in Jewish teachings that I still proudly carry. I thank all my friends from my Stanford undergraduate years, who made my early years on ‘The Farm’ a great experience.

I owe another thanks to all the VLF group members with whom I’ve interacted. Marek Gólkowski has been a very able collaborator in planning so many HAARP experiments (and absurd arctic adventures), and a reliable scientific counsel. Denys Piddychiy and George Jin were extensive contributors to the late night chat room watches during campaigns. Robb Moore, Joe Payne, and Nikolai Lehtinen paved the way for this thesis with excellent earlier work. Tim Bell provided some valuable counsel with this dissertation.

Justin Tan and Eddie Kim were critical in developing the ‘AWESOME’ receiver with me, which has by now gotten so much use worldwide, and serves as the primary source of data for this thesis. Ev Paschal, with his decades of experience in hardware design, was a treasure trove of information on VLF receivers and field installation.

Although not part of this dissertation effort, for the exciting ‘AWESOME’ International Heliophycial Year (IHY) global distribution program, I worked extensively with Sheila Bijoor, Ben Cotts, and Naoshin Haque. Debbie and Phil Scherrer were instrumental in the program’s development. I thank all our AWESOME collaborators and site hosts around the world for their friendship.

Many other VLF members have been colleagues and friends. I’ve learned a lot from Ryan Said, Prajwal Kulkarni, Jeff Chang, Charles Wang, Mark Daniel, Brant Carlson, Bob Marshall, Dan Golden, Nader Moussa, Kevin Graf, Robert Newsome, Max Klein, and others.

I thank Shaolan Min and Helen Niu for keeping so much important VLF group business running smoothly, and Dan Musetescu for managing so much data and keeping it all organized.

The operation of the HAARP facility has been possible thanks in part to the hard work of Mike McCarrick, Helio Zwi, and David Seafolk-Kopp. I would like to thank Doyle and Norma Traw, of Chistochina Bed and Breakfast, in Alaska, for helping with receiver maintenance and always being great hosts during my various trips there.

The experience working with my advisor, Umran Inan, has been terrific, as from it I have learned so much. The journey has been long since I took on my first VLF project (rather unrelated to this thesis) as a college junior, but through several different widely disparate projects I was never short of opportunities to grow, develop, and pursue new ideas. For that reason my time in this research group has never felt static at all. Thanks for giving me the chance.

*This work has been supported by the Defense Advanced Research Projects Agency and the Air Force Research Laboratory under Office of Naval Research (ONR) grants N00014-09-1 and N00014-06-1-1036 to Stanford University.*

# Contents

<b>Abstract</b>	<b>v</b>
<b>Acknowledgements</b>	<b>vi</b>
<b>1 Introduction</b>	<b>1</b>
1.1 The ionosphere . . . . .	1
1.2 Magnetosphere-ionosphere coupling . . . . .	4
1.3 ELF and VLF waves . . . . .	7
1.4 ELF/VLF wave generation . . . . .	9
1.5 Some history . . . . .	13
1.6 Review of past work . . . . .	18
1.6.1 Local geomagnetic conditions . . . . .	19
1.6.2 Earth-ionosphere waveguide injection . . . . .	20
1.6.3 Harmonic radiation and saturation . . . . .	21
1.6.4 Magnetospheric injection . . . . .	22
1.6.5 Mobile heated region . . . . .	23
1.6.6 Beam painting . . . . .	24
1.6.7 Alternative methods . . . . .	24
1.6.8 Ionospheric array . . . . .	25
1.7 Scientific contributions . . . . .	26
1.8 Approach . . . . .	27
<b>2 ELF/VLF Generation and Propagation Physics</b>	<b>28</b>
2.1 Waves in plasmas . . . . .	28



2.1.1	Plasma properties . . . . .	29
2.1.2	Magnetic field and the whistler wave . . . . .	30
2.1.3	Anisotropy . . . . .	31
2.1.4	Collisions . . . . .	32
2.1.5	The $D$ -region . . . . .	35
2.2	HF heating theory . . . . .	38
2.2.1	Electron temperature . . . . .	39
2.2.2	Modified ionosphere . . . . .	41
2.2.3	HF wave propagation . . . . .	44
2.3	Model construction . . . . .	45
2.3.1	Energy balance at one altitude . . . . .	45
2.3.2	Vertical structure . . . . .	50
2.3.3	Extension to 3D . . . . .	57
2.4	The Earth-ionosphere waveguide . . . . .	65
2.4.1	Reflection coefficients . . . . .	68
2.4.2	Modal solutions . . . . .	70
2.4.3	Propagation model . . . . .	70
2.5	Model results . . . . .	73
<b>3</b>	<b>HF Beam Motion: Experiments</b>	<b>79</b>
3.1	ELF/VLF generation and beam motion . . . . .	80
3.2	Implementation . . . . .	84
3.3	Experimental setup . . . . .	85
3.4	Comparative frequency response . . . . .	90
3.4.1	Generated amplitudes from beam painting . . . . .	91
3.4.2	Directionality from beam painting . . . . .	93
3.4.3	Generated amplitudes from geometric modulation . . . . .	94
3.4.4	Directionality from geometric modulation . . . . .	95
3.4.5	Geometric modulation compared to oblique-AM . . . . .	95
3.4.6	Summary of ground-based observations . . . . .	97
3.4.7	Magnetospheric injection . . . . .	99

<b>4</b>	<b>HF Beam Motion: Modeling</b>	<b>100</b>
4.1	Modulated currents . . . . .	100
4.2	Fields on the ground . . . . .	103
4.3	Magnetospheric injection . . . . .	112
4.4	Directional pattern . . . . .	115
<b>5</b>	<b>Physical Mechanisms</b>	<b>120</b>
5.1	Heat-cool duty cycle . . . . .	120
5.2	Phasing from oblique heating . . . . .	127
5.3	HF pulsing . . . . .	132
5.4	ELF/VLF phased array control . . . . .	136
5.5	Phased array parameters . . . . .	140
5.6	Discussion . . . . .	143
<b>6</b>	<b>Summary and Suggestions for Future Work</b>	<b>144</b>
6.1	Future work . . . . .	145
6.1.1	Equatorial electrojet . . . . .	146
6.1.2	Intersweep delay times . . . . .	146
6.1.3	HF heating model with lookup table . . . . .	146
6.1.4	Parallel conductivity changes . . . . .	147
6.1.5	Directional pattern . . . . .	147
6.1.6	Beam painting diurnal variations . . . . .	148
6.1.7	Variation with HF frequency . . . . .	148
6.2	Concluding remarks . . . . .	148
<b>A</b>	<b>Long Distance Reception</b>	<b>149</b>
<b>B</b>	<b>HAARP HF Radiation Pattern</b>	<b>152</b>
<b>C</b>	<b>ELF/VLF Reception and Detection</b>	<b>155</b>
C.1	Antenna characteristics . . . . .	156
C.2	System design . . . . .	158
C.3	Calibration . . . . .	162

C.4	Gain and sensitivity . . . . .	164
C.5	Timing accuracy . . . . .	167
C.6	Cross-modulation and cross-coupling . . . . .	171
<b>D</b>	<b>Power Line Interference Mitigation</b>	<b>174</b>
D.1	Adaptive filtering . . . . .	177
D.1.1	Theory . . . . .	178
D.1.2	Implementation . . . . .	180
D.2	Least squares estimation . . . . .	186
D.3	Examples . . . . .	190
<b>E</b>	<b>ON/OFF Duty Cycle Observations</b>	<b>193</b>

# List of Tables

1.1	Ionospheric heating facilities . . . . .	15
B.1	Radiated power (and ERP), in Megawatts, of HAARP beam modes .	154

# List of Figures

1.1	The ionosphere . . . . .	2
1.2	The magnetosphere in the solar wind . . . . .	5
1.3	The auroral electrojet . . . . .	6
1.4	A VLF transmitter . . . . .	11
1.5	Illumination by an ionospheric source . . . . .	13
1.6	The HAARP HF heating facility . . . . .	18
2.1	Coordinate system for ionospheric conductivity . . . . .	33
2.2	Ionospheric plasma parameters . . . . .	37
2.3	Variations of ionospheric conductivities as a function of temperature .	42
2.4	Heating and cooling dynamics at 75 km altitude . . . . .	47
2.5	Hall conductivity modulation vs. height, frequency, and HF power . .	49
2.6	Power density reaching higher altitudes . . . . .	51
2.7	Absorption of HF energy at 3.25 MHz . . . . .	53
2.8	Ionospheric modification at varying altitudes . . . . .	55
2.9	HF power at 60 km from HAARP . . . . .	57
2.10	2D interpolation of HF parameters . . . . .	59
2.11	Three-dimensional HF heating model results . . . . .	61
2.12	Time-evolution of vertical modulated currents . . . . .	64
2.13	Propagation in the Earth-ionosphere waveguide . . . . .	66
2.14	Reflection coefficients as a function of incidence angle . . . . .	69
2.15	ELF/VLF propagation simulations . . . . .	74
2.16	Hall, Pedersen, and Parallel conductivity contributions . . . . .	76
2.17	Horizontal magnetic field from current sources . . . . .	77

3.1	Amplitude modulation, beam painting, and geometric modulation . .	82
3.2	Classification of modulation techniques . . . . .	84
3.3	Map showing location of HAARP and ELF/VLF receivers . . . . .	86
3.4	Transmission format and sample data from AWESOME receiver . . .	88
3.5	The generated amplitudes from beam painting . . . . .	91
3.6	Directionality associated with beam painting . . . . .	93
3.7	The generated amplitudes from geometric modulation . . . . .	94
3.8	Directionality associated with geometric modulation . . . . .	95
3.9	Comparison between oblique-AM and geometric modulation . . . . .	96
3.10	Experimental frequency response of HF heating . . . . .	98
4.1	Modeled Hall currents from modulated HF heating . . . . .	102
4.2	Modeled fields on the ground from 5 kHz modulated HF heating . . .	104
4.3	Modeled ground magnetic field compared, 5 kHz . . . . .	106
4.4	Modeled ground magnetic field compared at 2 kHz . . . . .	109
4.5	Theoretical response of modulated HF heating (on ground) . . . . .	111
4.6	Modeled fields at 700 km altitude from modulated HF heating . . . .	113
4.7	Modeled frequency variation of ELF/VLF power to 700km altitude .	114
4.8	Directional patterns in the Earth-ionosphere waveguide . . . . .	117
4.9	Directionality of the sawtooth-sweep as a function of frequency . . . .	118
5.1	Schematic effect of duty cycle on ELF/VLF generation . . . . .	121
5.2	Heating and cooling areas in geometric modulation . . . . .	123
5.3	Observed effect of duty cycle on ELF/VLF generation . . . . .	124
5.4	Generated amplitude as a function of HF ON and OFF durations . .	126
5.5	Schematic of oblique HF heating effect . . . . .	128
5.6	Received signals for oblique-AM HF heating at different azimuths . .	130
5.7	Comparison of oblique-AM with geometric modulation . . . . .	131
5.8	Temporal conductivity changes for rapid power modulation . . . . .	133
5.9	Effectiveness of beam painting by ERP and duty cycle . . . . .	135
5.10	ELF/VLF phased array concept . . . . .	137
5.11	Point-source, free space model of received fields . . . . .	138

5.12	Circle-sweep and sawtooth-sweep magnetic field on the ground . . . .	140
A.1	Global detection of ELF signals from HAARP . . . . .	150
B.1	HF power into the ionosphere from HAARP beam modes . . . . .	153
C.1	Photos and block diagram of the AWESOME receiver. . . . .	159
C.2	AWESOME Anti-aliasing filter . . . . .	161
C.3	Measured performance characteristics of the AWESOME receiver . .	165
C.4	AWESOME receiver timing . . . . .	169
C.5	Cross modulation in the AWESOME receiver . . . . .	172
D.1	Power-line frequency tracking . . . . .	183
D.2	Spectrum of ELF/VLF data as $a$ and $b$ parameters are varied . . . .	184
D.3	Variations of $a$ parameter . . . . .	185
D.4	Time series data for varying values of $a$ . . . . .	187
D.5	Examples of power-line filtered data . . . . .	191
E.1	Amplitudes of generated ELF waves as a function of duty cycle . . .	194
E.2	Efficiency of generated ELF waves as a function of duty cycle . . . .	196

# Chapter 1

## Introduction

Hello and welcome to my thesis. Relax and enjoy the ride. We will explore the generation of extremely low frequency and very low frequency (ELF/VLF) electromagnetic waves between 300 Hz–30 kHz. We consider a method of generation in which the Earth’s upper atmosphere (60–100 km) is modified in such a way that it becomes a large antenna. The modification occurs by heating of free electrons with High Frequency (HF) waves between  $\sim 3$  and 10 MHz. The applicability of this method arises from the fact that at ELF/VLF frequencies, wavelengths are extremely long (10–1000 km), making a more conventional antenna structure difficult, costly, and limited in ability. In this chapter, we discuss the general problem at hand and describe the physical environment in which our experimental observations and theoretical models operate. We also review the history of experimental and theoretical efforts in the field of ELF/VLF wave generation via ionospheric HF heating.

### 1.1 The ionosphere

The Earth’s atmosphere on the surface, where we breathe, consists almost entirely of neutral nitrogen and oxygen gas molecules. On the other hand, the space environment surrounding the Earth (known as the magnetosphere), consists almost entirely of charged particles (electrons, protons, or ions), the densities of which are many orders of magnitude lower than the air on Earth. Because the particles in the magnetosphere



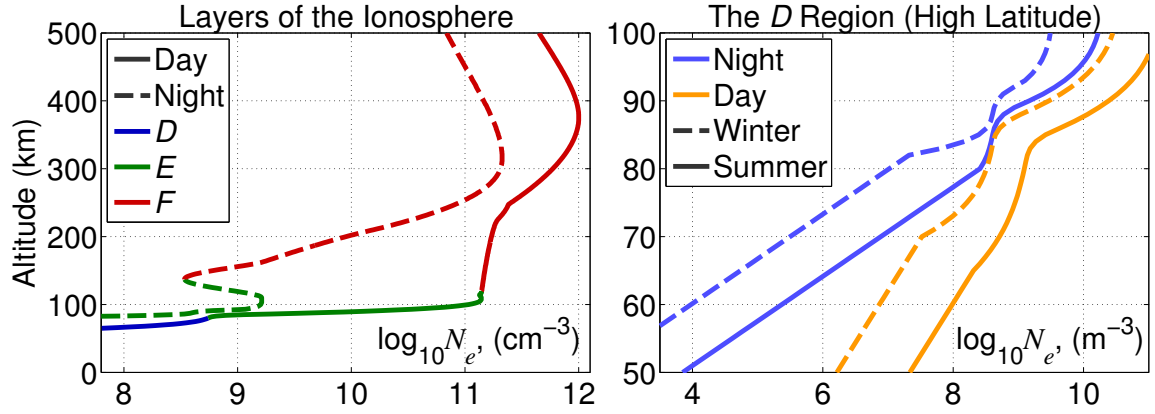


Figure 1.1: The ionosphere

are so spread out, collisions with one another and with ever fewer neutral molecules are rare, and their motion is greatly affected by the Earth's magnetic field. The ionosphere is essentially the transition between these two regions, extending over altitudes above the Earth's surface between 50 km and 1000 km. Both the ionosphere and magnetosphere are examples of plasmas, nominally the fourth state of matter (after solid, liquid, gas). In a plasma, a substantial number of charged particles exist to create a shielding effect (known as Debye shielding) which tends to acts against the development and maintenance of quasi-static electromagnetic fields (at least in a plasma without an externally applied magnetic field), since the charged particles rearrange so as to cancel out those fields. More details on the relevant physics are given in Chapter 2.

The left hand panel of Figure 1.1 shows the structure of the ionosphere's vertical profile, with electron density ( $N_e$ ) in logarithmic scale on the horizontal axis, as a function of the altitude above the Earth's surface on the vertical axis. The daytime ionospheric profile is shown with a solid line, the nighttime ionospheric profile in dashed line. The data come from the International Reference Ionosphere (IRI) 2007 model, an empirical model of ionospheric parameters taking into account basic diurnal, seasonal and geographic variations, for 01-Jan-2009, at the geographic location (0,0), at 00 UT (midnight) and 12 UT (high noon).

The sun's radiation dominates the dynamics of the ionosphere, as the impingement

of high energy (extreme ultraviolet and higher) photons on the atmospheric molecules is the primary source of ionization. For this reason, the structure of the ionosphere is radically different between nighttime and daytime. At night, with the sun's ionization source gone, the  $F$  region ionization level is maintained by a diffusive flow of plasma from the inner magnetosphere (where recombination is much slower, so the ionization persists), and this flow is subsequently forced back out during the daytime [Tascione, 1994, pg.96]. The  $D$  and  $E$  regions, on the other hand, are maintained at nighttime by a steady flow of cosmic rays from extrasolar sources.

The dynamics of the  $D$  and  $E$  regions are complicated. On top of strong diurnal and seasonal changes, the electron density can change drastically and rapidly as a result of energetic particle precipitation or other magnetospheric activity, particularly at night. The right panel of Figure 1.1 shows more detail on the electron density in the lower portion of the ionosphere, and its variability from day to night, and winter to summer. The IRI typically does not define the electron density in the lowest parts of the  $D$  region, since the numbers become so small and variable. Below this altitude, the electron densities are generally extrapolated with an exponential decrease, in line with a two-parameter ionosphere described by *Wait and Spites* [1964], defined by

$$N_e(h) = N_e^{h_{\min}} e^{-\beta h} \quad (1.1)$$

where  $N_e^{h_{\min}}$  is the lowest defined electron density in the IRI, and  $h$  is km below that altitude. The steepness parameter,  $\beta$ , is taken to be  $-0.15 \text{ km}^{-1}$  in the daytime, and  $-0.35 \text{ km}^{-1}$  in the nighttime. Some typical values of a two-parameter ionosphere in the  $D$  and  $E$  regions can be found in *Thomson et al.* [2007] and *Thomson* [1993].

The IRI inputs are calculated for the location  $62.39^\circ\text{N}$ ,  $214.85^\circ\text{E}$ , where the research facility in Alaska central to this work is located. The summer ionospheres are calculated for 01-Jul-2000, and winter ionospheres for 01-Jan-2000. The nighttime ionospheres are calculated for 02:00 local time, and the daytime ionospheres for 14:00 local time. The four ionospheres shown here are referred to repeatedly in this dissertation. The IRI also gives the ambient temperature, which varies between 180 and 240 K in this altitude range, and the neutral molecular densities.

## 1.2 Magnetosphere-ionosphere coupling

Although electromagnetic radiation from the sun and cosmic rays are chiefly responsible for the formation of the ionosphere, a larger region around the Earth, known as the magnetosphere, is shaped by the interaction of the so-called ‘solar wind’ with the Earth’s magnetic field. The solar wind consists mostly of protons and electrons at 1 keV energy, originating from the sun, traveling at  $\sim 400\text{--}500$  km/s, and consisting typically of  $\sim 5$  protons or electrons per  $\text{cm}^3$  [Tascione, 1994, ch.3]. The geomagnetic field of the Earth, however, acts to block this flow and deflect these particles. The result is that Earth’s magnetic field lines (which have roughly a magnetic dipole pattern within a few Earth radii of the surface) are squashed in on the day side of the Earth, and elongated into a tail on the night side. Figure 1.2 (available from NASA) shows the basic structure of the Sun-Earth system and formation of the magnetosphere (not to scale). The resulting current systems and dynamics of the magnetosphere driven by the solar wind interaction with the geomagnetic field are in general very complicated, and lead to a broad array of phenomena. For instance, some of the solar wind that penetrates into the magnetosphere becomes trapped by the geomagnetic field, forming two bands of energetic particles known as the Van Allen radiation belts.

In this dissertation, we are interested in one particular aspect through which the magnetosphere system couples with the ionosphere. Above a portion of the high latitude ionosphere known as the auroral zone, strong electric fields in the magnetosphere accelerate energetic electrons in the magnetosphere. Since electrical conductivity is much higher along the magnetic field in a magnetized plasma, the resulting current moves primarily along the geomagnetic field line. At high latitudes, the geomagnetic field lines are close to vertical, connecting the ionosphere to the magnetosphere, and driving a current upward into the magnetosphere (or, electrons accelerated downward into the atmosphere). The collision of these ‘precipitating’ electrons with the neutral atmosphere is primarily responsible for the aurora borealis (in the northern hemisphere) and the aurora australis (in the southern hemisphere), pictured in the right part of Figure 1.3, which arise from photons emitted as a result of these collisions.

Since these currents typically persist far longer than charges can be sustained in

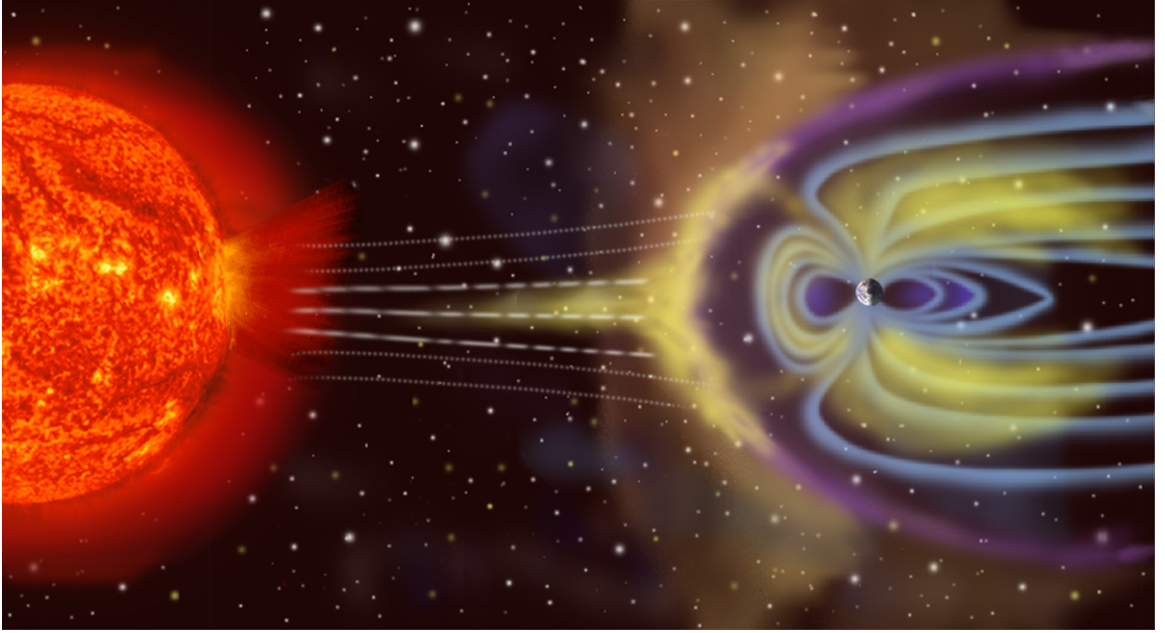


Figure 1.2: The magnetosphere in the solar wind

the plasma, the currents must in general be closed in a loop. An opposite current therefore must also be present coming into the ionosphere, forming what are often called Birkeland currents. The Birkeland currents connect at different latitudes, so there must also be electric fields horizontally within the ionosphere connecting these upward and downward currents, and this system is known as the auroral electrojet.

Figure 1.3, left panel, shows a schematic of the typical auroral electrojet system, as would be viewed from a point one Earth radius above the surface. The magnetic north pole is located at  $82.7^\circ\text{N}$ ,  $110.8^\circ\text{W}$  as of 2005. The so-called ‘auroral oval’ is shown in shades of red, and is the portion of the ionosphere with elevated conductivity as a result of electron precipitation, with brighter red indicating higher conductivity. The precipitation (and the conductivity) tends to be higher on the night side of the oval [Baumjohann, 1983]. In addition, the auroral oval is not exactly centered around the magnetic north pole, but is shifted by  $\sim 4^\circ$  away from the sun [Baumjohann, 1983].

The auroral electrojet is highly variable. Its size and extent is largely a function of solar and geomagnetic activity. During geomagnetic storms, the auroral electrojet

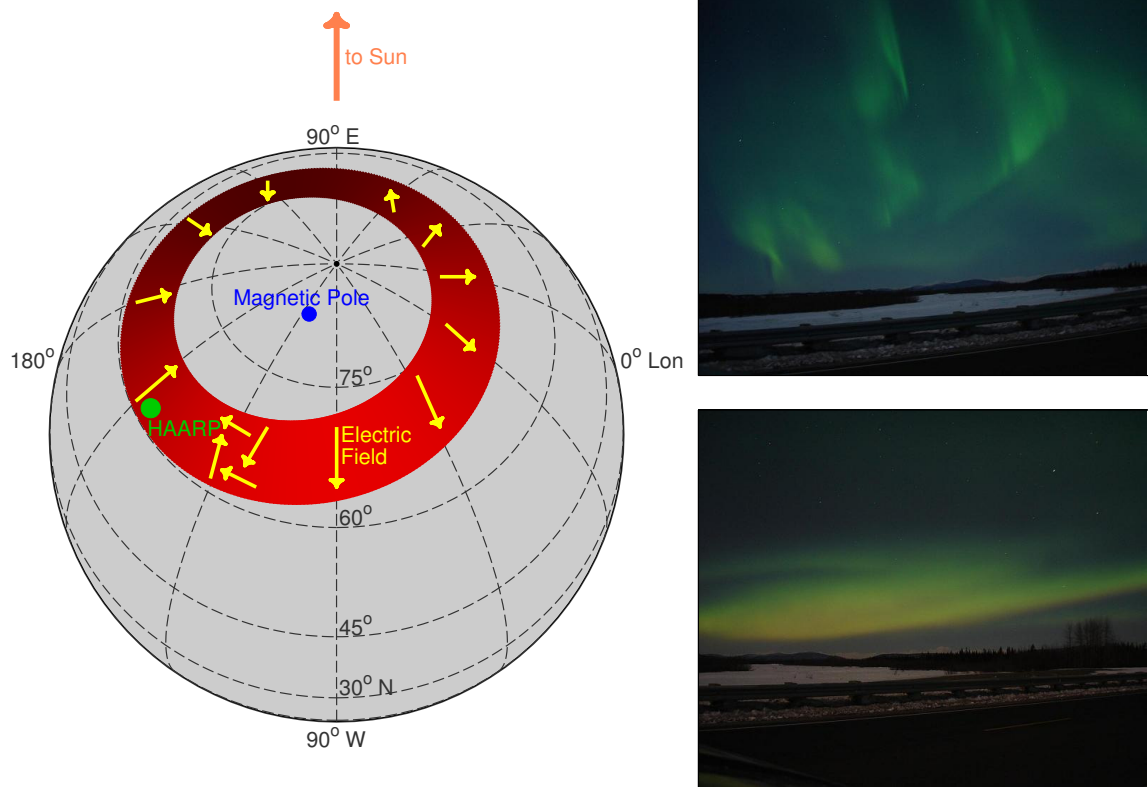


Figure 1.3: The auroral electrojet

region expands southward. The right hand photos in Figure 1.3 are taken near Chis-tochina, Alaska, of roughly the same portion of the sky, but only 4 minutes apart (the top photo being earlier), on the morning of 11-March, 2006. The structure and color of the aurora can be seen to dramatically change despite the small time between the two photos, showing that this particular signature of magnetosphere-ionosphere coupling can exhibit rapid variations.

The arrows in Figure 1.3 indicate the electric field lines, which are typically pointed roughly in the north-south geomagnetic direction, but there are two diurnal discontinuities [Baumjohann, 1983]. In the few hours before midnight, the direction of the electric field changes from northward to southward, and this transition is known as the Harang discontinuity [Baumjohann, 1983]. At midday, the auroral electrojet fields typically are weaker.

The electric field generally in the north-south geomagnetic direction also generates horizontal currents that are in the east-west direction (due to the anisotropic ionospheric conductivity discussed in Chapter 2). In this thesis, we consider a method of ionospheric variation which modulates a small geographic portion of these typically east-west auroral electrojet currents, by changing the conductivity of the ionosphere with radio frequency (RF) heating. The RF heating facility is known as the High Frequency Active Auroral Research Program (HAARP), whose location (indicated in green on the map) is typically near the southern edge of the auroral oval, at Gakona, Alaska.

### 1.3 ELF and VLF waves

The  $D$  region of the ionosphere lies at altitudes that are very difficult to access for the purpose of taking measurements. The current record-high (unmanned) balloon flight height reached 53 km, by Japan Aerospace Exploration Agency, in 2002. On the other hand, satellites cannot orbit below 200–400 km altitude, since the drag forces of the atmosphere would be too high. The inaccessibility of these altitudes to direct measurements have consequently earned the  $D$  region the title ‘ignorosphere’.

One method of deriving information about the ionosphere is to send rockets

through it, and record during the upward and downward passes. While rocket passes can provide direct information on the structure of the ionosphere, remote radio sensing is the only reliable means of continuous ionospheric monitoring. In particular, radio frequencies in the so-called Extremely Low Frequency (ELF, defined here as 300–3000 Hz) and Very Low Frequency (VLF, defined here as 3–30 kHz) are uniquely well suited to remote sensing of the  $D$  region, due to the fact that the  $D$  region reflects a significant portion of ELF/VLF energy (as is discussed in Chapter 2). Hence, changing conditions in the  $D$  region manifest as changes in the reflection conditions of these ELF/VLF waves. Disturbances in the  $D$  region can be associated with a wide variety of natural events, including solar flares [Mitra, 1974], lightning-induced heating and ionization [Inan *et al.*, 1993], lightning-induced electron precipitation [Peter and Inan, 2007], auroral precipitation [Cummer *et al.*, 1997], cosmic gamma-rays [Fishman and Inan, 1988; Inan *et al.*, 2007b], geomagnetic activity [Peter and Inan, 2006; Rodger *et al.*, 2007], and possibly earthquakes [Molchanov and Hayakawa, 1999].

ELF and VLF waves have also been observed to significantly impact the dynamics of energetic particles in the Van Allen radiation belts. For instance, it has long been known that lightning-generated ELF/VLF waves can escape the atmosphere, and propagate in the so-called whistler-mode, with right hand circular polarization in the magnetospheric plasma [Helliwell, 1965]. Under certain conditions, these whistler waves can interact with energetic electrons, causing precipitation of previously trapped particles [Inan *et al.*, 2007c]. In addition, the propagating whistler wave can exchange energy with the particles, and as the wave and particle properties evolve, the whistler wave can be amplified and exhibit nonlinear triggering of different frequencies [Gibby *et al.*, 2008, and references therein]. The magnetosphere can also generate its own ELF/VLF waves such as chorus [Sazhin and Hayakawa, 1992] and hiss [Hayakawa and Sazhin, 1992] under certain conditions.

Furthermore, the Earth (both land and sea) is a good conductor at ELF/VLF, so that wave energy is trapped in the so-called Earth-ionosphere waveguide between the ground and the  $D/E$  region, and signals can travel to global distances with minimum (a few dB per Mm) attenuation [Davies, 1990, pg.389]. For instance, it

has long been known that lightning strokes emit the bulk of their electromagnetic energy in the ELF/VLF frequency range [Uman, 1987, pg.118], due to the typical time scales involved. The electromagnetic signatures of these strokes, known as radio atmospherics, or ‘sferics’, can be detected at global distances from the source [Cohen *et al.*, 2006], and often reveal information about the characteristics of the lightning source [Reising *et al.*, 1996; Cummer and Inan, 1997; Inan *et al.*, 2006] as well the *D*-region ionospheric path in between [Cummer *et al.*, 1998].

In addition to its uses for geophysical remote sensing, the high reflectivity of ELF/VLF waves off the *D* region (and the Earth) suggests a number of practical benefits. For instance, precise navigation can be achieved by receiving signals from multiple VLF transmitters, and applying phase-coherent triangulation. The ‘Omega’ system [Swanson, 1983], in operation until 30-September 1997, enabled precise navigation on the surface of the Earth long before the advent of the Global Positioning System (GPS), using a set of VLF transmitters between 10 and 15 kHz frequencies scattered around the world. The smaller ‘Alpha’ system [Inan *et al.*, 1984], operated by Russia, is still in operation with three transmitters across Russia. The LOng Range Aid to Navigation (LORAN) network [United States Coast Guard, 1980], still in operation, utilizes waves in the Low Frequency band ( $\sim 100$  kHz), with dozens of transmitters around the world [Frank, 1983].

ELF/VLF waves are also practical for communications with submerged submarines, due to the extremely long wavelengths (10–1000 km), enabling the energy to penetrate many meters into highly conductive ( $\sigma \cong 4$ ) seawater, via the skin effect. The ground-penetrating applications of ELF/VLF waves also make it useful for geophysical prospecting [McNeil and Labson, 1991], and imaging of underground structures.

## 1.4 ELF/VLF wave generation

Despite the broad applications to remote sensing, navigation, communication, and geophysical prospecting, ELF/VLF waves are difficult to generate for the purpose of controlled experiments. Different kinds of traditional and novel antennas for electromagnetic wave generation are used for a dizzying array of applications, like television,



AM/FM radio, wireless phones, medical devices, aircraft communications, radars, and much more. But ELF/VLF waves are not so easy to generate with conventional antennas.

Consider the fact that the wavelength ( $\lambda$ ) at these frequencies is between 10–1000 km. Construction of a half-wave dipole would therefore need an antenna of these length scales. A practically realizable antenna, oriented vertically and powered from the ground, invariably has an extremely short length compared to  $\lambda$ . For such electrically short antennas, the entire conductor is quite nearly an equipotential surface, since the time it takes for the voltages to propagate from the feed point to the ends of the antenna is negligible compared to the ELF/VLF period. So applying a voltage to the feed point generates a current signal which propagates out to the ends of the antenna and reflects, with the reflected current nearly canceling the outgoing current. With only small net currents, charges cannot be separated along the antenna, and so potential differences along the antenna are also small. In essence, the resistance of the antenna for radiating is small, since a large current creates only small potential differences along the antenna. Antennas are often characterized by this ‘radiation resistance’, which, for an electrically short monopole antenna above a ground plane, is given by

$$R_s = 40 \left( \pi \frac{h}{\lambda} \right)^2 \quad (1.2)$$

where  $h$  is the length of the antenna and  $\lambda$  is the wavelength [Stutzman and Thiele, 1998, pg.66].  $R_s$  is therefore only 6.3 m $\Omega$  for a 100 meter tall antenna at 15 kHz. Therefore, radiation with any acceptable efficiency can only be achieved if the impedance of the source driving the antenna is close to this value (and this includes any ohmic losses from the finite conductivity of the antenna itself). Practically speaking, such small output impedances requires tuning of reactive load elements to cancel out as much of the impedance as possible, and this can only be achieved over a narrow resonant frequency range. A thorough discussion of the engineering tradeoffs involved in this type of design is given by Watt [1967, ch.2]. Even within this narrow frequency range, the voltages driving the antenna must be extremely high in order to

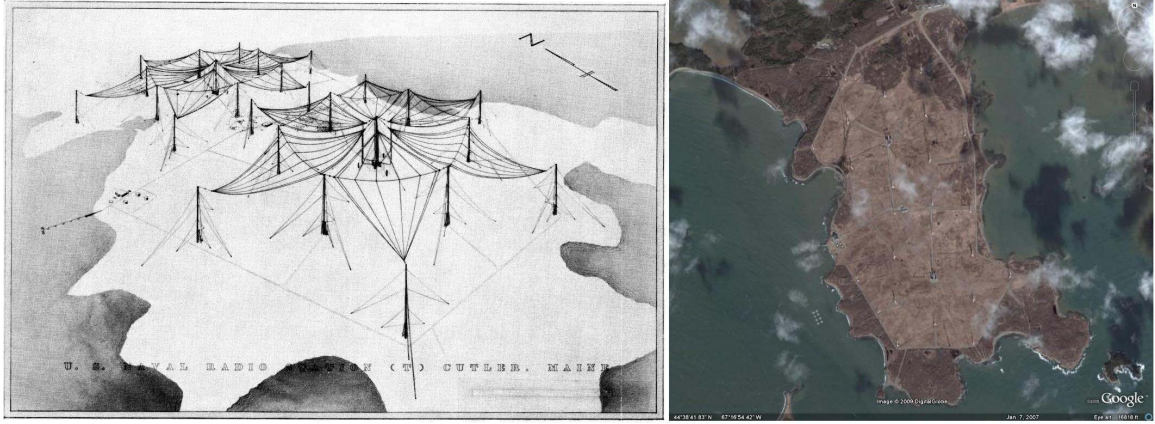


Figure 1.4: A VLF transmitter

have sufficient current, causing engineering problems with arcing. A number of these VLF transmitters are, nevertheless, currently in operation. The left side of Figure 1.4, adapted from Figure 2.8.11 of *Watt* [1967], shows a diagram of the NAA transmitter in Cutler, Maine, showing the complicated mast structure needed to erect and support the large VLF transmitter. A satellite image of NAA from Google Earth ( $44.646^{\circ}\text{N}$ ,  $67.281^{\circ}\text{W}$ ), is shown on the right side of Figure 1.4.

Below 10 kHz, the requirements of the tuning elements become sufficiently extreme (in order to match the small radiation resistance) that a vertical monopole is not practical [*Barr et al.*, 2000], and the radiation resistance must be increased with a longer antenna. *Koons and Dazey* [1983] report some success with ELF/VLF generation via an antenna with one end lofted up to 1.5 km high on balloons, achieving 100 W of radiated power at 6.6 kHz, but such a system would be difficult and costly to operate continuously. A second possible strategy is therefore to lay a long antenna along the ground, which can in practice be made much longer. Unfortunately, the presence of the conducting ground acts to effectively set up a nearly equal but opposite image current just below the ground, which cancels out the radiation. For instance, *Dazey and Koons* [1982] report on the use of 10.6 km long power transmission line at Kafjord, Norway, in order to transmit signals to the SCATHA and GEOS spacecrafts, but managed to radiate 0.17–0.79 W at 1280 Hz. The ELF facility located in Wisconsin and Michigan utilized grounded horizontal wire operated

at 76 Hz, but even with an antenna length of 150 km, managed to radiate only  $\sim 10$  W [Jones, 1995]. An ELF antenna operating at Siple Station, Antarctica [Helliwell and Katsufrakis, 1974], was able to effectively lift the antenna  $\sim 2$  km off the Earth (and therefore separate the image current from the antenna current by 4 km), since it was built on top of a thick (poorly conducting) antarctic ice sheet, but even so, was able to achieve radiation efficiency of only a few percent [Raghuram *et al.*, 1974] between 1 and 10 kHz. More recently, a 6.25 km long horizontal dipole antenna has been constructed at the South Pole for use as a VLF beacon, radiating a few hundred watts at 19.4 kHz [Chevalier *et al.*, 2007].

Both the vertical dipole (typically used for  $\sim 10$ – $30$  kHz) and the horizontal dipole (demonstrated at 76 Hz) are generally very expensive to build, cannot be moved, operate in only a narrow frequency range, and have no directional control of the radiated VLF waves.

A number of less conventional ELF/VLF wave generation techniques have tried to overcome the limitations of these antenna constructions. Gould [1961] used a conductor connected across an isthmus between two land masses in Scotland and observed resonances due to current flow around the two landmasses. Although small VLF fields were measured, the conductivity difference between the sea and the rocky land was insufficient to be effective [Galejs, 1962]. Barr *et al.* [1993] tried making a large loop antenna strung over the top of a mountain and through a tunnel passing inside it, in New Zealand, but only radiated at 0.00075% efficiency at 10 kHz. Longer VLF antennas deployed from balloons can achieve good efficiency [Field *et al.*, 1989], but obviously cannot be maintained and powered indefinitely.

In recent decades, considerable research effort has been directed toward the generation of a source of ELF/VLF waves embedded in the ionosphere. The idea is to turn the lower ionosphere into a large radiating antenna by modulating the ionospheric conductivity. In the presence of natural electric fields in the ionosphere, modulated ionospheric conductivity will also modulate these currents. A more detailed discussion of the physics is given in Chapter 2 of this dissertation. For now, it suffices to say that the modification is achieved with intense Radio Frequency (RF) radiation directed at the ionosphere in the presence of natural ionospheric currents. The auroral

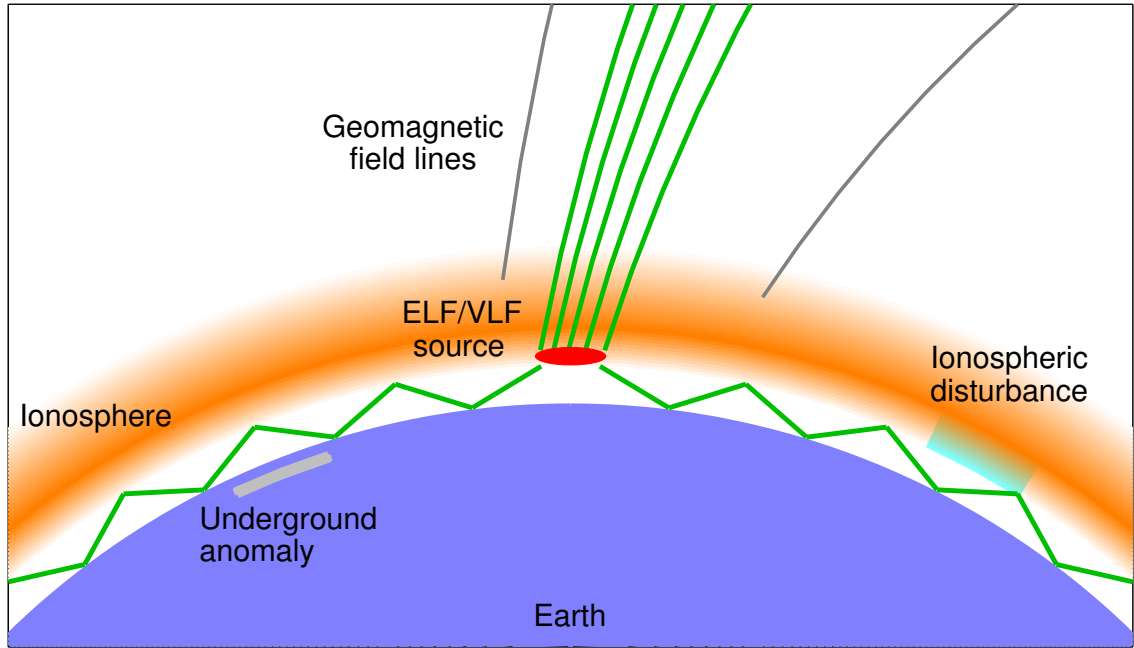


Figure 1.5: Illumination by an ionospheric source

electrojet currents are one such possible natural current system.

Figure 1.5 shows how an ionospheric source would illuminate both the Earth-ionosphere waveguide, and the magnetospheric region above. The Earth-ionosphere waveguide energy can be used to remotely sense ionospheric disturbances, or underground structures. Under special conditions, the ELF energy escaping into the magnetosphere can interact with radiation belt particles, undergo amplification, and be detected at the geomagnetic conjugate point or after reflection back to the source region [Inan *et al.*, 2004; Gołkowski *et al.*, 2008]. Both illumination of the Earth-ionosphere waveguide and magnetospheric probing with ELF wave injection are practical motivations for producing ELF/VLF waves via modulated HF heating.

## 1.5 Some history

Research in ionospheric modification with powerful RF waves, and more specifically, ELF/VLF wave generation, has been conducted at a number of facilities worldwide for

the past few decades. These antenna arrays are able to focus RF energy in a narrow beam upward, with constructive interference from an array of HF transmitters, often in a grid pattern. In focusing the RF energy, the power density in the center of the beam ( $S_{center}$ ) can be written as

$$S_{center} = \frac{GP_{rad}}{4\pi r^2} \quad (1.3)$$

where  $G$  is the ‘gain’ or directivity of the antenna,  $r$  is the distance to the antenna, and  $P_{rad}$  is the total radiated power.  $G$  is defined as the ratio of the maximum power density at any angle from the source to the average power density over all angles from the source, so  $S_{center}$  is equivalent to the power density from an antenna that has no directivity ( $G=1$ ), but has radiated power  $GP_{rad}$ . This quantity is known as the ‘effective radiated power’ (ERP), and measures the equivalent transmitting power level that would be required to produce the center-of-beam power density, if that transmitter radiated power evenly in all directions. Table 1.1 lists the ionospheric heaters that we refer to in this dissertation, along with the location,  $P_{rad}$ , ERP, and RF frequencies. All but one of the facilities utilize RF radiation generally in the High Frequency (HF, 3–30 MHz) range.

The earliest attempt (at least in the United States) to modify the ionosphere with high power RF radio waves may have been spearheaded by Stanford University [Potemra, 1963], but this effort apparently yielded no evidence of electron heating, even in the  $F$  region, perhaps due to the use of only 40 kW of power in an 8-element array. The first successful ionospheric modification experiments (at least in the United States) took place in Platteville, Colorado beginning in 1968. The first scientific results are given by [Utlaut, 1970], and the array itself is described in detail by Carroll *et al.* [1974]. Nominally built for modification of the  $F$  region, a number of measurable effects of the heating resulted, including spread- $F$ , broadband echoes, airglow, and infrared radiation [Utlaut and Cohen, 1971].

$D$  region modification was also observed in the Platteville experiments, using the technique of VLF remote sensing. When the HF heating was turned on, changes were observed in the amplitude and phase of a VLF transmitter signal originating 64 km

Location and Year	Coordinates	$f$ (MHz)	$P_{\text{rad}}$ (kW)	ERP (MW)
Platteville, Colorado (1968)	40.2°N	2.75	2000	50
	104.7°W	10.0	2000	50
Gor’kii, Russia (1973)	56.3°N	4.62	130	15
	44.0°E	5.75	130	22
SURA, Russia (1982)	56.3°N	4.5	750	150
	44.0°E	9.0	750	320
Monchegorsk, Russia (1976)	67.9°N	3.3	80	10
	32.9°E			
Tromsø, Norway (1980)	69.6°N	2.75	1200	300
	19.2°E	8.0	1400	350
Tromsø, Norway (1990)	69.6°N	5.42	1080	1000
	19.2°E			
Islote, Puerto Rico (1980)	18.5°N	3.0	800	160
	66.7°W	12.0	800	320
Jicamarca, Peru (1983)	12.0°N	49.9	350	5547
	76.9°W			
HIPAS, Alaska (1987)	64.9°N	2.85	800	70
	146.8°W	4.53	800	70
HAARP, Alaska (2003)	62.4°N	2.8	960	11
	145.2°W	9.5	960	330
HAARP, Alaska (2007)	62.4°N	2.8	3600	420
	145.2°W	9.5	3600	3800

Table 1.1: Ionospheric heating facilities

from Platteville and detected at a receiver site 64 km from Platteville in the opposite direction [Jones *et al.*, 1972]. Since VLF waves are reflected in the  $D$  region, this observation implied that electron temperature and collision frequency were modified well below the  $F$  region. The Platteville HF heater operated until 1984, but did not conduct experiments on ELF/VLF wave generation via modulation of the HF energy.

Much of the development of ELF/VLF wave generation experiments were conducted in parallel at facilities on both sides of the East-West Cold War division. However, the first observation that modulation of this HF heating can produce ELF/VLF waves were made by Getmantsev *et al.* [1974], at a facility near Gor’kii, Russia, though the initial suggestion dates back much earlier [Ginzburg and Gurevich, 1960]. For this reason, ELF/VLF wave generation via modulated HF heating is referred to by some Russian authors as the ‘Getmantsev effect’.

At Gor’kii, the HF power was amplitude modulated at a variety of frequencies between 1.2 and 7 kHz, and small signals ( $0.02 \mu\text{V/m}$ ) at the modulation frequency were detected. Budilin *et al.* [1977] confirmed that the signals originated from the lower ionosphere, by measuring the phase (and therefore the delay) as a function of ELF/VLF frequency. These experiments generated only weak signals in large part due to being at mid-latitudes, where only the weak ‘Sq’ wind-driven currents are present in the ionosphere [Belyaev *et al.*, 1987]. However, at the suggestion of Kotik and Trakhtengerts [1975], experiments are presented by Kapustin *et al.* [1977] near Monchegorsk, Russia, in the presence of the auroral electrojet. Although the lack of calibrated data made it impossible to directly compare the signal strengths to the mid-latitude observation, the amplitude of the resulting ELF/VLF signal is found to be a strong function of the electrojet location (as determined with magnetometer measurements) with a maximum when the electrojet was overhead, indicating that the electrojet acts to strongly enhance the wave generation by providing a natural current source. Research continued at the Gor’kii facility, and the HF heater was later upgraded and named ‘SURA’.

The HF array facility near Tromsø, Norway, operated by the European Incoherent Scatter Scientific Association (EISCAT), began operation in 1980 and was almost immediately used for ELF/VLF wave generation [Stubbe *et al.*, 1981], where one of

three different arrays (for three different HF frequency ranges) could be utilized. One of the arrays was subsequently upgraded in 1990 [Barr and Stubbe, 1991a].

The Islote facility, near Arecibo, Puerto Rico, operated in the absence of a dominant natural current system, similar to the facility in Gor’kii. *Ferraro et al.* [1982] present data showing detection of signal levels of  $\sim 10^{-9}$  A/m, between 500–5000 Hz, with further analysis of the signals by *Ferraro et al.* [1984].

The Jicamarca facility is a radar facility in the Very High Frequency (30–300 MHz) band. Although the operating frequency is much higher than the other facilities, the Jicamarca radar was able to generate ELF/VLF radiation at 2.5 kHz with pulsed (5% duty cycle) VHF [Lunnen et al., 1984]. Despite the pulsed nature and the higher frequency (which, as is discussed later, is less advantageous for ELF/VLF wave generation), the Jicamarca experiments had the advantage of lying beneath another natural current system known as the equatorial electrojet. There have been few experiments on modulation of the equatorial electrojet, and this topic could be a significant area of future research in ionospheric modification.

Two additional facilities were constructed in Alaska for the purpose of heating the auroral ionosphere. The High Power Auroral Stimulation facility (HIPAS) utilizes equipment and modified designs originally used at Platteville [Wong et al., 1990], and began operation in 1987. Like the Tromsø facility, HIPAS was almost immediately utilized to demonstrate ELF/VLF wave generation [Ferraro et al., 1989], with amplitudes as high as 0.8 pT.

The most recent facility to begin operation is the High Frequency Active Auroral Research Program (HAARP). The HAARP facility was built in three stages, the latter two being completed in 2003 and then 2007. Again demonstrating the strong interest in ELF/VLF wave generation, *Milikh et al.* [1999] conduct experiments on modulated heating even at the very early construction stage known as the ‘developmental prototype’, which produced only 10 MW of ERP. *Milikh et al.* [1999] are also the first to utilize two nearby HF heating facilities, with simultaneous detection of ELF/VLF signals from HAARP and HIPAS HF heating. In this dissertation, we use experimental data obtained with the HAARP facility. A picture of the HF antenna array, known as the Ionospheric Research Instrument, is shown in Figure 1.6, as of





Figure 1.6: The HAARP HF heating facility

August 2005. The HAARP facility utilizes 3.6 MW of power, but some power is reflected at the antenna array (due to imperfect impedance matching between the near-field coupled antenna elements), so actual radiated power is slightly less. Appendix B discusses the actual transmitted powers and ERPs for a number of different HAARP beam modes.

## 1.6 Review of past work

We now review some of the past efforts in the field of HF ionospheric heating, focusing specifically on ELF/VLF generation. We consider a number of broad topics that have been given significant research attention, both theoretically and experimentally.

### 1.6.1 Local geomagnetic conditions

Many of the earlier efforts in ELF/VLF wave generation concerned its connection to geomagnetic activity, such as the auroral electrojet strength and orientation, and ionospheric conditions above the heater. These studies essentially discuss the usage of HF heating facilities as a diagnostic tool for the ionosphere. For instance, some studies have compared ELF/VLF amplitudes with other instrumental diagnostics. *Rietveld et al.* [1983] show that the polarization of ELF/VLF signals observed near Tromsø were highly correlated with the direction of the auroral electrojet fields as measured by the Scandinavian Twin Auroral Radar Experiment (STARE) radar. *Rietveld et al.* [1987] tracked the measurements over a 32 hour period, comparing also to STARE, and data from a riometer and magnetometer. *Jin et al.* [2009] also compare ELF/VLF generated amplitudes with data from a series of magnetometers in Alaska. *Rietveld et al.* [1986] transmit HF pulses of varying lengths and observed the ionospheric response, thereby allowing estimation of the characteristic heating and cooling time constants. *Rietveld and Stubbe* [1987] discuss the possibility of using the pulses as a diagnostic for the horizontal electrojet field structure. *Papadopoulos et al.* [2005] discuss similar results and experiments on the variation in the detected field on the ground from HF heating of varying pulse lengths, at the HAARP facility. *Rietveld et al.* [1989] present a comprehensive examination of the amplitude and ionospheric source height as a function of ELF/VLF frequency.

At the HIPAS facility, *Li and Ferraro* [1990] discuss estimation of the *D*-region electron density by transmitting a series of ELF/VLF signals in frequency steps, coupled with theoretical calculations of the reflection and transmission coefficients. *Lee et al.* [1990] use ELF/VLF signal amplitudes and phases to detect and characterize geomagnetic pulsations. *Milikh et al.* [1994] present hypothetical calculations of the electron temperature and density that would result from the HAARP facility. *Payne et al.* [2007] use a model of ELF/VLF generation, and measurements of the vertical electric field on the ground and around the HAARP heated region, to determine the direction of the auroral electrojet currents and fields. *Cohen et al.* [2008a] also discuss the direction of the auroral electrojet fields, using measurements of the polarization of ELF/VLF pulses at  $\sim 700$  km distance from the HAARP facility.

### 1.6.2 Earth-ionosphere waveguide injection

A number of efforts have focused on characterization of the properties of the generated signals in illuminating the Earth-ionosphere waveguide. These studies have addressed the feasibility of HF heating as a communication system for ELF/VLF waves. Along with theoretical calculations, measurements are made at long enough distances for propagating Earth-ionosphere waveguide modes to dominate the signal. In a theoretical calculation, *Barr and Stubbe* [1984] evaluate the source power as a function of frequency and ionospheric conditions, using the theory of reciprocity to associate the ionospheric source with an equivalent ground-based source.

A number of experimental efforts have focused on detection of the ELF/VLF radiation at increasingly long distances from the HF heating facility. *Belyaev et al.* [1987] report that signals from Gor’kii were detected at  $\sim 500$  km distance, but provide no other details. Another early effort is the report by *Ferraro et al.* [1982] of the possible detection of 2073 Hz signals in Pennsylvania,  $\sim 6000$  km distance from Tromsø, although *Barr et al.* [1986] and *Barr et al.* [1991] strongly question the results. *Barr et al.* [1985a] report a set of ELF/VLF detections in the Earth-ionosphere waveguide, at distances of 200 km and 500 km from the Tromsø facility. *Barr et al.* [1986] made use of the polarization of these signals, and showed that the frequency-dependence of the polarization at these medium distance receivers is linked to ionospheric conditions. *Barr et al.* [1991] detect signals at several frequencies  $\sim 2000$  km from the Tromsø facility, and show a good match between the polarization of the received signals, and predictions from a theoretical propagation model. *Moore et al.* [2007] present a similar study at HAARP, with detection of 2125 Hz and 575 Hz at Midway Atoll,  $\sim 4400$  km from HAARP, currently the most distant such detection. Signal levels at Midway were  $\sim 5$  fT averaged over a 1-hour long integration. Using a propagation model to link the received field value to a source power under a variety of different ionospheric conditions, HF to ELF/VLF conversion efficiency of HAARP into the Earth-ionosphere waveguide is estimated to be 0.0006% to 0.0032%. *Cohen et al.* [2009, in press] present evidence of a much stronger detection at Midway Atoll, shortly after the HAARP facility was upgraded. Signal amplitudes were in the range 15–20 fT, and were strong enough to be detected with integration times of less than a

second. This particular instance is also presented in Appendix A of this dissertation.

*McCarrick et al.* [1990] show that frequencies in the Schumann resonance range (11–76 Hz) can be excited using an ‘array dephasing’ technique that spreads the beam power over a wider area, and found that the received signal (detected 35 km away from HIPAS) was well correlated with electrojet activity. *Carroll and Ferraro* [1990] present computer simulations of ELF/VLF injection into the Earth-ionosphere waveguide from an ionospheric source.

### 1.6.3 Harmonic radiation and saturation

Since the response of the ionospheric conductivity to HF heating is highly nonlinear, the harmonic content of generated ELF/VLF signals is not the same as the harmonic content of the HF heating modulation function. In addition, the nonlinear dependence on the conductivity change with HF power has produced interest in a saturation process, or a point of diminishing return beyond which increasing powers yield little or no enhancement in ELF/VLF wave amplitudes. Alternatively, it is suggested that an increasing HF power may eventually trigger the beginning of an electron runaway process which increases the efficiency [*Papadopoulos et al.*, 1990]. In response to these questions, a number of studies have sought to quantify the relationship between HF power levels and harmonic content of the ELF/VLF signals.

*James* [1985], *Rowland et al.* [1996], and *Pashin and Lyatsky* [1997] present a theoretical model of the HF heating process, tracking the ionospheric conductivities as a function of time, and analyzing the resulting harmonic content. *Barr and Stubbe* [1993] derive the heating and cooling time constants in the ionosphere experimentally, and find that odd and even harmonics apparently yield different time constants. *Barr et al.* [1999] take this one step further, finding that the odd and even harmonics are in fact generated at different altitudes. *Oikarinen et al.* [1997] present experimental observations of the harmonic content. *Barr et al.* [1999] deduce the ionospheric heating and cooling time constants from the harmonic content and suggest that different harmonics are sourced at different altitudes due to the nonlinear heating process.

*Barr and Stubbe* [1991a] experimentally explore the amplitude of generated ELF and VLF waves as a function of ERP of the HF beam at Tromsø, and find no evidence of a saturation process. On the other hand, *Moore et al.* [2006] explore the second and third harmonics, and conclude that saturation is detectable with the earlier 960 kW HAARP facility. *Moore* [2007] present statistics indicating that detection of saturation is a function of the HF frequency level, and the location of the receiver.

#### 1.6.4 Magnetospheric injection

Some of the interest in ELF/VLF wave generation is based on its potential uses for magnetospheric injection, for the purpose of controlled experiments on magnetospheric and radiation belt processes, such as wave-particle interactions and electron precipitation. A large number of satellites (mostly in low earth orbit, or LEO, <1000 km altitude) have observed ELF/VLF signals generated with HF heating. However, the nature of LEO satellite passes (i.e., rapid motion of the satellite during the brief pass) has made it difficult to fully characterize (at least experimentally) the extent and properties of magnetospheric injection.

*James et al.* [1984] observe ELF/VLF radiation from Tromsø on the ISIS-1 satellite and compare to simultaneous ground measurements. *James et al.* [1990] subsequently observe signals with the DE-1 spacecraft, and discuss the harmonic content of the received signal, spectral broadening and propagation delays. *Lefevre et al.* [1985] observe ELF/VLF signals on the Aureol-3 satellite, from the Tromsø facility. *Kimura et al.* [1991] and *Kimura et al.* [1994] observe signals from HIPAS and Tromsø, respectively, on the Akebono satellite. *Yagitani et al.* [1994] construct a theoretical model of the radiation to LEO altitudes, with *Nagano et al.* [1994] then presenting an experiment at HIPAS with accompanying theoretical calculations.

A number of more recent detections have focused on the HAARP ELF/VLF signal radiated into space. The particular interest in HAARP arises from its location, which is just inside the plasmapause much of the time, therefore making it a good candidate for magnetospheric injection that may lead to an amplification process, in particular, after propagation in a ‘duct’ guiding structure. *Platino et al.* [2004] observed signals at

27–29 Mm altitude, on the CLUSTER spacecraft. *Platino et al.* [2006] subsequently observed signals at LEO altitudes on the DEMETER spacecraft. Further analysis on DEMETER observations are presented by *Piddyachiy et al.* [2008], regarding a narrow column of radiation (predicted by *Lehtinen and Inan* [2008]) extending into the magnetosphere. Finally, magnetosperic injection with HAARP has yielded the first examples of detectable wave-particle interactions initiated by ELF/VLF signals from modulated HF heating, first reported by *Inan et al.* [2004], with additional analysis by *Gołkowski et al.* [2008]. *Gołkowski et al.* [2009] also report cross modulation between the signals returning to the HAARP region after two magnetospheric hops (and  $\sim 8$  seconds delay) and the modulated HF-heated ionosphere, strong evidence that the magnetospherically propagating signals are injected very close to the HAARP facility.

### 1.6.5 Mobile heated region

*Rietveld et al.* [1984] introduce beam steering to the Tromsø array, by varying the phase of the HF waveform along the rows of the array. This capability enabled direction of the beam in the north-south direction, up to  $37^\circ$  from vertical in each direction, so that the heated region of the ionosphere could effectively be moved horizontally. Variations in the ELF/VLF amplitude at a nearby receiver as the beam is directed are observed to be connected to changes in the auroral electrojet field strengths, as separately measured by the STARE radar [*Rietveld et al.*, 1984].

*Barr et al.* [1985b] observe diffraction or scattering of VLF waves off of the HF-heated portion of the ionosphere, detected at more distant transmitters. Using the beam steering capability to move the heated region and therefore change the transmitter to heated region to receiver angle, the scattering is found to be almost exclusively in the forward direction, meaning it could be observed only on receivers positioned such that the transmitter to receiver path crosses the heated region.

*Barr et al.* [1987] measure the ELF/VLF signal at a receiver  $\sim 500$  km to the South of Tromsø, as a function of the beam steering angle (also in the north-south direction), and showed that the phase of the data received could be largely attributed to Earth-ionosphere waveguide properties. *Barr et al.* [1988] subsequently presented

the amplitude data, and found that Earth-ionosphere waveguide propagation was not sufficient to explain the results, but that the signal was also affected by the differences in phase between different portions of the heated region, owing to the fact that the HF energy took a finite time to reach the ionosphere, and this time delay varied across the width of the HF beam.

### 1.6.6 Beam painting

In a significant effort to raise the efficiency of HF to ELF/VLF conversion, *Papadopoulos et al.* [1989] and *Papadopoulos et al.* [1990] introduce a technique which subsequently became known as ‘beam painting’. The basic idea of beam painting is that ‘matching the operation of the HF heater to the nonlinear response of the ionospheric plasma’ [*Papadopoulos et al.*, 1989] can be achieved utilizing motion of a very high ERP beam at rapid rate. The specifics of beam painting are described in Chapter 3, but it suffices here to say that the technique involves effectively increasing the size of the ionospheric antenna. *Barr and Stubbe* [1991b] and *Barr et al.* [1999] both perform tests with the Tromsø facility and find that the ERP of the HF beam (the highest in the world at that time) is not sufficiently high for beam painting to yield any practical benefit. It has therefore fallen to the upgraded HAARP facility, with its unprecedented ERP and rapid beam steering ability, to address this possibility more directly.

### 1.6.7 Alternative methods

In a continuing effort to increase the generated amplitudes of ELF/VLF waves, other generation methods have been explored, particularly as an alternative to simply utilizing amplitude modulation. Both *Villaseñor et al.* [1996] and *Barr and Stubbe* [1997] discuss a ‘dual frequency’ or ‘CW’ mode (respectively named) in which the HF array is split into two halves, and driven with HF frequencies differing by the ELF/VLF frequency to be generated, essentially a beat-frequency method. Both studies conclude that amplitude modulation generates stronger ELF/VLF signals than the beat-frequency technique. However, *Barr and Stubbe* [1997] suggested, based on theoretical

calculations, that the CW technique would become substantially stronger for frequencies above  $\sim 3$  kHz, in the direction from the array where the lower of the two HF frequencies drives the array. *Kuo et al.* [1998] present further theoretical calculations comparing beat-frequency with amplitude modulation.

*Milikh and Papadopoulos* [2007] discuss a method of increasing efficiency in which the ionosphere is first heated continuously for several minutes, in order to build up a higher electron density in the *D*-region and sharpen the gradient of the ionospheric electron density profile, by lowering the electron-neutral attachment through long-timescale heating. The higher and sharper electron densities could then be used in ensuing minutes to generate ELF/VLF with better efficiency.

### 1.6.8 Ionospheric array

Along with a search for increased HF to ELF/VLF conversion efficiency, or higher generated amplitudes, some effort has been made to generate an array of ionospheric sources using HF heating. Such an array would have the advantage of providing directionality to injected ELF/VLF signals, since ordinary VLF transmitters (and amplitude modulated HF heating) are unable to provide any directional control. A straightforward way to provide directional control would be to build several VLF transmitters nearby, and operate them in a phased-array configuration, but given the expense and difficulty of constructing and operating one VLF transmitters, the resources required to operate several would be prohibitive.

The most prominent experimental example of an ELF/VLF array is that of *Barr et al.* [1987], who discuss a novel experiment in which the HF beam is alternated between two locations in the ionosphere, one to the north, and one to the south, at rates up to 5 kHz. This operation creates two heated regions in the ionosphere, displaced by an amount that could be controlled, undergoing ON-OFF heating with modulation functions  $180^\circ$  out of phase. By varying the separation between the two regions, and measuring the signal at a receiver  $\sim 500$  km from Tromsø, it is found that the two regions act as a two-element ELF/VLF array. A signature of constructive and destructive interference is detected, since the maximum signal at the receiver occurred



when the two heated regions were separated by one half wavelength, representing the  $180^\circ$  phase shift between the two regions. *Villaseñor et al.* [1996] describe a similar technique performed at the HIPAS facility, referred to therein as ‘demodulation mode’.

Some theoretical work has also occurred on the topic of an ionospheric array. *Werner and Ferraro* [1987] derived an array factor specifically for ionospheric sources. *Papadopoulos et al.* [1994] discuss the effect of Cerenkov radiation, when a source of ELF/VLF radiation is moving close to the speed of light, with a particular emphasis on injection of ELF/VLF energy into the magnetosphere. *Borisov et al.* [1996] extend this discussion to illumination of the Earth-ionosphere waveguide.

## 1.7 Scientific contributions

The following advances to the field of ELF/VLF wave generation are developed and reported in this dissertation:

- A novel method is introduced of ELF/VLF wave generation via frequency-matched steering of a continuous HF beam (herein referred to as ‘geometric modulation’), an alternative to amplitude modulation in which the beam power is left on, but the beam is steered in a geometric pattern at the desired ELF/VLF generation frequency. Using amplitude modulation as a baseline for comparison, it is demonstrated that  $\sim 7$ -11 dB higher ELF/VLF amplitudes, and  $\sim 11$ -15 dB directional dependence result from geometric modulation, compared to amplitude modulated vertical HF heating.
- A previously proposed technique known as ‘beam painting’ is successfully implemented for the first time, in which rapid (100 kHz) beam motion effectively increases the area of the radiating region of the ionosphere. Beam painting is directly compared with geometric modulation, as well as amplitude modulation.
- The HF heating and electron cooling processes are theoretically modeled in three dimensions, yielding the predicted spatial distribution of the ionospheric current sources generated. These results feed into a second model simulating ELF/VLF propagation in the Earth-ionosphere waveguide (and into the magnetosphere),

to determine the radiated patterns up to 1000 km along the Earth, and up to 700 km into the ionosphere.

- Using a combination of experimental and theoretical results, the results achieved with geometric modulation are interpreted in terms of a controllable ELF/VLF multi-element phased array, which allows controllable directional launching of ELF/VLF energy in the Earth/ionosphere waveguide.

## 1.8 Approach

We have now introduced the environment that dominates the problem we consider, motivated the need for ELF/VLF wave generation, and reviewed past efforts in the field. The remainder of this dissertation is as follows: In Chapter 2, we illuminate the physics of the problem by describing a theoretical model, including HF ionospheric modification resulting in ELF/VLF generation, whose output drives a full-wave model of ELF/VLF wave propagation. In Chapter 3, we apply the experimental techniques to a set of modulation schemes which involve motion of the HF beam during the ELF/VLF period. In Chapter 4, we then analyze the theoretical modeling results, compare to experiment, and thereby predict features of the modulation techniques which would be measurable with additional receivers. In Chapter 5, we utilize a combination of theory and experiment to illuminate the degree to which four particular physical mechanisms impact our experimental and theoretical approach. Finally, in Chapter 6 we summarize and suggest additional future efforts.

## Chapter 2

# ELF/VLF Generation and Propagation Physics

In this chapter, we introduce the physical phenomena in the propagation of electromagnetic waves in a magnetized plasma, and describe a theoretical model to apply these principles to our problem of High Frequency (HF, 3–30 MHz) heating of the ionosphere, and ELF/VLF wave generation and propagation.

### 2.1 Waves in plasmas

The Earth's ionosphere and magnetosphere are both prominent examples of the plasma state of matter. Plasmas are sometimes referred to as the fourth state of matter, after solid, liquid, and then gas [*Bittencourt*, 2003, pg.1]. In a plasma, a large enough number of molecules have been split apart into positive and negative charged particles, like electrons, protons, and ions, with the net charge remaining zero. Waves propagating in a plasma have a number of unique characteristics as compared to propagation in simpler media, like free space or a dielectric. The effect of an externally applied magnetic field (such as that of the Earth's geomagnetic field) alters the physics additionally, most notably by introducing anisotropy to the problem. Collisions between particles have a further complicating impact. We begin by introducing the key concepts of plasmas that are needed to understand the problem.

Note that for the remainder of this dissertation, we use the term ‘electrons’ to refer exclusively to the free ionized electrons, as opposed to electrons which orbit around molecules. Although by definition, a plasma is quasi-neutral, consisting of equal amounts of positive and negative charge, it is the electrons that are chiefly responsible for the physical processes we describe here, whereas the positive ions, which are many orders of magnitude heavier (and thus harder to accelerate with electromagnetic fields), play a negligible role at the ELF/VLF and HF frequencies considered here.

Many treatments of plasma physics tend to give very mathematical descriptions of the various phenomena involved in wave propagation in a plasma. This fact is largely due to the highly complex nature of this subject, in which nearly all traditional ways of simplifying electromagnetics problems (homogeneity, isotropy, linearity, non-dispersiveness) are violated. On the other hand, while the mathematical results (adequately treated in other works) may be too highly nuanced for basic intuition, the basic physical processes which interplay to underlie all the physics of wave propagation in a plasma are well within reason. It seems somewhat of a lost art to recapture the physical intuition in plasma physics, so we focus here on illuminating the various physical components which contribute to wave propagation.

### 2.1.1 Plasma properties

Consider first a plasma with no externally-applied magnetic field, and a negligible number of collisions. The positive and negative particles can block electromagnetic fields from having an impact any more than a short distance away, by rearranging slightly to cancel out the fields, a phenomenon known as Debye shielding. Because electrons are so much lighter than ions, they are able to rearrange much more quickly, and thus in a typical plasma, the by-far dominant Debye shielding arises from electrons. The denser are the electrons, the quicker is the Debye shielding process, and this characteristic response time gives rise to the concept of the plasma frequency

$$\omega_{pe} = q \sqrt{\frac{n_e}{m_e \epsilon_0}} \quad (2.1)$$

Where  $N_e$  is the density of electrons,  $m_e$  is the mass of an electron, and  $q$  is the charge of an electron. An example of the derivation of the plasma frequency is done by *Budden* [1985, pg. 39]. The quantity  $\omega_{pe}$  can also be thought of as the natural frequency of oscillation of the electrons.

A wave propagating in such a plasma is thus unable to propagate unless its electromagnetic fields change faster than the plasma can shield and cancel the fields, that is to say, an electromagnetic wave is unable to propagate unless its frequency is above  $\omega_{pe}$ .

Even the relatively small electron densities in the  $D$  region are sufficiently high for Debye shielding to take place. For instance, the plasma frequency is 3 kHz for an electron density of  $\sim 1.1 \times 10^5 \text{ m}^{-3}$ , while electron densities in the  $D$  region (above 65 km) are substantially higher, as shown in Figure 1.1. So the plasma frequency is well above the wave frequency at all ionospheric altitudes, for ELF/VLF frequencies.

### 2.1.2 Magnetic field and the whistler wave

Based on the fact that the plasma frequency exceeds the ELF/VLF wave frequency at very low altitudes, it would seem that ELF/VLF waves should be blocked well before they reach the  $D$  region. However, the effect of the magnetic field and collisions prevent this from happening. Let us consider the effect of an externally applied magnetic field to the plasma, since the Earth's geomagnetic field appears across the ionosphere and magnetosphere, but at this point, we assume there are still no particle collisions.

Consider that in the presence of an externally applied magnetic field  $\vec{B}_0$  (such as the magnetic field of the Earth), a charged particle will experience the so-called Lorentz force

$$\vec{F} = q\vec{v} \times \vec{B}_0 \quad (2.2)$$

where  $m_e$  is the electron mass,  $\vec{v}$  is the velocity of the particle, and  $B_0$  is the applied magnetic field. For a homogeneous magnetic field, the Lorentz force will cause the particle to gyrate around the magnetic field at a specific frequency, known as the

gyrofrequency, in response to an applied electric field with a component orthogonal to the magnetic field. The gyrofrequency is given by

$$\omega_{ce} = \frac{qB_0}{m_e} \quad (2.3)$$

Thus, horizontal linear motion is allowed only along the magnetic field line, since the Lorentz Force in that direction is zero. Motion in the plane perpendicular to  $\vec{B}$  is constrained to follow circular motion. All the electrons present in a plasma are therefore constrained to orbit the magnetic field line at  $\omega_{ce}$ , with possibly some additional linear motion along the magnetic field line.

For a right hand circularly polarized wave at frequency below  $\omega_{ce}$ , the electron response to the wave involves motion around the magnetic field line at the wave frequency, and this motion then re-radiates electromagnetic energy that allows the wave to propagate. In essence, Debye shielding (which would otherwise short-circuit the wave electric field) is overcome because the electron response to the wave simply re-contributes the energy back to the wave via radiation. A nice discussion of this re-radiation process is given by *Ratcliffe* [1959, ch.3]. This special mode of propagation below the plasma frequency due to the applied magnetic field is known as the ‘whistler mode’. The whistler mode energy propagates at a slower velocity than the speed of light, particularly at frequencies well below  $\omega_{ce}$ .

### 2.1.3 Anisotropy

A second effect of the magnetic field is to introduce anisotropy to the ionosphere. For instance, consider that an electric field,  $\vec{E}$ , applied to the plasma causes electrons to respond and generate a current,  $\vec{J}$ . In isotropic media, Ohm’s law tells us that  $\vec{J} = \sigma \vec{E}$ , where  $\sigma$ , the conductivity, is a simple scalar. In a magnetized plasma, if  $\vec{E}$  is applied parallel to the magnetic field, electrons are accelerated strictly in that direction, since the Lorentz force equation (2.2) has no component along  $\vec{B}_0$ . In that sense, the magnetic field may as well not exist, and the scalar Ohm’s law is obeyed, as defined by the so-called parallel conductivity. On the other hand, for  $\vec{E}$  applied perpendicular to the magnetic field, electrons are not able to travel strictly

along  $\vec{E}$  due to the Lorentz force, and are forced also in the direction of  $\vec{E} \times \vec{B}_0$ . This forcing gives rise to the so-called Pedersen and Hall conductivities, referring to the ionospheric currents generated parallel to and perpendicular to  $\vec{E}$  (respectively), when  $\vec{E}$  is perpendicular to  $\vec{B}_0$ .

For this reason, we must write the conductivity as a tensor quantity ( $\bar{\bar{\sigma}}$ ), so that from Ohm's law we calculate the currents generated as

$$\vec{J} = \bar{\bar{\sigma}} \vec{E} \quad (2.4)$$

It is convenient to utilize a coordinate system in which the  $z$ -axis is along  $\vec{B}_0$ , the  $z$  axis is perpendicular to both  $\vec{E}$  and  $\vec{B}_0$ , and the horizontal axis defined so as to set up a right hand coordinate system ( $\hat{y} \times \hat{z} = \hat{x}$ ). This coordinate system is shown in Figure 2.1. We therefore have

$$\bar{\bar{\sigma}} = \begin{bmatrix} \sigma_P & -\sigma_H & 0 \\ \sigma_H & \sigma_P & 0 \\ 0 & 0 & \sigma_{\parallel} \end{bmatrix} \quad (2.5)$$

where  $\sigma_P$ ,  $\sigma_H$ , and  $\sigma_{\parallel}$  are the Pedersen, Hall, and parallel conductivities, respectively. The expressions for these conductivities are discussed later in this chapter.

### 2.1.4 Collisions

In the  $D$ -region of the ionosphere, the atmosphere is still thick enough that electrons frequently collide with neutrals. (In this context, 'frequently' means that there is a nonnegligible chance that an electron undergoes a collision during one cycle of the wave period.) Since there are many more neutral particles than ionized particles, collisions between two ionized particles are comparatively rare. The dominant form of collision, between electrons and neutral molecules, is much like a ping pong ball hitting a bowling ball, since the electron is extremely light compared to any neutral molecule. In each collision, an electron is scattered in some direction, and so after a few collisions, the electron carries no memory of what direction it moved earlier.

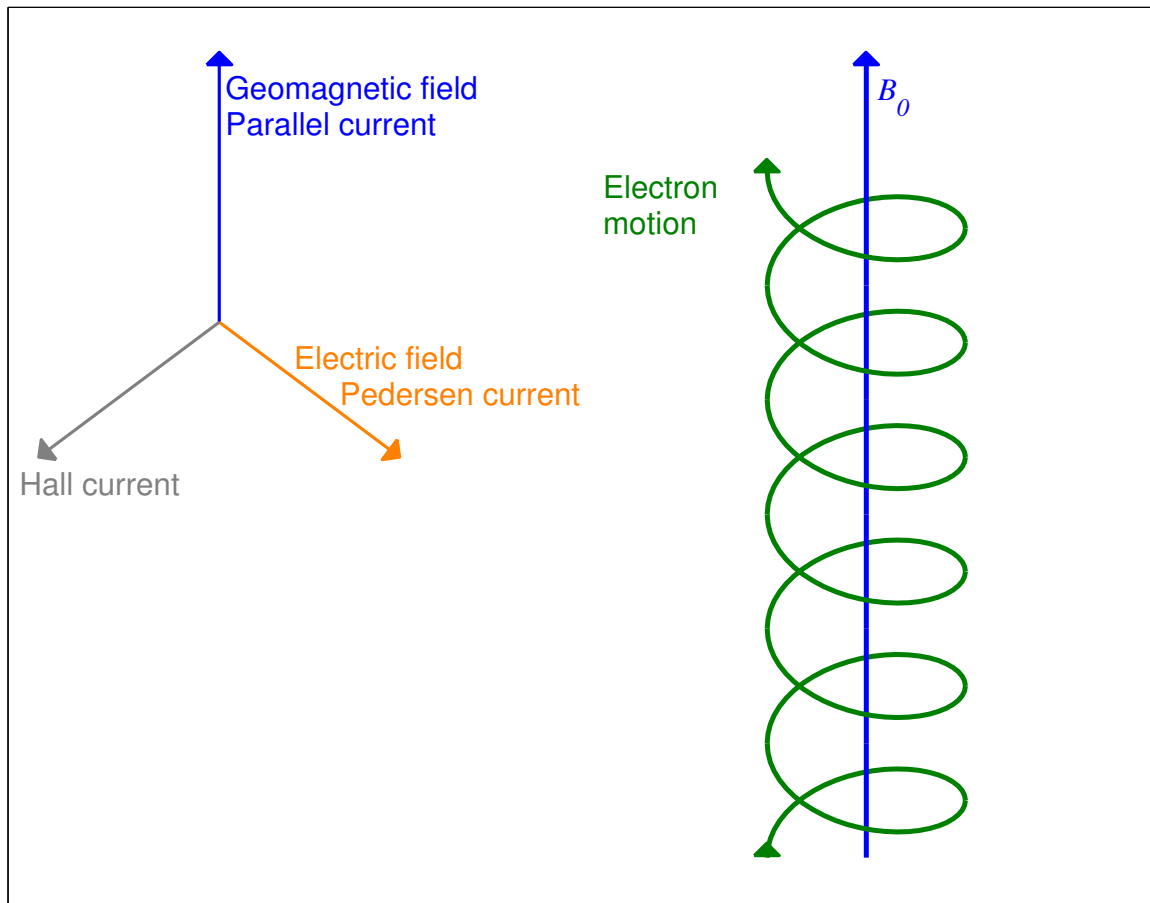


Figure 2.1: Coordinate system for ionospheric conductivity



The rapid electron-neutral collisions in the  $D$  region produce a mechanism by which a propagating wave can lose energy. A nice discussion of the microscopic reason for collisional damping of waves is given by *Ratcliffe* [1959, ch.5], and we focus here on a detailed qualitative description, since the details of the mathematics is adequately covered elsewhere. The basic idea is that the frequent collisions and associated redirecting of the each electron's velocity cause the orderly energy in the propagating wave to be converted to random heat energy, first in the electrons, and from there to the neutral molecules. (However, being composed of molecules that are so much more massive than electrons, the neutral atmosphere exhibits essentially no temperature rise as a result of this energy deposition, so in this context it is like an infinite energy sink).

Let us consider the case where an electromagnetic wave is at a frequency above the plasma frequency (such as for HF waves in the  $D$  region), so that Debye shielding does not adequately take place, and the wave is propagating. At any given time, electrons are being accelerated/decelerated by the electromagnetic field associated with the propagating wave, so that some electrons are gaining energy, and some are losing. The key, however, is that this combination results in a net gain of electron energy. As a simple example, consider two electrons traveling in opposite directions, with a speed  $v$ , in the presence of parallel electric field that changes the speed of each by  $0.1v$  in some given time span. One of the electrons is accelerated, the other decelerated, but the total kinetic energy ( $\frac{1}{2}mv^2$ ) of two electrons with speeds of  $1.1v$  and  $0.9v$  is higher than the total kinetic energy of two electrons both at speed  $v$ .

If there were no collisions, none of that would impact electron temperature, because whatever speed is gained/lost by an electron in the first half of the wave period is promptly reversed in the second half of the wave period (since the electric field is reversed), so that the electrons neither gain nor lose heat in the long term (i.e., this back and forth would constitute ordered energy, not random heat motion). In the presence of collisions, however, some number of electrons are accelerated/decelerated during part of the wave period, but then collide with a neutral molecule before the end of the wave period. The collisions scatter the added energy in random directions, thereby converting that energy it into heat.

Furthermore, the collision itself between an electron and a neutral molecule has a tendency to transfer energy from the more energetic of the two to the less energetic. As the electron temperature (or average energy) rises above the temperature of the neutral molecules, there is therefore a tendency for the electrons to lose that gained energy to the neutral atmosphere. A nice physical and mathematical discussion of this is given by *Huxley and Crompton* [1962, edited by Bates, D. R.].

In this manner, a propagating electromagnetic wave can be damped as it crosses a collisional plasma. The mathematics of this damping process are encompassed in the so-called Appleton-Hartree equation discussed below, and this ability for HF wave energy to be deposited onto free electrons via collisions as it crosses through this region is in fact the key field-matter interaction that drives our ability to modify the *D*-region with powerful HF waves. Unlike electron density, which in the *D* region varies heavily, the collision frequency is essentially constant in time (for a given electron temperature), since it depends on the neutral densities, which themselves remain constant.

### 2.1.5 The *D*-region

The comparative effects of the plasma frequency, geomagnetic field, and collisions, are often evaluated with three parameters which normalize the characteristic frequencies to the wave frequency,  $\omega$ . These three parameters are

$$X = \frac{\omega_{pe}^2}{\omega^2} \quad (2.6)$$

$$Y = \frac{\omega_{ce}}{\omega} \quad (2.7)$$

$$Z = \frac{\nu_{\text{eff}}}{\omega} \quad (2.8)$$

where  $\nu_{\text{eff}}$  is an effective electron-neutral collision frequency. *X* normalizes the wave frequency to the plasma frequency, *Y* normalizes the wave frequency to the gyrofrequency, and *Z* normalizes the wave frequency to collision frequency, so the three parameters tell us the impacts of Debye shielding, the magnetic field gyromotion,

and collisions, respectively, on the wave dynamics. For instance,  $Y \simeq 0$  indicates that the wave frequency is much higher than the gyrofrequency, so such a plasma can be treated as nonmagnetized, meaning that removing the magnetic field would have little or no impact on the dynamics.  $Z \simeq 0$  implies that collisions are too rare to have an impact on wave dynamics, therefore the plasma can be considered collisionless.

Figure 2.2 shows the three ionospheric parameters for the summer daytime and winter nighttime ionosphere shown in Figure 1.1. The plasma frequency equals the wave frequency (i.e.  $X=1$ ) somewhere below 50 km in the daytime, and  $\sim 73$  km at nighttime. In the absence of the geomagnetic field and collisions, a 3 kHz wave would be reflected at those altitudes. However, the high rate of collisions prevent the electrons from rearranging in an orderly matter, and this result then prevents the Debye shielding from occurring if  $Z > X$ . The reflection of the 3 kHz waves can thus be roughly considered to occur roughly at the point where collisions can no longer counteract the effects of Debye shielding, i.e.  $X = Z$ . In the daytime ionosphere shown here, and at 3 kHz, this condition occurs at  $\sim 61$  km, and for the nighttime ionosphere,  $\sim 80$  km. Experimental results for VLF transmitter frequencies around 20–30 kHz indicate that the reflection heights are more like 70 km and 85 km, for daytime and nighttime mid-latitude ionospheres, respectively [Thomson, 1993; Thomson *et al.*, 2007].

The calculation of the refractive index,  $n$ , in a magnetized collisional plasma requires use of the full Appleton-Hartree equation, which can be written in terms of  $X$ ,  $Y$ , and  $Z$ . The refractive index is an important quantity, since the real part drives the propagation of the waves through the medium, whereas the imaginary part (or the absorptive part) determines the absorption via collisions (a negative imaginary part indicates absorption). This important equation is:

$$n^2 = 1 - \frac{X}{1 - jZ - \frac{Y^2 \sin^2 \theta}{2(1-X-jZ)} \pm Y \sqrt{\frac{Y^4 \sin^4 \theta}{4(1-X-jZ)^2} + \cos^2 \theta}} \quad (2.9)$$

where  $\theta$  is the angle between the wave  $k$ -vector and the geomagnetic field. A derivation of the Appleton-Hartree equation is found in Budden [1985, ch.4]. The aforementioned phenomenon where an ELF/VLF wave reflects generally near the altitude where  $X=Z$

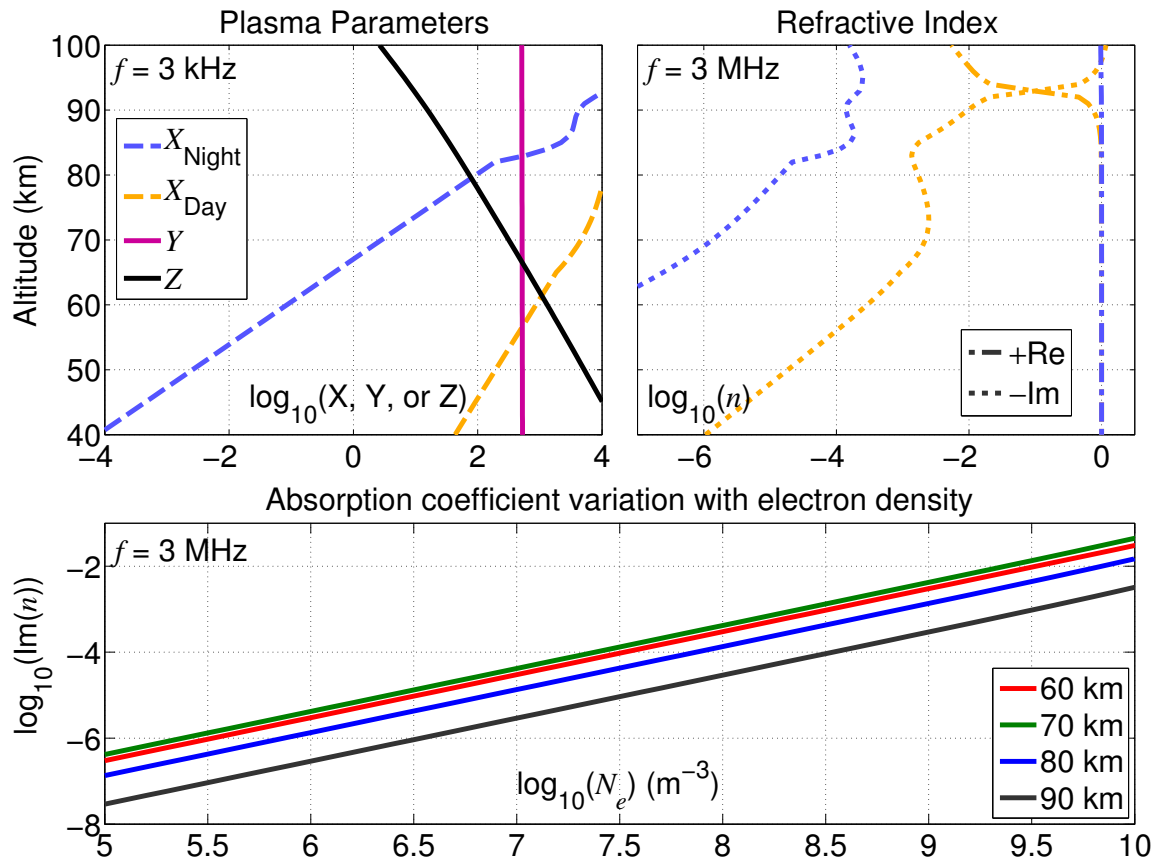


Figure 2.2: Ionospheric plasma parameters

can be seen mathematically, as well, since for  $X > 1$  and  $Z \gg X$ , the second term on the right side has a negligible effect. *Budden* [1961b, ch.16] gives a mathematical description of this reflection process in terms of a sharpening of the gradient of the refractive index with altitude near where  $X = Z$ .

The top right panel of Figure 2.2 shows the real and the negative of the imaginary part of the refractive index for a 3 MHz wave, for both the daytime (orange) and nighttime (blue) ionospheres. The real part of the refractive index remains close to 1 until  $\sim 85$  km. Above 85 km, the real part of the daytime refractive index rapidly shrinks, and the refractive index is dominated by the imaginary part. At night, though, electron densities are sufficiently low that the refractive index is dominated by the real part, which remains very close to 1.

The refractive index in the HF realm also demonstrates one important property which we refer to later in this chapter. As stated, the collision frequency does not change as a result of the highly variable electron densities. We can thus plot the absorptive part of  $n$  as a function of electron density, for several different altitudes, as is shown in the bottom panel of Figure 2.2. The important property to take note of is that over a wide range of electron densities and altitudes, the collisional absorption is essentially proportional to the electron density.

## 2.2 HF heating theory

We now describe the theoretical formulation of the HF heating model utilized in this dissertation. We are concerned with the generation of ELF/VLF waves based on Equation 2.4, where  $\bar{\sigma}$  has a quasi-static component (driven by ionospheric ambient conditions), and a component at the ELF/VLF frequency, driven by ionospheric modification. Since  $\vec{E}$  is the effectively constant electric field of the auroral electrojet, our goal is to determine the component of  $\bar{\sigma}$  which changes at ELF/VLF frequencies as a result of HF heating. So we seek to simulate and characterize a phasor value of  $\bar{\sigma}$  at the frequency of interest, which may vary spatially across the three dimensional volume of the ionosphere affected by HF heating.

### 2.2.1 Electron temperature

Our first goal is to track the electron energy distribution in the ionosphere as it responds to the heating (and as it subsequently recovers from lack thereof). In the absence of an external driving force, an ambient collisional plasma will tend toward a distribution of electron velocities known as the Maxwell-Boltzmann distribution *Bittencourt* [2003, pg.165],

$$f_e = N_e \left( \frac{m_e}{2\pi k_B T_e} \right)^{\frac{3}{2}} e^{-\frac{m_e v_e^2}{2k_B T_e}} \quad (2.10)$$

where  $N_e$  is the number density of electrons,  $v_e$  is the electron velocity,  $k_B$  is Boltzmann's constant, and  $T_e$  is the electron temperature. By integrating the distribution over  $v_e$ , the average energy turns out to be  $\frac{3}{2}k_B T_e$ , proportional to temperature.

The problem of tracking the evolution of this distribution in response to an external driving force may in general be quite complicated, since different electron energy levels absorb the wave energy, and then subsequently recover, at different rates. As a result, the heating and cooling dynamics must be separately tracked at all electron energies. For instance, in association with very intense heating of the ionosphere (such as heating from the electromagnetic pulse of lightning [*Taranenko et al.*, 1993]) the electron energies do not in general remain Maxwellian. A complete formulation therefore must track the more complete electron energy distribution as it evolves in time.

However, a number of past studies [*Stubbe and Kopka*, 1977; *James*, 1985; *Moore*, 2007] assumed that even the most powerful HF waves considered in ionospheric heating experiments are not powerful enough to significantly perturb the basic Maxwellian shape of the electron energy distribution. Although the electron temperature  $T_e$  may drastically change, the electron energy distribution remains roughly 'Maxwellian' [*Bittencourt*, 2003, pg.165]. This assumption greatly simplifies our task, since we can track the entire electron energy distribution with just a single parameter ( $T_e$ ), which gives us exceptional computational efficiency. We therefore apply this assumption for the remainder of this dissertation, and no longer refer to electron energies, but represent heating only in terms of the electron temperature.

The temporal evolution of the electron temperature requires the tracking the HF energy absorbed by the electrons as well as the energy lost to other particles (both occurring via collisions). The effects two balance out to a rate of change of electron energy  $\frac{3}{2}N_e k_B (dT_e/dt)$ , in an equation (adapted from *James* [1985]) that takes the form

$$\frac{3}{2}N_e k_B \frac{dT_e}{dt} = 2k\chi S - L_e \quad (2.11)$$

where  $k$  is the wavenumber of the HF wave ( $2\pi/\lambda$ ),  $-\chi$  is the imaginary part of the refractive index  $n$  (calculated from the aforementioned Appleton-Hartree equation), and  $S$  is the power density of the HF wave. In this equation, the left hand term shows the time-varying electron energy, the first term on the right is the absorbed HF power, and the second term ( $L_e$ ) is the electron loss rate.

The electron loss term,  $L_e$ , is a sum of losses from elastic collisions, rotational excitation, and vibrational excitation, for both molecular nitrogen ( $N_2$ ) and oxygen ( $O_2$ ). These equations are compiled by *Rodriguez* [1994, pg.175-178], with the elastic loss rates given by *Banks* [1966], the rotational excitation loss rates given by *Mentzoni and Row* [1963] and *Dalgarno et al.* [1968], and the vibrational excitation loss rates given by *Stubbe and Varnum* [1972]. These equations are as follows:

$$L_{\text{elast}}^{N_2} = 1.89 \times 10^{-44} N_e N_{N_2} (1 - 1.21 \times 10^{-4} T_e) (T_e - T_0) \quad (2.12)$$

$$L_{\text{elast}}^{O_2} = 1.29 \times 10^{-43} N_e N_{O_2} (1 - 3.6 \times 10^{-2} \sqrt{T_e}) (T_e - T_0) \quad (2.13)$$

$$L_{\text{rot}}^{N_2} = 4.65 \times 10^{-39} N_e N_{N_2} \frac{T_e - T_0}{\sqrt{T_e}} \quad (2.14)$$

$$L_{\text{rot}}^{O_2} = 1.11 \times 10^{-38} N_e N_{O_2} \frac{T_e - T_0}{\sqrt{T_e}} \quad (2.15)$$

$$L_{\text{vib}}^{\text{N}_2} = 4.79 \times 10^{-37} N_e N_{\text{N}_2} e^{f_{\text{N}_2}(T_e - 2000)/(2000T_e)} [1 - e^{-g(T_e - T_0)/(T_e T_0)}] \quad (2.16)$$

$$L_{\text{vib}}^{\text{O}_2} = 8.32 \times 10^{-38} N_e N_{\text{O}_2} e^{f_{\text{O}_2}(T_e - 700)/(700T_e)} [1 - e^{-2700(T_e - T_0)/(T_e T_0)}] \quad (2.17)$$

where  $T_0$  is the ambient temperature,  $N_{\text{N}_2}$  and  $N_{\text{O}_2}$  are the number densities of molecular nitrogen and oxygen, respectively, and  $f_{\text{N}_2}$ ,  $f_{\text{O}_2}$  and  $g$  are dimensionless quantities given by

$$f_{\text{N}_2} = 1.06 \times 10^4 + 7.51 \times 10^3 \tanh[0.0011(T_e - 1800)] \quad (2.18)$$

$$f_{\text{O}_2} = 3300 - 839 \sin[0.000191(T_e - 2700)] \quad (2.19)$$

$$g = 3300 + 1.233(T_e - 1000) - 2.056 \times 10^{-4}(T_e - 1000)(T_e - 4000) \quad (2.20)$$

### 2.2.2 Modified ionosphere

Although we now have the ability to track the changing electron temperature, our actual objective is to deduce the modified electrical properties of the ionosphere, and the induced modulated currents in the presence of the auroral electrojet system, so the electron temperature must be related to ionospheric conductivity. We first calculate the modified collision frequency as a result of the changing electron temperature (as in *Rodriguez* [1994, pg.176]) as a sum of the average collision rates with  $\text{O}_2$  and  $\text{N}_2$

$$\nu_{\text{eff}}^{\text{N}_2} = \frac{5}{3} \nu_{\text{av}}^{\text{N}_2} = \frac{5}{3} \cdot 2.33 \times 10^{-17} N_{\text{N}_2} (1 - 1.25 \times 10^{-4} T_e) T_e \quad (2.21)$$

$$\nu_{\text{eff}}^{\text{O}_2} = \frac{5}{3} \nu_{\text{av}}^{\text{O}_2} = \frac{5}{3} \cdot 1.82 \times 10^{-16} N_{\text{N}_2} (1 - 3.60 \times 10^{-2} \sqrt{T_e}) \sqrt{T_e} \quad (2.22)$$

For the purpose of calculating the ionospheric conductivity, the average collision rate  $\nu_{\text{av}}$ , is multiplied by an additional factor of  $\frac{5}{3}$ , because Equation 2.9 assumes a velocity-dependent collision frequency. The factor  $\frac{5}{3}$ , derived by *Sen and Wyller* [1960], yields an effective collision frequency,  $\nu_{\text{eff}}$ , which, for quasi-transverse propagation, may be



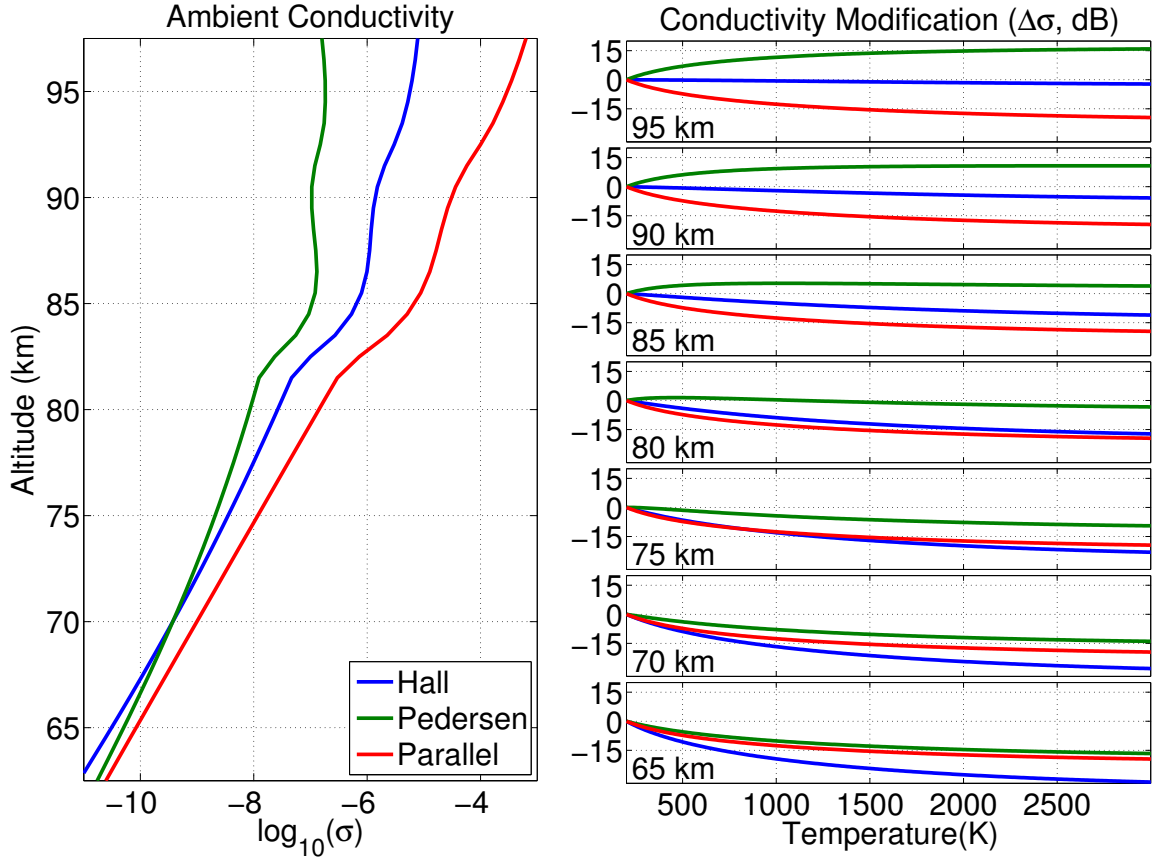


Figure 2.3: Variations of ionospheric conductivities as a function of temperature

used in Equation 2.9 when  $|\omega \pm \omega_{ce}| \gg \nu_{av}$ , as is the case for altitudes above 65 km or so.

The ionospheric conductivity components as in Equation 2.5 are derived in *Tomko* [1981, pg. 137] from kinetic calculations, and are given as a function of the driving frequency. However, since the auroral electrojet is treated here as constant, we can rewrite those expressions as

$$\sigma_P = \frac{4\pi q^2}{3m_e} \int \frac{\nu_{av} v_e^3}{\nu_{av}^2 + \omega_{ce}^2} \frac{\partial f_e}{\partial v_e} dv_e \quad (2.23)$$

$$\sigma_H = \frac{4\pi q^2}{3m_e} \int \frac{\omega_{ce} v_e^3}{\nu_{av}^2 + \omega_{ce}^2} \frac{\partial f_e}{\partial v_e} dv_e \quad (2.24)$$

$$\sigma_{\parallel} = \frac{4\pi q^2}{3m_e} \int \frac{v_e^3}{\nu_{av}} \frac{\partial f_e}{\partial v_e} dv_e \quad (2.25)$$

where  $f_e$  is the electron distribution function (the number density of electrons as a function of energy).

Figure 2.3 shows the relationship between temperature and ionospheric conductivity. The left panel shows the ambient ionospheric conductivities, based on the nighttime ionosphere shown in Figure 2.2. Due to the high conductivity of a magnetized plasma along the magnetic field,  $\sigma_{\parallel}$  is the highest conductivity at all altitudes, especially at higher altitudes where collisions are very low. At an altitude of  $\sim 70$  km,  $\sigma_H = \sigma_P$ , and above this altitude,  $\sigma_H$  increasingly dominates over  $\sigma_P$ .

The right hand panels of Figure 2.3 show the relationship between increasing temperature and the three ionospheric conductivities (the dB values are in comparison to  $T_e=200$  K), at several different altitudes. At all altitudes shown,  $\sigma_H$  and  $\sigma_{\parallel}$  decrease with electron heating, by as much as 30 dB at 65 km and 3000 K. This decrease is due to the heated electrons colliding much more often and therefore having a lower mobility. The Hall conductivity, however, changes very little with temperature at the highest altitudes.

The changes to  $\sigma_P$  are quite different in character. Below  $\sim 80$  km,  $\sigma_P$  is decreased by as much as 15 dB, but above 80 km,  $\sigma_P$  is enhanced as a result of electron heating. The fundamental reason is that the higher collisions impede the electrons from gyrotating around the magnetic field line, so the Pedersen conductivity, which has a component in the direction of the electric field, is boosted (at the expense of less Hall conductivity). This behavior is one of the reasons that modulation of  $\sigma_P$  is believed to be less important in the context of ELF/VLF generation, since the regions above and below 80 km have opposite reactions to electron heating in terms of  $\sigma_P$ , which means the generation effects may counteract and tend to cancel one another.

### 2.2.3 HF wave propagation

One final complication arises from the fact that HF waves propagating in the ionosphere do not in general travel in a straight line at the speed of light. *Moore* [2007, pp. 22-26] discusses the main principles, which we briefly review here. There are two main sources of bending of the HF wave. Assume that the HF wave is incident on a sharp boundary from a medium with refractive index  $n_1$  into a medium with refractive index  $n_2$ . Assume the wave normal is incident at an angle  $\theta_1$  with respect to the boundary normal, and is refracted into the second medium at an angle  $\theta_2$ . The first source of wave bending is from Snell's law, which causes the HF ray to bend according to

$$\Re(n_1) \sin(\theta_1) = \Re(n_2) \sin(\theta_2) \quad (2.26)$$

However, the anisotropy of the ionosphere also causes the HF energy to travel in a different direction from the wave normal, and this angular separation is governed by

$$\tan(\Delta\Theta) = \frac{1}{n} \frac{\partial n}{\partial \Theta} \quad (2.27)$$

where  $\Theta$  is the angle between the wave normal and the Earth's magnetic field line, and  $\Delta\Theta$  is the deflection of that angle away from the magnetic field. For HF waves in the *D*-region, the ionosphere can be divided into a series of horizontal layers, and the propagation of the HF energy through each boundary is a good approximation of the propagation through the more smoothly varying ionosphere, a technique known as ray tracing [*Budden*, 1985, ch.14]. At each boundary, the HF energy is refracted according to the above two laws. Finally, we must also keep track of the group velocity ( $v_g$ ) of the HF energy, which is derived by [*Budden*, 1985, pg.130] and given as

$$v_g = c \frac{\partial \omega}{\partial(\omega n)} \frac{1}{\cos(\Delta\Theta)} \quad (2.28)$$

In practice, the bending and slowing of HF energy as it encounters an increasingly dense ionosphere has a rather small effect on our theoretical results, since most of the

bending and slowing of the HF wave occurs above the altitude where most of the HF energy is absorbed. However, it is worth noting that the ray tracing properties do not change appreciably during the HF heating process, since the real part of  $n$  is largely unchanged by HF heating. Hence, tracking the ray tracing properties requires just one set of calculations for a given ionosphere, and does not have to be recalculated at each time step. Given the meager computational resources required, in the HF heating model described here we nevertheless choose to fully track the bending and slowing of the HF energy.

## 2.3 Model construction

The difficulty with constructing a model to predict the ionospheric response to HF heating from the ground is that the energy balance equation (defined by Equation 2.11) is nonlinear and time-variant, so that an analytical solution is difficult, if not impossible. We can, however, break up these nonlinearities into two separate pieces, and describe each one separately.

### 2.3.1 Energy balance at one altitude

First, consider the three terms of the electron energy balance (Equation 2.11). It can be seen that both the left hand term, and the right hand term (reflected in Equations 2.13-2.17) are proportional to the electron density  $N_e$ . However, as can be seen from Figure 2.2, the absorption coefficient  $\chi = -\Im(n)$  is also approximately proportional to  $N_e$  for the range of electron densities and collision frequencies considered here. Therefore, the dependence on  $N_e$  can be effectively removed from Equation 2.11, yielding an equation dependent only on  $\nu_{av}$  and the HF wave power density  $S$ .

It can also be seen that Equation 2.22 which converts electron temperature to collision frequency, is not dependent on  $N_e$ , but rather is only dependent upon the neutral densities of molecular nitrogen and oxygen, and the electron temperature. And finally, the expression for ionospheric conductivity (Equations 2.25) is strictly proportional to  $N_e$  (via the term  $\partial f_e / \partial v_e$ ), so that the dependence of conductivity

changes on electron density is linear and straightforward.

This important result implies that the nonlinear dynamics of heating and cooling at a given altitude do not depend on the highly variable electron density conditions at that altitude, but only on HF power density and collision frequency. In the larger context, the amount of HF power that reaches a certain altitude is dependent on the absorption below that altitude, which is a strong function of the ionospheric electron densities, but this aspect can be separately treated later. For now, we can begin by exploring the ionospheric modification independently of the ambient ionosphere, as long as we consider one altitude and input HF power level at a time. One might consider this a zero-dimensional simulation.

Let us consider the response of the ionosphere to an HF heating input, at one isolated point. We calculate the relevant parameters forward in small time increments, and at each time step, Equation 2.11 is discretized, and an incremental temperature change is calculated. We can then update the electron temperature from time point  $m$  to  $m + 1$  according to

$$T_e^{m+1} = T_e^m + \Delta t \frac{dT_e}{dt} \quad (2.29)$$

The time step  $\Delta T$  must be chosen small enough that the linearization of Equation 2.11 is a valid approximation. In the simulations performed throughout this thesis,  $\Delta T = 1 \mu s$  is found to be sufficiently short. Simulations repeated with  $\Delta T = 0.5 \mu s$  confirm that results do not change as a result of numerical inaccuracies.

At each time step, the value of  $T_e$  determines the modified values of  $\nu_{av}$ ,  $\sigma_H$ ,  $\sigma_P$ , and  $\sigma_{\parallel}$ . It is also crucial that the modified value of  $\nu_{eff}$  be used as input into the next time step, since the amount of HF energy absorbed is affected by  $\nu_{eff}$ .

Figure 2.4 shows an example of the ionospheric response to modulated HF heating. In this example, we consider the ionosphere at 75 km with an HF input power ( $S$ ) at 3.25 MHz sinusoidally varying between 0 and 3 mW/m<sup>2</sup>, as shown in the top panel. In this first simulation, the magnetic field is assumed to be vertically oriented, and the HF power arrives vertically.

The remaining four panels of Figure 2.4 show the electron temperature, collision

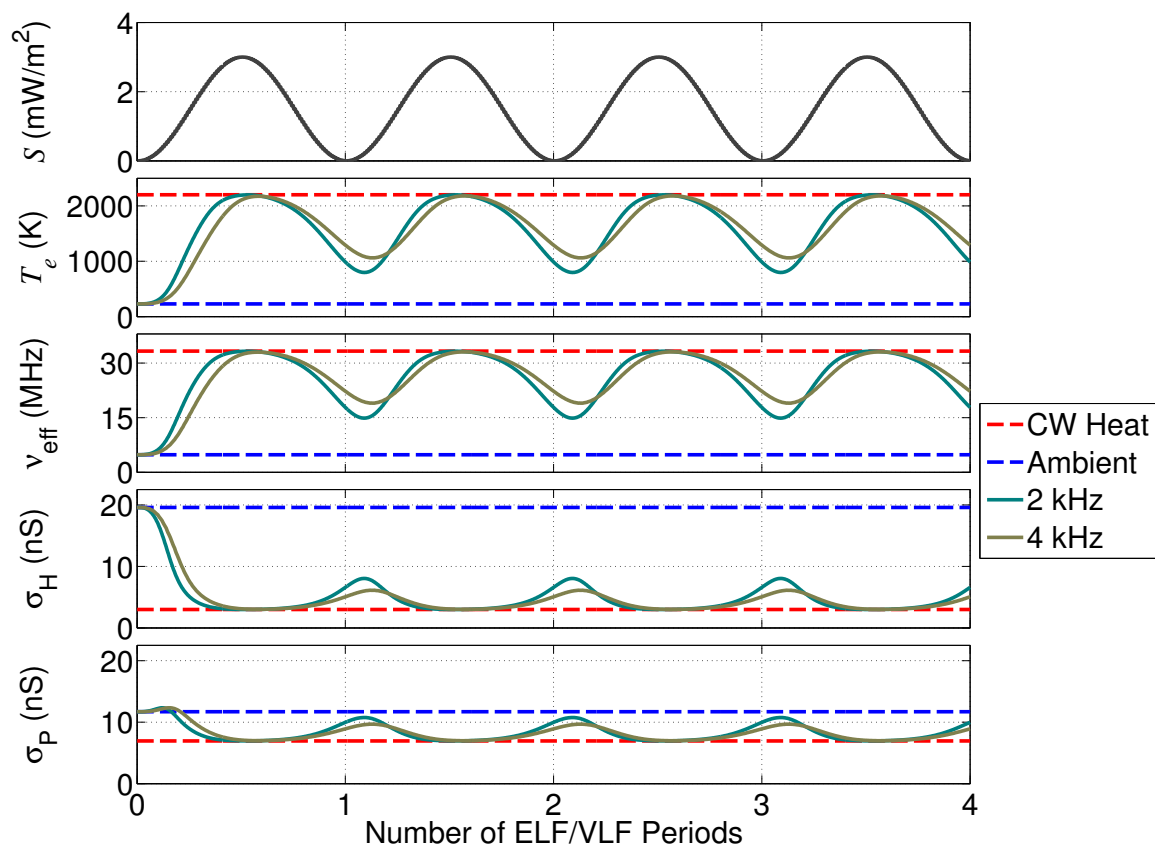


Figure 2.4: Heating and cooling dynamics at 75 km altitude

frequency, Hall conductivity, and Pedersen conductivity, respectively, as a function of time. The blue lines show the ambient levels, and red line shows the level that results from continuous wave (CW) heating. Results for periodic modulated heating at both 2 kHz and 4 kHz are also shown. An electron density of  $10 \text{ cm}^{-3}$  is assumed, although we stress again that the plot data are independent of this electron density, except for a linear scaling of the conductivities. The simulation requires at least a few ELF/VLF periods in order for a sinusoidal steady state to be reached.

For the purpose of ELF/VLF generation, temporal development of the ionospheric conductivity is most important, since it is this parameter which modulates the auroral electrojet currents. Ideally, to maximize the HF to ELF/VLF conversion efficiency,  $\sigma_H$  and  $\sigma_P$  would vary between the red line and the blue line, utilizing the maximum possible conductivity depth. Clearly this is not the case, in fact  $\sigma_H$  changes by only about one fourth of the available conductivity depth. Although the electrons recover much closer to the ambient values,  $\sigma_H$  changes most drastically at the lower temperatures, as can be seen in Figure 2.3.

The nonlinearities inherent in the energy balance equation dictate that the conductivity modulation function is not in general sinusoidal, so that higher harmonics of the modulation frequency are also be generated, even though the HF power envelope contains only one frequency.

Comparison between the 2 kHz and 4 kHz traces show that the heating and cooling dynamics do depend on frequency. In both cases, the ionospheric parameters reach the CW level, which is the strongest possible ionospheric modification for this particular situation. However, heating at 2 kHz allows more time for the ionosphere to recover closer to its ambient state. In neither case does it fully recover, hence for both frequencies, some fraction of the HF power is wasted on sustained heating of the electrons, which does not contribute to periodic modulation of the ionospheric conductivity. Since this waste appears to be smaller at 2 kHz compared to 4 kHz, we have a hint that the ionospheric response to HF heating at this altitude may function as a lowpass filter within the ELF/VLF range, as higher frequencies are too fast for the electron recovery rates.

To illustrate this, we can repeat the single-point simulation at many different

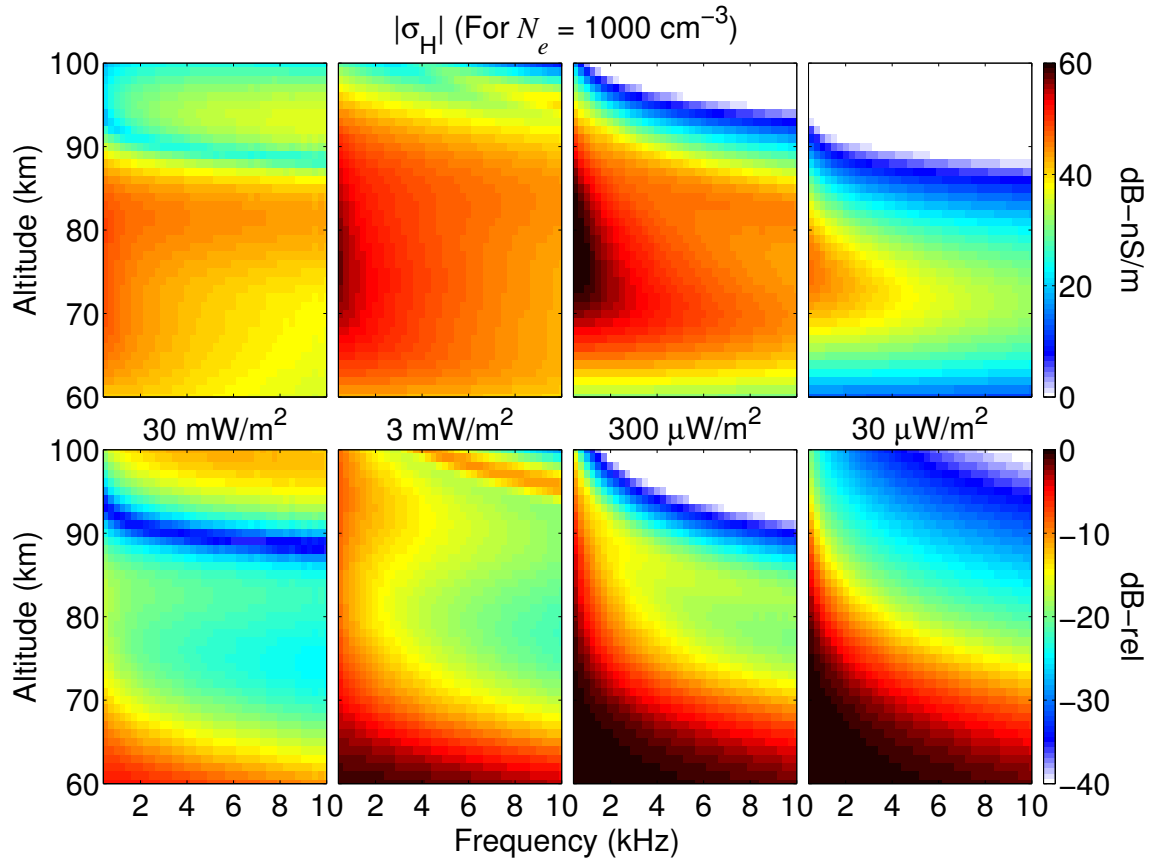


Figure 2.5: Hall conductivity modulation vs. height, frequency, and HF power



frequencies and altitudes. Figure 2.5 shows the results, with the frequency on the horizontal axis, the altitude on the vertical axis, for four different HF power densities (all sinusoidally varying in time), and at 3.25 MHz. We note here that the maximum possible ERP with HAARP at 3.25 MHz and 9.50 MHz is currently  $\sim 575$  MW and  $\sim 3.8$  GW, respectively, which implies a power density of  $S=9.3$  mW/m<sup>2</sup> and 61.7 mW/m<sup>2</sup>, respectively, at an altitude of 70 km, in the absence of absorption below that altitude.

The quantity shown in color in the top plots is the magnitude of the Hall conductivity modulation (for  $N_e = 100\text{cm}^{-3}$ , after Fourier-extraction at the fundamental frequency once sinusoidal steady state has been reached, on a decibel (dB) scale with respect to 1 nS/m. Since we have assumed  $N_e$ , the quantity plotted is independent of the ionospheric variation, and represents the conductivity modulation induced per 1000 cm<sup>3</sup> of electrons. There is a strong dependence on height, frequency, and HF power density, of the amount of conductivity modulation achieved with HF heating. The highest altitudes (above 85 km) have increasing conductivity modulation as the HF power increases, at least through 30 mW/m<sup>2</sup> at 3.25 MHz. However, at the altitudes between 70 and 85, the normalized conductivity modulation appears to saturate between 300  $\mu\text{W}/\text{m}^2$  and 3 mW/m<sup>2</sup>. The lowest altitudes (below 70 km) also saturate but at a higher HF power level.

In the bottom plots of Figure 2.5, the values at each altitude (for horizontal row) from the top plots have been normalized to the maximum possible conductivity depth (i.e., the difference between  $\sigma_{\text{Ambient}}$  and  $\sigma_{\text{CW}}$ ). This normalization brings out the efficiency, or full utilization of the maximum possible conductivity modulation. The lower altitudes generally contribute more to ELF/VLF generation. Additionally, increasing the HF power density yields increasingly inefficient conductivity modulation.

### 2.3.2 Vertical structure

Having described the dynamics of HF heating at a single point, we extend our zero-dimensional model to cover a one-dimensional line extending vertically through the ionosphere. In other words, we are now considering the HF energy to enter the lowest

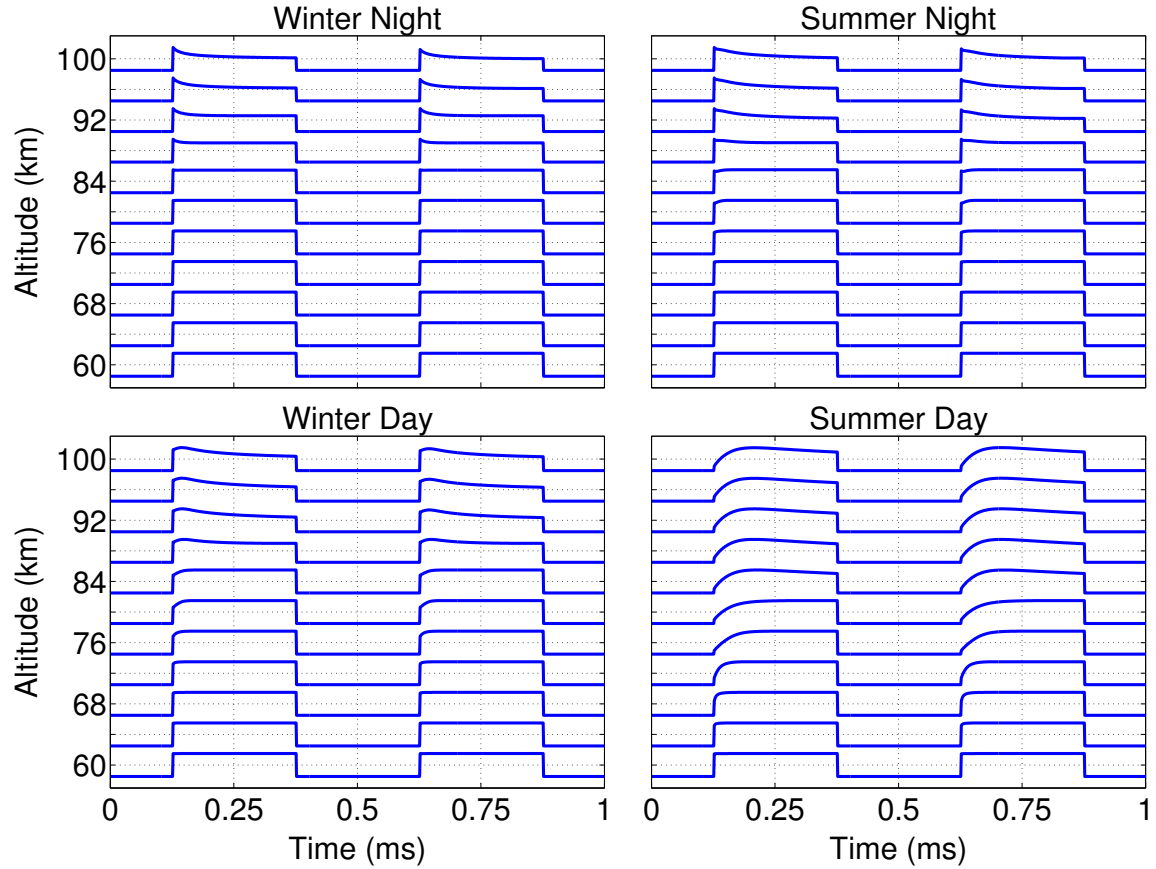


Figure 2.6: Power density reaching higher altitudes

altitudes and propagate upward in small vertical steps through the ionosphere. At each step, some of energy is absorbed, and the remaining HF energy is passed on to the higher altitude. Although we are restricting our consideration here to a one-dimensional structure, we must also account for the  $r^{-2}$  spreading of the HF energy at each altitude step, which decreases the HF power density at higher altitudes even in the absence of absorption.

In determining the HF power density at various altitudes, we are integrating the absorption upward from the ground (or the lowest relevant altitude), and subtracting the integral from the initial power density. The upward steps of this integration through the ionosphere are separated by an altitude difference  $\Delta h$ , which must be small enough that the absorptive properties do not drastically change over that length.

However, as is shown later, the absorption rate in the ionosphere can change sharply over a few km altitude. Thus, in order to preserve the accuracy and stability of this vertical integration without using excessively small values of  $\Delta h$ , a classic 4th order Runge-Kutta method is applied between each upward step. In this dissertation, we find that  $\Delta h=1$  km is adequately small to produce accurate results. Accuracy is verified by repeating identical simulations, with  $\Delta h=0.5$  km, to ensure that results do not significantly change. We must also ensure that the vertical extent spanned by the model includes the entire altitude span over which significant HF absorption occurs. As before, we must track the effects of the changing ionosphere between time steps, so that the vertical distribution of the HF power density must also be tracked as a function of time.

Since our previous formulation takes into account the ionospheric dynamics at a given altitude, we focus first on the evolution of the HF power absorption as it propagates through the ionosphere. Since the previous section dealt with ionosphere-independent dynamics, here we are considering the only aspect of HF heating and cooling that is largely responsive to ionosphere conditions, i.e., the vertical structure of absorbed HF power.

Figure 2.6 shows the importance of the HF absorption as a function of both altitude and time. The four panels plot the shape of the HF power density as a function of time received at altitudes between 60 km and 100 km, for the four different ionospheres in Figure 1.1. The plots are shown in altitude increments of 4 km, although the simulation is performed with 1 km increments. In this case, the HF power applied at the bottom is  $12.7 \text{ mW/m}^2$ , at 3.25 MHz, and it is modulated with a 100% depth, 50% duty cycle square wave, and modulation frequency of 2 kHz. The curves here are normalized to show the qualitative changes, and the delay of the HF power propagating upward (which is substantial compared to the ELF/VLF period) is also removed for the sake of visual clarity. The temporal shape of the square wave is morphed as it propagates through the ionosphere, an effect known as self-absorption, discussed in detail by [Moore, 2007].

For instance, in the winter nighttime ionosphere, the power density at the highest altitude (100 km) decreases during the ON portion of the HF heating (whereas it

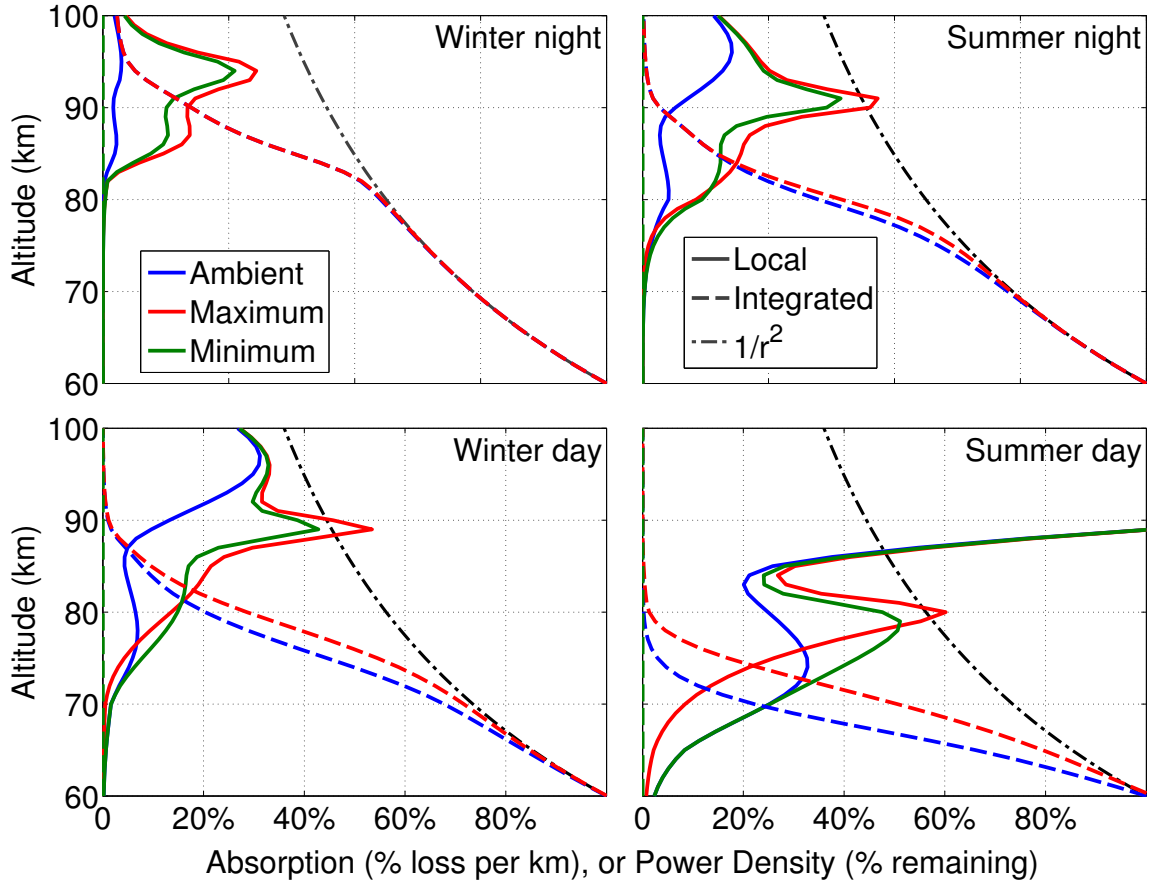


Figure 2.7: Absorption of HF energy at 3.25 MHz

is constant at the bottom of the ionosphere). As a result of the change in collision frequency at the lower altitude, more absorption takes place and less power becomes available at the highest altitudes. On the other hand, the strongly ionized summer daytime ionosphere shows quite a different character, with the HF power density at higher altitudes increasing during the ON portion, so the absorption at lower altitudes decreases as a result of HF heating.

A more quantitative description of the HF absorption can be found in Figure 2.7, for the same HF heating conditions. For the four ionospheres, the dashed lines show the HF power density as a function of altitude, as a percentage of the power at the bottom of the ionosphere (in this case,  $12.7 \text{ mW/m}^2$ ). The gray dashed line shows the power density that would result from strictly  $1/r^2$  reduction in the power density

(which would be the case for free space propagation). The red and green dashed curves show the maximum and minimum HF power densities (respectively) during the ELF/VLF cycle. The solid curves show the absorption rate of the ionosphere per kilometer (i.e., the derivative of the total absorption, or  $(1 - e^{-2k\chi S})$ ), for the same maximum and minimum points (red and green, respectively) as well as the ambient ionosphere. At the altitude where the absorption rate becomes substantial, the power density falls below the free space curve.

It can be seen here that the absorptive part of the ionosphere changes significantly over small altitude differences (a few km). For this reason, the upward integration is achieved with fourth-order Runge-Kutta technique, so the propagation of the HF energy to the next higher altitude slab requires four steps. We can also see that the altitude where the HF energy is deposited varies significantly as a function of the ionosphere. In general, the more ionized is the ionosphere, the lower is the altitude at which the bulk of the HF energy is deposited. At 3.25 MHz, most of the HF energy is absorbed, though at higher frequencies (where the ionospheric parameter  $Z$  is smaller), a higher fraction of the power escapes the  $D$  region entirely.

Figure 2.8 shows the ionospheric modification at five different altitudes between 70 and 90 km, resulting from the winter daytime ionosphere HF heating case shown in Figure 2.7, from which we can see the altitude dependence of the key ionospheric modification panels. The top left panel of Figure 2.8 shows the temperature variation in time. The lag of the rising portion of the temperature waveform at the highest altitude is simply due to the delay of the HF power propagating upward from the ground. The electrons are heated to the highest temperature at an altitude near 80 km, even though the highest absorption rate, as can be seen in Figure 2.7, occurs closer to 85-90 km. This difference is because at 80 km, there are fewer electrons, so the power absorbed is concentrated on a smaller number of particles, in addition to the fact that there is simply less HF power density at 90 km compared to 80 km, so if the fractional absorption were the same between 80 km and 90 km, that would mean less power absorbed at 90 km.

The top right panel of Figure 2.8 shows the collision frequency as a function of time. Although 85-90 km is the peak power absorption rate altitude, and 80 km

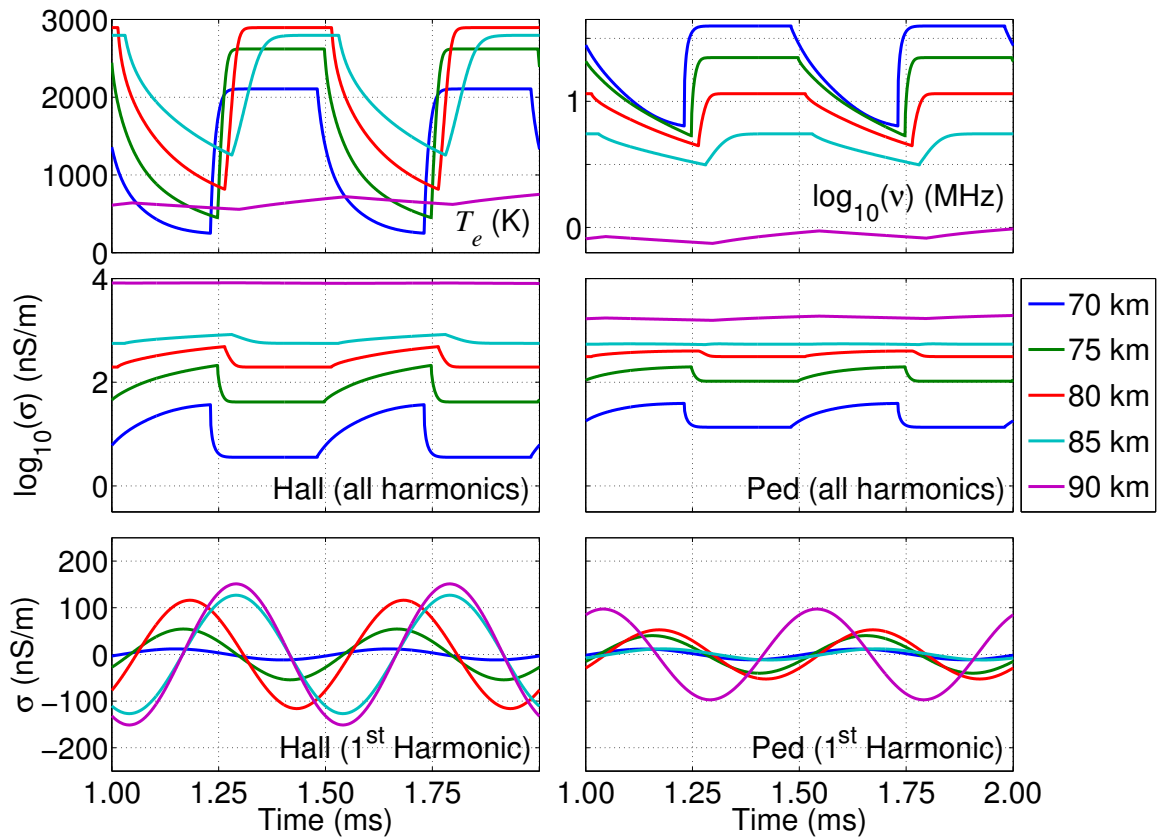


Figure 2.8: Ionospheric modification at varying altitudes

is the altitude of peak temperature modulation, the strongest effect on the collision frequency occurs at 70 km (the lowest of the four altitudes), due largely to the fact that the ambient collision frequency is higher to begin with.

The middle panels of Figure 2.8 show the temporal development of the Hall (left) and Pedersen (right) conductivities in the ionosphere, plotted on a logarithmic scale. Proportionally, the strongest change in conductivity occurs at the lowest altitude (70 km), whose Hall conductivity rises by about an order of magnitude. On the other hand, at 90 km, the modulation of the conductivity can barely be seen. These plots again show that the conductivity modulation in general has a harmonic content different from the harmonic content of the HF heating envelope (a square wave in this case).

The bottom plots of Figure 2.8 show the Fourier-extracted first harmonic of the curves in the middle plots, and plotted now on a linear scale. The strongest conductivity modulation, for both the Hall and Pedersen conductivities, occurs at 90 km, even though the proportional change in the conductivity is small, since the conductivity at 90 km is so much higher to begin with. The phases of the extracted sinusoid shift later in part due to the group delay of the HF signal, but they are also affected by the slower rise time and fall time evident in the upper panels, which causes the phase of the first harmonic to additionally lag at 90 km.

It should be emphasized, however, that the comparative role of different ionospheric altitudes in ELF/VLF wave injection cannot be determined strictly on the basis of the amplitude of the conductivity modulation. Thus, even though 90 km appears to be the altitude of highest conductivity modulation (and therefore, generate the highest ELF/VLF currents for a homogeneous electrojet field), the ELF/VLF signal on the ground or in space may be dominantly due to the conductivity modulation at a different altitude, due to nontrivial propagation effects of the ELF/VLF signal through the ionospheric plasma. This propagation aspect is considered later in this chapter. For instance, the generated signals observed on the ground may appear to be originating from an effective (or dominant) altitude, which may be different for magnetospheric injection.

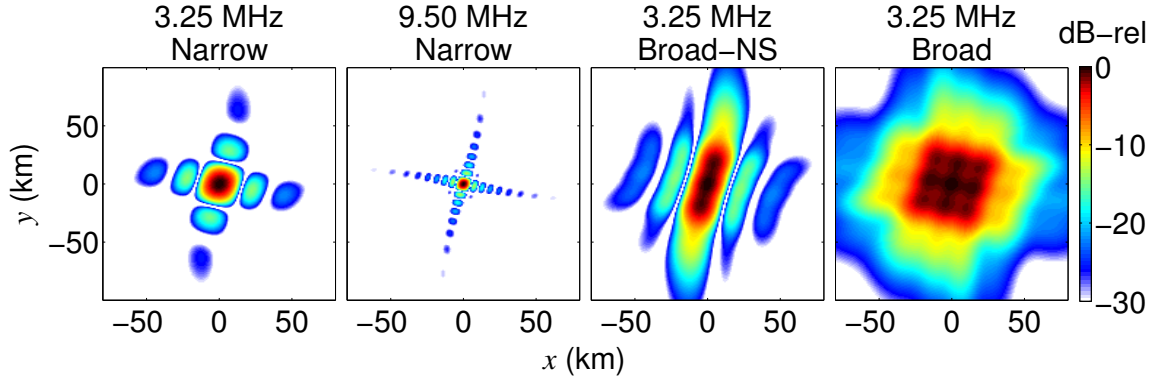


Figure 2.9: HF power at 60 km from HAARP

### 2.3.3 Extension to 3D

Now that we have described the vertical distribution of the HF energy deposition, our remaining task is to extend the model to three-dimensions. For this purpose, the horizontal space at each altitude is divided into segments of equal length  $\Delta x$ , which must be small enough to capture the structure of the input radiated pattern from HAARP, as well as any small scale structures induced in the ionosphere.

Let us first describe the input HF power from the HAARP phased-array HF heating facility, since the experiments conducted here take place with HAARP. The HF frequency can vary between 2.75 MHz and 9.9 MHz. At a given frequency, HAARP can operate in a number of modes of operation, a few of which are shown in Figure 2.9. The power density arriving at 60 km altitude is plotted on a logarithmic scale, where the center of the horizontal region shown is directly above the location of HAARP on the ground. The most straightforward mode of operation involves driving all the HF antennas in phase, shown in the left two panels (for 3.25 MHz and 9.50 MHz, respectively), which maximizes the vertical beam focusing and therefore the ERP. However, since the HF array is finite in size, some of the power also leaks into the sidelobes which can be seen forming a ‘+’ shape around the main beam. The ‘+’ shape is oriented  $14^\circ$  East of geographic North, which is the orientation of the rows and columns of HF transmitters at HAARP.

The sidelobe power density delivers no more than  $-15$  dB power density compared



to the main lobe. At higher frequencies, as the space between the HF transmitting elements on the ground (some tens of meters) becomes a larger fraction of an HF wavelength, the power becomes even more tightly focused into a smaller main beam (hence the ERP at 9.5 MHz is  $\sim 8.2$  dB higher than at 3.25 MHz), although the sidelobes are also more numerous at 9.50 MHz. HAARP also has the ability to broaden the beam, as can be seen by the right two panels of Figure 2.9, and this broadening can be performed in one direction, or in both directions. The broadening effectively merges the main lobes with the sidelobes, spreading the beam power over a wider area, thereby decreasing the ERP. This mode is achieved by varying the radiating phases of the HF elements on the ground but is not utilized in the experiments of this dissertation, though it has been used in a number of ELF/VLF wave generation experiments with HAARP. The ERPs and power densities into the ionosphere for a variety of different HF frequencies, and beam broadening modes are given in Appendix B.

Any of these modes can also be combined with beam tilting, where the center of the main beam is not in the vertical direction, but is off by a zenith angle of up to  $30^\circ$  from vertical, and any azimuth. This beam tilting ability is extensively used in this dissertation.

The two-dimensional power density input into the bottom of the ionosphere consists of a series of HF rays at each grid point. For this plane at the lowest altitude, the propagation from the ground is assumed to be through free space, so that the group delay at each location is simply the free space propagation delay from the HF array location to the base of the ionosphere, and both ray direction and the wave normal direction are equal to the free space arrival direction from the HF array to the grid point at the bottom of the ionosphere. The power density is calculated using realistic data of the HAARP array's directional pattern, including the sidelobes, assuming the HF energy spreads as  $1/r^2$  as it propagates to the base of the ionosphere. From this input two-dimensional plane, the propagation upward through the ionosphere is carried out in a series of vertical steps, separated by  $\Delta h$ .

Figure 2.10 shows an interpolation method applied with each altitude step in the upward integration. Each HF ray at the grid points (in red dots) is projected upward

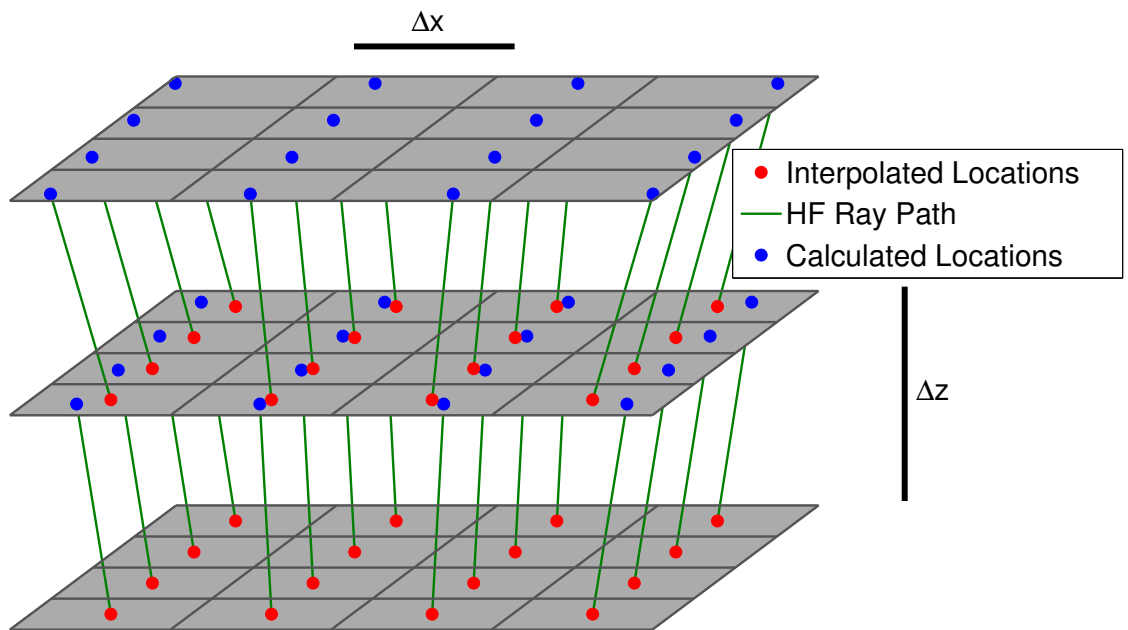


Figure 2.10: 2D interpolation of HF parameters

to the next altitude (shown with the green traces), intersecting that altitude at a certain location offset from the grid (shown with blue dots). The HF densities at the next altitude, however, are reduced by a  $1/r^2$  spreading factor, as well as the calculated absorption in between the two altitude slabs, taking into account the fact that the HF ray travels a distance  $\Delta h \cos \theta$  in between each altitude step, where  $\theta$  is the ray angle from vertical.

A 2-D linear interpolation is then applied to calculate the values of the HF power density at each of the grid points. The ray bending and slowing as a result of Snell's law and the magnetic field anisotropy is then calculated, and the HF ray directions and group delay are updated accordingly.

The angle between the HF rays and the geomagnetic field must also be tracked, and we utilize a realistic value and orientation of the geomagnetic field obtained from the 10th generation International Geomagnetic Reference Field (IGRF-10) model (values available from <http://www.ngdc.noaa.gov/geomagmodels/IGRFWMM.jsp>). At 75 km altitude above HAARP, the geomagnetic field is  $\sim 53.29 \mu\text{T}$  in the downward direction,  $\sim 12.57 \mu\text{T}$  to the North, and  $\sim 4.99 \mu\text{T}$  to the East. These values vary by a small amount ( $<1\%$ ) as a function of altitude between 50 and 100 km. The declination (orientation of the horizontal component with respect to geographic north) is  $\sim 21.65^\circ$  to the East, and the inclination (or zenith tilting of the field from vertical) is  $\sim 14.24^\circ$ .

The absorbed energy calculated in the horizontal slab is then applied as before to a discretized form of Equation 2.11. Once the short HF pulse of duration  $\Delta t$  has been propagated through the ionosphere, the next time step integration is performed using the ionosphere left behind by the previous time step. In the next time step, the HF power input into the ionosphere may be different. Usually, the HF heating model is run for several ELF/VLF periods, so that a periodic steady state of all the ionospheric parameters is reached, typically after simulating a few milliseconds.

The calculation of the collision frequency enables the ionospheric conductivity to be determined as a function of time, and this step is performed during the calculations. However, since we are interested in specific generated frequencies, we must utilize Fourier extraction to withdraw the amplitudes and phases of individual frequencies. Since the signal is periodic at a fundamental frequency, we can extract

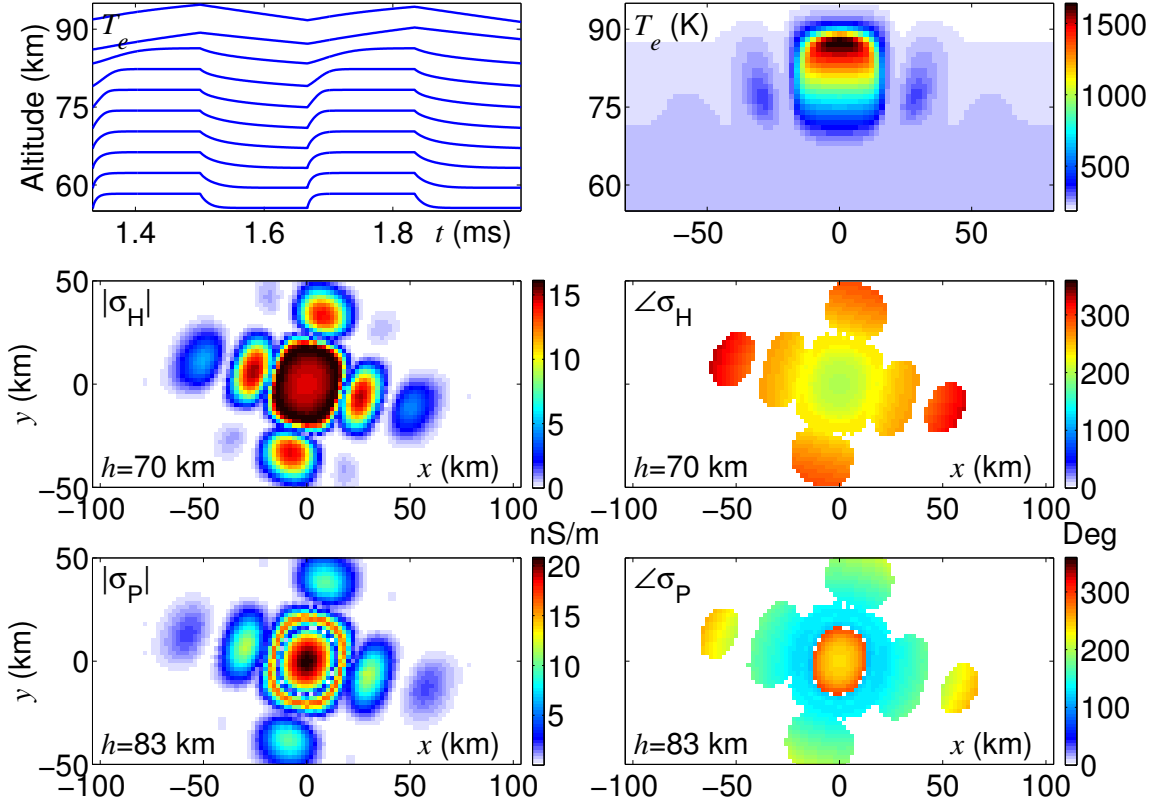


Figure 2.11: Three-dimensional HF heating model results

these amplitudes and phases according to

$$A_N = \sum_{m=1}^{T/\Delta t} \bar{\bar{\sigma}} e^{-2\pi i f m \Delta t N} e^{-2\pi i f t_d N} \quad (2.30)$$

where  $f$  is the fundamental frequency, and  $N$  is the harmonic of that frequency we want to track,  $T$  is the ELF/VLF period (or  $1/f$ ). The group delay  $t_d$  of HF energy from the ground, and  $\bar{\bar{\sigma}}$ , the conductivity tensor at each location (or, more specifically,  $\sigma_H$ ,  $\sigma_P$ , and  $\sigma_{\parallel}$ ) are stored for each location in the three-dimensional grid. In this dissertation, we are primarily concerned with the amplitude and phase of the fundamental frequency (i.e.,  $N=1$ ), calculated over the last ELF/VLF period simulated (i.e., when steady state has been achieved). These quantities are the end goal of this HF heating simulation.

Figure 2.11 shows results from the three-dimensional simulation. The HF heating is taken to be at 3.25 MHz, with the beam oriented vertically, and amplitude modulated at a frequency of 3 kHz, in the presence of a winter daytime ionosphere. The top two panels show  $T_e$ , on the left as a function of time, for points along the center of the main beam (normalized to show the qualitative shape, as in Figure 2.7), and on the right over a two-dimensional slice, vertically through the ionosphere. The temperature slice is taken at the end of the period shown in the top left plot, so that the values  $T_e$  represent the point in the ELF/VLF cycle where electron temperatures have recovered closest to their ambient values (which is still as high as 1600 K, well above the ambient value). The radiating pattern of the HAARP HF beam and its two main sidelobes are evident in the plot.

The lower four panels of Figure 2.11 show horizontal slices of the ionosphere, with the color indicating the amplitude (left) and phase (right) of the Fourier-extracted Hall conductivity at the fundamental frequency (3 kHz). The middle plots are at 70 km altitude and show  $\sigma_H$  (a phasor quantity), whereas the bottom plots are at 83 km altitude and show  $\sigma_P$ . The pattern of the HAARP beam and its sidelobes are again visible.

At 70 km, the strongest (highest amplitude) values of  $\sigma_H$  occur not in the center of the main beam, where the power density is strongest, but at the outside of the main beam. This behavior is due to the effects of self absorption; in this case, higher power densities are often needed in order to penetrate higher into the ionosphere. It is also due in part to the fact that the HF energy at the outside of the main beam travels slightly obliquely, so that it passes through longer length of ionosphere in between each altitude slab, which also causes the HF energy to be deposited at lower altitudes. The phase plot at 70 km shows the variable propagation delay from ground to the ionosphere, with  $\sigma_H$  on the outside lagging in phase mainly due to a longer group delay.

On the other hand, the character of  $\sigma_P$  at 83 km is markedly different. In particular, the strongest conductivity modulation occurs in two distinct regions: in a narrow area in the center of the main beam, and then another thin ring of high conductivity modulation at the edge of the main beam, with a null in between the two regions.

The reason for these distinct regions can be seen in Figure 2.3. Between 80 and 85 km, as  $T_e$  is increased,  $\sigma_P$  first rises, and then falls, thus depending on the maximum and minimum temperature, the net change in  $\sigma_P$  may be either positive or negative. Since the maximum and minimum temperatures are dependent on the HF power density, it is not surprising that there are two distinct regions of  $\sigma_P$  at this altitude. Further evidence of this effect can be found in the bottom right panel of Figure 2.11, which shows that the phase of the conductivity modulation changes by  $\sim 180^\circ$  at the boundary between the two regions of conductivity modulation, corresponding to a transition between a regime where  $\sigma_P$  rises, and where it falls, with increasing  $T_e$ . In fact, this self-cancellation by the two regions of Pedersen conductivity modulation, with opposite phase, is part of the reason that the Hall conductivity is believed to be dominant in the generation of ELF/VLF signals radiated to longer distances by HAARP.

Figure 2.12 shows the evolution of the modulated currents over an ELF/VLF period ( $T$ ), taking into account both the phase of the Fourier-extracted conductivity waveform, and the delay from the HF propagation from the ground through the ionosphere. The left hand six panels show a vertical slice (at  $y=0$ ) of the Hall currents, while the right panels show the Pedersen currents. The panels show frames spaced out at six locations within the ELF/VLF period.

As a result of the delay in the HF signal, the conductivities at the highest altitudes rise and fall slightly later than the conductivities at the lowest altitudes. As can be seen in the left hand plots, the modulated Hall currents are phased in such a manner so as to create an effective moving source in the vertical direction, at close to the speed of light (since the HF is also traveling close to the speed of light). This vertical phasing is intrinsically part of every modulated HF heating experiment, and likely gives an advantage to modulated heating for magnetospheric injection that is not present for injection via a ground-based transmitter. This effect may also play some role in the formation of the so-called ‘column’ of radiation observed over HAARP [Piddychiy *et al.*, 2008].

It can also be seen that the side lobes modulate the conductivity at a lower altitude compared to the main lobe, another indication of the effect of HF power density on

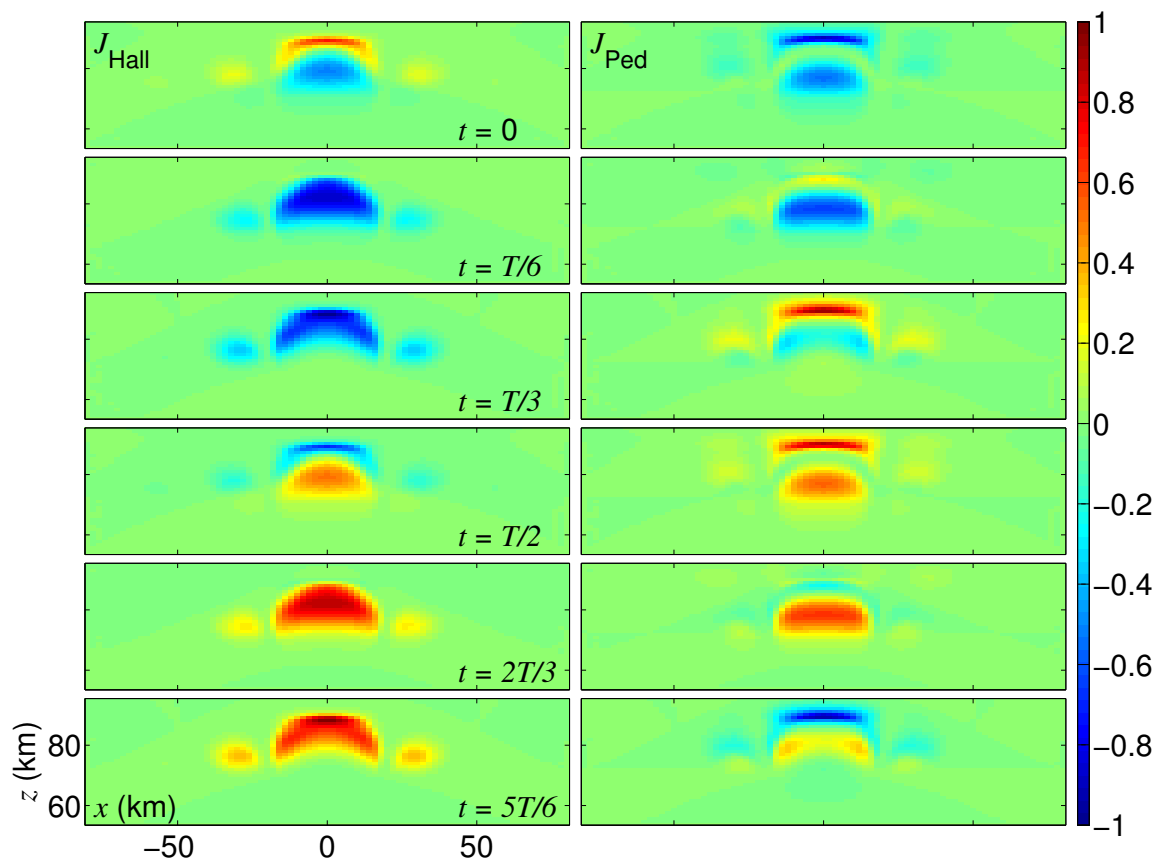


Figure 2.12: Time-evolution of vertical modulated currents

the altitude distribution of energy deposition in the ionosphere.

Since  $\bar{\sigma}$  is now specified at a given frequency in phasor form, for each point in our three dimensional modified ionospheric space, with the use of the HF heating model, determining the modulated ELF/VLF currents generated by HF heating simply requires multiplication with the electric field, as in Equation 2.4. As discussed in Chapter 1, the auroral electrojet field is typically oriented in the North-South direction and has amplitude of 10s of mV/m, and we assume in these simulations a value of 10 mV/m. The auroral electrojet fields are taken to be perpendicular to the geomagnetic field, so that because of the small inclination of the geomagnetic field, there is also a small vertical component of the modulated current sources. For each location in the HF heating grid, a current density vector is calculated, and radiation observed at any point in space is simply a linear sum of the radiation contributions from each point in the modified ionosphere.

## 2.4 The Earth-ionosphere waveguide

Until now, we have concerned ourselves entirely with the propagation of HF waves in the ionosphere, entirely independently of the fact that the HF waves also generate ELF/VLF waves. At this point, however, we divorce ourselves entirely from all HF heating matters, and assume that we simply have a series of ELF/VLF current sources in the ionosphere. Our remaining task is to determine how these current sources electromagnetically illuminate the space around them. Unfortunately, the propagation of ELF/VLF waves in and around the ionosphere and magnetosphere cannot be solved with a raytracing solution as we have applied for HF waves, so an entirely new model is needed.

Figure 2.13 shows schematically how the ELF/VLF currents are placed into a proper model of wave propagation (although the parallel conductivity is not applied, as is discussed later). The model we utilize is described in detail by *Lehtinen and Inan* [2008] and *Lehtinen and Inan* [2009], and only the basic concepts are reviewed here. The Earth is treated as an imperfect (but isotropic) conductor.

The propagation model utilized here is based on a long history of ELF/VLF



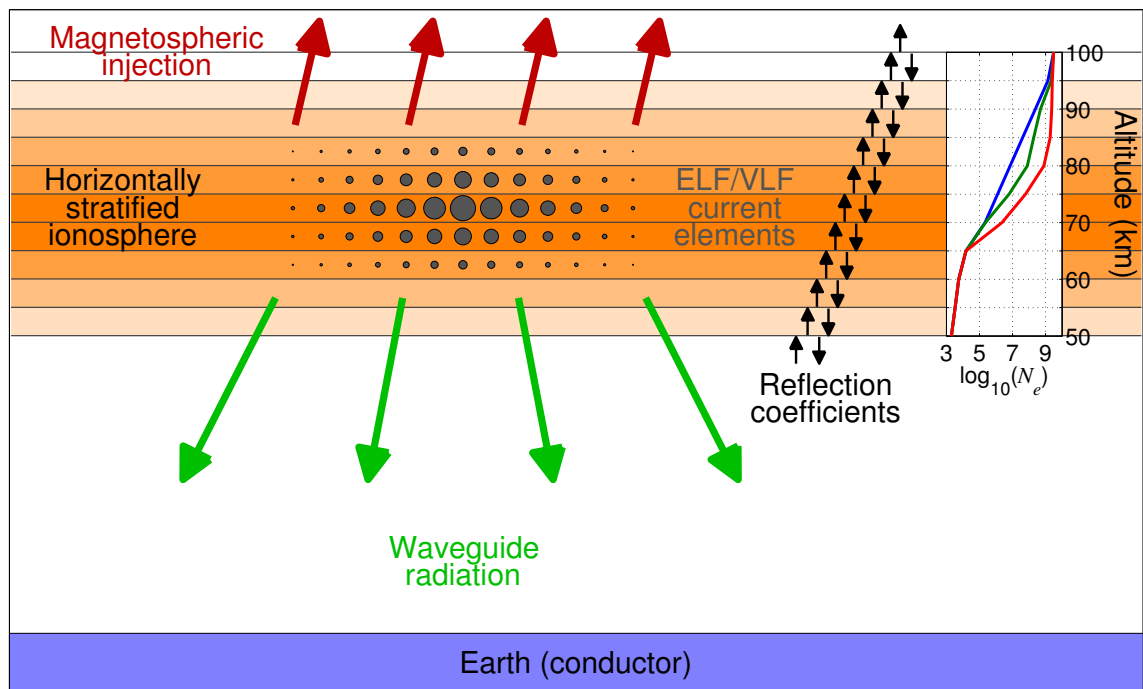


Figure 2.13: Propagation in the Earth-ionosphere waveguide

wave propagation techniques. The most comprehensive early reviews can be found by *Budden* [1961a] and *Wait* [1962], two independent yet similar approaches to the problem of ELF/VLF wave propagation. The Earth-ionosphere waveguide is roughly analogized as an ideal parallel plate waveguide [*Inan and Inan*, 2000, ch.4], which consists of two flat, parallel, and infinite perfectly conducting plates, separated by some distance  $a$ . The key boundary conditions which dictate wave propagation are simply that the electric field in the direction along the conductor at the walls of the waveguide must be zero. This condition implies that any wave incident on a perfectly conducting boundary must be accompanied by a reflected wave, whose electric field component in the direction parallel to the conductor is equal and opposite the incident wave very close to the boundary, so they cancel. The reflection coefficient of the boundary, therefore, is  $-1$ .

Once a second parallel conductor is added, any propagating wave must be able to simultaneously satisfy the boundary conditions at both boundaries. A more extensive analysis can be found in [*Inan and Inan*, 2000, ch.4], but it turns out that the solutions that satisfy both conditions come in the form of discrete modes, or plane waves which zigzag at a specific angle. The specific angle is just right at a given frequency so as to satisfy the boundary conditions for the electric field at both ends. These modes are orthogonal, so any propagating solution can be decomposed into a superposition of modes. Depending on the frequency, there may be just one propagating mode, or many.

Although the above discussion is a good starting framework, in reality the Earth-ionosphere waveguide does not conform to these ideal conditions. Adjustments must be made to account for three imperfections, the imperfect conductivity of both the ground and the ionosphere, the anisotropy of the ionosphere, and the curvature of the Earth. A proper formulation must take all three aspects into account, although in this dissertation, we utilize propagation results for short enough distance (i.e.,  $<1000$  km from the source) that the curvature of the Earth can be ignored.

### 2.4.1 Reflection coefficients

One of the early breakthroughs that drove the development of ELF/VLF propagation theory came via the calculation of the reflection coefficients from the ionosphere, which effectively accommodates the first two of the nonidealities. This calculations is by no means trivial, because the reflection coefficient is dependent on the incidence angle and the orientation of the incident wave (both of which affects the angle with respect to the geomagnetic field), and the finite value of the conductivity throughout the ionosphere (which causes the reflections to be imperfect). The reflection coefficient is usually treated as a tensor quantity as described by [Budden, 1955], and given by the following:

$$\overline{\overline{R}}_i(\theta_i) = \begin{bmatrix} {}_{\parallel}R_{\parallel} & {}_{\parallel}R_{\perp} \\ {}_{\perp}R_{\parallel} & {}_{\perp}R_{\perp} \end{bmatrix} \quad (2.31)$$

where  $\theta_i$  is the angle of incidence with respect to the boundary normal. The diagonal terms are the reflection coefficients for incident waves that are polarized with electric fields parallel to, and perpendicular to, the plane of incidence, respectively. The off-diagonal terms represent conversion from parallel incidence to perpendicular reflection ( ${}_{\parallel}R_{\perp}$ ), and vice versa ( ${}_{\perp}R_{\parallel}$ ). This particular phenomenon, of a parallel polarized wave yielding some perpendicular polarized reflection, and vice versa, is known as mode conversion, as results from the anisotropy of the ionosphere introduced by the geomagnetic field. It should be noted that mode conversion can also occur from horizontal discontinuities in the Earth-ionosphere waveguide, but the propagation model utilized here assumes horizontal stratification, so this source of mode conversion is not applicable.

The ionospheric reflection tensor  $\overline{\overline{R}}_g$  can be calculated in a manner first outlined by Budden [1955]. Using the complex permittivity at each altitude, the ionosphere can be divided into horizontal layers, with each layer causing some reflection and transmission of the wave. Two initial solutions satisfying in-plasma boundary conditions at high altitude are separately integrated downward through each of these layers

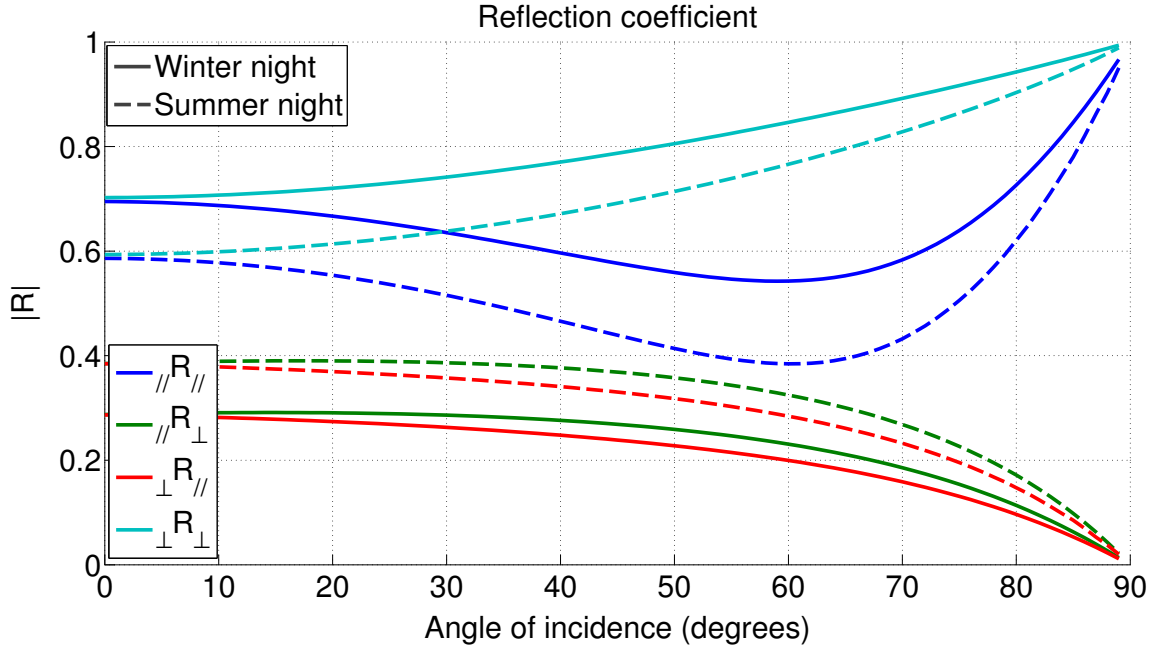


Figure 2.14: Reflection coefficients as a function of incidence angle

in the ionosphere until a free space point below the ionosphere is reached. The two resulting solutions are separated into upward and downward propagating waves and normalized to the value of the input wave.

An example of this calculation is shown in Figure 2.31, at a frequency of 2 kHz, for both the winter and summer nighttime ionospheres defined in Figure 1.1, and a realistic geomagnetic field for the ionosphere above HAARP. The four components  $\overline{\overline{R}}$  are plotted as a function of the angle of incidence. For a nearly vertically incident wave ( $\theta=0$ ),  $_{//}R_{//}$  and  $_{\perp}R_{\perp}$  merge to the same value, because for vertical incidence, the two polarizations are nearly indistinguishable. At the highest angle of incidence,  $_{//}R_{//}$  and  $_{\perp}R_{\perp}$  both approach unity, since the wave is just barely grazing the ionosphere, so that perfect, isotropic-like reflection takes place. A second consequence of the imperfect reflection from the anisotropic ionosphere is that some amount of ELF/VLF energy leaks through, that is to say the transmission coefficient is nonzero.

### 2.4.2 Modal solutions

With knowledge of the reflection coefficients, a complete solution of propagating modes involves the determination of the propagation conditions for the various modes that satisfy the electromagnetic boundary conditions at both boundaries. So let us now assume that the ionosphere is defined as a sharp boundary, at a height  $a$  above the ground, but one with reflections defined by Equation 2.14. *Budden* [1961a, pg.116] defines the fundamental equation of mode theory as

$$\overline{\overline{R}}(\theta)R_g(\theta)e^{-2ika\sin\theta} = \overline{\overline{I}} \quad (2.32)$$

where  $R_g(\theta)$  is the scalar reflection coefficient from the ground,  $k$  is the free space propagation constant (which may be complex),  $\theta$  is the angle of incidence, and  $\overline{\overline{I}}$  is the  $2 \times 2$  identity matrix. The mode equation states the following: If a wave satisfying the mode equation begins at the ground, propagates up to the ionosphere (electric field phasor multiplies by  $e^{-ika\sin\theta}$  again), reflects from the ionosphere (electric field phasor multiplies by  $\overline{\overline{R}}_i(\theta)$ ), returns to the ground level (electric field multiplies by  $e^{-ika\sin\theta}$ ), and reflects from the ground (electric field phasor multiplies by  $R_g(\theta)$ ), then it should be at the same amplitude and phase as the original wave. If it is not, then the wave solution does not constitute a valid time-harmonic mode (i.e., it is not self-consistent of self-propagating).

### 2.4.3 Propagation model

The search for combinations of  $\theta$ ,  $a$ , and  $k$ , that satisfy the conditions leads to a complete solution of ELF/VLF propagation in the Earth-ionosphere waveguide, under the assumption that the waveguide can be treated as having two sharp boundaries. However, a more proper and thorough treatment considers the ionosphere as plane stratified, or consisting of various layers stacked on top of each other, with a separate reflection coefficient tensor at each boundary. Solving for the modes in this more complicated case leads to a fourth order polynomial equation known as the Booker

quartic [Booker, 1938], whose four roots must be determined. Numerically, however, this determination turns out to be difficult [Budden, 1985, ch.6]. We utilize a particular method of solving for these modes which is described in more detail by *Lehtinen and Inan* [2008].

The model described therein calculates reflection and transmission coefficients between each layer, as shown in Figure 2.13. The full-wave solution therefore intrinsically calculates the radiation both into the Earth-ionosphere waveguide, and upward into the magnetosphere, for all three components of both the electric and magnetic fields. This model has been utilized to model propagation of ELF/VLF waves to 700 km altitude, and compared to observations of intense HAARP-radiated signals by the DEMETER satellite [Piddychiy *et al.*, 2008]. It has also been used to model transionospheric propagation of VLF waves *Lehtinen and Inan* [2009], and so-called ‘V-shaped streaks’ of sferics from power thunderstorms observed by DEMETER [Parrot *et al.*, 2008].

The model as utilized in this dissertation makes three important assumptions. The first is that both the ionosphere and the geomagnetic field are homogeneous in the horizontal plane. The second is that the Earth is taken to be flat (effects of the curvature have not been included). However, we limit our discussion of the radiated power to within 1000 km of the source, so that the Earth within this region can be safely considered to be flat.

However, the assumption that the ionosphere is horizontally stratified is somewhat unrealistic, in that the patch of the ionosphere above HAARP has a higher collision frequency than the rest of the ionosphere considered. It should be noted, however, that *Lehtinen and Inan* [2008] discuss this error and conclude that it is no worse than 3% for the (more important) Hall conductivity sources. In addition, the results obtained with this model have been compared to a complete Finite-difference time domain (FDTD) technique (presented by *Payne et al.* [2007]), which includes the effect of the modified ionosphere, and the results were found to be similar.

It is also assumed that the generated ELF/VLF electromagnetic fields are not so large as to perturb the auroral electrojet fields themselves (thereby making the propagation problem nonlinear). Consider a first order expansion of Ohm’s law into a

DC component (from the auroral electrojet), and an AC component (from modulated HF heating)

$$\vec{J} = (\bar{\sigma}_{DC} + \bar{\sigma}_{AC})(\vec{E}_{DC} + \vec{E}_{AC}) \quad (2.33)$$

$$= \bar{\sigma}_{DC}\vec{E}_{DC} + \bar{\sigma}_{AC}\vec{E}_{DC} + \bar{\sigma}_{DC}\vec{E}_{AC} + \bar{\sigma}_{AC}\vec{E}_{AC} \quad (2.34)$$

where  $\vec{J}$  is the current in the ionosphere,  $\bar{\sigma}_{DC}$  is the ambient ionospheric conductivity,  $\bar{\sigma}_{AC}$  is the HF-generated conductivity modulation,  $\vec{E}_{DC}$  is the electrojet electric field, and  $\vec{E}_{AC}$  is the electric field generated by the modulated current.

The first term of Equation 2.34 is simply the background auroral electrojet field, which is constant and therefore does not contribute to ELF/VLF radiation. The second term is the modulated source currents calculated from the HF heating model. The third term includes the polarization currents from the modulated source currents, and is intrinsically calculated by the propagation model via the reflection and transmission coefficients in the stratified ionosphere. The fourth term takes into account the cross modulation of the ionospheric conductivity changes with the modulated source currents and the polarization currents. This term is nominally at twice the AC frequency (and at DC), but if it is especially large, it is also cross modulated with the polarization fields and the source currents, yielding a component at the AC frequency which acts against the second and third terms. Under this condition, a first order expansion of Ohm's law is not appropriate, and application of Ohm's law becomes a nonlinear problem.

For the Hall and Pedersen conductivities, the fourth term (as can be verified by the model results) is indeed too small to be of significance. However, because the Parallel conductivity is so much larger, the fourth term is in fact sufficiently strong so as to negate the polarization field, especially since the auroral electrojet field is very small along the geomagnetic field line. In other words, the plasma conductivity in the parallel direction is so high that it does not allow quasi-static fields to build up in the vertical direction. Hence, in the propagation model, we neglect the Parallel modulated currents, and utilize only the Hall and Pedersen currents.

Other workers have discounted the impact of  $\sigma_{\parallel}$  [Stubbe and Kopka, 1977; Moore, 2007; Payne, 2007]. It is also worth noting that Payne *et al.* [2007] evaluated experimental data in which a null in the electric field pattern is found as the modulated HF heating beam is steered in a circular pattern around a receiver close to HAARP. This null arises from the directionality of the auroral electrojet. A theoretical model including only Hall and Pedersen conductivities produces matching results, so there is some experimental evidence that the parallel conductivity may not have a large impact on the radiated ELF/VLF signals.

However, the precise evaluation of the impact of  $\Delta\sigma_{\parallel}$  on the radiation pattern from HF heating is outside the scope of this work (though it could be an interesting topic for future study), so for the purposes of this dissertation, we retain the assumption used in the past that  $\Delta\sigma_{\parallel}$  can be discounted.

## 2.5 Model results

Some results of the complete HF heating and ELF/VLF propagation model are shown in Figure 2.15. The input currents come from the HF heating model simulation shown in Figure 2.11, and with an auroral electrojet field assumed to be 10 mV/m in the geomagnetic north direction ( $\sim 22.4^\circ$  East of geographic north). The left panels show the fields on the ground, over a region 2000 km  $\times$  2000 km, centered at the HF heater. The top left panel shows the total horizontal component of the magnetic field, and bottom left panel shows the vertical component of the electric field. The horizontal electric field, and vertical magnetic field are not shown because they are negligibly small (since the ground is a good conductor at these frequencies), though they are nonetheless calculated by the propagation model.

The pattern of electromagnetic fields on the ground resembles that of a single dipole immediately above HAARP, whose orientation is roughly in the northeast direction. In particular, a null in the electric field can be seen near the center point, where HAARP is located, and extending along a line oriented on the northwest-southeast direction. Payne *et al.* [2007] utilize vertical electric field measurements to detect the orientation of this null, and thus the orientation of the effective dipole



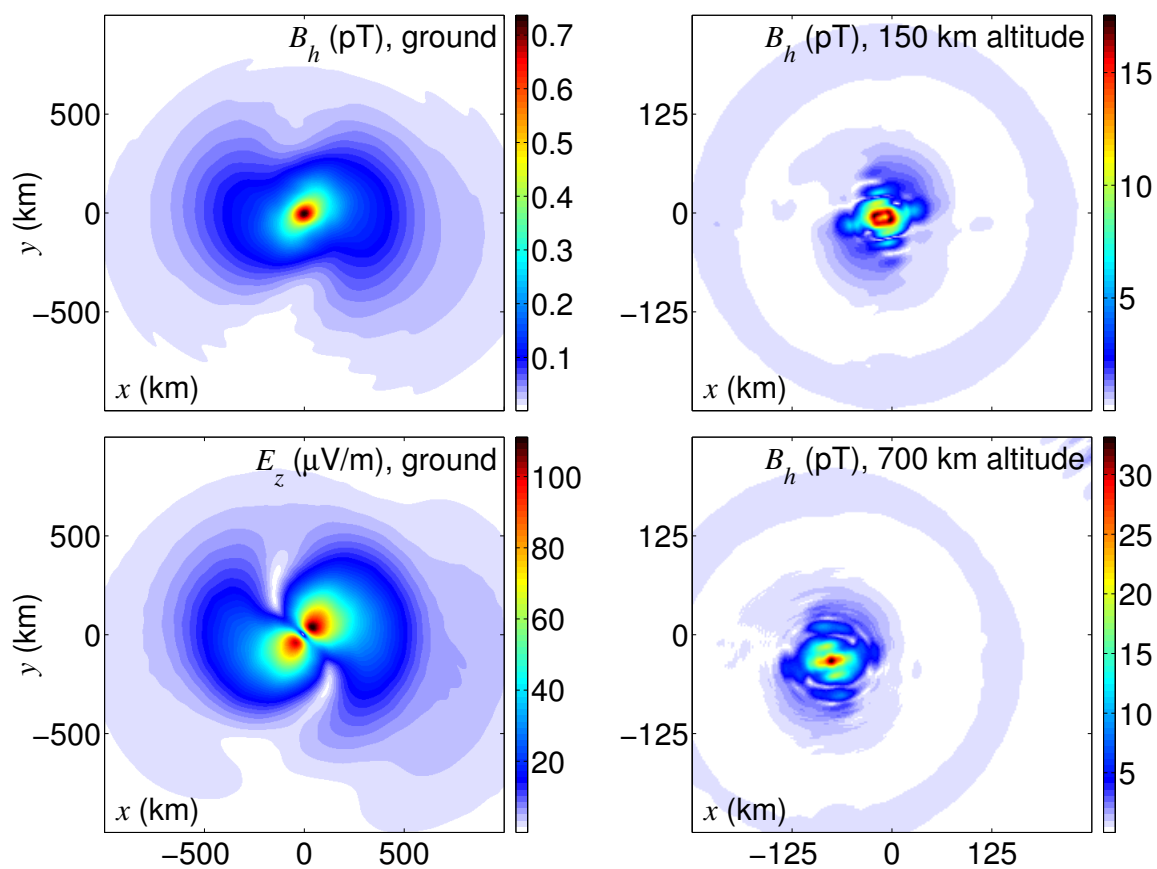


Figure 2.15: ELF/VLF propagation simulations

generated above HAARP. The orientation of the effective dipole is related to, but not precisely the same as, the orientation of the auroral electrojet field, as discussed by *Cohen et al.* [2008a]. *Cohen et al.* [2008a] also observe a directionality inherent in HF heating experiments, resulting from the orientation of the effective dipole above HAARP, which affects the signal amplitudes to distances of 700 km by 5–10 dB as a function of direction. This observed directionality can be seen also in the top left plot of 2.15

Although the model utilized here calculates the electric field, all ground measurements used in this thesis are of the horizontal magnetic field, so we focus on this quantity for the remaining theoretical results presented.

The right hand panels of Figure 2.15 show the ELF/VLF radiation detected at altitudes of 150 km (top), and 700 km (bottom). Unlike the radiation that goes into the Earth-ionosphere waveguide, propagation of signals upward into the whistler-mode is confined to remain close to the field lines due to the anisotropic refractive index profile for whistler-mode propagation [*Helliwell*, 1965]. In fact, the whistler-mode radiation remains so tightly bound in the column, that the distinct sidelobe pattern can be observed in the radiation at 150 km altitude, even though the ELF/VLF waves are generated below 100 km altitude.

The geomagnetic field lines over HAARP, however, are not vertical but are tilted by  $\sim 16^\circ$  from vertical, so in following these lines, the radiated region shifts to the southwest by the time it reaches 700 km altitude. The strong tendency of the ELF/VLF radiation into space to remain in a tight, intense column propagating up the field line has been predicted theoretically [*Payne et al.*, 2007; *Lehtinen and Inan*, 2008] and observed experimentally [*Piddyachiy et al.*, 2008].

Figure 2.16 shows the results of two propagation simulations, with  $\sigma_H$  and  $\sigma_P$  separated, for the same HF heating conditions as in Figure 2.11 and Figure 2.15. Although in real life, the three conductivities cannot be decoupled, the linear nature of the propagation model allows the conductivities to be separated and their radiation patterns calculated independently. This decoupling enables us to see the relative contributions of the two conductivities, for both Earth-ionosphere and magnetospheric injection.

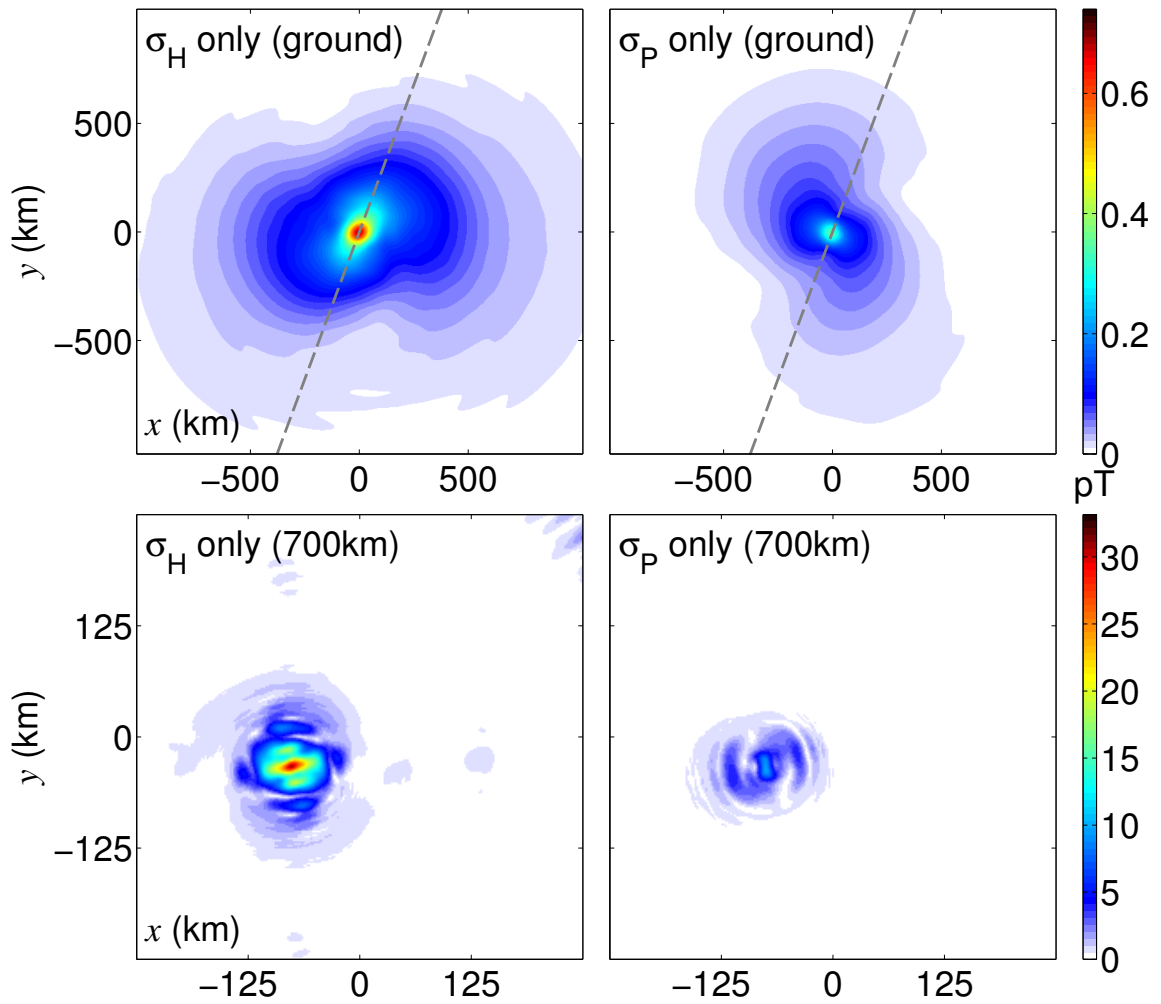


Figure 2.16: Hall, Pedersen, and Parallel conductivity contributions

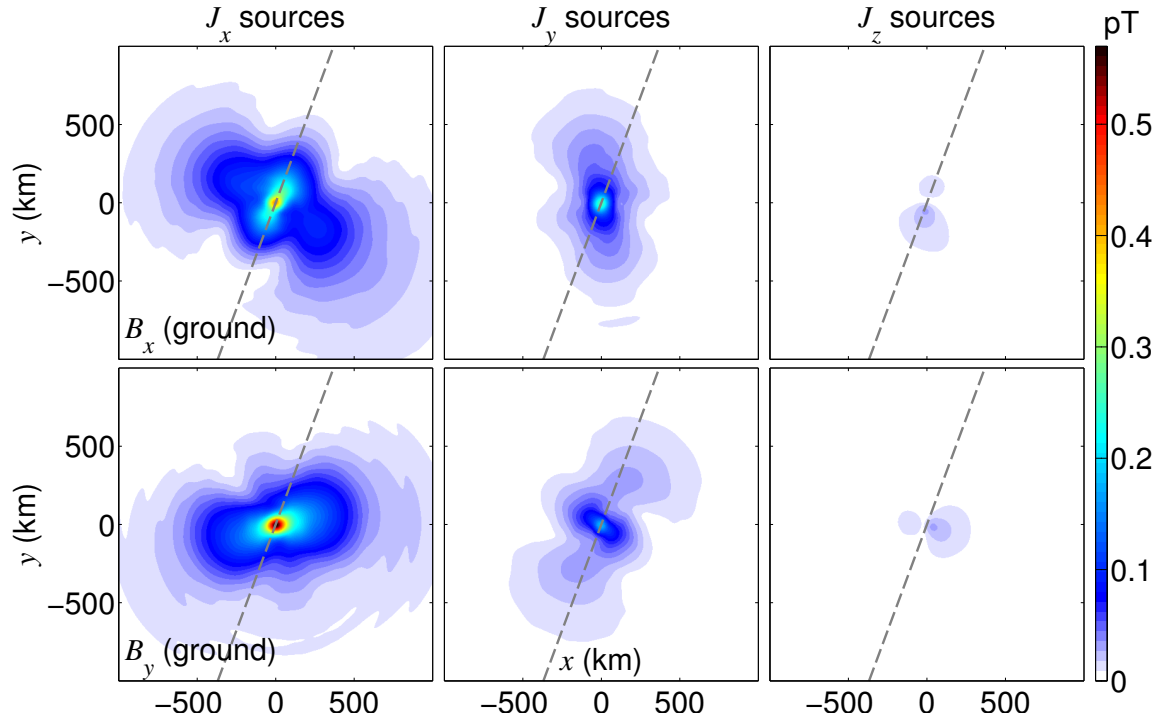


Figure 2.17: Horizontal magnetic field from current sources

In the top two plots, the horizontal magnetic field is plotted along the ground, over a square 2000 km long centered at HAARP. The dashed gray line shows the geomagnetic north-south direction, passing through HAARP. The radiated fields from  $\sigma_H$  current sources (left) appear to be significantly stronger than those from  $\sigma_P$  current sources (right), indicating that the Hall conductivity modulation does play a dominant role in determining ELF/VLF signals observed on the ground. The bottom two plots show the magnetic field over a 500 km square, at an altitude of 700 km. Similar to the ground prediction, the contribution of the Hall conductivity appears to be substantially stronger, for both the ground magnetic field, and the magnetic field injected to 700 km altitude.

Figure 2.17 shows the comparative effect of horizontal sources in the ionosphere. The top three panels show the  $x$  component of the magnetic field, the bottom three panels show the  $y$  component. The three columns show simulations with the same HF heating input as before, except divided up with only the current source components

in the  $x$  (left),  $y$  (center), and  $z$  (right) directions. The sources in the  $z$  direction arise only because of the slight tilt of the magnetic field, and are therefore smaller than the  $x$  and  $y$  components, but on the other hand, a vertical dipole is believed to be substantially more efficient at directing signals into the Earth-ionosphere waveguide.

Dividing the sources into its three components, and observing the resulting  $B_x$  and  $B_y$  fields on the ground suggests that the radiation pattern on the ground can be separated into two components: One larger component closely resembling the pattern from an effective electric dipole above HAARP, and another component resulting from the effects of anisotropy and mode conversion in the ionosphere.

For instance, for the  $x$  component of the current sources, the field on the ground is dominated by the  $B_y$  component (bottom left plot), whereas the  $B_x$  component (top left plot) is smaller. The  $B_y$  radiation pattern is stretched in a direction close to East-West, consistent with a dipole oriented in the East-West direction (where all the sources are oriented), although some rotation in the apparent direction results, likely from rotation of the wave polarizations as they exit the ionospheric plasma. However, the pattern on the ground of the weaker  $B_y$  component (top left plot) is aligned in a symmetric fashion about the geomagnetic North-South line (shown in dashed gray), and this alignment is consistent with the notion that the  $B_y$  component arises from anisotropy and conversion between differently polarized modes, which also have a direction of symmetry in the geomagnetic North-South direction. The same separation of components appears to be the case for the  $y$ -directed current sources (middle plots), which dominantly produces  $B_x$  fields on the ground, and  $B_y$  fields are symmetric about the geomagnetic North-South line. Finally, the two right hand plots show that the small vertical component of the modulated currents in the vertical direction appears to be very weak, despite substantially more favorable efficiency of a vertical dipole for injecting power into the Earth-ionosphere waveguide. Nonetheless, the small vertical sources are included in all model results reported in this dissertation.

Having now described an end-to-end model of HF power from HAARP, to ELF/VLF fields receivers on the ground in the space, we are now ready, in the remainder of this dissertation, to apply this model to both the observed phenomena that we will describe in Chapter 3.

## Chapter 3

# HF Beam Motion: Experiments

Ever since the first observations of ELF/VLF waves by *Getmantsev et al.* [1974], there has been an active search for the most effective way to generate ELF/VLF power by varying the HF beam parameters, which include HF frequency, beam direction, and power modulation envelope. Despite these efforts, most ELF/VLF wave generation experiments have continually been performed with amplitude modulated HF radiation, where the beam power is turned ON and OFF at the desired ELF/VLF rate, since no clear cut advantage could be found with any other modulation technique.

Alternative methods may be advantageous in one (or both) of two ways: they may bring about increased total power of ELF/VLF generated (or, alternatively, the HF to ELF/VLF conversion efficiency), or the ability to provide directional control of the ELF/VLF energy, particularly into the Earth-ionosphere waveguide. We therefore must develop metrics for both measures of merit in any complete comparison of HF heating methods in the context of ELF/VLF generation.

In this chapter, we describe and implement two classes of ELF/VLF wave generation via HF heating, known as beam painting and geometric modulation, which rely prominently on changing beam direction in an effort to generate stronger ELF/VLF signals. Much of the material in this chapter has been published by *Cohen et al.* [2008b] and *Cohen et al.* [2009, in press].

### 3.1 ELF/VLF generation and beam motion

Since the first report of HF beam steering capability at Tromsø [Rietveld *et al.*, 1984], some efforts have been made to utilize this capability in ELF/VLF wave generation experiments. Barr *et al.* [1987] alternated the HF beam between two locations in the ionosphere, with the beam spending half the ELF/VLF period on each spot. The two locations were displaced by a controllable zenith angle, between 0 and  $\pm 37^\circ$ . Observations of the generated ELF/VLF waves were made at a distant receiver ( $\sim 500$  km to the South). Barr *et al.* [1987] report observations at that receiver which resemble that which would result from two independent ionospheric sources operating  $180^\circ$  out of phase, as was demonstrated via an interference pattern (as a function of frequency) observed at the distant receiver.

Villaseñor *et al.* [1996] also utilize a so-called ‘demodulation mode’, where the beam points vertically for half the ELF/VLF period, and points toward two regions on either side of vertical for the second half of the cycle. The demodulation mode is similar in concept to the two-location technique reported by Barr *et al.* [1987], and signal strengths about half compared to AM are reported therein, measured within 150 km of the HIPAS facility. Papadopoulos *et al.* [1994] and Borisov *et al.* [1996] theoretically describe a coherent sweep, with a source moving along a line at rates close to the phase velocity of propagating waves, in order to generate Cerenkov radiation.

In a larger and more general extension of this concept, the first experiments of a new technique known as geometric modulation are presented by Cohen *et al.* [2008b] and constitute one of the key contributions of this dissertation. Geometric modulation involves the HF beam moving in a geometric pattern at ELF/VLF rates, with no power modulation. The period of traversing the geometric pattern dictates the fundamental ELF/VLF frequency generated, since a given location within the pattern undergoes modulated ON-OFF heating at that rate. Due to the rapid (100 kHz) beam steering rates possible with HAARP, nearly arbitrary geometric patterns are possible. In a ‘circle-sweep’, for instance, the HF beam sweeps along a circular pattern, with either clockwise or counterclockwise rotational sense. In a ‘sawtooth-sweep’, the HF

beam traverses a line in one direction, over a period equal to one ELF/VLF period, and can be oriented in an arbitrary direction.

In a separate theoretical effort, *Papadopoulos et al.* [1989] suggest a so-called ‘beam-painting’ technique, where the HF heating beam scans rapidly over a large area during the ON portion of the ELF/VLF period, returning to each location before the electrons have cooled. Although still possessing the ON-OFF pattern to the HF power as amplitude modulation, beam painting enables a much larger area of the ionosphere to be heated, potentially enabling stronger ELF/VLF generation, particularly at the lowest frequencies.

*Barr et al.* [1999] experimentally determined that beam-painting would likely not be effective at the Tromsø facility, as the technique of beam-painting requires high-ERP HF heating so that the characteristic heating rates can be much faster than the cooling rates. Also, the Tromsø facility possessed a beam scanning ability along one dimension (first reported by *Rietveld et al.* [1984]) but not rapid enough to fully implement the beam painting technique. Nonetheless, it is found that the ERP of the Tromsø heater was not sufficiently high [*Barr et al.*, 1999].

The upgraded HAARP facility was specifically designed to combine the highest ERP among worldwide HF heating facilities along with the ability to very rapidly (i.e., 100-kHz rates) steer the beam over a cone within  $\sim 30^\circ$  of vertical. As such, HAARP is uniquely suited to investigate ELF/VLF wave generation with this beam painting technique. In this chapter, we implement the technique and describe its results.

Figure 3.1 schematically shows how the HF beam evolves over the ELF/VLF period (at 2.5 kHz, or 0.4 ms period) for amplitude modulation, beam painting, and geometric modulation, with the row showing the position of the beam (or no beam if HF power is OFF) at five points within the ELF/VLF period. The HF energy can be seen to begin at the ground, reach the ionosphere, and heat a region of the ionosphere shown in red. The light blue elliptical regions represent where the beam had previously heated during the ELF/VLF cycle.

The upper panel shows the progression of the HF beam at five points within the ELF/VLF cycle (assuming 2.5 kHz, so the total ELF/VLF period is 4 ms). The



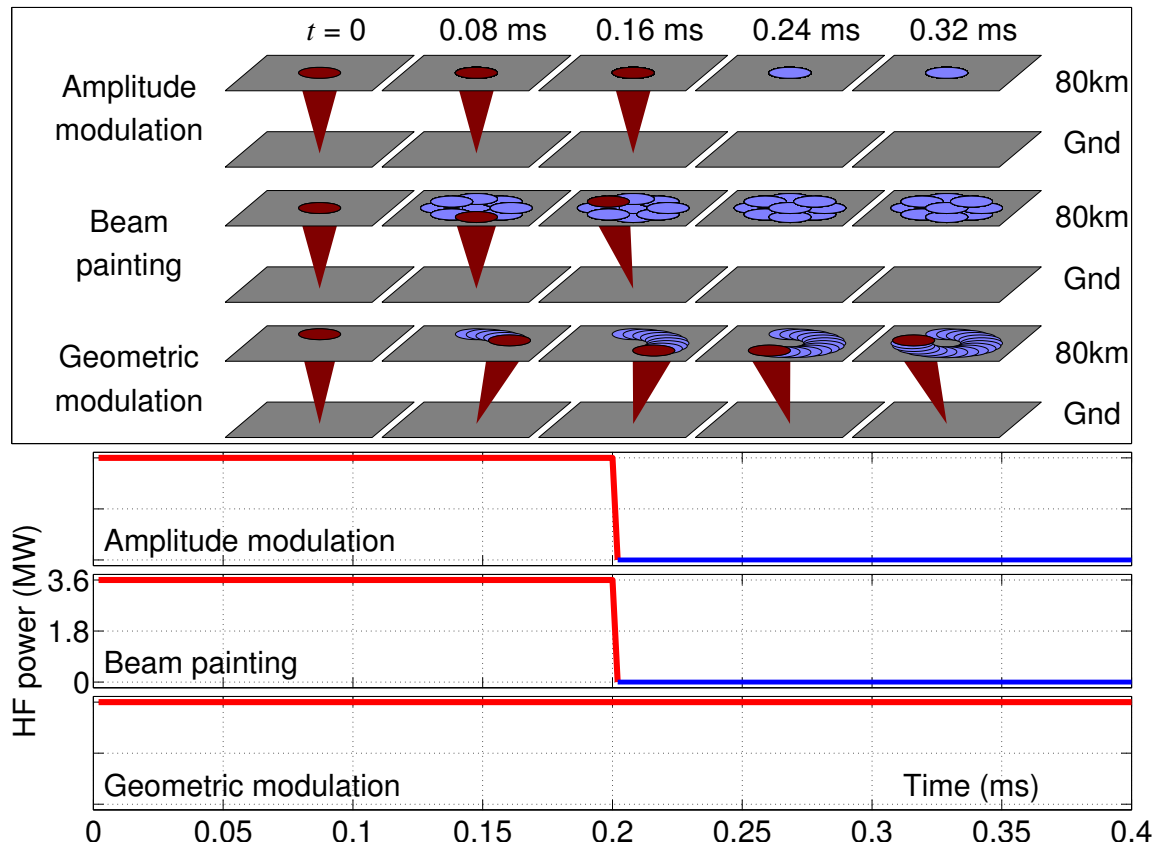


Figure 3.1: Amplitude modulation, beam painting, and geometric modulation

lower panel shows the HF power as a function of time. In amplitude modulation, the HF beam orientation is kept constant during the experiment, but the HF power is multiplied by an envelope function (in this case, a square wave with 50% duty cycle) at the desired ELF/VLF frequency. During beam painting, the HF power is also multiplied by a square-wave envelope function, but the beam is additionally steered very rapidly (i.e., 10  $\mu$ s dwell times) between a number of locations during the ON portion of the ELF/VLF period. For geometric modulation, the HF power is left ON continuously, but the beam is slowly (i.e., in 40 steps) swept along a geometric pattern, so that the geometric pattern is traversed in one ELF/VLF period.

One of the potential advantages of geometric modulation arises from its unmodulated HF power, so it inherently injects twice as much HF power into the ionosphere compared to 50% duty cycle square wave amplitude modulation. We can therefore expect that for the same HF-ELF/VLF conversion efficiency, stronger ELF/VLF signals would be observed in general. Some efforts have been previously made to generate enhanced ELF/VLF waves with a continuous wave (CW) HF heating process. One of the most straightforward ways is presented by *Barr and Stubbe* [1997], which split the Tromsø HF array into two halves, and drove them with two different CW HF frequencies, differing by 565 Hz or 2005 Hz. They find that this CW method produced  $\sim 11$  dB weaker signals compared to amplitude modulation. However, calculations therein suggest that the generation might increase above 2 kHz, specifically in the direction of the array half with a lower HF frequency, though it would decrease in the opposite direction. *Villaseñor et al.* [1996] tried a similar arrangement (referred to therein as double-frequency excitation) at the HIPAS facility and also found generally weaker signals compared to traditional AM generation below  $\sim 2$  kHz, but comparable signals at times between  $\sim 3$  kHz and 14 kHz. This CW technique was also found to be more stable over time than the AM method.

Geometric modulation, however, implies operation of the entire HF array at one frequency, enabling the HF power to remain in a tightly formed, high-ERP beam. Yet, in moving the HF beam at an ELF/VLF rate, it nonetheless achieves an ON/OFF pattern at every location in the ionosphere, although the ON and OFF times are different for different portions of the heated region, a key aspect we discuss later.

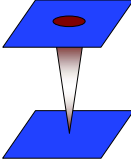
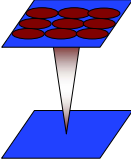
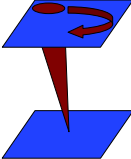
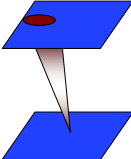
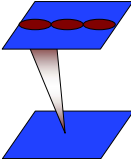
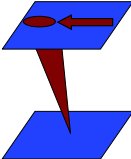
	Amplitude modulation	Beam painting	Geometric modulation
Symmetric	 Vertical-AM	 Grid-paint	 Circle-sweep
Directed	 Oblique-AM	 Line-paint	 Sawtooth-sweep

Figure 3.2: Classification of modulation techniques

## 3.2 Implementation

For each instance of amplitude modulation, beam painting, and geometric modulation, we may utilize either an axially symmetric implementation (where the beam locations do not favor a particular direction), or a directed implementation (where the beam locations are arranged so as to favor a particular direction), as shown in Figure 3.2. For AM modulation, the HF beam can be directed vertically (symmetric, referred to here as ‘vertical-AM’) or at an oblique angle along some azimuth (directed, referred to here as ‘oblique-AM’). The beam-paint locations may be organized with 9-points to fill a grid area (symmetric, referred to here as ‘grid-paint’), or a 3-point paint to illuminate an azimuth line (directed, referred to here as ‘line-paint’). The geometric modulation pattern may be a circle (symmetric, referred to here as ‘circle-sweep’), or a line traversed in only one direction (directed, referred to here as ‘sawtooth-sweep’).

The axially symmetric implementations are useful for understanding the total wave generation achieved with a particular format, since those implementations do

not intrinsically favor a certain direction in the Earth-ionosphere waveguide as a result of the HF beam direction, and thus can be more directly compared to vertical-AM. The directed implementation is useful for characterizing the directionality of the modulation technique, which can be inferred by varying the azimuth chosen. The HAARP array capabilities enable beam locations within  $\pm 15^\circ$  angular region to be included in these formats, so that this specification dictates the radius and length of the geometric modulation sweeps and the spacing of the beam paint locations. This  $\pm 15^\circ$  limitation is applied in all experiments presented here. The name of each implementation, and their correspondence to amplitude modulation, beam painting, and geometric modulation, are used throughout this dissertation and are summarized in Figure 3.2

A comparison between beam painting and geometric modulation is of particular interest, since the techniques illuminate an area of the ionosphere of roughly the same size, whereas amplitude modulation illuminates a smaller region corresponding to a single beam width. However, an important differentiating characteristic between geometric modulation and beam painting is that for the latter, the heated region of the ionosphere radiates ELF/VLF roughly in phase, whereas for geometric modulation, the slower scanning dictates a progressive phase. For instance, the elements on opposite sides of the circle illuminated by the circle-sweep radiate ELF/VLF  $180^\circ$  out of phase.

In all the experiments described herein, amplitude modulation is achieved with 50% duty cycle, 100% depth square wave modulation, at either 3.25 MHz or 2.75 MHz.

### 3.3 Experimental setup

ELF/VLF data are taken with the Atmospheric Weather Electromagnetic System for Observation Modeling and Education (AWESOME) receiver, which is described in detail in Appendix C, and by *Cohen et al.* [2009b]. The AWESOME receivers consist of two orthogonal air-core loop antennas, sensitive to the horizontal magnetic field between  $\sim 0.3$ –47 kHz. A third channel, which can be used for the vertical component

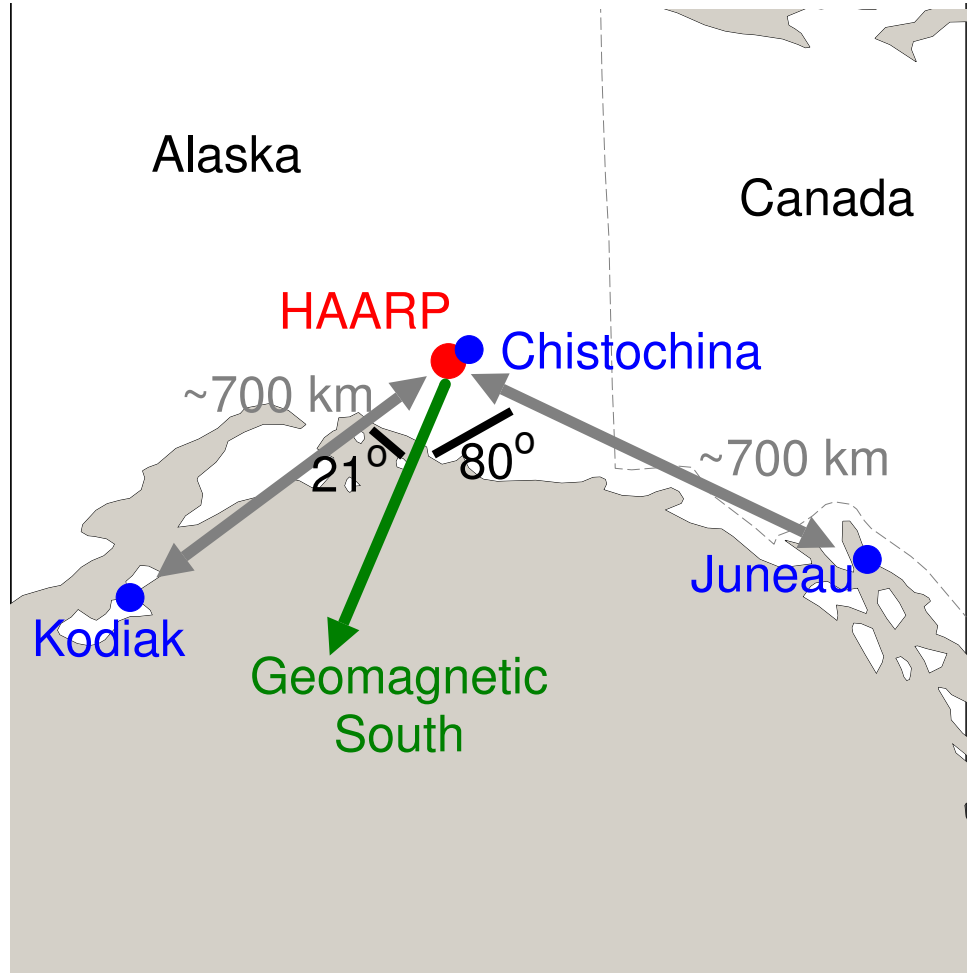


Figure 3.3: Map showing location of HAARP and ELF/VLF receivers

of either the magnetic field or electric field, is not utilized in these observations. Data are sampled at 16 bits at 100 kHz, and synchronized to GPS and provide  $<100$  ns absolute timing accuracy. Receiver noise levels vary depending on antenna size and frequency but are in the range of  $\sim 0.001$  picoteslas per  $\sqrt{Hz}$  in the pass band. Calibration is performed by injection of a signal reference into the front end of the receiver, which enables the recorded digital values to be directly related to magnetic field values at all frequencies. The data can be rotated in post processing, so that the magnetic field can be obtained both in the radial direction (parallel to the source-to-receiver path), and the azimuth direction (orthogonal).

Figure 3.3 shows a map with the three receiver locations utilized in this work: Chistochina ( $62.62^\circ\text{N}$ ,  $-144.62^\circ\text{W}$ , 37 km from HAARP), Juneau ( $58.59^\circ\text{N}$ ,  $134.90^\circ\text{W}$ , 704 km from HAARP), and Kodiak ( $57.87^\circ\text{N}$ ,  $152.88^\circ\text{W}$ , 661 km from HAARP). Chistochina is located near to the HAARP facility, while Juneau and Kodiak are located in roughly orthogonal directions from HAARP, but at similar distances.

The design of an experiment to compare various modulation techniques must take into account the rapidly varying natural generation conditions (namely, the auroral electrojet strength and direction, and the lower ionospheric density profile), which can drastically change (by as much as a factor of 100) on the order of tens of seconds (although at other times they can remain remarkably steady), and can additionally be radically different from day to day. To compare the effect of various modulation techniques, we transmit a series of tones at several different frequencies for each technique. The tones are typically only a few seconds long to minimize the effect of naturally changing conditions, while still allowing unambiguous detection in the receivers.

Figure 3.4 shows a portion of a transmission format intended to evaluate the frequency responses of the six types of modulation. The upper panel shows the frequency-time signature transmitted by HAARP on 19-March, 2009. A sequence of six 2-second long tones at different frequencies allow the frequency response to be assessed on the ground, and is repeated for each modulation scheme. The upper panel in fact shows only a portion of the transmission format, since the directed implementation (dashed lines) are repeated for 8 different direction. The entire transmission format lasts 6 minutes.

The bottom panel of Figure 3.4 shows an example of the ELF/VLF signals detected at a receiver in Chistochina, Alaska. The data are displayed in the form of a spectrogram, where the magnetic field time-series are divided into overlapping bins (in this case, 75% overlapping) of a certain length (in this case,  $1/80$  second), and a Fast Fourier Transform (FFT) is performed on each bin (in this case, with zero padding by a factor of two). The spectrogram displays the amplitude of the FFT of each bin with a logarithmic colorbar scale. The spectrogram enables the frequency content of a dynamically changing signal (such as that of VLF broadband data) to

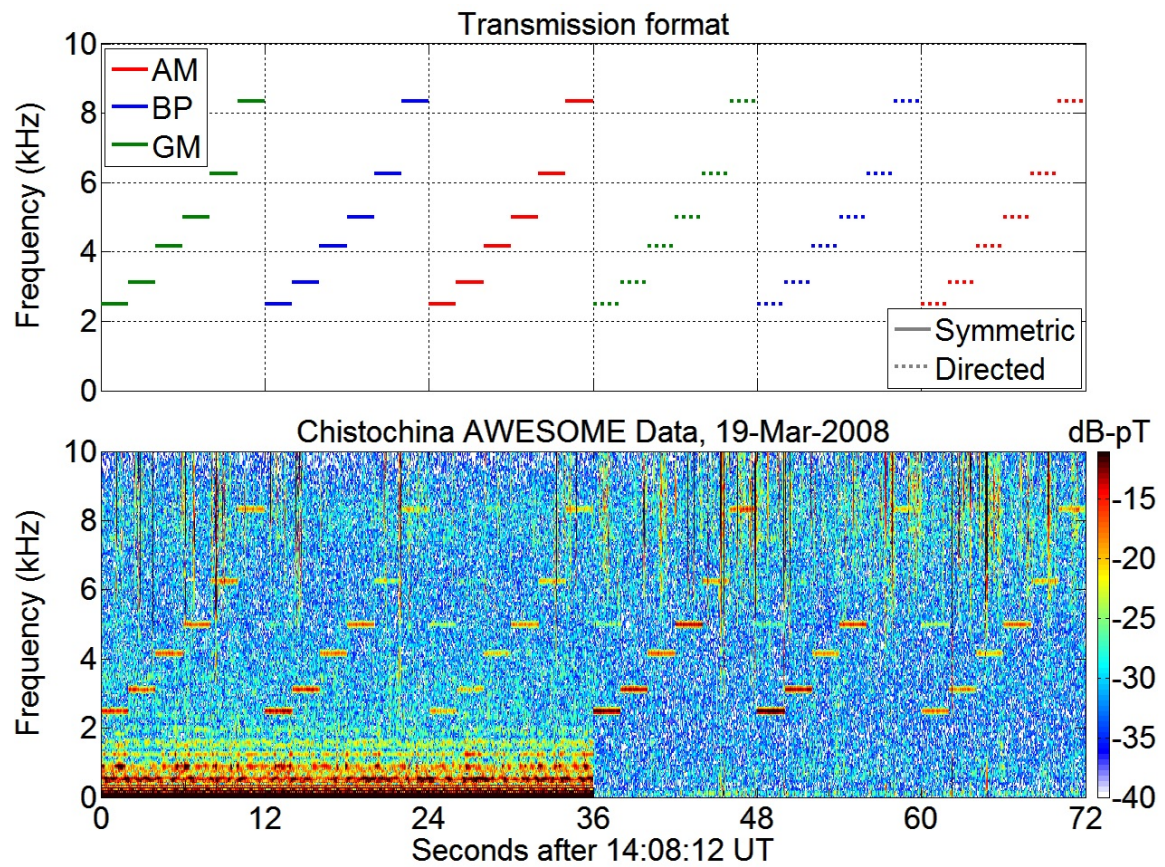


Figure 3.4: Transmission format and sample data from AWESOME receiver

be concisely presented. For instance, the tones are clearly detected in the form of horizontal lines, and appear with very high signal-to-noise ratio. There are also other features in the data. The thin vertical lines are radio atmospherics, so-called ‘sferics’, which are impulsive radiation originating from lightning strokes which may be at global distances from the receiver.

The bottom portion of the spectrogram, below 2 kHz, shows significant interference from power lines, in the form of 60 Hz coupled energy, along with many higher-order harmonics, colloquially known as ‘hum’. It is possible, nonetheless, to remove this steady interference, and in the second half of the record, we have applied a technique to mitigate the hum. Appendix D of this dissertation describes two such techniques for achieving power line interference mitigation, one optimized for computational efficiency (usable in a real-time system) and another optimized for optimal subtraction (useful for limited post-processing applications).

To further mitigate changing electrojet and ionospheric conditions, and to enable meaningful long term averages, the transmission format is repeated for long periods (typically an hour or more), after which the following averaging technique is applied (also utilized by *Cohen et al.* [2008b]). For each received single-frequency tone, the complex phasor amplitudes of both the radial and azimuthal magnetic fields are calculated by integrating the demodulated data in the baseband over the duration of the tone. The phasors over the many repetitions of the format can then be averaged, since the phasor is represented by a single complex number. The phasors are separately averaged for the radial and azimuthal fields, and the final results then summed in quadrature.

Averaging the signals in complex phasor form instead of just their amplitudes has the advantage of significantly improving the signal to noise ratio (SNR). When averaging a large number of complex phasors, incoherent noise destructively interferes, whereas coherent signals with the same phase add constructively, thereby enabling detection of weaker signals. The same process can then be repeated at neighboring frequencies without HAARP transmissions, to determine comparative noise levels (and therefore the uncertainties via the SNR). We note that if this technique is applied during periods when the polarization or phase of the received signals change



substantially over time (for instance, when the ionospheric conditions or auroral electrojet orientation change), the averaged phasor values may not accurately represent the average signal amplitudes, since the signals would not maintain constant complex phase. We therefore repeat this experiment on multiple days, to confirm that the comparative results shown here hold consistently, although only one representative example from a single day is shown here.

All HF heating experiments described here are carried out with X-mode heating at 2.75 MHz or 3.25 MHz, the lowest HF frequencies available with HAARP, and also those that have been observed to produce the strongest ELF/VLF amplitudes on the ground (due to higher absorption in the *D*-region). The ERPs at these frequencies are  $\sim 420$  MW and  $\sim 575$  MW, respectively.

The geometric modulation and beam painting experiments involve changing the phase of the HF signal radiating from each antenna element, in order to change the direction of the HF beam at each of the many discrete steps. We must, however, account for the possibility that the HF beam shape does not remain constant as a result of the beam stepping. Though not shown here, it is observed with an HF receiver underneath the HAARP facility that the antenna array undergoes a transition period, a few  $\mu$ s long, at each step of the beam motion. During this period, the beam location may slew back and forth slightly, nevertheless the shape of the HF beam and its sidelobes remain largely intact, with the ERP likely not reduced by any more than 1 dB. Hence, the transition period between successive beam steps likely has a small, if any, impact on the HF power densities delivered to the ionosphere, as compared to amplitude modulation with a stationary beam.

### 3.4 Comparative frequency response

A single comprehensive experiment which quantitatively compared the above six modulation schemes was conducted on 16 March 2008, between 1300 UT and 1600 UT. Each technique is implemented in symmetric form (top row) and directed form (middle and bottom rows directed to Juneau and Kodiak, respectively). The observed fields, with error bars, calculated as discussed above, are shown at Chistochina (left

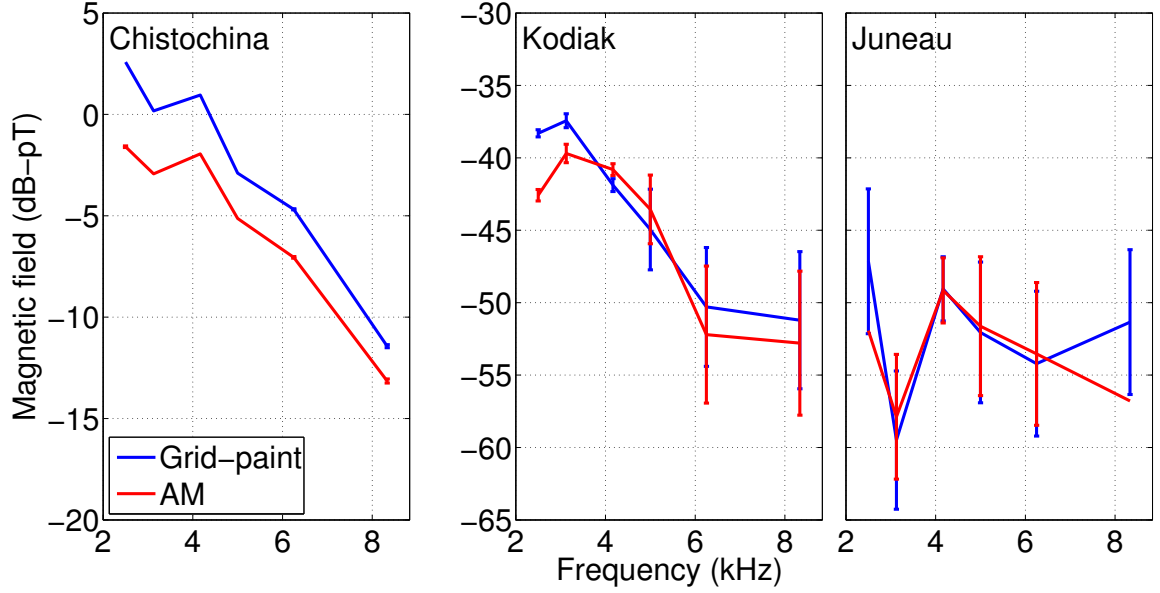


Figure 3.5: The generated amplitudes from beam painting

column), Juneau (center column), and Kodiak (right column), although the error bars at Chistochina are too small to be visible (due to the very high SNR). We note again that since Juneau and Kodiak are at close to orthogonal azimuths from HAARP, they sense nearly orthogonal elements of the radiation pattern from the HAARP ELF/VLF ionospheric source region. The locations of the receivers in Alaska, with respect to the HAARP, are shown in the map in Figure 3.3.

### 3.4.1 Generated amplitudes from beam painting

Since amplitude modulation represents the benchmark in the history of ELF/VLF wave generation, we now compare both geometric modulation, and beam painting, against amplitude modulation, for both symmetric and directed forms. Figure 3.5 shows the average phasor magnetic field amplitude for Chistochina, Kodiak, and Juneau, with vertical-AM shown in red, and the grid-paint shown in blue. The response of amplitude modulation generally drops off with frequency above the 2–4 kHz range, consistent with past experiments which have found decreasing generation efficiency with increasing frequency [Stubbe and Kopka, 1977]. But since this aspect

is common to all HF heating experiments, our focus is on the comparative frequency response between vertical-AM and the other modulation techniques. In addition, signals are 5–10 dB weaker at Juneau compared to Kodiak, likely due to the orientation of the effective HAARP dipole, as observed and discussed by *Cohen et al.* [2008a]. In particular, an effective ELF/VLF dipole above HAARP oriented roughly in the geomagnetic East-West direction (roughly towards Juneau) has weaker radiated signals in that direction.

The grid-paint is implemented with the HF beam alternating among 9 locations with 10  $\mu$ s dwell times at each of them. The nine locations consist of the vertical direction, and eight locations at 15° zenith angle, and azimuths spanning a complete circle at 15° increments. The beam therefore spends 1/9 of the ON portion of the ELF/VLF cycle, at each of the nine beam locations, but according to the proposed idea of beam painting, sufficiently high ERP would be required such that the heating during that small portion of time is strong and fast enough to sustain the electron temperatures at a high level during the other 8/9 steps in the ON cycle.

At Chistochina, which is very near to the HAARP facility, the ELF/VLF signals are substantially stronger than the comparative noise floor (which is no higher than –60 dB-pT), so that the error bars are not even visible in the plot. At Kodiak or Juneau, the error bars are larger. Measurements are taken at six frequencies (2.5, 3.125, 4.167, 5, 6.25, and 8.333 kHz).

At Chistochina, the grid-paint is stronger by 2–4 dB compared to vertical-AM, with the gap being smaller at the highest ELF/VLF frequency. All six ELF/VLF frequencies verify the same observation. However, at the two more distant sites ( $\sim 700$  km), the two curves are indistinguishable within the error bars, although at the two lowest frequency measurements taken at Kodiak, grid-paint appears to be yielding a  $\sim 2$ –4 dB advantage. On the basis of the experimental measurements here, beam painting appears to generate a detectable boost in signal amplitudes only at sites near the HAARP facility, whereas there seems to be no advantage at longer distances.

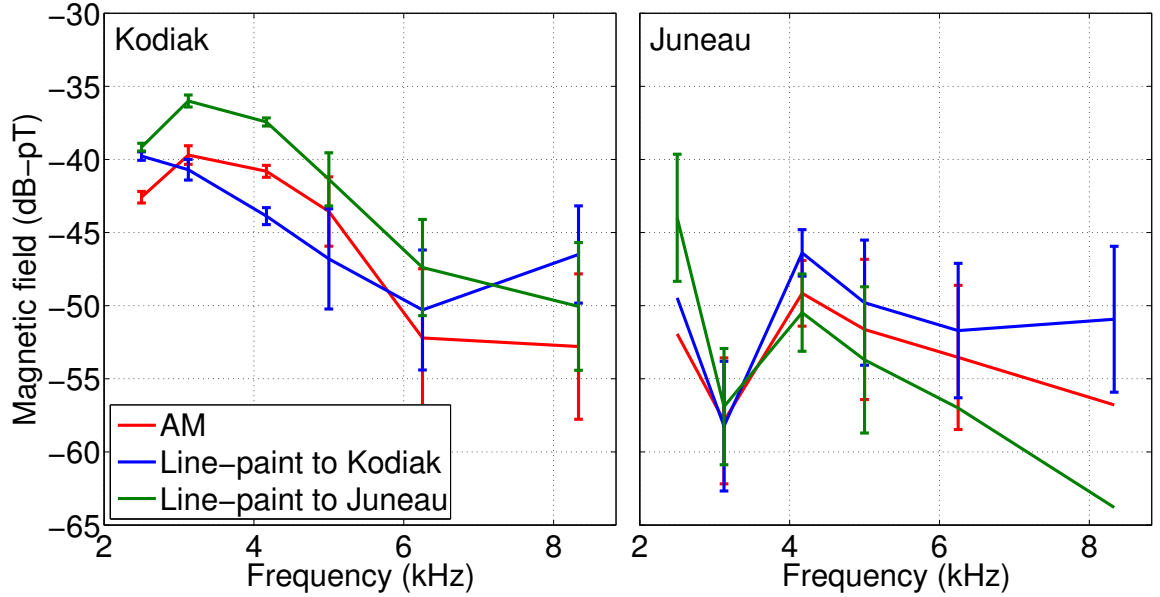


Figure 3.6: Directionality associated with beam painting

### 3.4.2 Directionality from beam painting

The directionality of beam painting is evaluated via the line-paint. The line-paint is implemented with three beam locations, one vertical, one directed toward a specific receiver at  $15^\circ$  angle, and one directed away. The beam alternates between these three locations with  $10 \mu\text{s}$  dwell times. We plot in Figure 3.6 the magnetic field received at Kodiak (left) and Juneau (right), as a function of frequency, for vertical-AM (red), a line-paint oriented toward Kodiak (blue), and a line-paint oriented to Juneau (green). Since Kodiak and Juneau are at close to orthogonal directions from HAARP, they effectively sense two orthogonal components of the directional radiation pattern, especially since they are both at very similar distances.

Changing the azimuth of the line-paint between the HAARP-to-Kodiak direction and the HAARP-to-Juneau direction affects the received ELF/VLF amplitudes by 4–6 dB, particularly at Kodiak (where the error bars are smaller). Directing the line-paint to Kodiak generates stronger signals at Juneau, orthogonal to the orientation of the line of the line-paint. We can thus place a lower bound of 4–6 dB on the directional control inherent to the line-paint scheme.

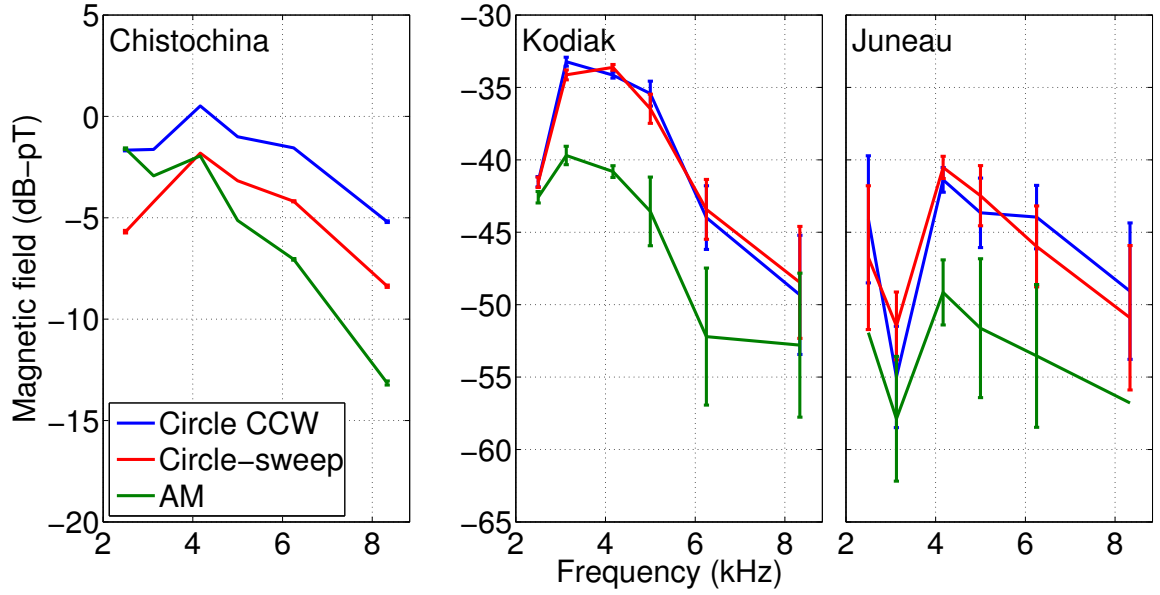


Figure 3.7: The generated amplitudes from geometric modulation

### 3.4.3 Generated amplitudes from geometric modulation

We now describe the observed properties of geometric modulation. Figure 3.7 shows a comparison between the circle-sweep and vertical-AM, analogous to Figure 3.5. At Chistochina, the comparative frequency response between the circle-sweep and vertical-AM is a strong function of frequency, more so than in the case of the grid-paint comparison to vertical-AM. between 2–4 kHz, the circle-sweep is less effective, but above 4 kHz, the circle-sweep ELF/VLF field exceeds that of vertical-AM by as much as  $\sim 5$  dB.

As in the case of the grid-paint in Figure 3.5, the behavior looks substantially different at the more distant sites, Kodiak and Juneau. There, the circle-sweep generates stronger ELF/VLF waves by 7–11 dB. Similar to the behavior observed at Chistochina, the circle-sweep appears to become increasingly advantageous compared to vertical-AM for the higher frequencies, i.e., above 4 kHz, whereas grid-paint and vertical-AM, observed at long distances, appears to yield the same result regardless of frequency.

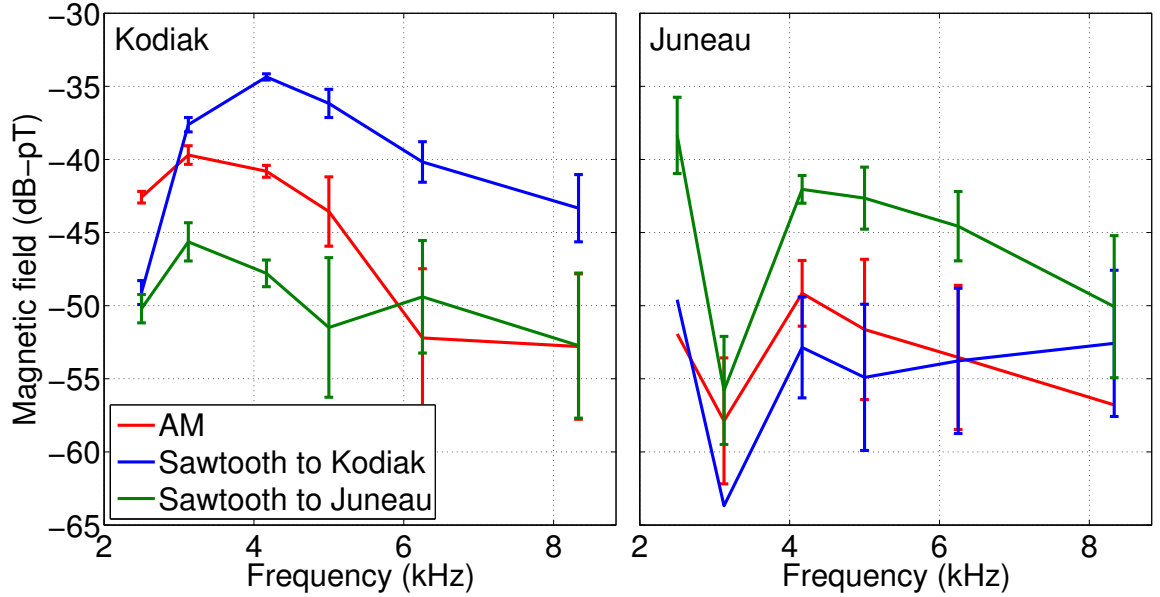


Figure 3.8: Directionality associated with geometric modulation

### 3.4.4 Directionality from geometric modulation

We now explore the directionality of geometric modulation as achieved via the sawtooth-sweep. Figure 3.8 shows sawtooth-sweeps oriented to Kodiak, and oriented to Juneau, compared to vertical-AM. In these cases, the directional control apparently exhibited by the sawtooth-sweep is very large, as high as 11–15 dB. This directionality is most apparent at Kodiak, where the SNR is higher than at Juneau. Even at Juneau, though, the sawtooth-sweep oriented in its direction is unambiguously stronger than either vertical-AM, or a sawtooth-sweep to Kodiak. The sawtooth-sweep appears to have directionality inherently opposite to that demonstrated by the line-paint, in that it directs ELF/VLF radiation in the direction of the sawtooth-sweep azimuth.

### 3.4.5 Geometric modulation compared to oblique-AM

In light of the commentary put forth by *Moore and Rietveld* [2009], and the subsequent response by *Cohen et al.* [2009a], it is worth considering the comparative advantage of the sawtooth-sweep and circle-sweep over simply tilting the HF heating beam and

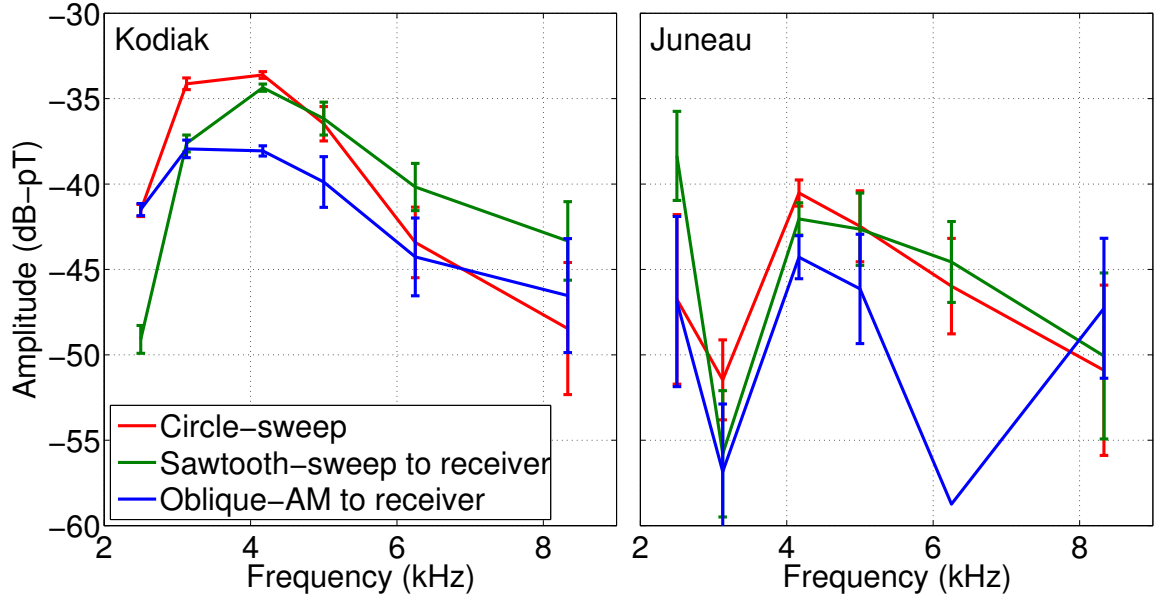


Figure 3.9: Comparison between oblique-AM and geometric modulation

utilizing amplitude modulation (i.e., oblique-AM).

A comparison between the relevant techniques is shown in Figure 3.9. The circle-sweep yields 3–6 dB stronger signals compared to oblique-AM directed at that receiver, particularly in the frequency range between 3 and 6 kHz. Similarly, comparison between the sawtooth-sweep directed to either Juneau or Kodiak and oblique-AM directed to the same receiver indicates that the sawtooth-sweep yields 3–6 dB stronger signals at that receiver, particularly in the frequency range above 4 kHz, at least as high as 8 kHz. Hence, the geometric modulation techniques appears to produce amplitude gains at a distant receiver that cannot be explained strictly by the tilted-beam nature.

We also note that although the  $15^\circ$  oblique angle as discussed here enables a more direct comparison with geometric modulation, the current hardware limitations of HAARP allow oblique-AM heating at up to  $30^\circ$  from vertical, whereas geometric modulation and beam painting are currently restricted to a  $\pm 15^\circ$  cone from a given location. It is possible, however, to conduct geometric modulation and beam painting experiments with the center point located  $15^\circ$  off vertical (whereas in this paper the

center point is strictly vertical. Such a strategy may capture additional directionality and amplitude gains. For example, a future experiment may compare oblique-AM HF heating at  $30^\circ$  from vertical with a circle-sweep in which the center of the circle is inclined by  $15^\circ$  from vertical.

### 3.4.6 Summary of ground-based observations

Figure 3.10 presents the complete experimental results in a comprehensive fashion. The columns show received signals at Chistochina (CH), Juneau (JU), and Kodiak (KO), and the colored plots refer to geometric modulation (green), beam painting (blue), and amplitude modulation (red). From this display, the key features of the modulation scheme can again be observed. Beam painting yields a small enhancement in amplitudes (2–4 dB) when observed near HAARP compared to vertical-AM, but this enhancement is not apparent farther away. Geometric modulation, on the other hand, generates 7–11 dB stronger signals than those of vertical-AM at sites far away from HAARP, although the difference is smaller near HAARP, and even smaller below 3–4 kHz.

It seems that the relative advantage of geometric modulation circle-sweep in generating stronger ELF/VLF is not apparent at observation sites near HAARP. As discussed further in Chapter 5, this observation likely arises from the pattern of ELF/VLF phase in the HF heated region. For instance, since opposite sites of the circle-sweep radiate ELF/VLF out of phase, the radiation from the circle-sweep would produce a null at the center. The lack of a complete null at Chistochina is likely due to nonidealities of the sources, namely, the finite size of the HF beam, and also the effects of its sidelobes. Additionally, Chistochina is displaced from the HAARP facility by  $\sim 37$  km (and therefore, from the location on the ground below the center of the circle-sweep).

Finally, we have the observation that 4–6 dB of directional control can be achieved by rotating the azimuth of the line-paint, with radiation preferentially injected orthogonal to the azimuth. On the other hand, the sawtooth-sweep appears to yield 11–15 dB of directional control by rotating the azimuth of the sawtooth-sweep, with



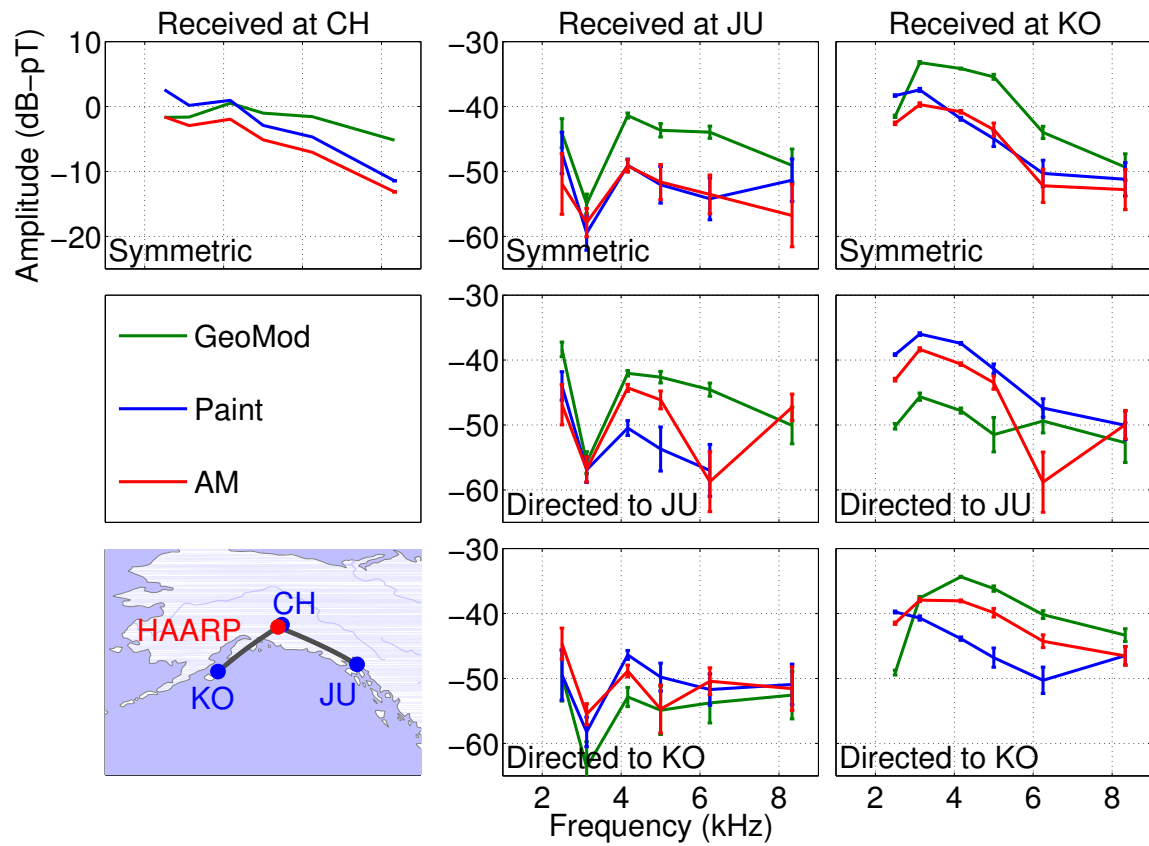


Figure 3.10: Experimental frequency response of HF heating

preferential radiation in the direction of the sweep (opposite to that observed with the line-paint)

### 3.4.7 Magnetospheric injection

All of the observations presented here concern ground-based observations, so they specifically refer to Earth-ionosphere waveguide injection. We are also interested in the comparative magnetospheric injection capabilities of these modulation schemes. In general, we cannot assume that the signal received on the ground demonstrates similar behavior as a function of HF beam modulation and frequency, compared to the signal injected into the magnetosphere.

Unfortunately, measurements at the edge of the magnetosphere (500–1000 km altitude) can only be made by satellites in low Earth orbit (LEO) such as the DEMETER spacecraft [Parrot, 2002]. These spacecrafts cannot record continuous HAARP-transmitted signals, since they pass over the HAARP region only a few times per day, and move quickly (many km per second) during these passes. These passes also have different trajectories over HAARP, and record during different ionospheric conditions, so that combining many satellite measurements statistically is rather difficult. As such, a direct experimental comparison of amplitude modulation, beam painting, and geometric modulation in the context of magnetospheric injection is extremely difficult to obtain at this time, although some limited and inconclusive observations have been made. We therefore discuss this exclusively in Chapter 4, in the context of simulation results.

# Chapter 4

## HF Beam Motion: Modeling

The experiments in Chapter 3 yielded the first quantitative experimental comparison between amplitude modulation, beam painting, and geometric modulation, and discussed a number of implementations of each one. However, the experimental evidence presented here is invariably limited by the number of available/suitable receivers, since one cannot place receivers at each and every location.

In this chapter, we apply the complete theoretical model introduced in Chapter 2 to the experimental techniques discussed in Chapter 3. A quantitative comparison between theory and experiment may help validate our theoretical framework and allow us to identify any missing physics that may need to be introduced. More importantly, a validated theoretical model can be used to predict features not observable from current experiments, such as the ELF/VLF power injected into space resulting from amplitude modulation, beam painting, and geometric modulation.

### 4.1 Modulated currents

We begin by quantitatively comparing the ionospheric modulated currents from the various modulation techniques. Figure 4.1 show a horizontal slice of the Hall currents, with each of the six implementations from Figure 3.2 represented in a column. The simulation shown is for 3.25 MHz HF heating, at 3 kHz modulation frequency. The dwell time for the beam painting experiments in each location is taken to be  $2\ \mu\text{s}$ ,

and the number of steps in the geometric modulation modeling is taken to be 20. The limit of  $\pm 15^\circ$  rapid beam steering is also taken into account, so that the implementation of the HF modulation in the simulation matches that of the experiments. The directed implementations are modeled with favorable azimuth  $127^\circ$  East of North, which is toward the Juneau receiver from HAARP (roughly toward the Southeast). The ionospheric model utilized is based on the winter daytime electron density profile presented in Chapter 1, since the main experimental results presented in Chapter 3 were conducted during a winter daytime ionospheric condition. A realistic empirically determined HF radiation pattern from the HAARP array is used to determine the spatial distribution of HF wave power.

The rows show the magnitude of the currents (normalized to the maximum value) at six points during the first half of the HF heating cycle, in a horizontal slice at 75 km altitude. The red areas are positive currents (i.e., in the direction of the  $\vec{E} \times \vec{B}_0$ ), and the blue areas are currents in the opposite direction. Since we plot here the Fourier extracted first harmonic of the currents, all currents and fields simply vary sinusoidally with some amplitude and phase.

Since time increases in the downward direction, we can observe the timing behavior of the different modulation schemes by examining the lower panels. For instance, in the vertical-AM column, the currents in the center of the main beam reach a peak value slightly earlier than the currents at outside edges of the main beam. The same result can be seen for the grid-paint, oblique-AM, and line-paint schemes. However, in those modulation schemes, the currents are generally in phase apart from this timing correction. In most of the panels for those four columns, the currents are either all positive, or all negative.

The circle-sweep and sawtooth-sweep currents, in the third and sixth columns, however, appear to behave quite differently. Here, we have both positive and negative currents present at any given time. In fact, as time advances, the entire pattern of positive and negative currents can be seen to move. The circle-sweep forms two swaths of currents, one positive and one negative, which rotates in a circular manner, much like a dog chasing its own tail. The sawtooth-sweep contains a few swaths, which travel along a line to the southeast direction. So the two geometric modulation

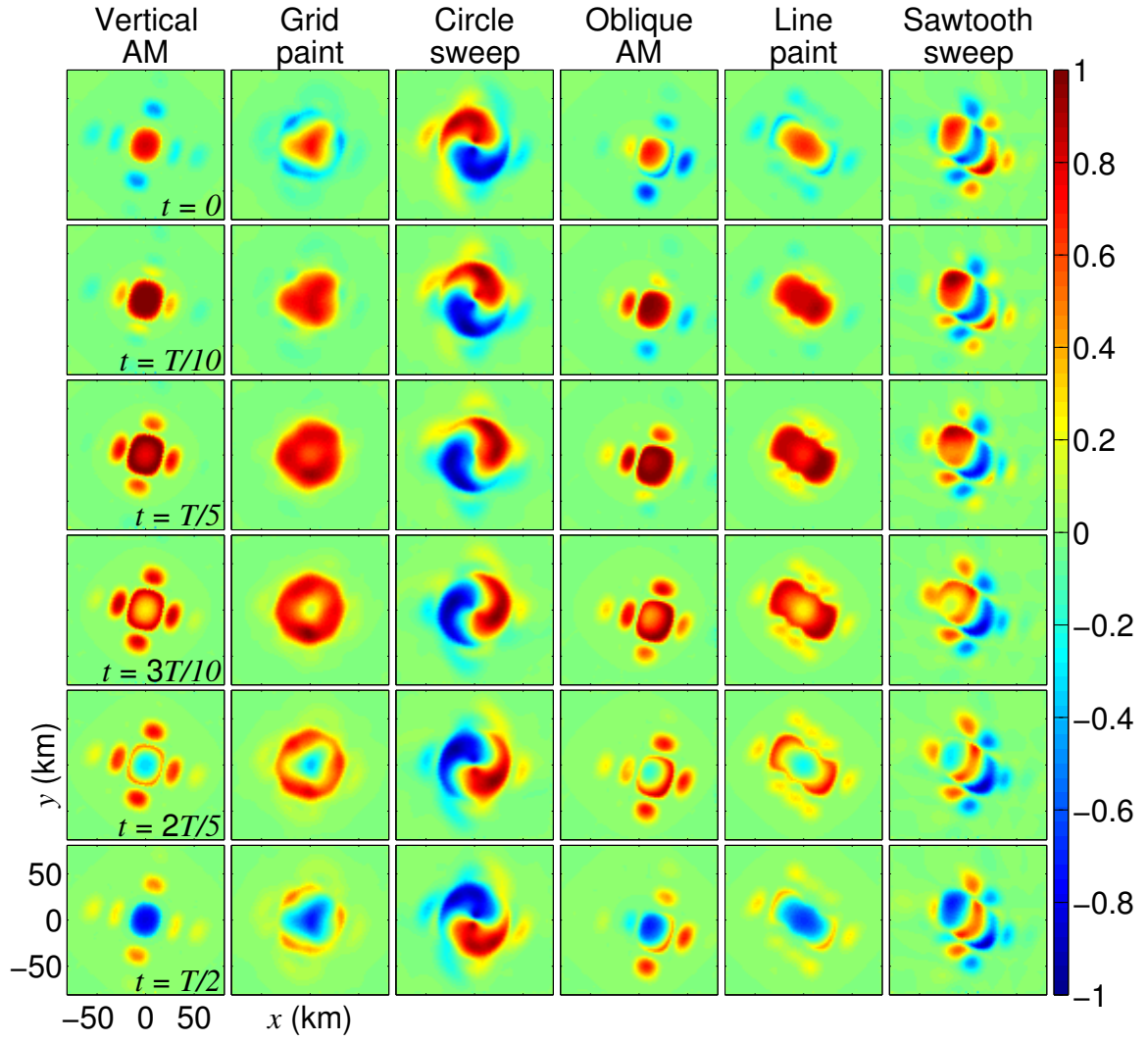


Figure 4.1: Modeled Hall currents from modulated HF heating

schemes appear able to generate a moving source, which move in the direction of the beam sweep.

## 4.2 Fields on the ground

Figure 4.2 shows the result of the propagation model with three dimensional currents from 5 kHz square wave amplitude modulation of 3.25 MHz HF heating. The horizontal magnetic fields on the ground are shown over a  $200 \text{ km} \times 200 \text{ km}$  region centered at HAARP. The model is applied assuming the same winter daytime ionosphere utilized in the HF heating model. The horizontal magnetic fields correspond to the experimental measurements presented in Chapter 3.

The propagation model assumes a flat Earth, so the locations of the receivers are approximated to correspond to their distances and azimuths on a curved Earth. Juneau is taken to be at an azimuth of  $127^\circ$ , and a distance of 704 km from HAARP, while Kodiak is taken to be at an azimuth of  $217^\circ$ , and a distance of 661 km, from HAARP, although these sites are not within the grid of locations shown in Figure 4.2.

The three columns show the horizontal magnetic field on the ground from amplitude modulation (left), beam painting (center), and geometric modulation (right). The three rows show the symmetric implementation (top), directed implementation toward Juneau (JU, middle), and directed implementation toward Kodiak (KO, bottom), as shown in Figure 3.2. Although the locations of Juneau and Kodiak are outside the grid of locations shown in Figure 4.2, the arrows in the middle and bottom rows show the direction toward Juneau and Kodiak, respectively, from the origin.

The radiation pattern on the ground relatively near HAARP varies substantially depending on the HF beam modulation function. For both amplitude modulation and beam painting, the strongest magnetic fields occur close to the HAARP facility, i.e., closest to the radiating ionospheric region. However, the oblique-AM panels (directed amplitude modulation) appear to shift the center of the high-magnetic-field patch away from the origin, and toward the direction of the beam tilting. The effect of the four sidelobes can also be seen in the symmetric amplitude modulation panel,

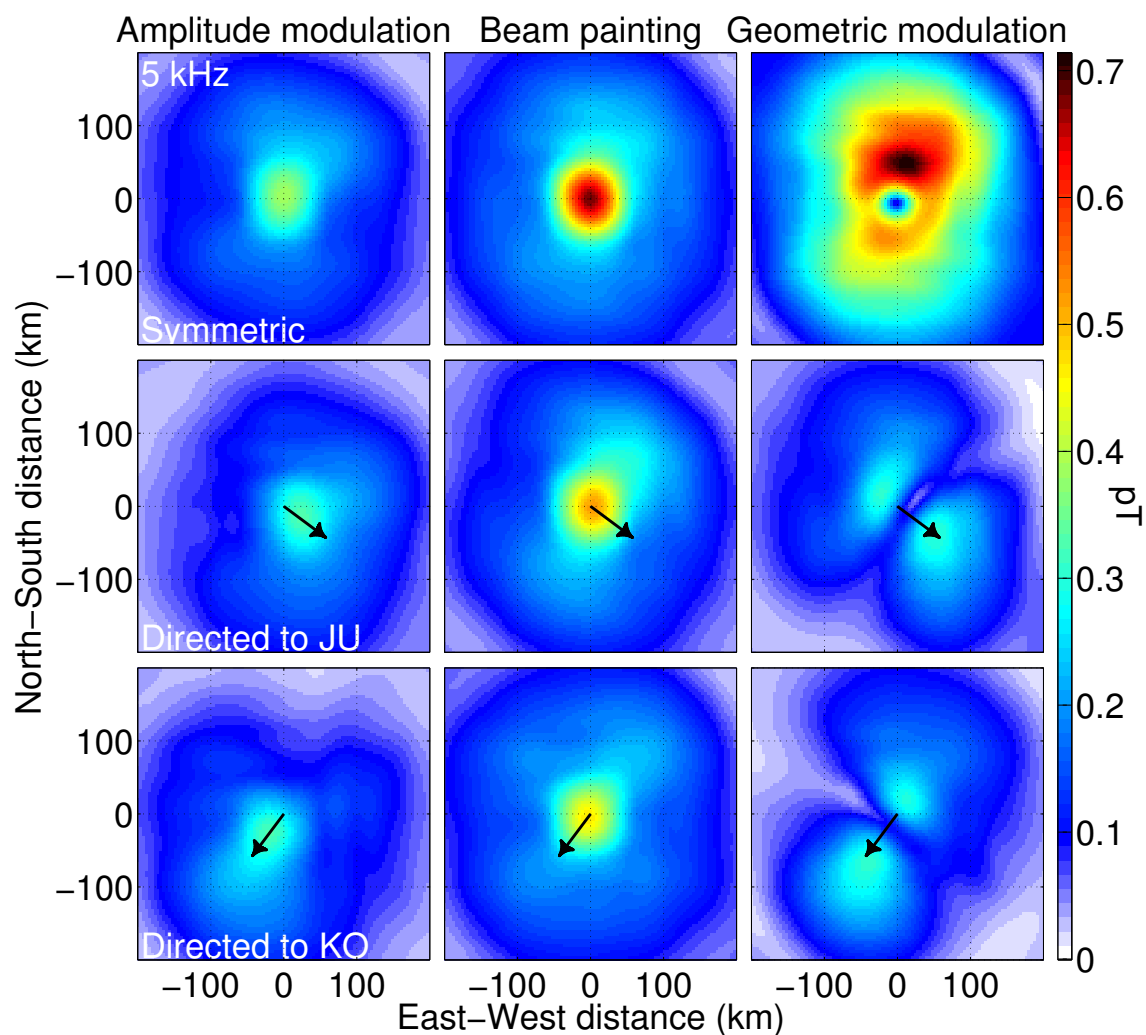


Figure 4.2: Modeled fields on the ground from 5 kHz modulated HF heating

manifesting as four patches of enhanced magnetic field in the four corners surrounding the central patch.

The magnetic fields near the origin for the three beam painting techniques appear to be stronger than for the corresponding amplitude modulation techniques. However, apart from this patch of strong magnetic field near HAARP, the amplitude modulation and beam painting appear to be generally similar.

In contrast, the character of geometric modulation appears to be radically different from the other two. In all three implementations, there is a local minimum underneath the heated ionosphere, despite the fact that the origin location is closest to the center of the radiating sources. For the circle-sweep (or symmetric geometric modulation), this local minimum is a small circular patch, centered roughly at the origin,  $\sim 30$  km in radius, where the fields are a factor of  $\sim 5$  lower than they are at  $\sim 60$  km distance from the origin. For the sawtooth-sweep (or directed geometric modulation), the local minimum is a swath passing through the origin,  $\sim 20$  km thick, where the fields are  $\sim 5$  times weaker than they are at  $\sim 60$  km distance from the origin toward the sawtooth-sweep azimuth.

The nulls near the heated region apparent for the geometric modulation schemes are in fact consistent with our experimental observations noted in Chapter 3. In particular, at Chistochina, the receiver near HAARP, the effectiveness of the geometric modulation circle-sweep and sawtooth-sweep appeared to be similar to amplitude modulation, and less than that of beam painting, i.e., no enhancement in the ELF/VLF magnetic field is observed from geometric modulation at Chistochina. On the other hand, at Juneau and Kodiak,  $\sim 700$  km away, the circle-sweep, and sawtooth-sweep directed to the receiver generated substantially stronger signals. This behavior would appear to be explained by the theoretical results, which demonstrate a null underneath the heated region. Chistochina is  $\sim 37$  km away from HAARP, which places its location near the edge of the null in the circle-sweep radiation pattern.

Although the magnetic field within 200 km of the HF heater may be helpful in understanding the basic physical differences in the radiation from the HF modulation techniques, the more relevant application regards the injection of signals farther into the Earth/ionosphere waveguide. Figure 4.3 shows the horizontal magnetic field on



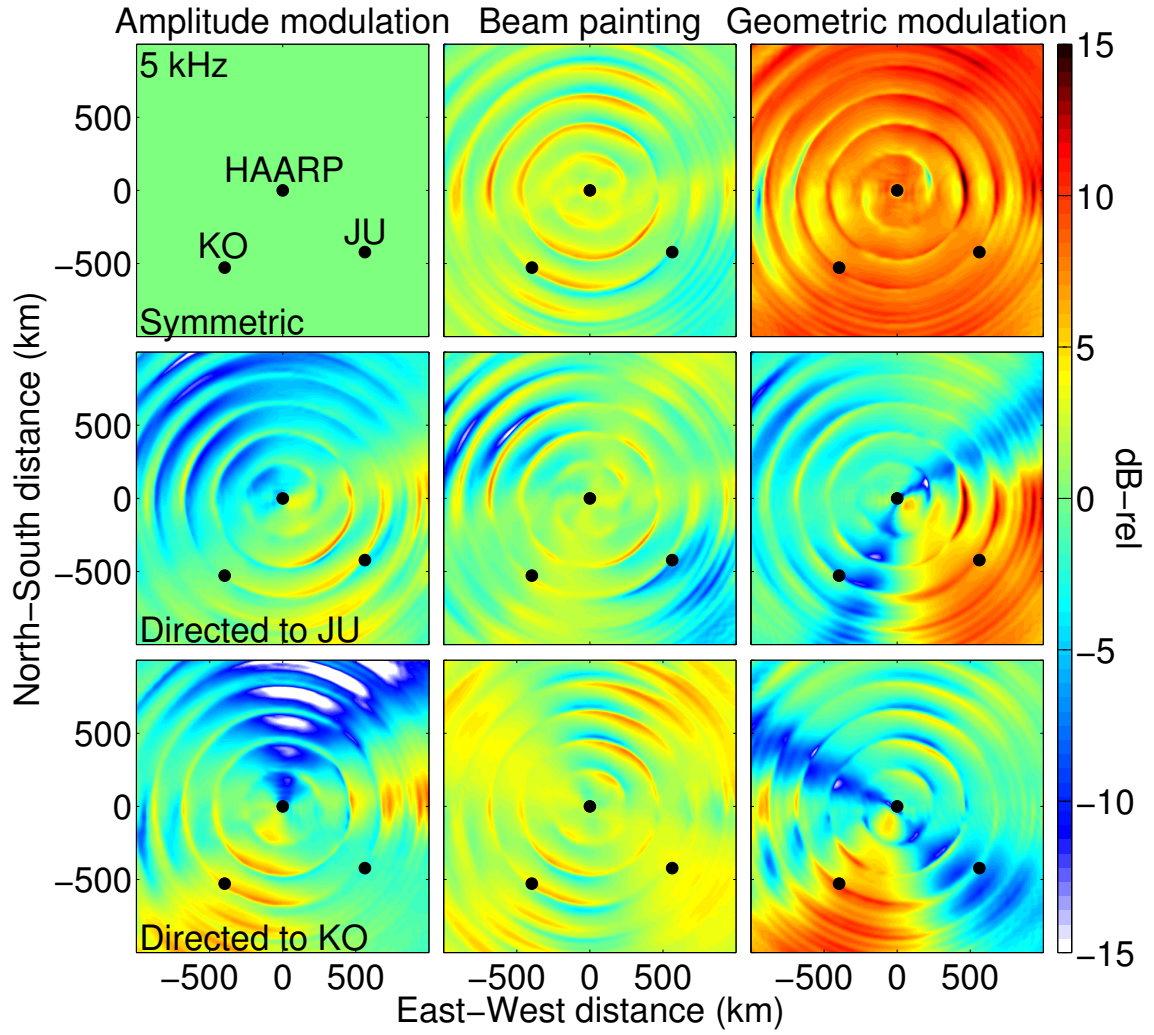


Figure 4.3: Modeled ground magnetic field compared, 5 kHz

the ground up to a distance of 1000 km away from HAARP. The rows and columns use the same model simulations as in Figure 4.3. The locations of HAARP, Kodiak (KO), and Juneau (JU) are indicated with black dots on each plot.

Each grid point in the horizontal plane is normalized to the magnetic field amplitude for vertical-AM, since this represents our baseline for comparison. The red and yellow areas indicate stronger signals compared to vertical-AM, and blue areas indicate weaker magnetic field signals compared to vertical-AM. Since the top left plot is therefore normalized to itself, its values are 0 dB throughout. All the other plots exhibit a series of concentric circles of peaks and nulls. These circles result from the interference pattern of the multi-mode ELF/VLF waves propagating away from the source, especially at a frequency of 5 kHz (which is significantly above the Earth-ionosphere first and second order mode cutoff frequencies of  $\sim 1.8$  kHz and  $\sim 3.6$  kHz, respectively). When the ionospheric source is translated horizontally, or enlarged in size, as they are for all but the vertical-AM simulation, the interference pattern on the ground is different. An exact experimental measurement of the comparative effectiveness between these modulation techniques may therefore be sensitive in part to the exact receiver location, with a few dB of variation. It is for this reason that the experiments in Chapter 3 were repeated multiple times, in order to ensure consistent results. The lack of precise consistency among the observations at Juneau and Kodiak may also be explained as a result of this interference pattern.

Despite the undulations from the interference pattern, it is nonetheless possible to deduce the general characteristics of each HF modulation scheme. First, we compare the symmetric implementations, which relate more closely to the total ELF/VLF wave power launched into the waveguide. The grid-paint magnetic field appears to be similar overall compared to vertical-AM, apart from the oscillations associated with the interference pattern. There are about equal amounts of light blue area as there are light red areas, so within a few dB, the wave amplitudes from the grid-paint and vertical-AM appear to be the same, regardless of the direction from HAARP. Our experimental measurements shown in Figure 3.5 establish a similar trend (the small patch of enhanced amplitude associated with the grid-paint that is visible in Figure 4.2 is underneath the black dot in the top center panel of Figure 4.3).

On the other hand, the circle-sweep panel shows stronger signals almost uniformly over the 1000 km region, by an amount very similar to the 7–11 dB observed and discussed in Chapter 3 (as in Figure 3.7). In other words, our theoretical calculations appear to be consistent with an observed 7–11 dB increase in amplitude in the Earth-ionosphere waveguide via usage of the circle-sweep as opposed to vertical-AM.

The comparative directionality of the three modulation types can be observed in the middle and lower rows. For amplitude modulation, directing the beam toward either Juneau or Kodiak appears effective in increasing the radiation in those directions, respectively. Additionally, a significant null is created in precisely the opposite direction, so a receiver located opposite to Kodiak with respect to HAARP would apparently observe equal and opposite magnetic field changes compared to the receiver at Kodiak, for amplitude modulation, and with the beam steering along the azimuth toward or away from Kodiak. The additional radiation directed to Kodiak is confined in a cone  $\sim 45^\circ$  wide, although the width of this cone, as we discuss later in this chapter, is a function of the ELF/VLF frequency. The enhanced radiation directed toward Juneau also appears to be slightly weaker than the enhanced cone of radiation toward Kodiak, and appears to be spread out over a wider angular range ( $\sim 90^\circ$ ).

The directionality of beam painting (center column) is different from that of amplitude modulation. When a line-paint is directed to Kodiak, a cone of enhanced radiation appears in the orthogonal direction, toward Juneau, and when the line-paint is directed to Juneau, a cone of enhanced radiation is directed to Kodiak, although the cone itself is not as intense as the cone associated with oblique-AM heating. This behavior appears to be consistent with observations in Figure 3.6, that ELF/VLF radiation is directed opposite to the line-paint azimuth, with  $\sim 5$  dB of directional control.

Once again, however, geometric modulation shows markedly different behavior than either amplitude modulation or beam painting. The radiation pattern includes a very intense cone, with magnetic fields  $>10$  dB stronger than the field which would be present from vertical-AM. The cone is similar in width to the cone from the oblique-AM heating ( $\sim 45^\circ$  wide directed toward Kodiak, and  $\sim 90^\circ$  wide directed

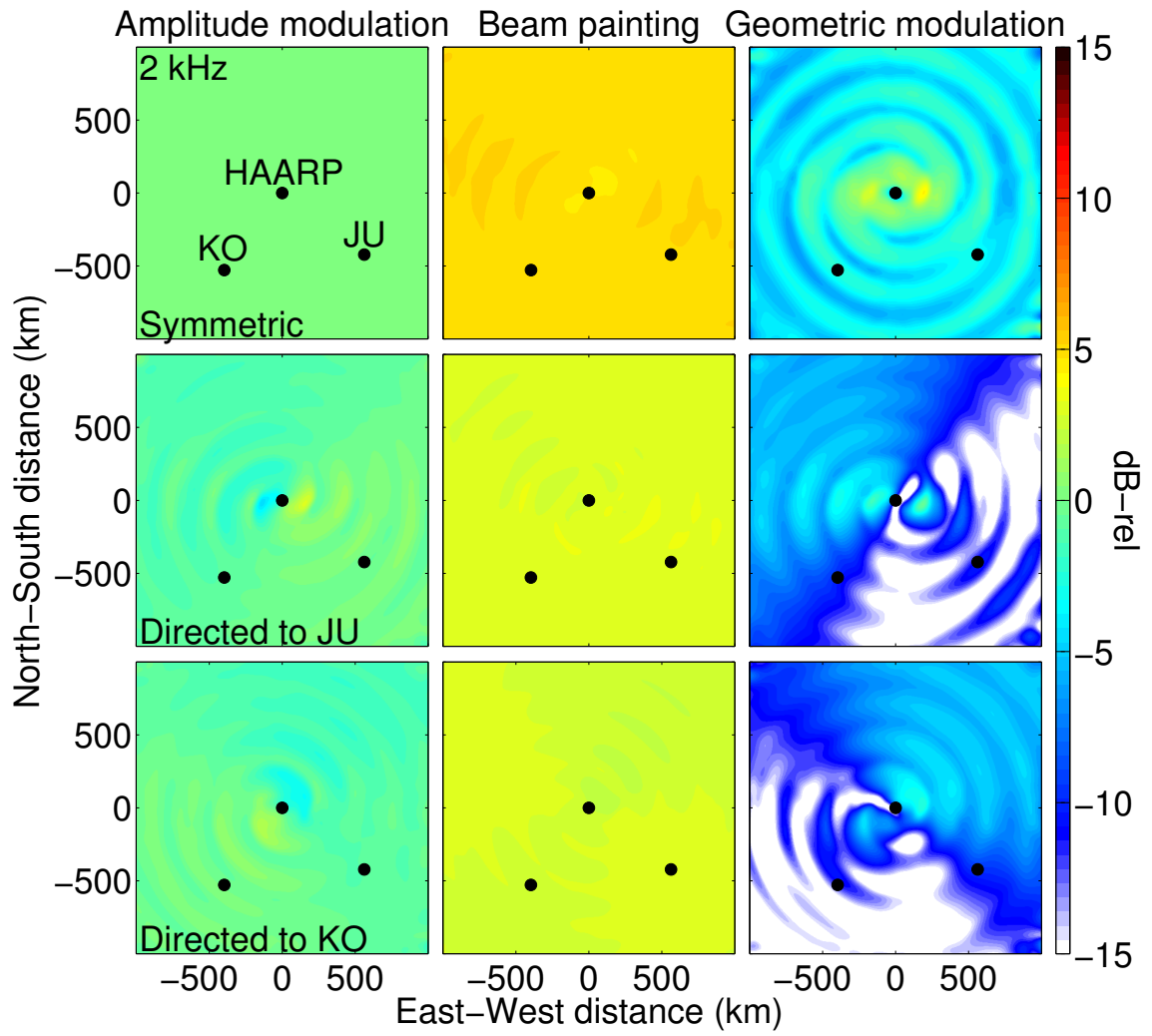


Figure 4.4: Modeled ground magnetic field compared at 2 kHz

toward Juneau). However, unlike the oblique-AM pattern on the ground, there is equal and opposite null pattern on the other side from the direction of the sawtooth-sweep. Rather, there are two thinner nulls roughly orthogonal to the cone directed to the azimuth of the sawtooth-sweep. It therefore seems that geometric modulation has a directionality which is different in nature from that of oblique-AM heating.

To further compare experimental data with theoretical results, we repeat in Figure 4.2 the same plots as Figure 4.3), but at a lower ELF/VLF frequency (2 kHz). The pattern on the ground is easier to interpret at this lower frequency, since the interference pattern on the ground is much weaker and sparser than it is for the 5 kHz example. It is therefore more directly visible that the grid-paint gives  $\sim 5$  dB stronger signals than vertical-AM, while the line-paints generate  $\sim 3$  dB stronger signals. On the other hand, the geometric signals are in fact very weak at longer distances, as much as 5 dB weaker compared to vertical-AM. There is very little directionality evident in the radiation pattern for any of the formats, although the weak sawtooth-sweeps may demonstrate  $\sim 5$  dB of directional dependence. These results are all consistent with our observations in Chapter 3, where beam painting proved more effective at the lowest frequencies, whereas geometric modulation demonstrated equal if not smaller signal amplitudes below 3 kHz.

The reason for such a strong variation in the characteristics with ELF/VLF frequency is a byproduct of the wavelength of ELF/VLF signals, and their relation to the size of the ionospheric heated region (tens of km across in the  $D$  region). The free-space wavelength at 2 kHz is 150 km, which is substantially larger, but on the other hand, a 5 kHz wave has a wavelength of 60 km, which is significant compared to the size of the HF heated region.

We have carefully described two frequencies and discussed the variations in the horizontal magnetic field calculated at the Earth's surface for a number of HF modulation techniques. For the sake of a complete comparison, the results of the theoretical modeling at all frequencies are presented in Figure 4.5, which can be directly compared with 3.10. The simulations are repeated for 1 kHz increments between 1 kHz and 9 kHz.

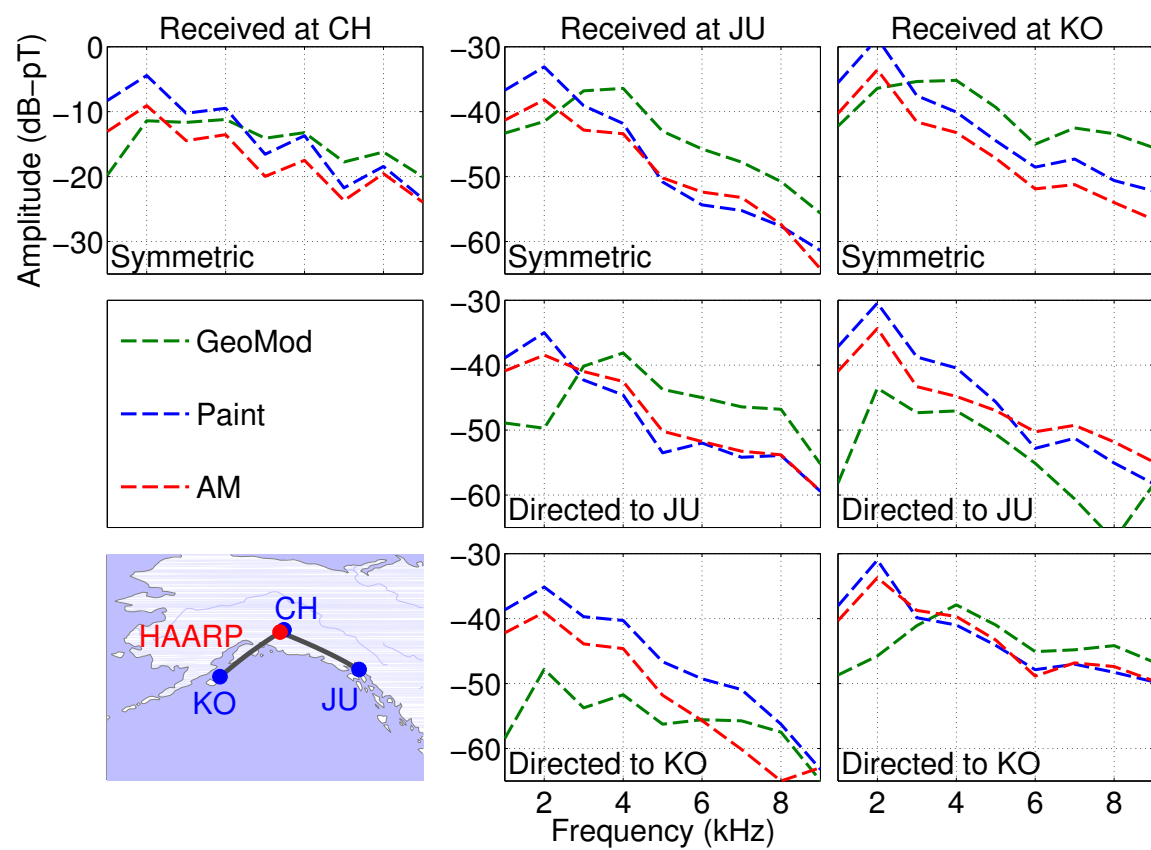


Figure 4.5: Theoretical response of modulated HF heating (on ground)

### 4.3 Magnetospheric injection

The good overall agreement between the theoretical calculations for the magnetic field on the ground, and the observed magnetic field on the ground, both near HAARP and further away, is suggestive that the modeling utilized here is capturing the most important physical principles. It is therefore useful to now extend this model to predict the electromagnetic fields injected into space. The connection between the Earth-ionosphere waveguide illumination and magnetospheric injection is poorly understood, so that our experimental observations on the ground may reveal very little about the properties of amplitude modulation, beam painting, and geometric modulation, for magnetospheric wave injection.

Injection of waves to the edge of the magnetosphere could couple the signals into field-aligned guides called ‘ducts’, which may lead to ELF/VLF wave interactions with radiation belt particles [Inan *et al.*, 2004; Gołkowski *et al.*, 2008], so it is useful to discuss this aspect. In this context, we therefore discuss injection up to an altitude of 700 km, which is located at the topside of the ionosphere, and is also an altitude where a number of low earth orbiting satellites (e.g., DEMETER) orbit. We note, however, that the propagation model does not take into account irregularities in the ionosphere, particularly those which may be present due to the HAARP HF heating effects in the *F* region of the ionosphere. Such irregularities may be responsible for a significant disparity between theoretical amplitudes of VLF signals in the magnetosphere, and those observed by satellites [Starks *et al.*, 2008; Lehtinen and Inan, 2009].

Figure 4.6 shows the horizontal magnetic field, in the same plot format as Figure 4.2, and at a modulation frequency of 2 kHz. The radiation pattern from all of the techniques remain tightly bound to the field line, so that the spatial structure of the electromagnetic fields is quite similar to the spatial structure of the currents in the *D* region, even after propagation to 700 km altitude. For instance, the null in the center of the circle-sweep is clearly present.

As shown in Figure 4.4, the fields on the ground from 1 kHz modulation are substantially weaker from geometric modulation compared to beam painting. However, at 700 km altitude, this is clearly not exhibited. The geometric modulation schemes,

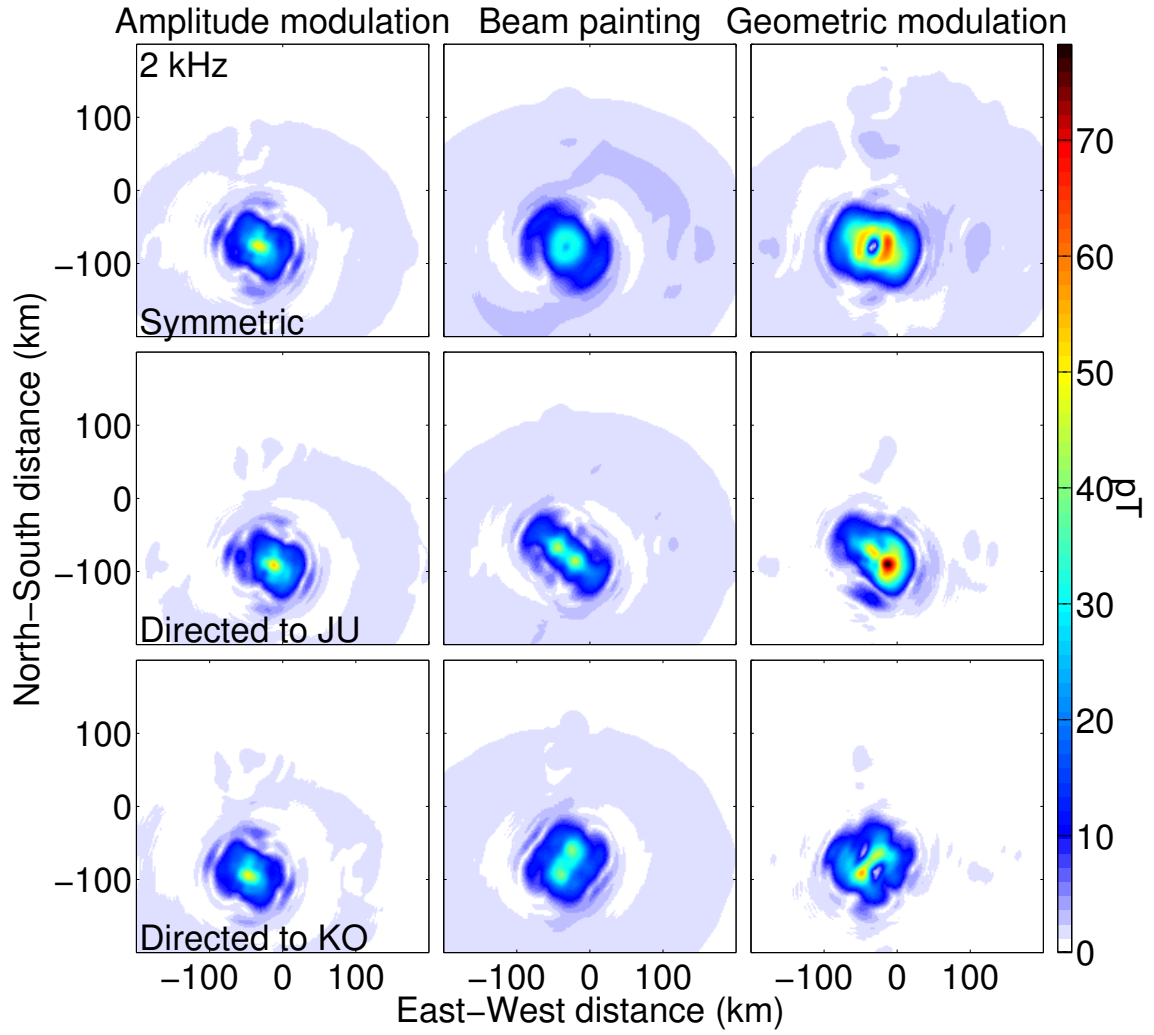


Figure 4.6: Modeled fields at 700 km altitude from modulated HF heating



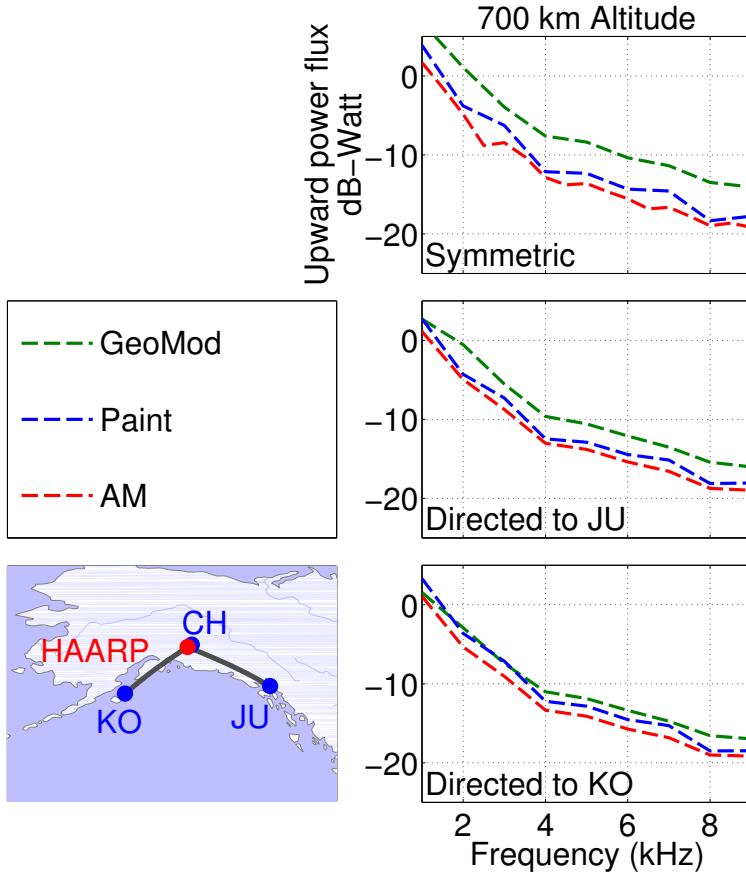


Figure 4.7: Modeled frequency variation of ELF/VLF power to 700km altitude

especially the circle-sweep, seem to produce the strongest magnetic fields, and covering the widest possible area. This result suggests that the behavior of geometric modulation may be even more advantageous for magnetospheric injection than it is for Earth-ionosphere waveguide illumination.

We can evaluate this possibility theoretically. The total power injected into the magnetosphere can be determined by calculating the Poynting vector ( $\vec{E} \times \vec{H}$ , where  $\mu\vec{H} = \vec{B}$ ) at each location. The upward component of the Poynting vector gives the power density in the vertical direction, which can be integrated over a planar area at 700 km altitude. These power flux results are summarized in Figure 4.7, after repeating the simulation in 1 kHz increments between 1 kHz and 9 kHz, with the vertical axes displaying power, in units of dB-Watts.

The  $\sim 20$  dB drop in power with increasing frequency between 1 and 9 kHz common to all panels is due to the decreasing efficiency of ELF/VLF wave generation for higher frequencies, as reflected in Figure 2.5. For the symmetric implementations, geometric modulation injects 3–6 dB more power into the magnetosphere, but this advantage does not appear to be a function of frequency, unlike the ground-based experimental and theoretical results. Beam painting also appears to yield a smaller ( $< 3$  dB) boost in the total power injected into the magnetosphere, compared to amplitude modulation. Finally, although the simulations are repeated for the directed formats, the results are not substantially different, unlike the ground-based results, where the direction of the formats mattered. We note that the relative effectiveness of amplitude modulation, beam painting, and geometric modulation for magnetospheric injection does not appear to be a strong function of frequency, unlike the observed behavior for Earth-ionosphere waveguide illumination.

## 4.4 Directional pattern

It is also useful to use our theoretical results to describe the complete radiation pattern of the different modulation techniques, i.e., the magnetic field received at certain distance away from HAARP, for receivers at various azimuths. Experimental measurement of this pattern requires a large number of receivers, spanning multiple concentric circles around the HF heating facility. Unfortunately, we are limited here to only two receivers, albeit ones well chosen to be in orthogonal directions and similar distances from HAARP.

Figure 4.8 shows the directional patterns derived from the model simulations. The squared magnetic field on the ground (proportional to the power flux) for a certain radius is calculated at each azimuth from the HF heater. The results are shown in polar plots, for a radius of 50 km (left column), 500 km (center column), and 1000 km (right column). The red traces correspond to amplitude modulation, blue traces for beam painting, and green traces for geometric modulation. The top row covers the symmetric implementations, and the bottom row shows the directed implementations. The directed implementations are made in the direction of Juneau, whose direction

from HAARP is indicated by the black line in each plot. The results here are for the modulation frequency of 5 kHz, i.e., the same simulations presented in Figure 4.3.

For each trace, the magnetic field power is normalized to the azimuth-integrated average magnetic field power around the circle, so that a radiating pattern with no directionality would be a constant value of 1 across all azimuths. The azimuth  $0^\circ$  corresponds to geographic North, and the azimuth  $90^\circ$  corresponds to geographic East.

At 50 km radius, very little directionality is evident in the symmetric implementations, which is not surprising since this location is quite close to the HF heater. At 500 km and 1000 km radii, some directionality becomes evident for the symmetric radiation, with some preference to direct the signals to the north, and less so to the East or West. This effect is reasonably consistent for amplitude modulation, beam painting, and geometric modulation, so this directionality like does not arise from the particular properties of the beam, but simply a result of ELF/VLF wave generation via HF heating in general (i.e., propagation effects, and auroral electrojet direction).

The directed implementations in the bottom row are more likely to show significant directivity, since the HF modulation itself favors a certain direction. The directivity of all three formats generally grows with increasing radius for the three points shown. This dependence occurs because the horizontal phasing of the current structure in the ionosphere has a strong impact on the interference pattern, and this effect is maximized for locations more to the side of the heated ionosphere, as opposed to immediately below it.

At 1000 km, geometric modulation generates a gain of  $\sim 6$  dB, whereas the amplitude modulation and beam painting yield gains of  $\sim 5$  dB and  $\sim 3$  dB, respectively. Also, the geometric modulation directivity is in a direction closer to the actual azimuth of the sawtooth-sweep, but still  $\sim 15^\circ$  to the South. This result arises because the directionality inherent to the modulation technique is superimposed on top of the modulation inherent to ELF/VLF generation in general (which is more favorable to the south and north).

Finally, the directionality of the sawtooth-sweep can be seen to be a function of frequency. Figure 4.9 shows the polar plot of the sawtooth-sweep (directed to Juneau,

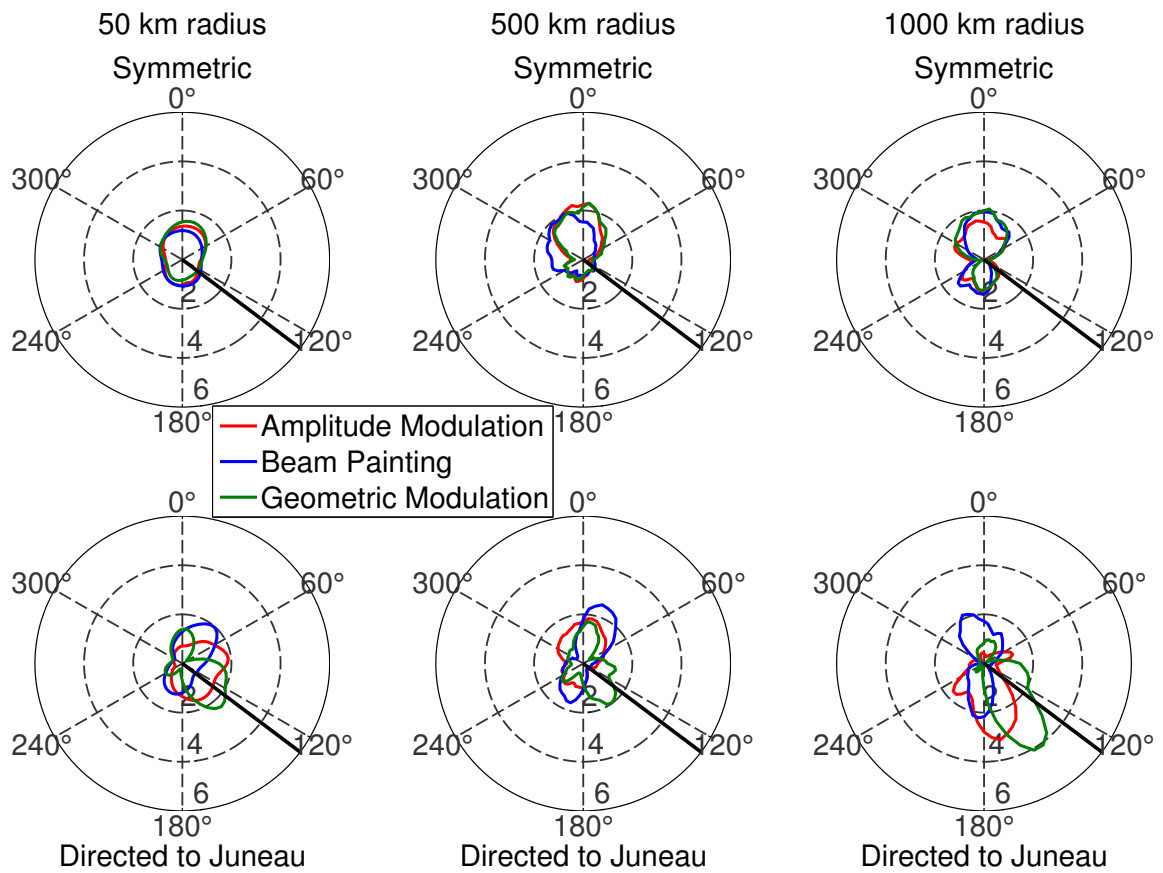


Figure 4.8: Directional patterns in the Earth-ionosphere waveguide

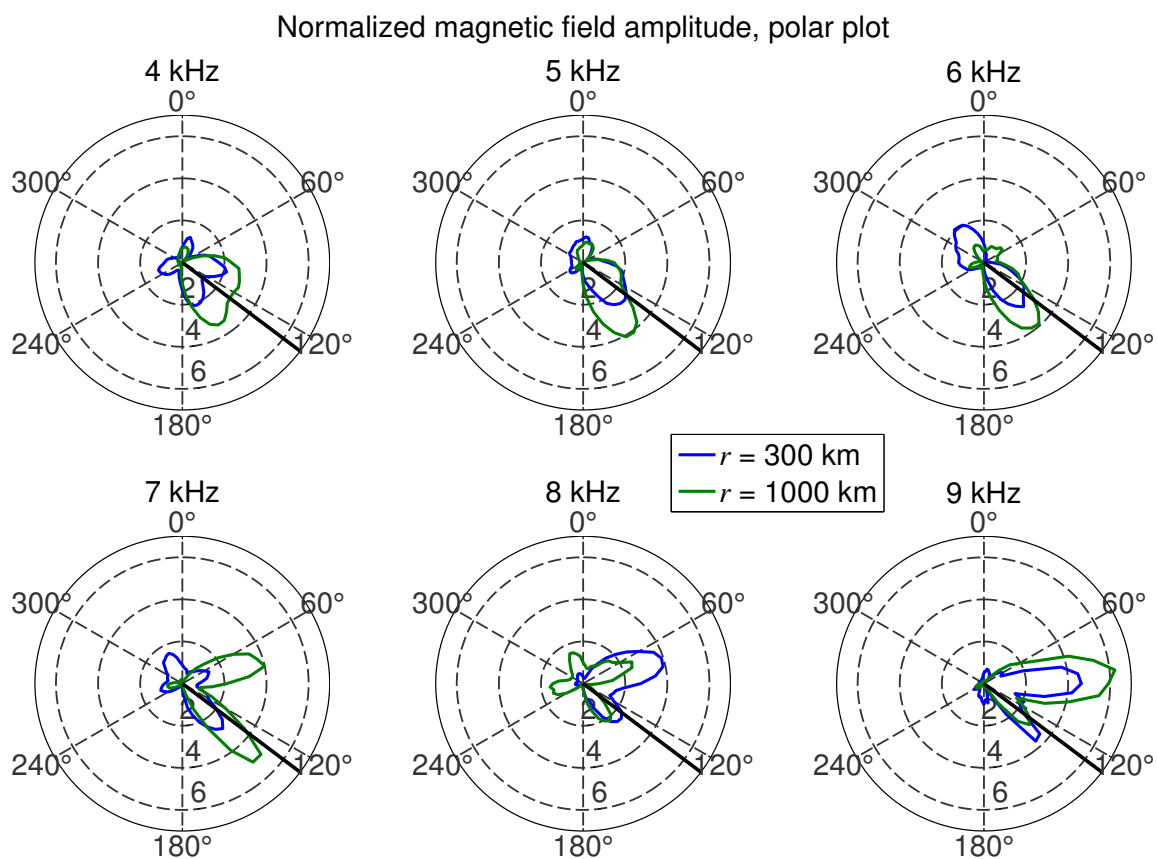


Figure 4.9: Directionality of the sawtooth-sweep as a function of frequency

toward the black line) for a radius of 300 km (blue curves) and 1000 km (green curve), and for six different modulation frequencies between 4 and 9 kHz. As the frequency increases between 4 and 6 kHz, the sawtooth-sweep becomes increasingly directional. However, beginning at 7 kHz, the main directional lobe splits into two, so that radiation is not optimally directed toward Juneau, but is indeed directed in two directions on opposite sides of Juneau.

# Chapter 5

## Physical Mechanisms

Having discussed the comparative behavior of amplitude modulation, beam painting, and geometric modulation, both for total power illumination of the Earth-ionosphere waveguide, directional illumination of the Earth-ionosphere, and magnetospheric injection, we now seek to discuss the underlying mechanisms which control the behavior of the modulation techniques.

We focus on four physical properties that distinguish amplitude modulation, beam painting, and geometric modulation. By exploring each one individually, we can quantify their contributions to the observed behavior. The four properties we discuss here are: Heat-cool duty cycle, heat-cool time constant disparity, phasing from oblique heating, and ELF/VLF phased array control.

### 5.1 Heat-cool duty cycle

Duty cycle refers to the fraction of the ELF/VLF period during which heating occurs, as opposed to allowing electrons to cool.

Figure 5.1 shows schematically how a varying duty cycle may impact the results. The black curves in the three panels show two possible modulations of the HF power, the top panel is with 50% duty cycle (i.e., equal duration ON and OFF), the middle panel shows 25% duty cycle, and the lower panel shows 10% duty cycle. The ionospheric response to that HF, however, is not instantaneous. The green curves show

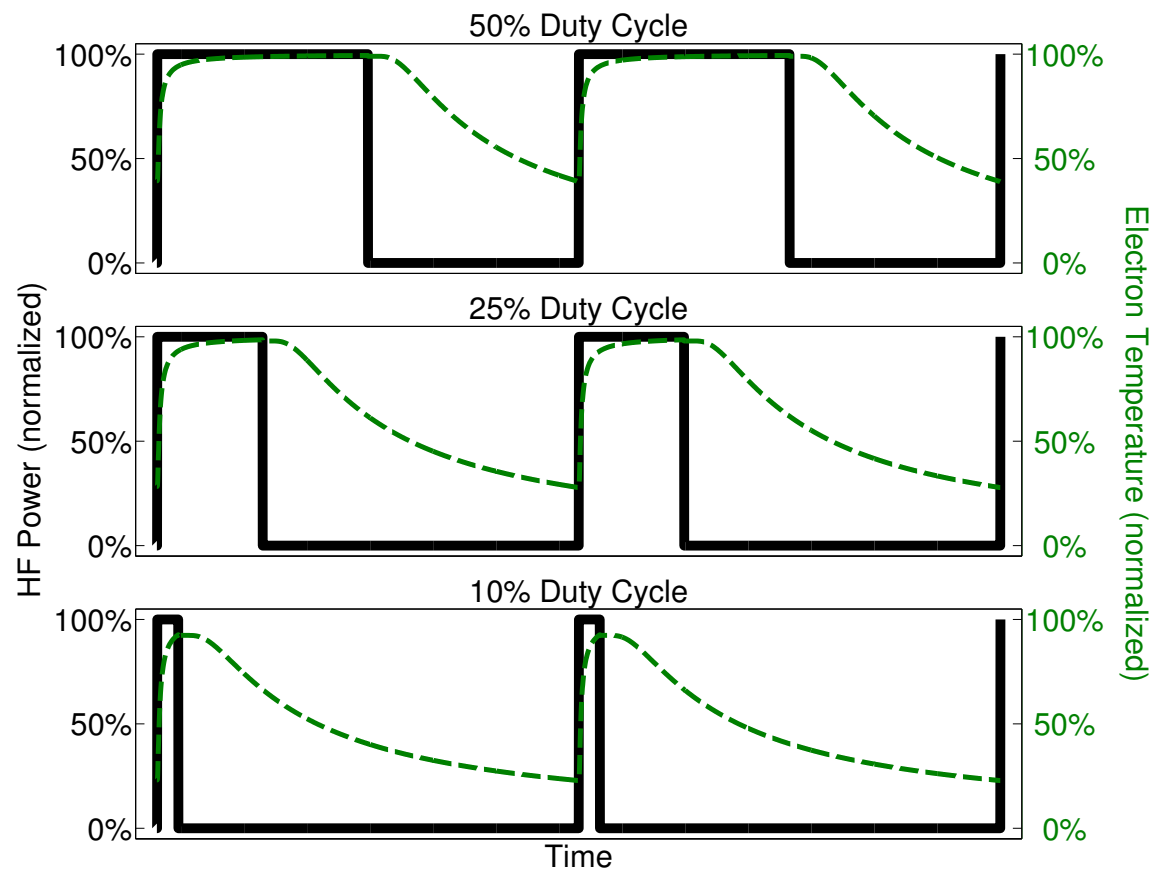


Figure 5.1: Schematic effect of duty cycle on ELF/VLF generation



how the electron temperature (normalized to the maximum) may respond to the HF heating and subsequent recovery duration, given an exponential rise and decay with different characteristic time scales (i.e., the electrons may heat very quickly, but recover more slowly, or vice versa). In the top plot, the electron recovery is sufficiently short so as to allow recovery to only  $\sim 40\%$  of the maximum level. On the other hand, shortening the HF heating to 25% duty cycle (as in the middle plot) allows more duration for the electrons to cool, so that the electrons recover further, to 25% of the maximum level. But if the HF heating is too short, the electrons are not heated as much as they could be (bottom plot). In this manner, there may be an optimum duty cycle that maximizes the depth of conductivity modulation, and this optimum duty cycle may be a function of altitude, HF frequency, modulation frequency, and HF power density.

The importance of this effect lies in the fact that the amplitude modulation, beam painting, and geometric modulation intrinsically utilize different duty cycles. In the amplitude modulation experiments and modeling results described here, the ON portion (heating) of the ELF/VLF period corresponds to 50% of the ELF/VLF period (though this can be controlled). However, due to the continuously ON nature of geometric modulation, the fraction of the ELF/VLF period during which heating occurs at a given location is not necessarily the same, nor is it fully controllable. Rather, the duty cycle is more generally set by the ratio of the area of the heated region to the total area illuminated during the geometric modulation format. Figure 5.2 shows a schematic of the size of the beam (red) where heating occurs, and the area covered by the rest of the beam motion (blue), where electron cooling occurs, for both the circle-sweep (left panel) and the sawtooth-sweep.

For instance, at 3.25 MHz, the 3-dB width of the HF heating beam is  $\sim 15.8^\circ$  and  $\sim 12.7^\circ$  in the north-south and east-west directions, respectively, or  $\sim 360 \text{ km}^2$ . The total area covered by the beam if circled at a  $15^\circ$  angle from vertical is  $\sim 3000 \text{ km}^2$ , so the average duty cycle is  $\sim 12\%$ . For the sawtooth-sweep, the total area covered by the beam is  $\sim 1360 \text{ km}^2$ , so the average duty cycle is  $\sim 26\%$ . For most amplitude modulation experiments run previously with square wave modulation (as opposed to sinusoidal modulation), however, the duty cycle has been 50%, to maximize the

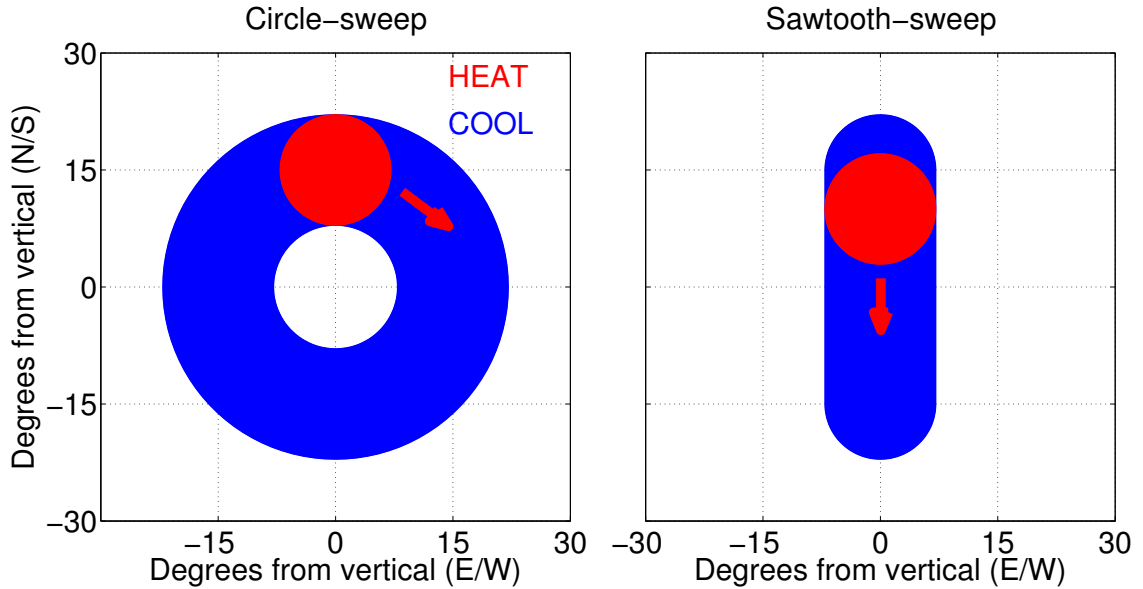


Figure 5.2: Heating and cooling areas in geometric modulation

harmonic content of the fundamental frequency.

To understand and quantify the importance of the substantially different duty cycle intrinsic to geometric modulation, we conduct an experiment in which the duty cycle of AM heating is varied between 15% and 60%, at several different ELF frequencies. The HF beam is square wave amplitude modulated and directed vertically. These data are presented in Figure 5.3, for five different ELF/VLF frequencies, observed at both the Chistochina and Juneau receivers. The analytical harmonic content of a square wave with varying duty cycle is also shown with a dashed line; this result would be expected if the ionosphere responded much faster than ELF/VLF time scales. The data from the two locations demonstrate similar results, although the Juneau receiver detects the signals with lower SNR as a result of the  $\sim 700$  km distance from HAARP to Juneau.

For all ELF/VLF frequencies shown in Figure 5.3, the peak amplitude occurs for duty cycles between 30% and 50%. These results can be explained in the context of the ionospheric response to heating, and recovery back to ambient conditions. Earlier workers *Rietveld et al.* [1986]; *Barr et al.* [1999] approximated the ionospheric changes

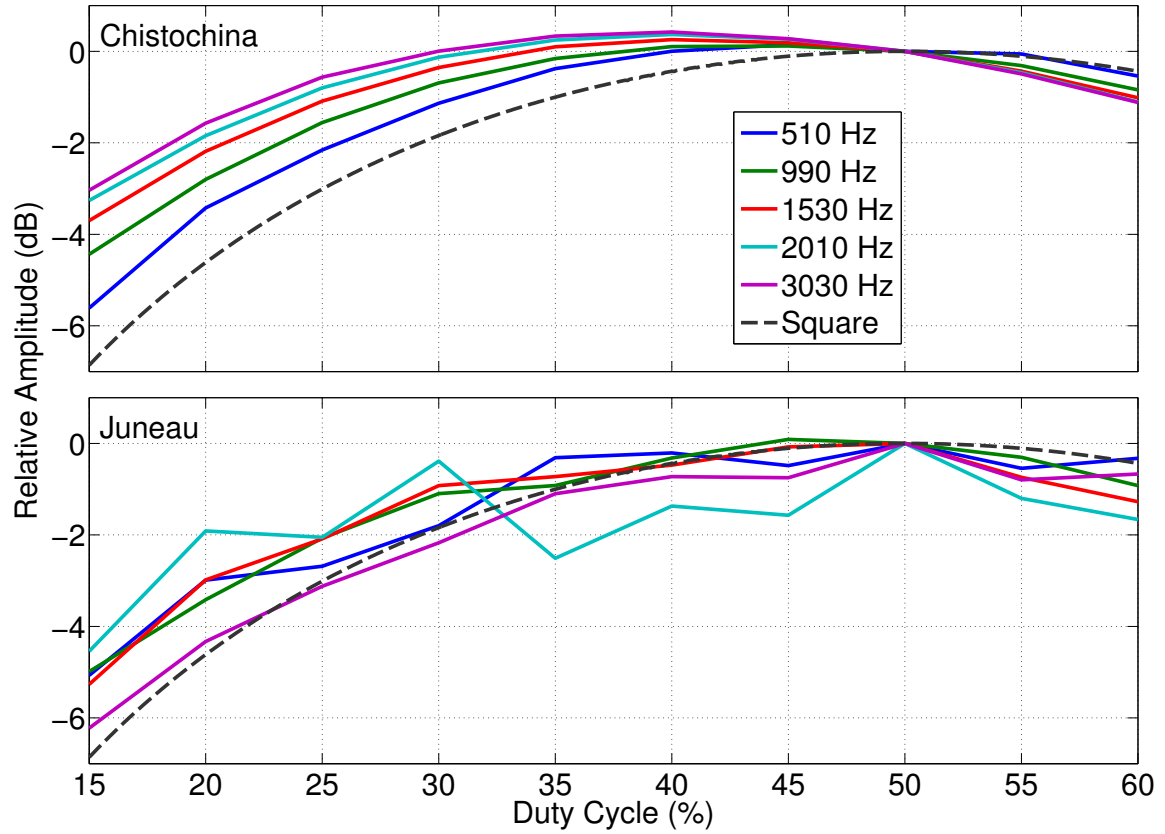


Figure 5.3: Observed effect of duty cycle on ELF/VLF generation

as resembling an exponential approach toward a steady state value (for heating) or ambient value (for cooling) with characteristic heating and cooling time constants, and in these past studies it has been possible to empirically determine these time constants with ELF/VLF data generated with HF heating of the ionosphere.

If the ionospheric temporal response is considered as such, then a duty cycle below 50% would be more effective at maximizing the amplitude if the cooling time constant were substantially longer than the heating time constant, since the HF beam need not waste time heating the electrons beyond steady state, but does need to allow time for the electron temperatures to return closer to the ambient values.

The optimal duty cycle also decreases with increasing ELF/VLF frequency (at least at Chistochina), where the OFF durations are too short to allow sufficient recovery of ionospheric electron temperatures. On the other hand, at the lowest frequency,

510 Hz, the temporal evolution of the electron temperatures most resembles a square wave (shown in gray dashed line), since the ON and OFF durations are the longest (compared to the characteristic heating and cooling time constants).

We are particularly interested in the role of the reduced duty cycle in the observations presented earlier. Although duty cycle variations between 30% and 55% are associated with only small (i.e.,  $<1.5$  dB) changes in the received ELF/VLF amplitude, duty cycles substantially lower (i.e.,  $<20\%$ ) result in a 2–6 dB loss in the received amplitude, with the loss being smaller at the highest ELF/VLF frequencies. Therefore, for the 3.25 MHz circle-sweep, where the duty cycle is only  $\sim 12\%$ , generation strength may be adversely affected by the lower duty cycles, particularly at the lowest ELF/VLF frequencies. This frequency-dependent loss due to lower duty cycle is similar to the frequency dependence observed in *Cohen et al.* [2008b] where geometric modulation becomes increasingly more effective (compared to vertical-AM) above 3 kHz.

The optimal duty cycle is likely a function of the electron recovery rates, which are functions of altitude. Experimental observations cannot (at least in a reliable manner) distinguish the optimal duty cycle at all altitudes, since the radiation components from all altitudes are combined into a single observation at the ground, with one altitude range likely dominating the observed signal at Chistochina. Hence, to describe the effect of heating and cooling durations, it is helpful to use theory. In particular, we use the single altitude simulation as used to produce the results of Figure 2.5, especially since it is independent of the ionospheric electron density profile. Utilizing an assumed maximum HF power density, we can simulate the heating and cooling dynamics for different combinations of ON and OFF duration. For each simulation, we extract the first harmonic of the Hall conductivity modulation, as is also done in Figure 2.5. As discussed in Chapter 2, the Hall conductivity modulation dominates the ELF/VLF radiation, so we specifically focus on that as opposed to the Pedersen conductivity.

Figure 5.4 shows the results of repeated HF heating simulations with an HF power density of  $20 \text{ mW/m}^2$  at 3.25 MHz, and square wave amplitude modulation with ON and OFF durations varying between  $50 \mu\text{s}$  and 4.5 ms. The three columns correspond

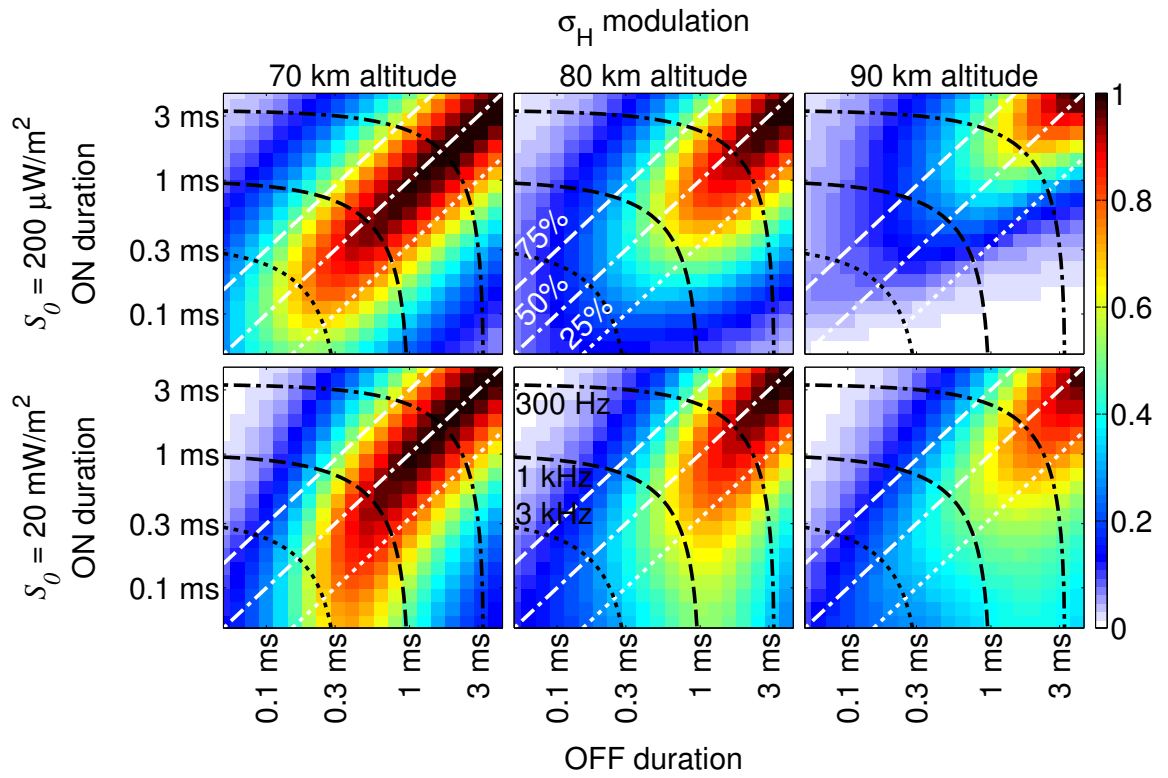


Figure 5.4: Generated amplitude as a function of HF ON and OFF durations

to simulations with the neutral densities at altitudes of 70 km (left), 80 km (center), and 90 km (right). The amplitude of the Fourier-extracted Hall conductivity is shown normalized to the maximum in each panel. In each plot, the three white reference lines indicate the locus of points with duty cycle 75% (upper), 50% (center), and 25% (lower), while the three black reference lines correspond to 300 Hz (upper), 1 kHz (center), and 3 kHz (lower). The top row is for an HF power density of  $20 \mu\text{W}/\text{m}^2$ , the bottom row is for  $20 \text{ mW}/\text{m}^2$ .

The conductivity modulation is substantially weaker at the lower left of each panel, since this region consists of very high ELF/VLF frequencies, where both the ON duration and OFF durations are too short. The upper right portion of each panel has the strongest conductivity modulation, since at these very low frequencies, the ionospheric recovery rates are much shorter than the HF ON and OFF durations. This frequency dependence (lower frequencies being more efficient) appears to be a function of the altitude, with the higher altitudes acting like a low-pass filter with a lower cutoff frequency, due to the higher recovery times of the electrons.

It can also be seen that optimal duty cycle varies with HF power density. In the top row, the maximum modulation amplitude occurs close to the line of 50% duty cycle, whereas for  $20 \text{ mW}/\text{m}^2$ , the optimal duty cycle is between 50% and 25%. The optimal duty cycle also drops for the highest frequencies, consistent with the experimental observations shown in Figure 5.3.

Additional information on the generated amplitudes as a function of duty cycle can also be seen by examining the higher harmonics of the received ELF/VLF signal, and comparing the observed amplitudes as a function of duty cycle to those of generic waveforms. More information on this is presented in Appendix E of this dissertation.

## 5.2 Phasing from oblique heating

Figure 5.5 shows schematically how the oblique nature of the HF beam may impact the phase distribution of the current elements in the heated region. The effect of phasing from oblique heating was first explored by *Barr et al.* [1988]. As shown in the two cartoons on the left of Figure 5.5, the three propagation paths of the HF

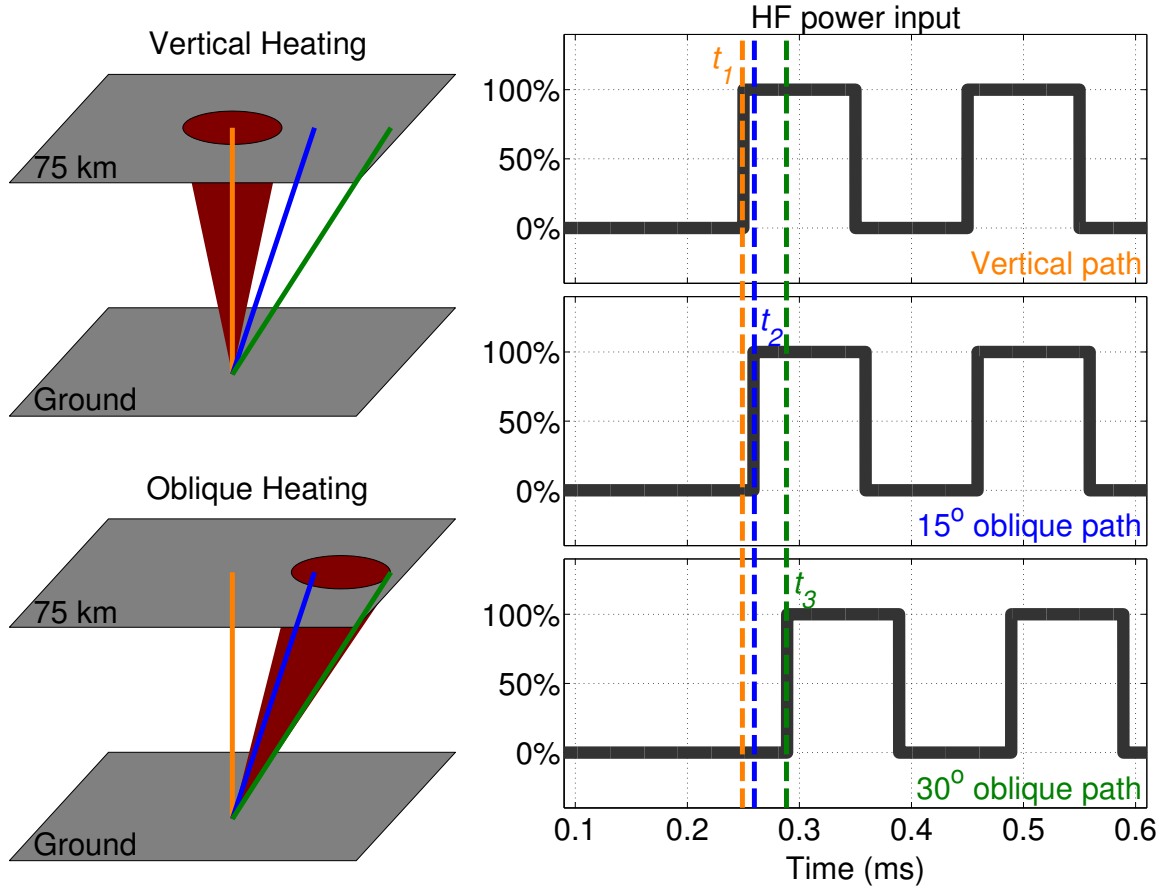


Figure 5.5: Schematic of oblique HF heating effect

energy corresponding to vertical (orange),  $15^\circ$  oblique angle (blue) and  $30^\circ$  oblique angle (green), are of differing lengths.

The three panels on the right of Figure 5.5 show the corresponding HF heating modulation function, assuming that at time  $t=0$ , amplitude modulation is applied at 10 kHz. The propagation delays to 75 km altitude are reflected by  $t_1$ ,  $t_2$ , and  $t_3$  for the three plots. The difference between  $t_3$  and  $t_1$  is about  $\sim 39 \mu\text{s}$ , or 39% of the ELF/VLF period at 10 kHz. This difference means that the ELF/VLF energy at the ionosphere at a  $30^\circ$  beam angle radiates with a phase lag of  $\sim 140^\circ$  compared to the part of the ionosphere close to directly overhead from the HF heater.

In particular, when the beam is tilted at an angle from vertical, the finite extent of the beam results in a substantially variable propagation delay from one side of the

beam to the other, resulting in a phase gradient, particularly at higher frequencies where the VLF period is shorter.

The resulting phase gradient appearing across the heated region causes the radiation to be directed toward the beam tilt, as noted by *Barr et al.* [1988]. Although the difference in detected signal strengths at a distant receiver is only 3–5 dB in *Barr et al.* [1988], *Moore and Rietveld* [2009] claim that this factor may account for most of the 7–11 dB enhanced amplitude, and 11–15 dB directionality of geometric modulation. On the other hand, *Cohen et al.* [2009a] demonstrate that this effect can at best be responsible for only a small portion of the amplitude enhancement and directionality associated with geometric modulation.

To experimentally determine the effect of phasing from oblique heating with HAARP, we employ 50% amplitude modulation, while tilting the beam at an angle of  $15^\circ$ , and separately measure the received signal with this tilt at different azimuths around the circle (in  $18^\circ$  increments). We note that  $\pm 15^\circ$  is currently the largest angle over which HAARP can perform geometric modulation (or other rapid beam motion experiments), although the HF beam can be more generally steered over a  $30^\circ$  angle from vertical. For this reason, AM modulation with a  $\pm 15^\circ$  oblique tilting is helpful in addressing the role that this phase gradient plays in the 7–11 dB amplitude gain, and 11–15 dB directionality, observed in *Cohen et al.* [2008b] and confirmed here.

In the absence of receivers at all azimuths in a circle surrounding HAARP, we effectively rotate the source region in order to derive the directional radiation pattern of oblique heating based on observations at a single receiver site. We once again measure the signals both at the nearby Chistochina receiver, and the more distant Juneau receiver. Figure 5.6 shows a polar plot of the amplitudes received, as a function of the azimuth of the off-vertical tilt. The red line indicates the direction toward the receiver. An approximately  $\sim 3$ –4 dB enhancement in the amplitude is observed when the AM beam is directed toward the receiver. It should be noted, however, that the amplitude enhancement observed at Chistochina (unlike that at Juneau) is largely a function of proximity to the heated region, which changes noticeably with azimuth of the oblique heating angle. The observations at Juneau are consistent with the amplitude observations of *Barr et al.* [1988], despite the somewhat different HF



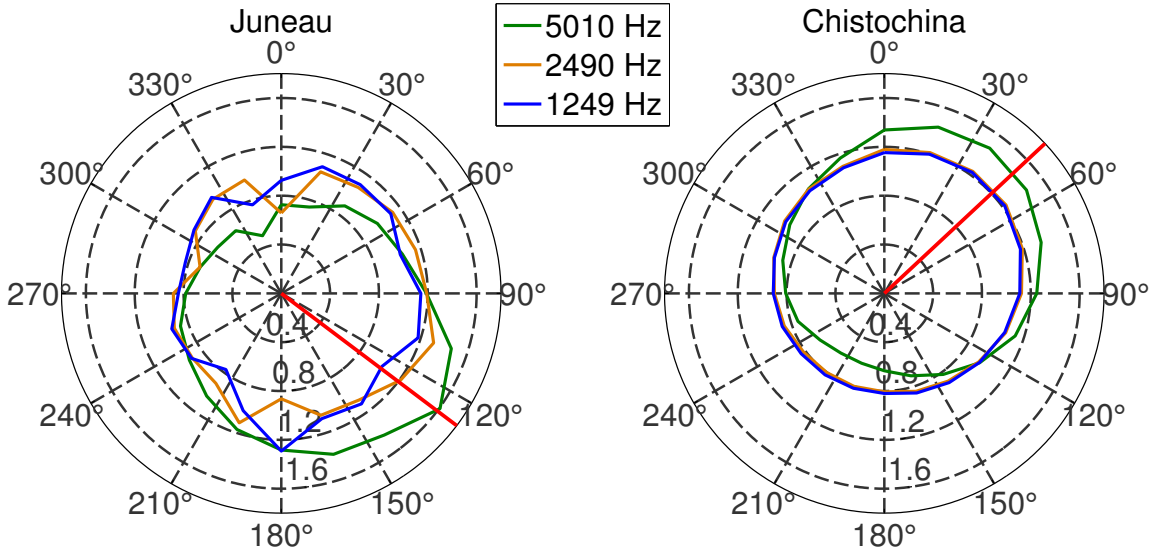


Figure 5.6: Received signals for oblique-AM HF heating at different azimuths

array properties between HAARP and the Tromsø heater. This difference is small compared to the 7–11 dB enhancement, and 11–15 dB azimuth dependence, observed in association with the circle-sweep and sawtooth-sweep, respectively.

In addition, the enhancement at Juneau from phasing due to oblique heating is strongest at the highest ELF/VLF frequencies, consistent with the explanation of *Barr et al.* [1988] that a phase gradient across the heated region results from the propagation delays of the HF signal to the ionosphere. At the highest frequencies, the difference in speed-of-light propagation time between vertical propagation to 80 km altitude, and propagation at 30° oblique angle, is  $\sim 0.04$  ms. At 5 kHz, this difference begins to approach a significant fraction of the 0.2 ms period. An alternative explanation is that the horizontal extent of the heated region begins to approach the ELF wavelength (60 km at 5 kHz).

A more direct comparison between geometric modulation and oblique-AM HF heating is shown in Figure 5.7, utilizing the same data shown in Figure 3.10. At both Kodiak and Juneau, both the circle-sweep and the sawtooth-sweep directed to the receiver generates higher amplitudes for at least a large position of the frequency measurements, despite the fact that the geometric modulation formats (particularly

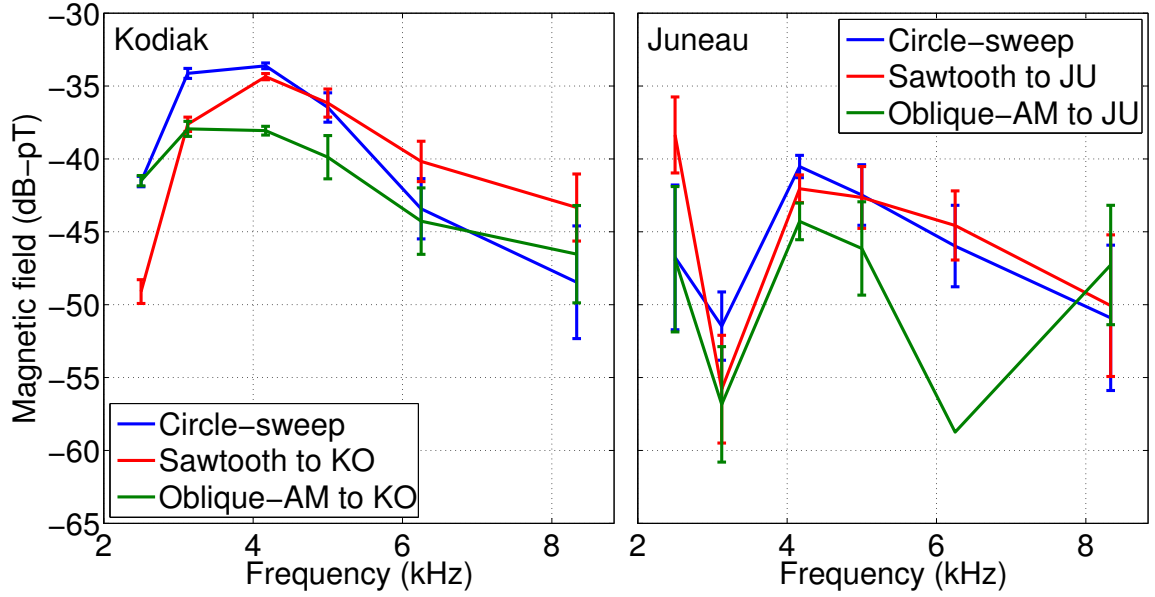


Figure 5.7: Comparison of oblique-AM with geometric modulation

the circle-sweep) suffers from the detrimental impacts of duty cycle, as discussed earlier. Hence, the oblique tilting angle inherent in geometric modulation appears to be insufficient to explain the increased amplitudes and directionality experimentally observed from geometric modulation.

It is also worth noting that beam painting inherently includes the effect of this phase gradient, yet does not behave in a manner similar to geometric modulation, as discussed in Chapter 3. Furthermore, the magnitude and frequency dependence of the amplitude changes associated with the phasing from oblique heating is roughly equal and opposite to the size and frequency dependence of the amplitude changes associated with a low ( $<20\%$ ) duty cycle. For this reason, the adverse impact of the low duty cycle present in the circle-sweep appears to be roughly compensated by the enhancement resulting from the phasing due to oblique heating. Furthermore, changing the angle of tilt (i.e., the radius of the circle-sweep) reduces the effect of both. While the duty cycle increases with a smaller tilt angle, closer to  $50\%$ , the effect of the oblique tilting is also reduced.

Consequently, in terms of comparing amplitude modulation to geometric modulation, two of the key physical differences that distinguish them, that of heat-cool duty cycle, and oblique heating, appear to both have small and counteracting effects on the generated signal strengths, so that the enhanced amplitudes and directionality observed from geometric modulation must be attributed at least in significant part to another mechanism.

### 5.3 HF pulsing

We now explore an important physical aspect that relates exclusively to beam painting. As can be seen in Figure 3.1, the technique of beam painting requires rapid motion of the HF beam in order to maintain a larger heated region of the ionosphere. A larger antenna gives the potential for more radiation. There is a tradeoff however, because if the HF beam must scan between  $N$  locations, then during the ON portion of the ELF/VLF cycle, each point in the ionosphere is not heated continuously, but is heated in short pulses (with HAARP capable of pulses as short as  $10\ \mu\text{s}$ ). Effective beam painting as originally proposed by *Papadopoulos et al.* [1989, 1990] therefore requires a very high power density in the HF beam (a level discussed later), which implies a heating time constant much shorter than the cooling time constant, so that in the time between the pulses (when the beam is directed elsewhere) the electrons have not cooled much.

Figure 5.8 shows schematically how an increasingly rapid heating rate enables the short pulses to sustain ionospheric conductivity. The black traces show the ON-OFF power density at a given ionospheric location. In this case, we show three  $10\ \mu\text{s}$  long pulses, separated by  $20\ \mu\text{s}$ , corresponding quite closely to the line-paint, since the HF beam scans between 3 ionospheric locations. The green curve shows an exponential curve which exponentially approaches either 0, or 1, depending on the HF power. The heating and cooling occur exponentially, with characteristic times  $\tau_{\text{Heat}}$  and  $\tau_{\text{Cool}}$ , respectively. This is a first order approximation of the heating and cooling dynamics, but one that has been employed previously [*Barr et al.*, 1999]. Let us assume that  $\tau_{\text{Cool}}=165\mu\text{s}$ , consistent with the estimate given in *Barr et al.* [1999]

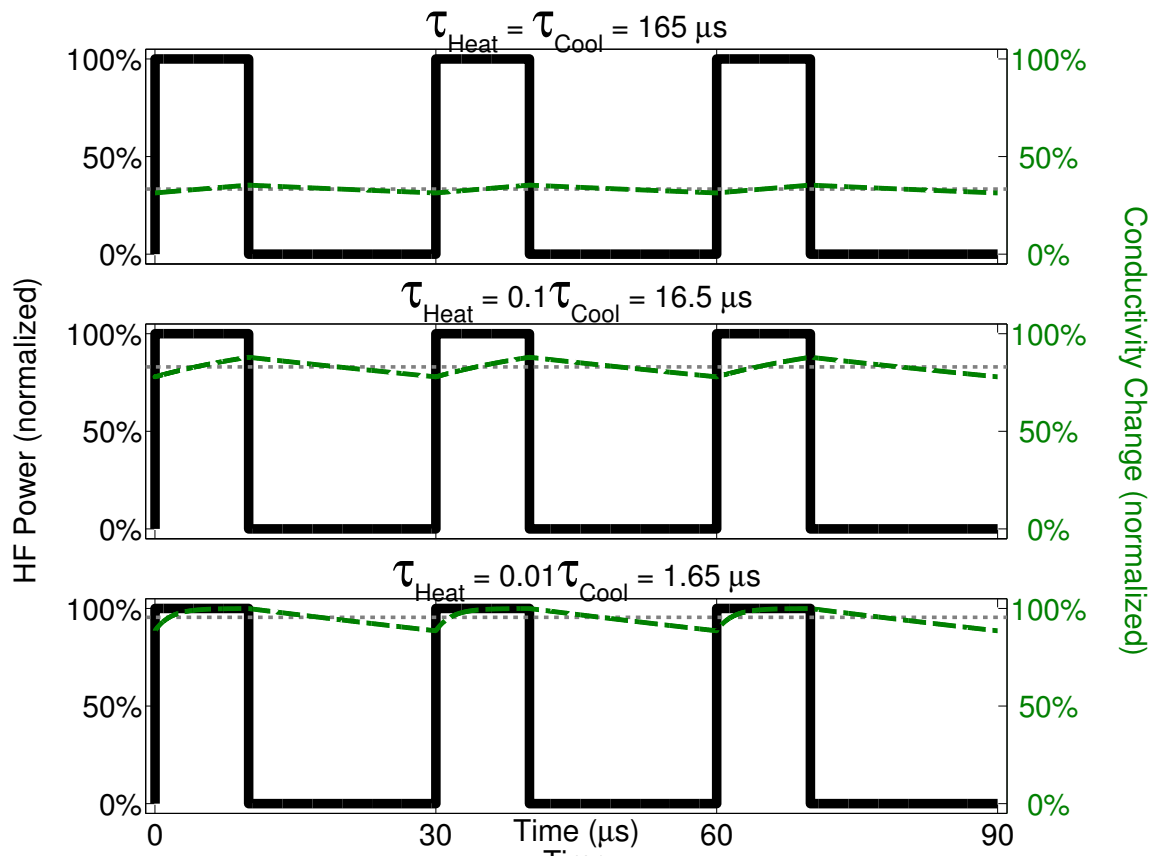


Figure 5.8: Temporal conductivity changes for rapid power modulation

for the fundamental frequency, and a daytime ionosphere.

The top panel shows the case where the heating and cooling time constants are equal, the middle panel shows the case for  $\tau_{\text{Heat}}$  ten times shorter than  $\tau_{\text{Cool}}$ , and the lower panel shows the case  $\tau_{\text{Heat}}$  is 100 times shorter than  $\tau_{\text{Cool}}$ . As the heating time constant decreases, the average value of the conductivity (shown with the dashed gray line) rises closer to 100%, despite the fact that the pulse are on for only one-third of the time. For each panel, the fractional loss (i.e., the amount the gray line drops below 100%) corresponds to an amount of conductivity modulation lost as a result of the pulsing nature, as compared to a single long-duration pulse. This loss is the basic tradeoff of allowing the HF beam to heat multiple locations simultaneously, but for a very fast heating rate, this tradeoff becomes negligible.

Previous studies at the Tromsø facility [Barr and Stubbe, 1991b; Barr *et al.*, 1999], using a similar exponential model, have concluded that the ERP levels there are not sufficiently high to allow beam painting to work as proposed. Although the HAARP facility has a higher ERP at 3.25 MHz (575 MW) compared to Tromsø (300 MW), it is not certain that this ERP level is high enough, as well. To evaluate this (at least theoretically) for the HAARP facility, we once again utilize the single-altitude HF heating simulation, extracting the first harmonic of the Hall conductivity as in Figure 5.4. We repeat the simulation for a series of HF power densities between 1  $\mu\text{W}/\text{m}$  and 100  $\text{mW}/\text{m}$ , and a series of rapid (50 kHz cycle) ON-OFF fluctuations with duty cycles varying between 2% and 98%. In following this procedure we account for the complete dynamics of the electron heating and recovery rate, and nonlinear conversion to conductivity changes, rather than assuming an exponential behavior to the conductivity. We once again focus on the Hall conductivity, due to its dominance in generating the long-distance radiation from HAARP. As discussed in Chapter 2, utilization of the single-altitude model also allows us to remove ionospheric variability and provide a more generalized solution, and consider only the variation across altitudes, and HF power densities.

Figure 5.9 shows the average conductivity change induced by pulsed HF heating. The left panel shows schematically some samples of the HF power modulation function applied, with varying duty cycle. The middle and right panels show the average Hall

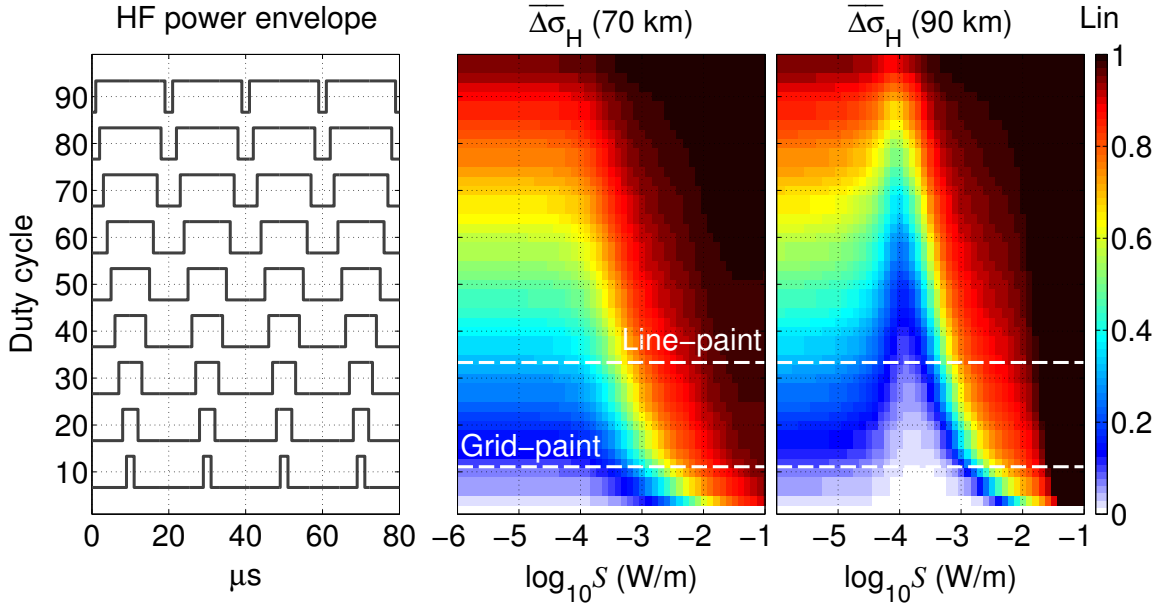


Figure 5.9: Effectiveness of beam painting by ERP and duty cycle

conductivity change in steady state, at altitudes of 70 km and 90 km, respectively. The conductivity modulation is normalized to the maximum possible Hall modulation depth, as in the third panel of Figure 2.4. At the 100% duty cycle level, the average conductivity change is 100% of the maximum, whereas at 0%, no heating occurs so the conductivity change is also 0. Everywhere else, the value of the colorbar measures a loss of conductivity modulation as a result of the finite ERP. The higher the value of the power density, the lower the duty cycle that can be sustained before this loss of conductivity is significant, since higher power densities will heat the electrons to the maximum temperature increasingly fast. Since the line-paint involves cycling the HF beam between 3 locations, the rapid duty cycle is 33%, as indicated with the upper dashed line in the two left panels. The grid-paint involves alternating the HF beam between 9 locations, corresponding to an 11% rapid duty cycle.

For the 575 MW ERP of HAARP at 3.25 MHz, the power density at 70 km altitude is  $\sim 9.3 \text{ mW/m}^2$  for free-space conditions, as calculated from Equation 1.3. In addition, since the ionospheric absorption below 70 km is small, even for a daytime ionosphere (as can be seen in Figure 2.7), the actual power density at 70 km is likely

close to this value. For the line-paint, the loss at the 9.3 mW power level is  $\sim 14\%$ , and for the grid-paint,  $\sim 5\%$ . At 90 km altitude, a significant portion of the HF power density has been absorbed, as can be seen in Figure 2.7). Assuming a remaining power density of  $1 \text{ mW/m}^2$ , the conductivity loss is  $\sim 24\%$  for the line-paint (33% duty cycle), and 73% for the grid-paint. This conductivity loss may account for part of the fact that beam painting is apparently no more effective than amplitude modulation at longer distances from HAARP in the observations of Chapter 3.

Although the beam painting technique relies on a high ERP, it seems that even the newly upgraded HAARP facility does not always have a sufficiently high ERP (at 3.25 MHz) to completely sustain high conductivity during the beam painting technique, but this limitation does seem to relate to only a small fractional loss at the lower altitudes, and at the highest HF power levels. Furthermore, at higher HF frequencies, the ERP of the HAARP facility is substantially higher (as much as 3.8 GW at 9.5 MHz), and so the losses associated with the pulsing of beam painting may in fact be entirely negligible for higher HF frequencies.

## 5.4 ELF/VLF phased array control

We now discuss the notion of ELF/VLF phased array control. *Barr et al.* [1987] describe the creation of a two-element phased array, as a result of having alternated the beam location between two locations in the ionosphere. Although only two independent spots ( $180^\circ$  out of phase) were possible with the Tromsø facility, the distance between the two spots could be controlled.

A significant extension of this concept is achieved via geometric modulation. Since there can be dozens of beam locations within the ELF/VLF cycle, individual beam locations create separate and independently radiating regions, whose phases can be controlled by the order in which those regions are heated [*Cohen et al.*, 2008b, 2009a]. This particular aspect is unique to geometric modulation, at least in a more generally controllable manner. For instance, if the beam locations in the circle-sweep can be thought of as forming a set of point sources, then those point sources would be radiating with phases varying around the circle and distributed equally. On the other

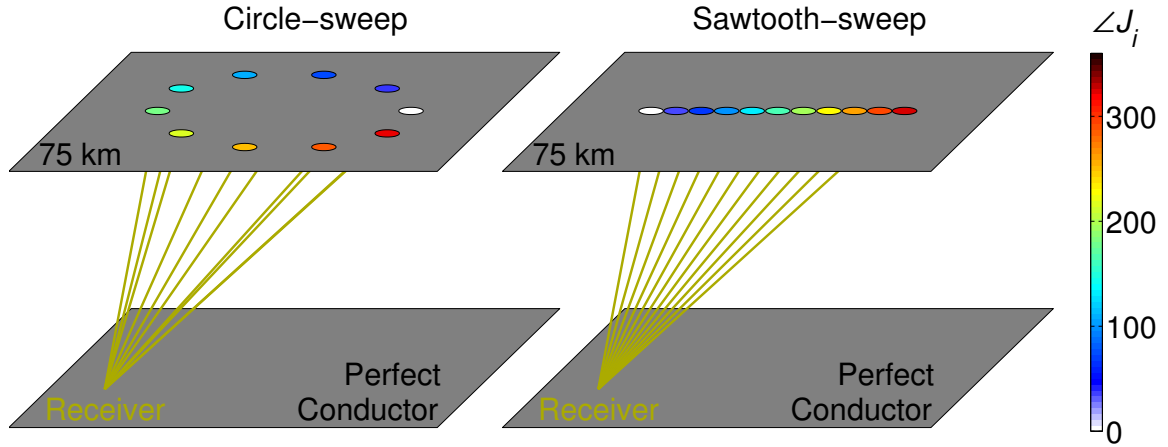


Figure 5.10: ELF/VLF phased array concept

hand, one could just as easily form a nonprogressive circle-sweep, where the angular steps between the beam locations are smaller for part of the circle-sweep, and larger for other parts. The phases of the beam locations would then not be uniformly distributed around the outside of the circle.

We seek to address the importance of this ELF/VLF phased array in controlling the radiation from geometric modulation. However, isolating the effect of the phased array via experiment is difficult. The effect of the oblique heating, for instance, cannot be independently removed, i.e., the HAARP HF beam cannot be made into an infinitely thin beam. So to evaluate the effect of the ELF/VLF phased array, we utilize a simplistic model in which all the more complicated physics of the problem is neglected, including the complex ionospheric plasma response, the Earth-ionosphere waveguide propagation effects, and the effect of phasing from oblique heating. The model is similar to that used in *Payne* [2007, pg.130].

Figure 5.10 shows the structure of this simplified model. The plane 75 km above a perfectly conducting ground is assumed to contain a series of ideal horizontal point current sources (10 are shown in the figure), radiating with unit current magnitude, but with phases varying progressively between 0 and  $360^\circ$  (as reflected by the color of the dot in the diagram). Apart from the perfectly conducting ground (upon which the receiver is located), the medium is assumed to be free-space.



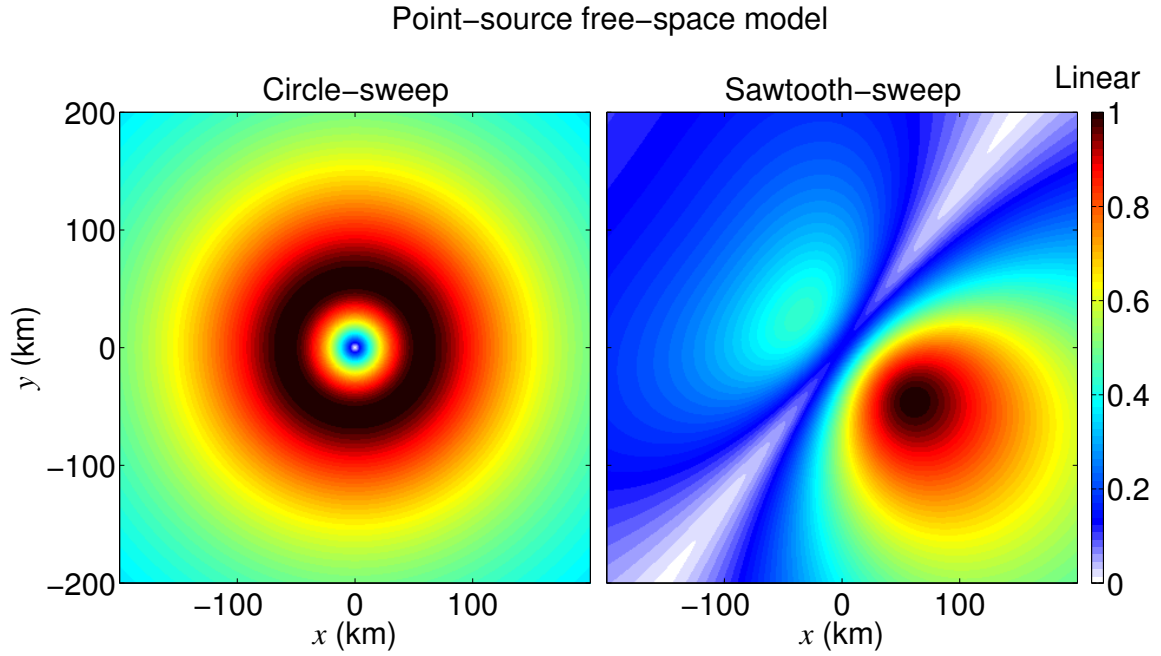


Figure 5.11: Point-source, free space model of received fields

The fields at a given location on the ground can be calculated using the magnetic retarded vector potential,  $\vec{A}$ , given as

$$\vec{A}(\vec{r}) = \frac{\mu_o}{4\pi} \sum_i \vec{J}_i \frac{e^{-k|\vec{r}-\vec{r}_i|}}{|\vec{r}-\vec{r}_i|} \quad (5.1)$$

where  $\vec{J}_i$  and  $\vec{r}_i$  are the currents (as a phasor) and locations of the point sources, respectively, with respect to the origin,  $k$  is the free space wavenumber, and  $\vec{r}$  is the location of the receiver. In addition, the method of images [Griffiths, 1999, pg.121] is used to account for the ground plane, allowing the entire problem to be treated as homogeneous free space. Every current element is accompanied by an image current, at the opposite location on the other side of the ground plane, with horizontal current magnitude in the opposite direction.

The magnetic field at the location  $\vec{r}$  is then calculated from

$$\vec{B}(\vec{r}) = \nabla \times \vec{A}(\vec{r}) \quad (5.2)$$

*Payne* [2007] also utilized a full theoretical model consisting of the HF heating model similar to the one here, as well as a Finite Difference Time Domain (FDTD) solution to ELF/VLF wave radiation. The radiation pattern on the ground from a planar ‘disk of current’ is found to be similar to the results of the complete model (See Figure 4.13), indicating that at least for distances within 50 km of HAARP, a simple free-space model fairly accurately reproduces the radiation on the ground.

Our purpose here is to utilize this simplified model to isolate only the physical effects of the ELF/VLF phased array aspect (which comes about via the distributed phases of the point sources). Figure 5.11 shows the horizontal magnetic field pattern on the ground (normalized) from the simplified free-space model, within 200 km of HAARP, for both the circle-sweep (left panel) and sawtooth-sweep (right panel). There are 20 ideal sources placed in the ionosphere, at an altitude of 75 km. The sawtooth-sweep is oriented toward Juneau, roughly to the Southeast from HAARP. Figure 5.12 shows the same results from the complete theoretical model presented in Figure 4.2.

A number of important aspects are common to both Figures 5.11 and 5.12. For the circle-sweep, there is a clear null in the center, a few 10s of km wide, directly underneath the center of the circle-sweep. The sawtooth-sweep features two regions/lobes of radiation on the ground, one larger lobe directed toward Juneau, and another smaller lobe immediately in the opposite direction. In between the two lobes is a null line, extending from Northeast to Southwest, orthogonal to the direction of the sawtooth-sweep. The similarities of these characteristics are an indication that the ELF/VLF phased array plays a dominant role in determining the magnetic field structure on the ground.

There are nonetheless some differences between the results from the point-source model (Figure 5.11) and the results from the full theoretical model (Figure 5.12). For instance, in the full theoretical model, the null in the center is not surrounded by a symmetric ‘donut’ of radiation, as it is in the free-space model result. Since the sources in real life are embedded in a plasma rather than free space, this asymmetry may result from anisotropy of the ionosphere, or from the fact that the Earth’s magnetic field is inclined by  $16^\circ$  from vertical. It is worth noting that the peak of the magnetic

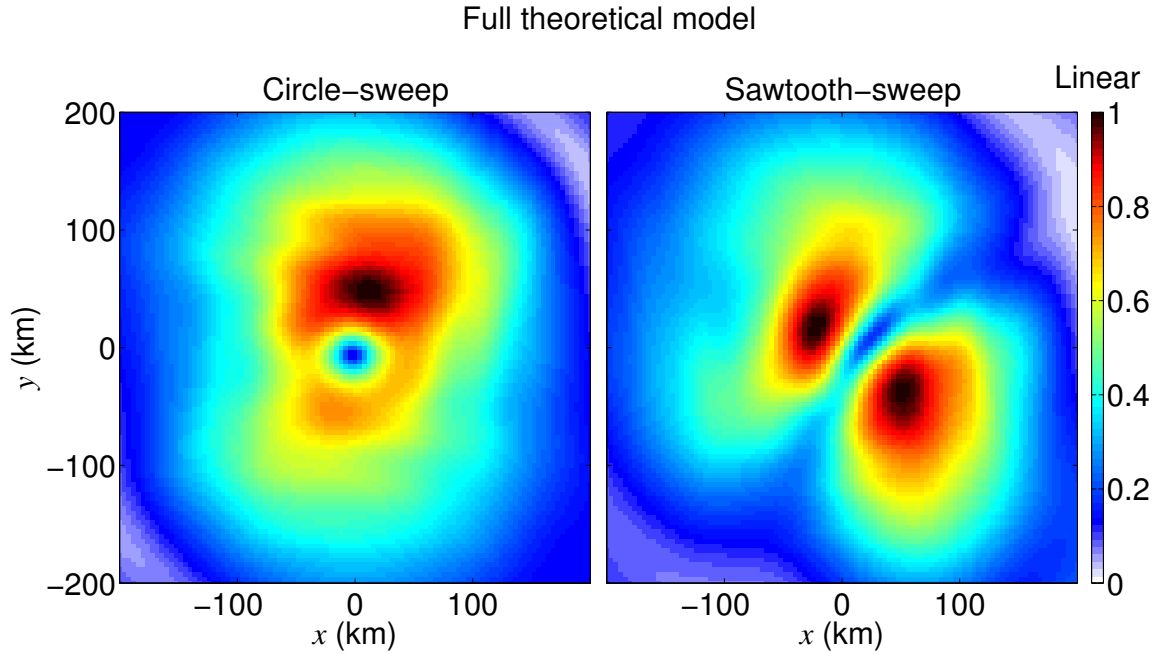


Figure 5.12: Circle-sweep and sawtooth-sweep magnetic field on the ground

field around the ‘donut’ in Figure 5.11 occurs almost precisely in the geomagnetic northward direction from HAARP. In addition, for the case of the sawtooth-sweep, the smaller lobe toward the Northwest is much smaller than the main lobe for the point-source model, whereas for the full theoretical model, there is about equal magnetic field values in each. This effect likely arises from the finite size of the HF heating beam, or the nonlinear response of the ionosphere to HF power.

## 5.5 Phased array parameters

Having now discussed how an ELF/VLF phased array drives a significant portion of the observations of amplitudes and directionality associated with geometric modulation, we now seek to characterize the phased array.

Geometric modulation and beam painting share two important features: that the region of the ionosphere heated by the HF beam is substantially larger than that

of either vertical-AM or oblique-AM modulation, and that the beam motion invariably involves heating with a beam that is off-vertical. Despite this feature, the two techniques act quite differently from each other, in that the amplitude enhancement associated with beam painting appears to be observed only near HAARP, whereas that of geometric modulation is observable also at larger distances. Additionally, the directionality inherent in the sawtooth-sweep is opposite to that of the line-paint, in that it directs radiation along its azimuth, rather than orthogonal.

These differences likely arise from the fact that the radiating ionosphere associated with the sawtooth-sweep and the line-paint may be characterized as line sources *Stutzman and Thiele* [1998, ch.4], or an array of point sources aligned along an azimuth. The line-paint acts as a broadside antenna, since there is no phase shift along the line source [*Stutzman and Thiele*, 1998, pg.37]. However, the sawtooth-sweep has an associated phase shift of  $\sim 8.7^\circ$  per km, since the total phase shift along the line is  $360^\circ$ , and the length of the sawtooth-sweep at  $\pm 15^\circ$  is  $\sim 43$  km at an altitude of 80 km. The sawtooth-sweep, acts in a manner that tends toward an endfire antenna array. The 43 km length corresponds to a free-space wavelength at  $\sim 7$  kHz, so near this frequency, the sawtooth-sweep likely acts closest to an ideal endfire array.

At 7 kHz, the horizontal motion of the beam in the sawtooth-sweep also closely matches phase velocities of propagating waves in the Earth-ionosphere waveguide (which are close to the speed of light, particularly for the lower order modes). In other words, the phase of a propagating wave in the Earth-ionosphere waveguide in the direction of the sawtooth-sweep shows the same spatial phase variation as the radiated ELF/VLF from the sawtooth-sweep, which [*Borisov et al.*, 1996] suggests may be produce Cerenkov radiation. At the lower frequencies, the phase variations do not line up, because the HF beam moves slower than the speed of light. This phase incoherence may also explain in part why geometric modulation appears to provide a smaller advantage compared to vertical-AM at the lower frequencies. This effect also serves to explain the frequency dependence of the sawtooth-sweep radiation pattern as observed in Figure 4.9. At frequencies above 7 kHz, the interaction region of the HF beam at 80 km altitude moves faster than the speed of light. Thus, while a wave traveling in the direction of the sawtooth-sweep azimuth has a phase velocity in the

horizontal direction below that of the HF beam, a wave traveling obliquely to the sawtooth-sweep azimuth does have the same phase velocity in the direction of the HF beam. Hence, the directional pattern of the sawtooth-sweep splits into two lobes above the frequency of 7 kHz, as reflected in Figure 4.9.

Furthermore, in Figure 3.9, it can be seen that the frequency range where the sawtooth-sweep provides an advantage compared to oblique-AM is upshifted compared to the frequencies where the circle-sweep provides an advantage over oblique-AM, which may be due in part to the speed of the ELF/VLF source as compared to the speed of light. In particular, the ELF/VLF source moves at a faster spatial rate for the circle-sweep than it does for the sawtooth-sweep at the same ELF/VLF frequency, since the circumference of the circle is longer than the length of the sawtooth-sweep. Hence, the speed of the source in the circle-sweep matches the speed of light at a lower ELF/VLF frequency as compared to the sawtooth-sweep.

Unlike the line-paint, the phases of the ionospheric sources of geometric modulation can be more generally controlled by the sequential order in which the HF beam heats the ionosphere, which dictates the relative phases of each beam location. In essence, the end result is a much larger extension of the two-element array reported by *Barr et al.* [1987]. *Cohen et al.* [2008b] therefore suggest that geometric modulation effectively creates a controllable large-element ELF/VLF phased array, and that this feature at least in part accounts for the amplitude enhancement and directionality associated with geometric modulation.

It is practically impossible to control the phase of an infinite number of locations, because the finite size of the HF beam limits the spatial resolution of the phased radiating ionosphere, and therefore the number of independent elements. For instance, the size of the beam at 3.25 MHz is  $\sim 360 \text{ km}^2$  at 80 km altitude, but the total area of the ionosphere covered during the  $15^\circ$  circle-sweep is  $\sim 3000 \text{ km}^2$ , or  $\sim 8$  times larger. With the 3.25 MHz beam at HAARP implementing a circle-sweep, the maximum number of beam spots which can be independently controlled is  $\sim 8$ , since a larger number of locations requires that they overlap, in which case they are cannot be independently controlled. The sawtooth-sweep at 3.25 MHz allows  $\sim 4$  independent beam spots.

## 5.6 Discussion

There are a number of ways to further analyze the results of the novel observations presented in Chapter 3. In Chapter 4, we endeavored to reproduce results using a complete theoretical model including all the physics that are most important to the problem. Although this approach yielded good results, our purpose in this Chapter has been different. Since the behavior of geometric modulation, beam painting, and amplitude modulation as observed in Chapter 3 appears to be very complicated, the purpose here is to break down the observations into its contributing pieces, each of which varies in a somewhat more simplistic fashion.

We have discussed in this chapter several different physical mechanisms each of which contributes to the behavior of ELF/VLF radiation from modulated HF heating. The relative contributions of these processes are functions of many parameters, including HF beam power and radiation pattern, electrojet spatial variations, HF frequency, ELF/VLF frequencies, and others. Future experiments involving beam motion should take these separate contributions into account for the particular parameters of an experiment, including the possibility of utilizing beam motion of ELF/VLF wave generation at other HF heating facilities.

## Chapter 6

# Summary and Suggestions for Future Work

Despite a long history of efforts, ELF/VLF wave generation remains greatly limited. One of the more promising techniques, involving modulated HF heating of the auroral electrojet, remains inefficient. In this thesis, we have explored the properties of ELF/VLF wave generation via HF heating of the lower ionosphere, in particular, making full use of motion of an HF beam. In particular, the High Frequency Active Auroral Research Program (HAARP) facility has at this point in time broken the record for the highest ERP levels of any HF heating facility, and has implemented the fastest beam steering ability to date.

In Chapter 1 of this thesis, we reviewed the basic characteristics of the ionosphere, magnetosphere, and one point of coupling between the two that takes place via the auroral electrojet. We illustrated the usefulness of ELF/VLF radio waves, both natural and manmade, in sensing and studying the physics of the ionosphere and magnetosphere, and we described the problem of ELF/VLF generation. We then presented a history of the efforts to produce ELF/VLF waves with HF heating of the ionosphere.

In Chapter 2, we reviewed the basic magnetoionic principles that dictate the plasma physics of the  $D$  and  $E$  region of the ionosphere. We then described the details of a physical model to simulate the propagation and energy deposition of

an HF wave passing through the ionosphere, and subsequent ionospheric reaction and recovery, leading to time-varying ionospheric conductivity. Next, we outlined a model of ELF/VLF Earth-ionosphere waveguide propagation, which begins with the conductivity changes and simulates the illumination of Earth and magnetosphere by the radiated ELF/VLF waves. Particular results for amplitude modulated heating were also shown.

In Chapter 3, we utilized an extensive experiment to compare amplitude modulation, beam painting and geometric modulation. The former is used as a baseline due to its long history as the baseline for ELF/VLF wave generation experiments, and latter two are techniques made possible only as a result of HAARPs new capabilities. We find that the three behave quite differently depending on frequency and location of receiver, and discuss both wave generation, and directionality.

Chapter 4 presented a theoretical equivalent of the same results, utilizing the model in Chapter 2, and found generally good agreement between theory and experiment. The model was then extended to discuss the complete directional pattern in the Earth-ionosphere waveguide, and injection into the magnetosphere, both being topics of interest which are difficult to address with experiment.

Finally, in Chapter 5 we presented four underlying physical mechanisms, and used a combination of theory and experiment to address the role of each in the observed (and modeled) behavior of amplitude modulation, beam painting, and geometric modulation. We find that geometric modulation can be interpreted in large part in the context of an ELF/VLF phased array, offering unprecedented levels of directionality than is currently available for such long wavelength applications.

## 6.1 Future work

Any successful research effort invariably leaves further topics to be explored. A few items which are not covered in this dissertation but which would be potentially exciting areas for future research are discussed below.



### 6.1.1 Equatorial electrojet

HF heating of the equatorial electrojet offers a potentially superior alternative to the auroral electrojet, in part because of its relative stability, as well as the vertical orientation of the driving electric fields. On the other hand, there is not currently a facility available to test ELF/VLF wave generation at the equator. A theoretical effort could be undertaken to evaluate the potential effectiveness of geometric modulation and beam painting (compared to amplitude modulation) for the specific conditions present near the equatorial electrojet.

### 6.1.2 Intersweep delay times

The implementation of geometric modulation herein assumes that the HF beam remains unmodulated, but this is in general not required. In Chapter 5, it is discussed that for the sawtooth-sweep at 7 kHz, the speed of the interaction region between the HF beam and the ionosphere moves at close to the speed of light (i.e., roughly the phase velocity of subionospherically propagating signals). At lower frequencies, however, the beam moves slower than the speed of light. This fact may contribute in part to a lessening of the effectiveness of geometric modulation at lower frequencies. One possible way to get that advantage back is to add idle times between each sweep. For instance, a sweep at 3.5 kHz could be conducted where the beam traverses the sawtooth pattern in  $143\mu\text{s}$  (i.e., half the ELF/VLF period) and then stays idle for  $143\mu\text{s}$ . This technique could therefore recover the possible benefits of the ideal phasing of the beam steps, since during this modified sawtooth-sweep, the beam moves at the same speed as a 7 kHz sawtooth-sweep with no idle time. On the other hand, since only half the HF power is used compared to a slower 3.5 kHz sawtooth-sweep, this technique may adversely impact the results. Experimental evaluation of the effect of idle times between sweeps may shed more light on this possible approach.

### 6.1.3 HF heating model with lookup table

In Chapter 2, we presented a novel method of dividing the HF heating into two components. The first tracks the nonlinear heating and cooling dynamics as a function of

HF power density and neutral densities, so that the dynamics can be understood without regard to the ionospheric variations. The second component is the distribution of the HF power density in the ionosphere, which is strongly ionosphere dependent. In most HF heating models, including the one here, the two are treated together. However, separating the two may achieve much faster HF heating calculations, and/or extension of the model to completely kinetic calculation.

Such an implementation may utilize a lookup table for each altitude, to calculate the electron temperature change depending on the HF energy at a given altitude without solving the energy balance equation. If that is achieved, then the only quantity that would have to be explicitly calculated is the distribution of HF power densities at each altitude, depending on absorption.

#### **6.1.4 Parallel conductivity changes**

In Chapter 2, we made the assumption that the parallel conductivity changes induced by HF heating can be ignored, as has been done in a number of past works. However, with the advent of more sophisticated propagation models running FDTD models, it is worth exploring this aspect more directly, so that assumption can be more thoroughly justified.

#### **6.1.5 Directional pattern**

Our formulation of Chapter 4 included a discussion of the complete directional pattern radiated in the Earth-ionosphere waveguide by various forms of HF heating. However, at this time, extensive receivers on the ground are not yet available to validate these predictions, apart from the results of Juneau and Kodiak in Chapter 3. A more extensive network of receivers across Alaska could, particularly to the North of HAAR, could begin to unravel the experimental directional pattern and therefore the directional gain from the sawtooth-sweep, for example.

### 6.1.6 Beam painting diurnal variations

In Chapter 5, it is found that the ERP of HAARP is sufficiently high for conductivity modulation at 70 km to occur without losses from short timescale electron recoveries. At 90 km, however, the ERP appears to be still too small (at least at 3.25 MHz). This result suggests that there may be a diurnal variation in the efficiency of ELF/VLF generation via beam painting that is not present in amplitude modulation or geometric modulation, since daytime and nighttime distribution of the ELF/VLF source height is very different. Repetition of these comparative formats, such as those presented in Chapter 3, for many different times of day, can statistically answer this question.

### 6.1.7 Variation with HF frequency

Due to limitations of experiment and theory, we have utilized an HF frequency of 3.25 MHz in nearly all our experiments and simulations here. The function of these results on HF frequency should be explored, since this affects not only the amount of ionospheric absorption of the HF waves, but also the shape (and ERP) of the HF beam. The ERP and radiated pattern from HAARP is given in Appendix B.

## 6.2 Concluding remarks

I hope you've enjoyed reading this dissertation as much as I have in producing it. As with many scientific works, there are as many questions newly raised as there were answered. So while the material here certainly contributes to our understanding of the auroral ionosphere, of ELF/VLF wave generation, and of ELF/VLF wave propagation, there is undoubtedly more work to be done. I can only hope that the methods of analysis, and way of posing the problem can be of as much value in solving future problems as the actual scientific results themselves. I look forward to witnessing the continuing development of this exciting field of study.

# Appendix A

## Long Distance Reception

Figure A.1, top left panel, shows the placement of some AWESOME receivers for detection of subionospherically propagating VLF signals generated above the HAARP facility using AM modulated HF heating, at three different sites in Alaska: Chis-tochina ( $62.61^{\circ}\text{N}$ ,  $144.62^{\circ}\text{W}$ , 37 km from HAARP), Juneau ( $58.59^{\circ}\text{N}$ ,  $134.90^{\circ}\text{W}$ , 704 km SE of HAARP), and Kodiak ( $57.87^{\circ}\text{N}$ ,  $152.88^{\circ}\text{W}$ , 661 km SW of HAARP). Each of the Alaska sites use large  $1\Omega$  antennas  $18\text{ m}^2$  in area or larger. Midway Atoll is located at  $21.21^{\circ}\text{N}$ ,  $177.38^{\circ}\text{W}$ , 4466 km SE of HAARP, where a substantially smaller  $1.7\text{-m}^2$  antenna is used. The lower left hand panel shows the detected 2375-Hz signals from HAARP for each of the four sites, on 01-Mar-2007, during a 37-minute period when the transmission format was consistent, and the signal generation process in the ionosphere was particularly effective.

*Moore et al.* [2007] integrated ELF/VLF data for 60 minutes at Midway in order to detect signal levels from HAARP at  $\sim -55\text{ dB-pT}$ , the farthest such unambiguous detection of ELF signals generated via this technique. However, in 2007, the HAARP input power was increased from 960 kW to 3.6 MW, which also increased generated ELF signal strengths. Figure A.1 shows exceptionally strong signals received at Midway, up to  $-32\text{ dB-pT}$  (or,  $\sim 200$  times more power than the original detection of HAARP signals at Midway). These signal levels are strong enough to be easily detected in a spectrogram, so that the signal strength can be tracked on a seconds-long time scale over a long period (in this case, 40 minutes long), as shown in the lower

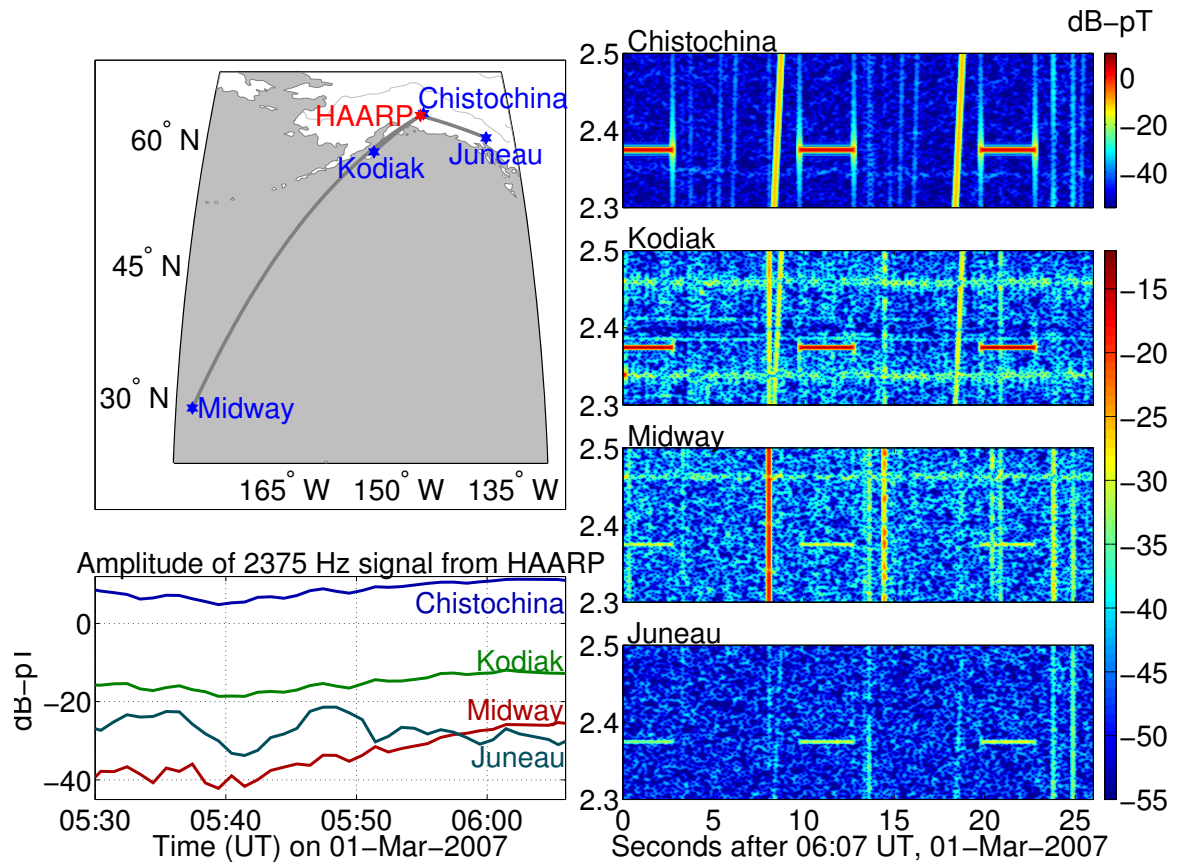


Figure A.1: Global detection of ELF signals from HAARP

left panel of Figure A.1. The signal received is therefore a diagnostic both of the directionality and strength of the ionospheric source above HAARP, as well as the ionospheric paths in between HAARP and the various receivers.

In general, the amplitude of generated ELF signals via modulated HF heating of the auroral electrojet at substantial ( $>150$  km) distances is strongly dependent on the ionospheric conditions, the strength of the electrojet, the ELF frequency, and the parameters of the HF heating beam. The simultaneous detection of the HAARP-radiated signal at multiple sites of varying distances and direction enables greater understanding of these processes. For instance, the amplitude at Kodiak is both stronger (by 10–20 dB) and more stable than the signal at Juneau. *Cohen et al.* [2008a] attributes this to an effective dipole direction dictated primarily by the auroral electrojet direction (which, in this case, is likely oriented magnetically east-west, or generally toward Juneau). Therefore, the period between 0550 UT and 0600 UT, when the signal amplitudes at Juneau decreased while correspondingly growing at Kodiak, may indicate a slight and gradual rotation of the electrojet field directions, in such a way as to be more closely aligned with the direction to Juneau.

The network of AWESOME receivers also enables extraction of ionospheric propagation parameters. For instance, the Midway signal gradually strengthens compared to those at the other three sites. This result is possibly explained by the variation in ELF attenuation between daytime and nighttime. We note that the HAARP-Midway great circle path is at the same azimuth from HAARP as the HAARP-Kodiak path, so that the HAARP-Kodiak path is a diagnostic of the signal en route to Midway. During the 37-minute period shown here, the sunset terminator was in between Kodiak and Midway, so that during the 37-minute period shown here, the sunset terminator moved  $\sim 1.5$  Mm further down the HAARP-Midway path. Also, during this period, the amplitude between Midway and Kodiak decreased by  $\sim 9$  dB. If such a difference were explained by the higher attenuation on the daytime side of the terminator, then the daytime attenuation rate would therefore be  $\sim 6$  dB higher. For frequencies not far from the ionospheric cutoff of the first order modes ( $\sim 1.8$  kHz), such a difference is not unreasonable [*Davies*, 1990, pg.387].

# Appendix B

## HAARP HF Radiation Pattern

In this dissertation, we have extensively explored the use of motion of an HF heating beam in generation of ELF/VLF waves via HF heating of the ionosphere. In the experiments and theoretical investigations therein, the HF beam is taken to be in a mode which maximizes the ERP, and minimizes the width of the beam. However, a phased-array facility such as HAARP has considerably more flexibility in terms of the shape of the beam. For instance, the HAARP facility allows the HF power to be spread out in either of the two horizontal directions, or in both directions (although the total power transmitted is roughly the same). We have also considered only the lowest HF frequencies available with the HAARP facility, 2.75 MHz and 3.25 MHz.

However, further experiments involving beam motion may be possible with different beam shapes and HF frequencies. The data on the radiated HF pattern for various beam configurations is obtained from M. J. McCarrick and is reproduced here.

Figure B.1 shows the HF power reaching 60 km altitude from HAARP, over a 100 km $\times$ 100 km side square area, for a number of different HAARP modes. We consider six different HF frequencies (the rows of Figure B.1) and four different beam configurations (the columns of Figure B.1). Since the grid of the HAARP array is oriented 14° east of north, the broad-NS modes spread the power in the east-northeast direction. As the HF frequency increases, the size of the main beam gets smaller and more tightly focused, while the sidelobes become smaller but more tightly spaced. The spreading of the HF beam is achieved by dephasing the rows or columns (or

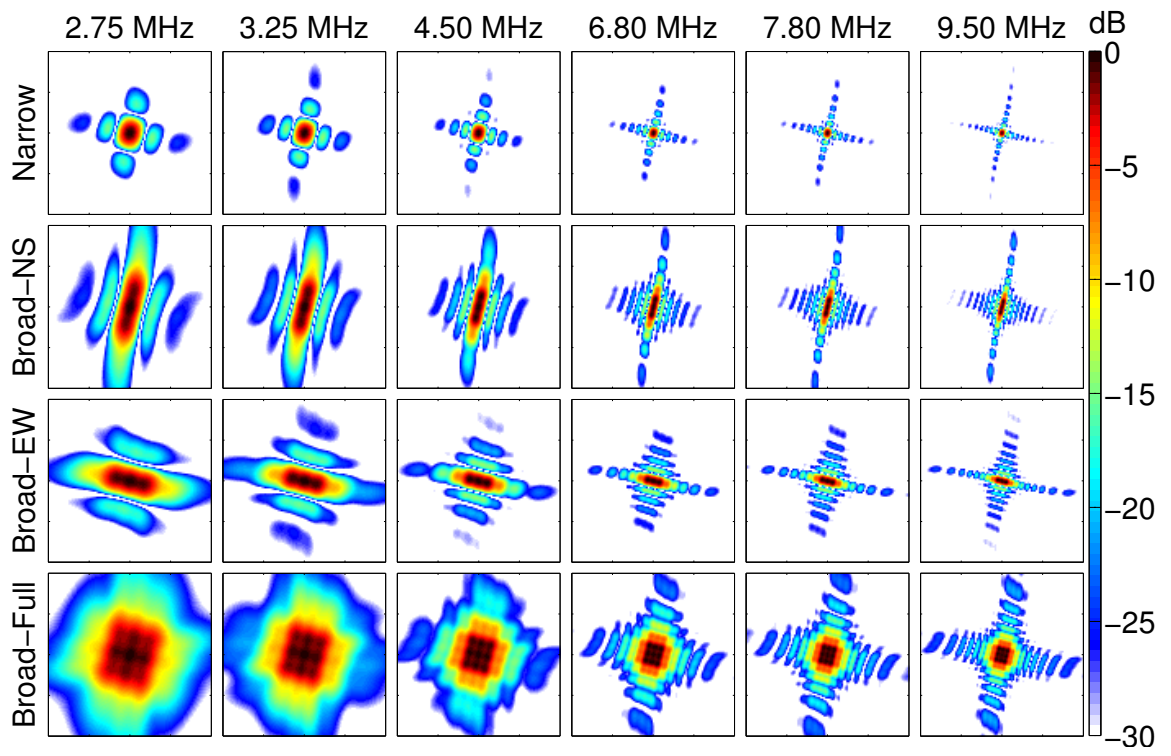


Figure B.1: HF power into the ionosphere from HAARP beam modes



$f$ (MHz)	Narrow	Broad-NS	Broad-EW	Broad-Full
2.75	3.24 (417)	2.66 (100)	2.84 (102)	2.27 (25)
3.25	3.35 (575)	3.02 (151)	3.17 (155)	2.81 (40)
4.50	3.13 (1023)	3.02 (269)	3.10 (275)	2.95 (72)
6.80	3.31 (2291)	3.28 (631)	3.31 (631)	3.28 (170)
7.80	3.24 (2884)	3.24 (776)	3.24 (776)	3.20 (214)
9.50	2.88 (3802)	2.88 (1023)	2.88 (1288)	2.88 (275)

Table B.1: Radiated power (and ERP), in Megawatts, of HAARP beam modes

both) of the HF array, which roughly combines the main beam with the immediate sidelobes.

Table B.1 shows the ERP resulting from each of the modes in Figure B.1. The power density at the center of the beam (the peak power density) is given by Equation 1.3, where the ERP replaces  $GP_{\text{rad}}$  in the numerator.

# Appendix C

## ELF/VLF Reception and Detection

The ELF/VLF receiver utilized for the measurements presented was developed in 2003 and 2004 by the author of this thesis along with Justin Tan and Evans Paschal. Although Stanford University has been building and utilizing ELF/VLF receivers for decades, steady updates in technology sometimes necessitate a redesign of key components. In particular, the advent of Global Positioning System (GPS) satellites, and subsequently cheaper GPS receivers, the cheaper cost of manufacturing printed circuit boards, plus advances in digitization hardware, and computer ability to digitize and process data in real time, have all contributed to the evolution of the ELF/VLF receiver beyond a simple antenna and low-noise amplifier (LNA). In this appendix, we describe this latest redesign of the receiver, and describe a number of performance characteristics. The receiver is more generally known as the Atmospheric Weather Electromagnetic System for Observation, Modeling, and Education (AWESOME). The AWESOME has been widely utilized both for global scientific measurements, as well as for scientific capacity building and educational outreach under the auspices of the United Nations sponsored International Heliophysical Year program [*Scherrer et al.*, 2008; *Thompson et al.*, 2009]. The AWESOME receiver is described by *Cohen et al.* [2009b], but the most important aspects for the purposes of this dissertation are reproduced here.

## C.1 Antenna characteristics

The AWESOME receiver uses wire loop antennas, each sensitive to the component of magnetic field in the direction orthogonal to the plane of the loop. With two loops, whose planes are orthogonal both to each other and to the ground, it is possible to record the horizontal (i.e., along the Earth's surface) magnetic field at any location. Though it is also feasible to set up a third loop whose plane is parallel to the ground, for many applications this measurement is not as useful since vertical magnetic fields are typically much smaller near the ground, except in the case of significant local subterranean inhomogeneities. The AWESOME receiver can also be configured to record a third signal from a vertical electric whip antenna, and though such a measurement is useful for certain specific applications, we focus here only on the electronics and measurements taken with two orthogonal magnetic loop antennas.

Choice in receiving antenna parameters is discussed by *Paschal* [1980] and *Harri-man et al.* [2009] and are briefly reviewed here. ELF/VLF magnetic-loop sensitivity and frequency response are controlled by four dependent antenna parameters: resistance ( $R_a$ ), inductance ( $L_a$ ), area ( $A_a$ ), and number of turns ( $N_a$ ). Sensitivity can be evaluated by comparing the antenna noise with the signal levels that would be induced from a certain magnetic field. Antenna noise is dominated by thermal noise of the wire resistance, given as

$$E_a = (4kTR_a)^{\frac{1}{2}} \quad (\text{C.1})$$

in units of  $\text{VHz}^{-\frac{1}{2}}$ , or noise spectral density, where  $k$  is Boltzmann's constant, and  $T$  is absolute temperature in Kelvin. From Faraday's law of induction approximated when the wavelength is large compared to the antenna size, the voltage induced in a wire loop from a magnetic field amplitude  $B$  at angular frequency  $\omega$  is given as

$$V_a = j\omega N_a A_a B \quad (\text{C.2})$$

The above equation allows us to relate a given voltage level at the input of the receiver to an equivalent magnetic field value, since the  $N_a$  and  $A_a$  are characteristics

of the antenna. This relation is an important property for calibration (discussed later), since the recorded values can therefore be converted to magnetic field values. Setting the noise level for a 1-Hz bandwidth in equation C.1 to be equal to the voltage from a given magnetic field in equation C.2, we can solve for the value of  $B$  to arrive at a field-equivalent and frequency-dependent signal level for  $E_a$ , written as

$$B_n = \frac{(4kTR_a)^{\frac{1}{2}}}{N_a A_a j\omega} \quad (\text{C.3})$$

The quantity  $B_n$  is a measure of the noise level intrinsic to the resistance of the antenna wire. We then normalize the result by  $1/f$  to obtain a sensitivity metric

$$\hat{S}_a = \frac{(4kTR_a)^{\frac{1}{2}}}{2\pi N_a A_a} \quad (\text{C.4})$$

in units of  $\text{THz}^{(1/2)}$ . The sensitivity as defined here is simply the magnetic-field-equivalent value of the antenna's thermal noise in a 1 Hz bandwidth, normalized by the factor  $1/f$ .

The other important antenna parameter is the turnover frequency,  $\omega_a = R_a/L_a$ . For values of  $\omega$  well above this frequency, the impedance of the antenna ( $Z_a = R_a + j\omega L_a$ ) is dominated by the inductance, and is therefore proportional to  $\omega$ . However, since the induced voltage in equation C.2 is also proportional to  $\omega$ , the current induced in the loop ( $V_a/Z_a$ ) will remain constant with respect to frequency. The result is a flat frequency response for the magnetic loop for frequencies well above  $\omega_a$ .

As mentioned earlier, it is possible to improve  $\hat{S}_a$  by simply increasing  $(A_a M)^{-\frac{1}{2}}$ , i.e., by increasing either the thickness of the wire, the area of the loop, or the number of turns. The antenna impedance also changes with these parameters, but for a specifically chosen antenna impedance (on the basis of the front end impedance of the preamplifier), a family of different antenna parameters (with significantly varying values of  $\hat{S}_a$ ) can satisfy the impedance requirements. Some examples of antenna parameters fitting the 1.00  $\Omega$  and 0.5–1.0 mH impedance are given in Table II of *Harriman et al.* [2009].

Using equation C.2, with values of  $N_a = 5$  and  $A_a = 25 \text{ m}^2$ , we see that a 1 pT amplitude signal at 10 kHz induces an electromotive force of only  $\sim 7.8 \text{ } \mu\text{V}$  in the

wire loop, so that even the most sensitive loop is only useful if followed by low-noise amplification. *Harriman et al.* [2009] describes the techniques for this amplification used in the AWESOME receiver, which consists of a transformer followed by a low-noise-amplifier circuit specifically designed for ELF/VLF signals. The transformer-amplifier pair involves balancing several tradeoffs, as described in *Harriman et al.* [2009], but is generally capable of achieving, over  $\sim 2$  decades of frequency range, sufficiently low noise-figure so to add minimally (i.e.,  $< 10$  dB) to the limiting antenna thermal noise, and is designed specifically to match a given antenna impedance.

## C.2 System design

We now describe the basic design principles of the AWESOME receiver. The top panels of Figure C.1 show photographs of the three main components of the AWESOME receiver: The antenna, preamplifier, and line receiver. The AWESOME receiver samples data at 100 kHz, nominally facilitating signal detection up to 50 kHz without aliasing. Furthermore, the 16-bit sampling nominally enables 96 dB of dynamic range, although the practical dynamic range (discussed later) is a function of the input-referred system noise compared to the signal level which saturates or ‘clips’ the receiver output.

In detecting magnetic field signals on the order of fT–pT, a dominant source of interference is local electromagnetic fields from 50/60 Hz power lines, whose harmonics can extend to many kHz, and whose strength can be orders of magnitude stronger than those of natural ELF/VLF signals. Some of the power-line interference can be tracked and subtracted in post-processing, provided that the level of power-line interference has not saturated the output, but it is nonetheless helpful to avoid this interference altogether by locating the loop antennas far away from such sources, whereas the recording computer must typically be placed indoors. Figure C.1, bottom panel, shows a block diagram showing how these goals are realized. The preamplifier, placed near the antenna, matches the impedance of the antenna and provides low-noise amplification. The preamplifier must be near to the antenna, as any long cable may contribute noticeable resistive losses compared to the  $1\Omega$  antenna resistance.

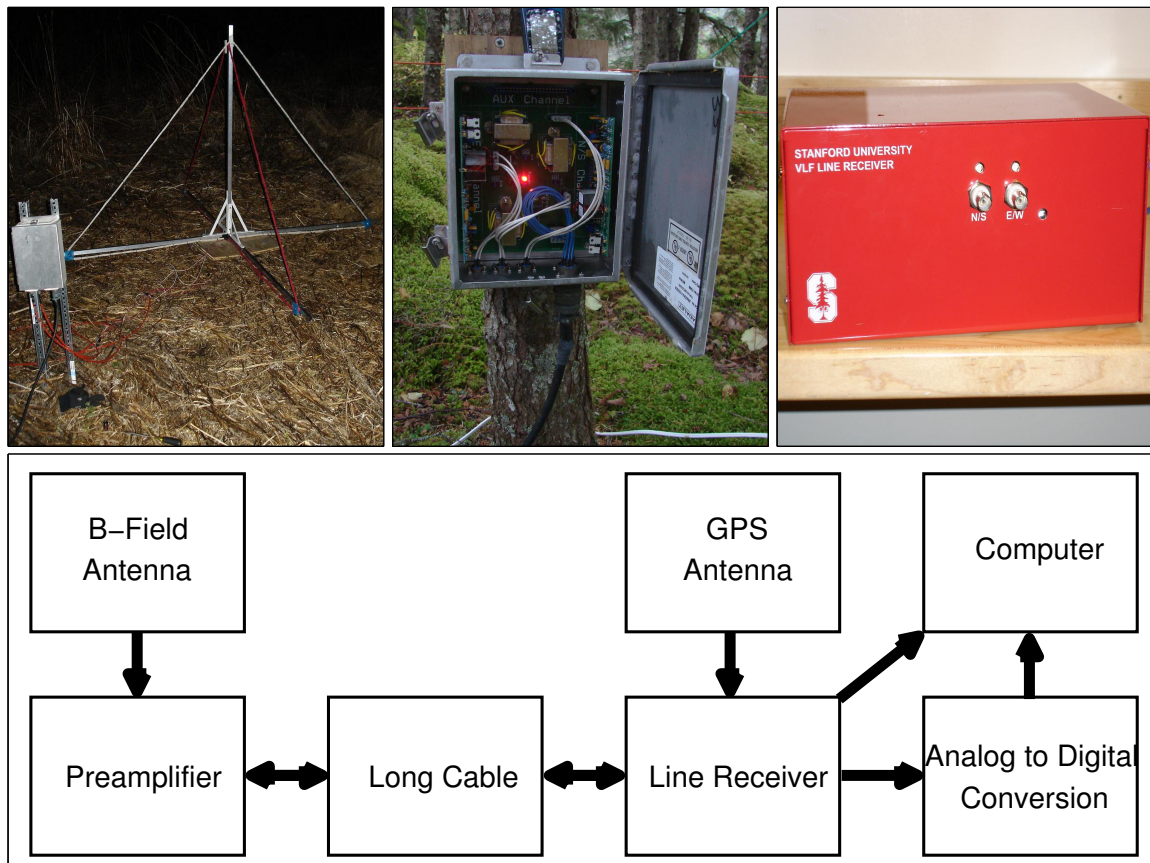


Figure C.1: Photos and block diagram of the AWESOME receiver.

At the output stage of the preamplifier, a variable-gain amplifier enables additional multiplication of the signal amplitude by either 00 dB, 10 dB, 20 dB, or 30 dB. The proper choice of gain level is described later, since it affects both the noise characteristics of the receiver and its saturation level, and may be different depending on application and choice of antenna.

The low-frequency response of the receiver ( $\sim 800$  Hz cutoff), is limited mostly by the line transformer which matches the preamplifier with the transmission line. However, the low frequency cutoff can be selected as 80 Hz, 350 Hz, 800 Hz, or 7 kHz. The first two are used for extremely quiet sites (i.e., located away from 50/60 Hz interference sources), and are achieved with a gain boost to the lower frequencies that roughly compensates the loss in frequency response below the turnover frequencies of the antenna and receiver, thus flattening the response at the low end. The third setting applies no frequency compensation. The 7-kHz high-pass filter is used at noisier sites, like rooftops of a building at a school or in general at urban sites, and generally in situations where only VLF transmitter signals in the 15–30 kHz range are of interest. The preamplifier also contains a passive RFI suppression circuit at the front consisting of a series inductor with shunt-to-ground capacitors at both antenna terminals to ensure that high frequency RF sources (like AM radio stations or HF transmitters) do not couple in to the receiver. The total power usage of the AWESOME preamplifier is  $\sim 1$  W, or  $\sim 33$  mA of current from the  $\pm 15$  V supply lines.

The line receiver, located indoors, performs anti-aliasing filtering, GPS time-stamping and synchronization, and passes both analog signal and sampling clock signal to a computer for digitization across a shielded cable. The line receiver also provides power to the preamplifier. Digitization is done with an internal PCI card in the computer, capable of up to three-channel, 16-bit sampling at 100 kHz per channel. We currently utilize a card developed by National Instruments, like the 6250M, or a previous two-channel model, 6034E. The anti-aliasing filter is applied separately on each channel, using a 12th-order elliptical filter at 47 kHz. The filter reaches  $\sim 95$  dB attenuation by 55 kHz, as shown in the simulated amplitude and phase response in Figure C.2. Though the use of filter orders above 8 is rare in practice, a 12th order

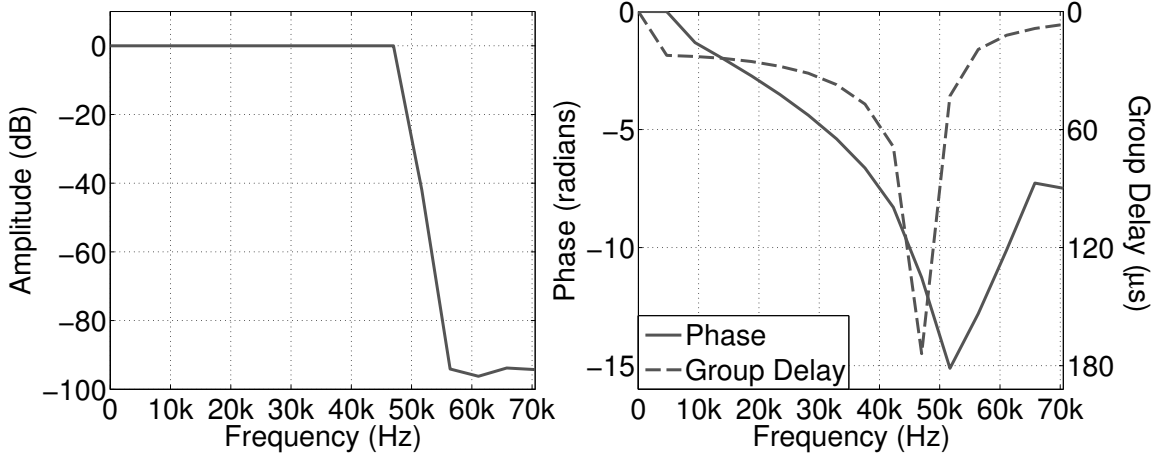


Figure C.2: AWESOME Anti-aliasing filter

filter was employed here in order to push the cutoff as close to 50 kHz as possible, so that VLF transmitter signals at 40.75 kHz (NAU, Puerto Rico), and 45.9 kHz (NSC, Italy), are within the passband of the receiver. The total power usage of the line receiver is  $\sim 5$  W.

A suitably long shielded multi-conductor cable (currently Belden 1217B) connects the preamplifier to the line receiver, and consists of four shielded 22 AWG twisted pairs, designated, respectively, to carry power from the line receiver to the preamplifier, and up to three data channels from the preamplifier to the line receiver. For the three data channels, at both ends of the transmission line, a custom designed line transformer matches the  $75\text{-}\Omega$  impedance to the output impedance of the preamplifier circuit and the input impedance of the line receiver ( $1.75\text{ k}\Omega$ ). Since the resistivity of the cable is rated as  $\sim 5\Omega$  per 100 m, and since the preamplifier regulates the  $\pm 15\text{-V}$  supply to  $\pm 10.8\text{ V}$  (and requires  $\pm 11.5\text{ V}$  minimum power voltage for supply line regulation), the maximum cable length given the preamplifier's  $\sim 1\text{W}$  power is  $\sim 2000$  m. Typically, however, 150–500 m is sufficient to locate the antenna far enough away from power lines.

Since broadband data are sampled at 100 kHz, and 16 bits per sample, data will accumulate at  $\sim 687$  MB per hour, per antenna. So, an entire 24-hour dataset on two orthogonal antennas will be  $\sim 32$  GB. To mitigate the large amount of storage



required to capture all of this, custom data acquisition software has been developed at Stanford. Broadband 100-kHz data can be saved for any desired daily schedule, in continuous fashion, or in synoptic mode (i.e. periodic short snippets), the latter often being necessary due to the large volume ( $\sim 1.5$  GB per hour) of data. Narrowband data can be saved for as many as 16 channels (limited only by the processing power of the computer), and is typically saved in a single block for the whole day due to the much smaller volume of data ( $\sim 15$  MB/hour). The software also enables selected amounts of data to be sent over the Internet to a server according to a daily schedule, or transferred to another hard drive or storage medium for occasional collection. Live, calibrated spectrograms can also be posted on the Internet. A so-called ‘pac-man mode’ is sometimes used, which enables continuous data to be archived for several days backlog, with the oldest day being then deleted to make room for the newest day, to serve as a large buffer useful in the event of geomagnetic storms, or other events in which the occurrence is not necessarily known until shortly thereafter. The data acquisition software also includes a number of features intended to recover automatically and gracefully from a power failure or computer crash. For instance, the software automatically reboots the computer in the event of an interruption with the receiver signals, or if the CPU is unable to keep up with the sampling process. Data are not currently being archived in a publicly accessible fashion, but such a system is currently being planned, and will be described elsewhere.

### C.3 Calibration

Calibration enables the digitally-recorded 16-bit output of the AWESOME receiver system to be directly related to wave magnetic field values, though the frequency-varying gain of the receiver must be taken into account. This result is achieved via injection of a series of known-amplitude signals at the input of the preamplifier, and measuring the values at the output. The corresponding value of the magnetic field is known through equation C.2, since the parameters of the antenna as well as the input impedance of the preamplifier are known.

Although the calibration reference signal can be injected manually at the receiver

input terminals (generally at a series of frequencies between DC and 50 kHz to span the whole receiver band), the AWESOME receiver includes an internal calibration circuit which generates a pseudo-random digital sequence 1023 bits long, with bit frequency  $\sim 256$  kHz. In the frequency domain, this sequence corresponds to a comb of signals at frequency multiples of  $\sim 250$  Hz, with equal amplitudes at all frequencies below 50 kHz. Therefore, a single calibration reference signal includes all the frequencies to sample the amplitude response of the receiver with  $\sim 250$  Hz resolution, since the individual frequency components can be separately treated in post-processing. This calibration technique has also been used in some earlier Stanford ELF/VLF receiver designed by *E. W. Paschal*.

By comparison of the calibration signal (separately at each frequency component) with the background noise level, we can also measure the noise levels intrinsic to the hardware of the receiver, including noise induced via its exposure to an electromagnetically noisy indoor environment (as electromagnetic noise may couple into the wires and circuit boards, particularly since shielding magnetic fields is generally not possible without the use of  $\mu$ -metal material enclosures). Noise which enters the system through the antenna can be excluded, since the calibration signal can be recorded without an antenna attached to the preamplifier, using a ‘dummy loop’ having the same impedance connected instead of the antenna. Furthermore, since the calibration signal corresponds to a specific magnetic field value for a given antenna (using equation C.2), the noise levels can be ‘input-referred’, or related directly to a magnetic field spectral density value, though a specific antenna configuration must then be assumed.

Although the pseudo-random calibration signal is incoherent, the phase response can be measured by injecting a signal from a sinusoidal source into one channel of the receiver, and simultaneously into the other channel of the ADC. Since the ADC records one channel directly from the source, and one channel from the source via the receiver, the phase difference in the recorded signal can be used to measure the delay in the signal, and can be repeated manually for many frequencies. In practice, however, it is found that the phase response varies by a negligible amount between different AWESOME receivers, although the amplitude response may vary slightly

( $\sim 1$  dB), due mostly to tolerances to the resistors used in the anti-aliasing filter. For this reason, an amplitude calibration is usually separately recorded for each receiver, when it is placed in the field, whereas a generic phase calibration can be applied universally.

## C.4 Gain and sensitivity

We now describe some of the measured performance characteristics of the AWESOME receiver. Figure C.3 shows some measured properties of the AWESOME receiver. The top left panel shows the AWESOME receiver frequency response (in units of mV at the output divided by picotesla at the input). Although the measurement is made separately in both channels, only one is presented. In addition, these characteristics vary by a small amount between physical receivers, owing to tolerances in the various components. The 3-dB cutoff points are at  $\sim 800$  Hz (where the line transformer begins to attenuate the signal) and at 47 kHz (where the anti-aliasing filter cutoff lies). In order to associate the calibration signal strength to an equivalent magnetic field, the size of the antenna must also be known. The frequency response is therefore presented for two different typical right isosceles  $1\text{-}\Omega$ ,  $0.5\text{--}1.0$  mH antenna sizes, a large loop ( $25\text{ m}^2$ ) consisting of a 10-m base and a 5-m height, and second being a smaller loop ( $1.69\text{ m}^2$ ) with 2.6 meter base and 1.3 meter height. We refer to these two sizes ( $1.69\text{ m}^2$  and  $25\text{ m}^2$ ) consistently throughout the description of the performance characteristics. It should be noted that although the calibration may vary slightly from receiver to receiver, the general characteristics described here apply consistently across all measured AWESOME receivers.

The phase response, shown in the bottom left panel of Figure C.3, is obtained by injecting a sinusoidal signal into the front end of one of the receiver channels, and also directly into the ADC as a reference. The derivative of the group delay with respect to frequency gives the group delay of the receiver. Within the passband (i.e., between 1 kHz and 45 kHz), the group delay is mostly between 25 and 35  $\mu\text{s}$  (or  $\sim 3$  samples at 10 kHz), rising above 50  $\mu\text{s}$  above 40 kHz as the frequency nears the 47-kHz cutoff of the anti-aliasing filter.

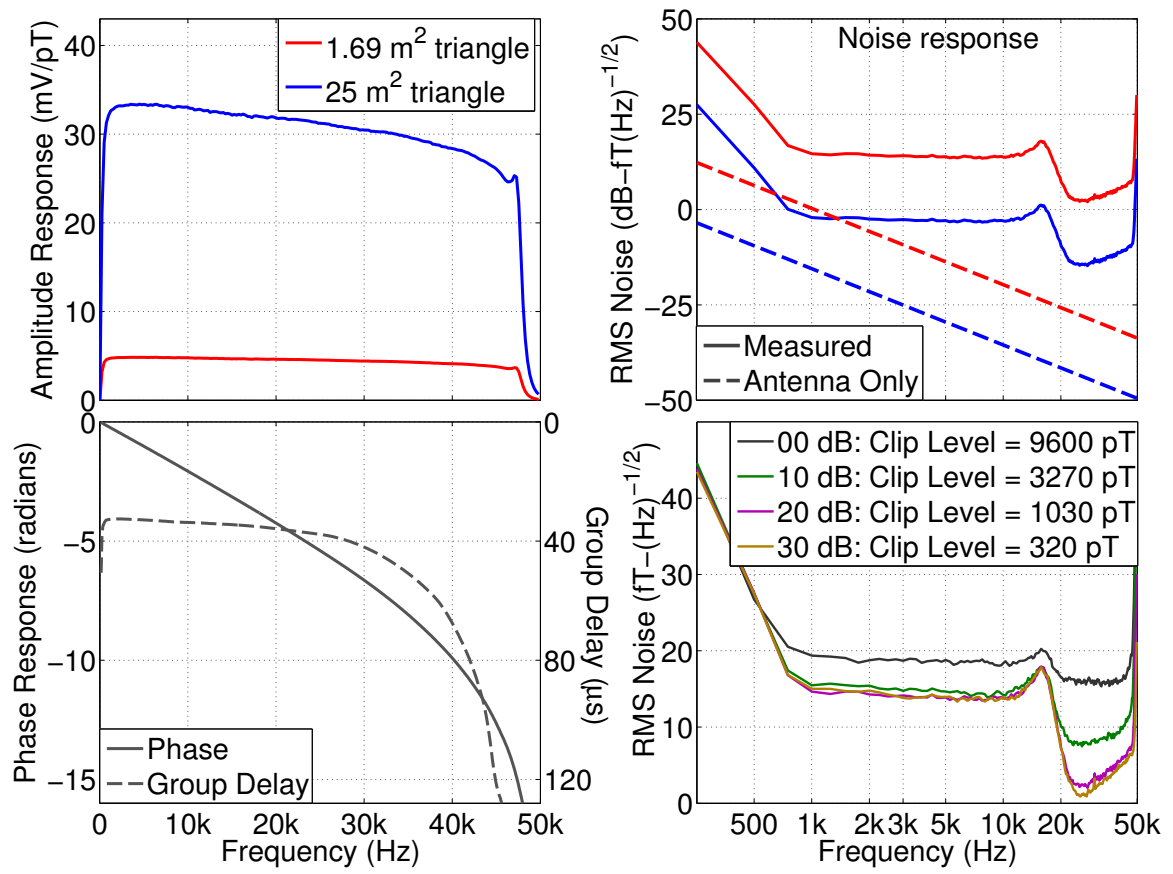


Figure C.3: Measured performance characteristics of the AWESOME receiver

The top right plot of Figure C.3 shows the measured input-referred RMS noise levels with solid lines, for the same two antenna sizes as in the top left panel. The theoretical noise level of a noise-free receiver (where only thermal noise from the  $1\ \Omega$ ,  $0.5\text{--}1.0\ \text{mH}$  antenna is present) is shown with dashed lines. The vertical separation between solid and dashed lines is therefore a measure of the noise added in the receiver electronics. We note that the noise measurements are taken when the receiver is deployed in the field, as opposed to inside a  $\mu$ -metal shielding chamber, so all effects of environmental noise coupling into electronics are inherently included. This particular noise response is shown for the 10 dB preamplifier gain setting.

We may use this noise floor to establish the minimum detectable signal (i.e., the smallest signal for which signal-to-noise ratio is 0 dB), which is a function of the bandwidth of the signal being detected (since the total noise power depends on the bandwidth), or, alternatively, on the integration time used in signal detection (which intrinsically sets the bandwidth). VLF transmitter signals operate over a  $\pm 100\ \text{Hz}$  bandwidth, in the frequency range between 18 and 30 kHz, where the receiver noise levels are  $\sim -10\ \text{dB-fT/Hz}^{1/2}$  amplitudes for the large antenna configuration, as shown in Figure C.3, top right panel. Hence, the 200-Hz bandwidth includes total receiver noise of  $\sim +13\ \text{dB-fT}$ , indicating that VLF transmitter signals in this configuration as low as  $\sim 4\text{--}5\ \text{fT}$  can be received with 200-Hz time resolution. Similarly, sensitivity over the ELF frequency range enables detection of signals over a 1-Hz bandwidth (i.e., for signals of longer-duration such as chorus needing only 1-s time resolution) as low as  $\sim 1\ \text{fT}$  with the larger ( $25\text{m}^2$ ) antenna configuration.

The natural ELF/VLF radio environment on the Earth is dominated by the presence of so-called radio atmospherics [*Chrissan and Fraser-Smith, 1996*], or ‘sferics’, impulsive ( $\sim 1\ \text{ms}$ ) broadband radiation originating from lightning strokes even at global distances from a given receiver. Typical sferic amplitudes at distances greater than 500 km are 1–100 picoteslas. Other natural sources of ELF/VLF radiation detected on the ground such as chorus [*Gołkowski and Inan, 2008*], hiss [*Hayakawa and Sazhin, 1992*], and whistlers [*Helliwell, 1965*], are often present with substantially smaller amplitudes ( $< 1\ \text{pT}$ ). The root-mean-square average spectral density of natural ELF/VLF noise is typically between  $1\text{--}100\ \frac{\text{fT}}{\sqrt{\text{Hz}}}$  in this frequency range

[*Chrissan and Fraser-Smith, 1996*]. Signals can also be generated artificially via High Frequency (HF, 3-10 MHz) heating of the auroral lower ionosphere, with amplitudes as strong as several pT [*Cohen et al., 2008a*] or greater. The AWESOME receiver is sensitive enough to detect even weakly present natural ELF/VLF signals.

The choice of gain settings may affect the noise performance of the receiver, at the expense of ‘clip level’, or the lowest amplitude signal which may cause saturation of the receiver output, which in turn affects the dynamic range. Figure C.3, bottom right panel, shows the input-referred noise response for the receiver (with the 1.69m<sup>2</sup> triangle antenna) using all four preamplifier gain settings. Since a higher gain may cause the noise levels generated in the preamplifier to be higher than the noise levels generated in the line receiver, increasing the gain from 0 dB to 10 dB lowers the input-referred noise response of the receiver (although increasing beyond 10 dB shows only marginal improvements). On the other hand, increasing the gain decreases the threshold clip level. The effective dynamic range can be taken to be between the receiver noise level and the clip level. For instance, using the 0 dB preamplifier gain setting with the larger (25m<sup>2</sup>) antenna configuration, the total noise level (i.e., the input-referred field spectral density integrated over the bandwidth) in the pass-band of the receiver (i.e. between 1 kHz and 47 kHz) is  $\sim 1.6$  pT, or  $\sim 75$  dB (12.5 bits) below the clip level. At 10 dB gain setting, the broadband dynamic range is  $\sim 71$  dB, while at 20 dB gain, the dynamic range is  $\sim 62$  dB, and at 30 dB gain, the dynamic range is  $\sim 53$  dB. Hence, while increasing the gain enables smaller signals to be detected, such a result comes at the expense of the ability to fully record the largest signals without incurring receiver saturation. For this reason, the 20 dB and 30 dB gain settings will likely only be used in situations where only small signals are of interest, since the high gain will reduce the effect of quantization noise, at the expense of dynamic range.

## C.5 Timing accuracy

An accurate 100-kHz sampling clock is crucial for phase-coherent measurements of VLF transmitters, and to maintain the possible use of VLF interferometry involving

coherent measurements between sites. For instance, a clock drift of even  $1\ \mu\text{s}$  (one tenth of a sample period at 100 kHz) represents  $9^\circ$  of phase uncertainty at 25 kHz, while ionospheric disturbances often occur with phase changes on the order of  $1^\circ$  or less [Wolf and Inan, 1990]. GPS devices often provide a 1 pulse per second (PPS) timing signal, from which the 100-kHz sampling signal must be derived. The GPS timing card used in the AWESOME line receiver (Motorola M12M OnCore) guarantees 10–20 ns absolute timing on its 1 PPS clock, but in order to extend this timing accuracy to the 100-kHz sampling signal, the AWESOME receiver uses a feedback scheme consisting of a 10-MHz voltage adjustable oscillator, whose control voltage is set by a complex programmable logic device (CPLD) via a 10-bit Digital to Analog Converter (DAC). The CPLD counts 10-MHz cycles between each 1-PPS GPS pulse, and adjusts the 10-MHz oscillator speed accordingly. The 10-MHz clock is then divided down to obtain the 100-kHz sampling clock, so maintaining an exact frequency of the 10-MHz clock drives the generation of an accurate 100-kHz sampling clock. Without the use of a feedback system, the 10-MHz clock is guaranteed accurate to 1 ppm (i.e.  $1\ \mu\text{s}$ ). A block diagram of the feedback scheme which improves this accuracy by a factor of 10–100 is shown in the top panel of Figure C.4.

At the start of each second, the 100-kHz clock is reset to force a rising edge, but the absolute timing may nominally drift over the course of the second, depending on the frequency error of the 10-MHz clock. In principle, the timing accuracy of such a system should be at least within 1 period of the 10-MHz clock (i.e. 100 ns or 0.1 ppm), since the CPLD can adjust the 10-MHz clock based on the integer number of cycles between each 1-PPS signal. However, even an error of a fractional number of samples per second of the 10-MHz clock would eventually cause it to overshoot or undershoot the number of counts within each second, so better than 100-ns accuracy should in general be achievable. Because the 10-bit DAC (i.e., 1024 states) adjusts the speed of the 10-MHz clock over a  $\pm 5$  parts per million range, an accuracy as good as  $\sim 0.01$  ppm (or 10 ns) may be achievable with this feedback system, if appropriate oscillator-adjustment schemes are chosen. By design, the timing feedback keeps the 10-MHz clock slightly slower than ideal, but the feedback scheme is designed to keep this margin as small as possible.

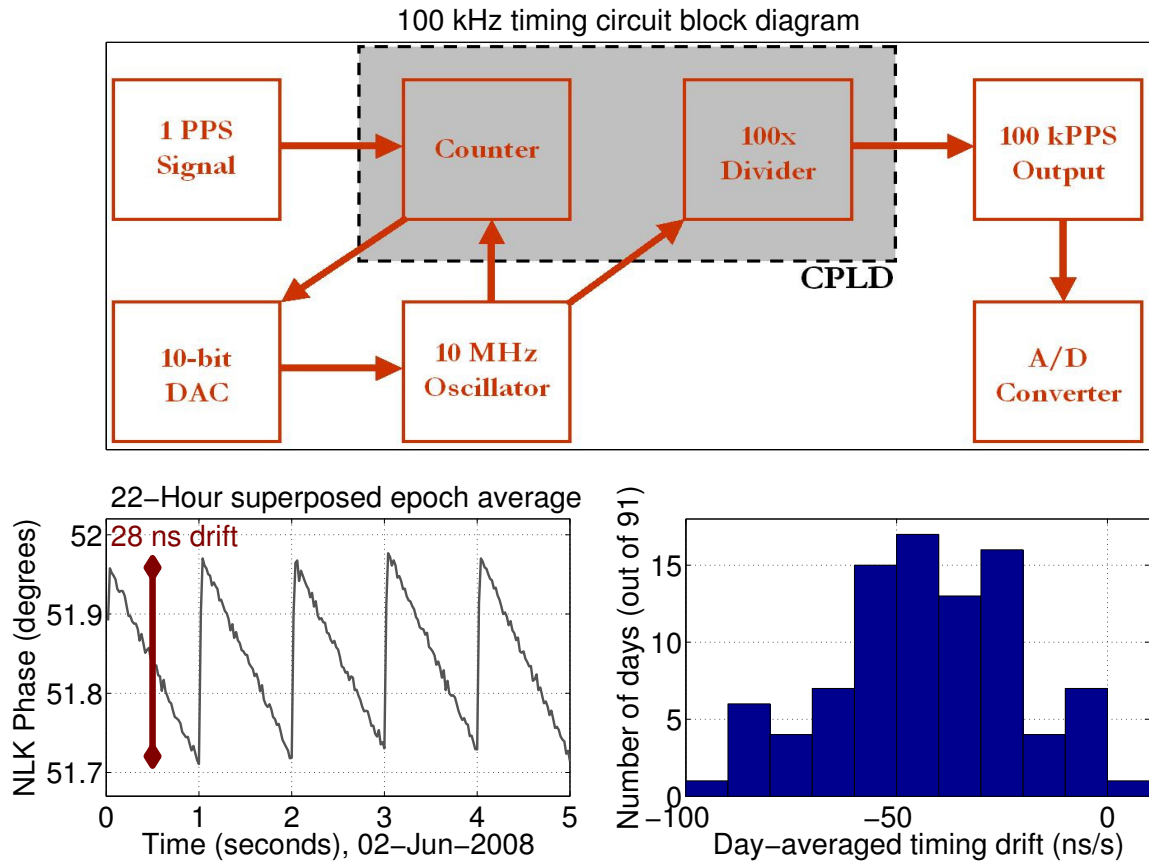


Figure C.4: AWESOME receiver timing



This drift present in practice can be quantified by monitoring the phases of VLF transmitter signals, which use extremely stable oscillators to maintain a consistent frequency for broadcast. These transmitter signals are typically modulated with a minimum shift keying (MSK) 200-baud communication scheme over a 200-Hz band. Software written at Stanford University for use with the AWESOME (and described later) is used for demodulating the MSK-related frequency variations, thereby obtaining an effective continuous wave (CW) signal with a known phase compared to GPS. Therefore, timing errors are reflected as a systematic drift in the recorded phase of these signals over the course of each second.

To detect this systematic drift, a number of consecutive periods of data can be summed up, i.e., an average epoch can be calculated by superimposing many epochs on top of each other. The bottom right panel of Figure C.4 shows a 5-second superposed epoch analysis of 23 hours of phase data from the NLK transmitter in Jim Creek, Washington, operating at one of two frequencies 24.85 kHz and 24.95 kHz, and recorded at Stanford on 02 June 2008. This result therefore represents the average of 16560 repetitions of the 5-second cycle, which makes any systematic recurrent drift evident above the general noise levels by effectively removing all variations that are not periodic at 0.2 Hz. The sawtooth variations of 1-second period clearly visible are the phase errors generated by the residual imperfection of the AWESOME's sampling clock, with the corrections occurring at the start of each second with synchronization of the sampling clock with GPS. In this case, the phase drift is  $\sim 0.2$  degrees at 24.8 kHz, corresponding to a timing error of  $\sim 28$  ns, or an accuracy of 0.028 parts per million of the 100-kHz sampling clock. The same test was repeated for 91 days from April through July, 2008 when both the NLK transmitter and AWESOME ELF/VLF receiver operated continuously, and the distribution of these day-averaged errors are shown in the lower right panel of Figure C.4. Of the 91 days, 81% showed phase drifts below 60 ns, and none showed a phase drift above 100 ns. The averaged timing drift is  $\sim 40$  ns. These results are consistent with a systematic timing drift time-varying between 0 and 100 ns per second. Additional improvement in the timing accuracy can be achieved by increasing the speed of the 10-MHz clock.

## C.6 Cross-modulation and cross-coupling

In addition to the need for highly phase-coherent sampling, a number of VLF experimental measurements rely on ionospheric modifications induced (either directly or indirectly) by a VLF transmitter, which affect the propagation of a second VLF transmitter path through the disturbed region [Inan, 1990]. Thus, an ON-OFF signal imposed onto the first source may also be imposed in the secondary source via this nonlinear coupling. Examples of this are transmitter-induced energetic electron precipitating [Inan *et al.*, 2007a], and radio wave ionospheric heating from VLF transmitters [Rodriguez and Inan, 1994] and HF antenna arrays [Barr *et al.*, 1985b]. However, such experiments can be complicated by the possibility of cross-modulation in the receiver, if the degree of possible cross-modulation in the receiver is not properly quantified, as by Inan [1990] and Moore [2007]. In addition, cross-coupling between two channels in the receiver can also affect these experiments, and may also adversely affect magnetic direction finding using the two channels, such as is done with radio atmospherics from lightning [Wood and Inan, 2002].

Figure C.5 shows the results of a test to characterize both the cross-modulation and cross-coupling effects. A 25-kHz signal is injected into one of the receiver channels, while the second channel is left with no signal. The top panels of Figure C.5 show the spectrum of both channels, with the 25-kHz input signal clearly visible in the top left panel. We note that the sidebands of the 25-kHz signal are a product of the spectrogram windowing, and are not really present in the receiver output. The top right panel shows that the injected signal does indeed cross-couple between the two channels, but at a recorded signal level that is  $\sim 70$  dB smaller than the original signal, the rest due to a small amount of coupling, perhaps from the grounding or shared power supply sources between the two channels. The second two panels in Figure C.5 show a narrowband filter applied around 25 kHz, with a  $\pm 25$ -Hz band, in order to extract the amplitudes of both the directly injected signal, as well as the cross-coupled signal. The lower four panels of Figure C.5 show identical narrowband filter, but applied at frequencies that are 400 Hz and 3 kHz higher than the 25 kHz input signal. As the third pair of panels show, a small cross-modulation effect can be

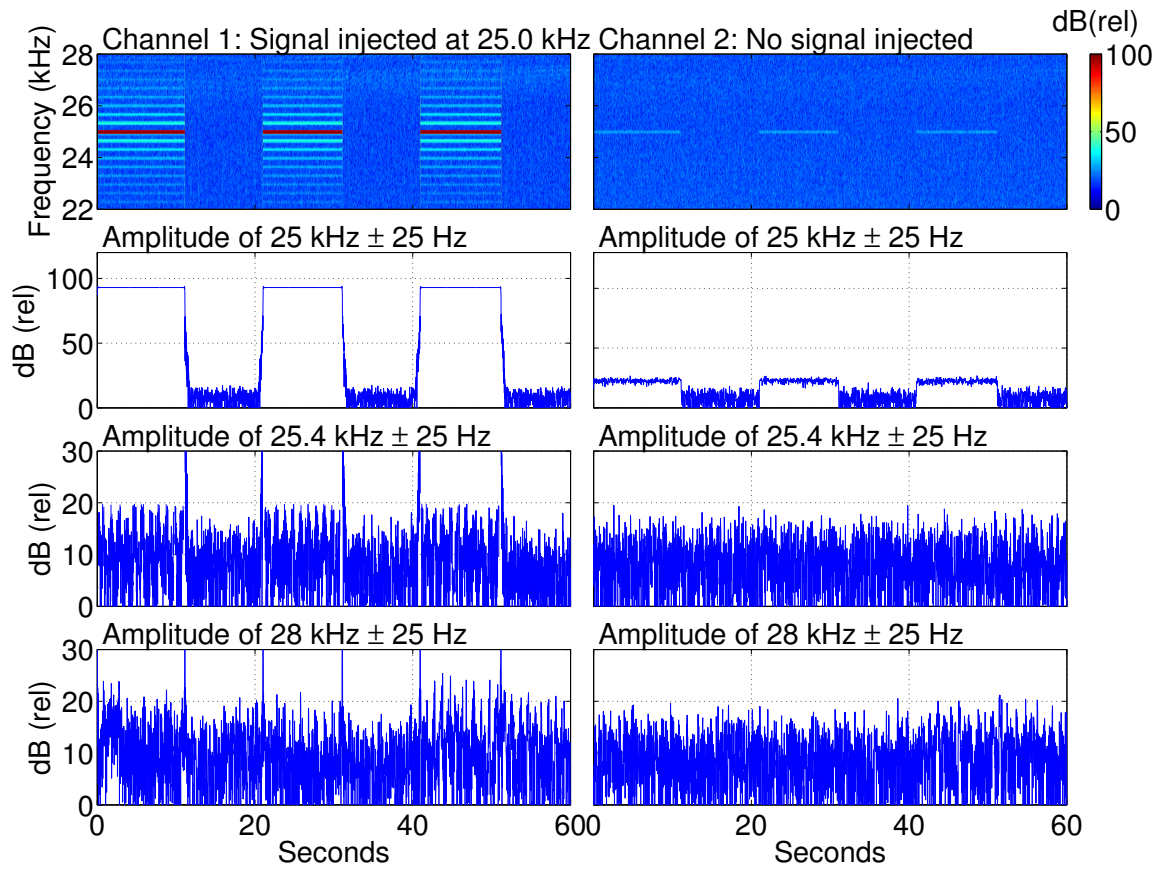


Figure C.5: Cross modulation in the AWESOME receiver

seen in the same channel as the injected signal at a frequency of 25.4 kHz, but this detected signal is again  $\sim 70$  dB smaller than the 25 kHz signal itself, and is due to the imperfections of the digital FIR filter applied. There is no cross-modulation on the other channel, and furthermore, there is no detectable cross-modulation (within at least 80 dB of the input signal) on either of the two channels at 28 kHz. Though not shown, similar tests at other frequencies yielded very similar results. The result implies that there will be no receiver-induced cross modulation between two strong signals, in particular, if one of those strong signals undergoes amplitude modulation, as in the case of VLF transmitter keying *Inan et al.* [2007a].

# Appendix D

## Power Line Interference Mitigation

Ground based measurement of ELF/VLF radio waves has long been a productive technique in the field of ionospheric and magnetospheric physics for remote detection and sensing of a variety of geophysical phenomena and structures (many of which are reviewed by *Barr et al.* [2000]) such as lightning, sprites, the ionospheric *D*-region, the Van Allen radiation belts, the effect of solar and cosmic activity on the ionosphere and magnetosphere, and electron precipitation from the radiation belts. Furthermore, due to its comparatively deep penetration into sea water, and efficient long-range propagation (attenuation rates typically a few dB/Mm [*Davies*, 1990, pg.389] following the establishment of waveguide modes in the first  $\sim 500$  km), ELF/VLF waves propagating in the so-called Earth-ionosphere waveguide have emerged as an important component of naval communications. ELF/VLF waves are also useful for geophysical prospecting [*McNeil and Labson*, 1991].

The natural ELF/VLF radio environment on the Earth is dominated by the presence of so-called radio atmospherics [*Chrissan and Fraser-Smith*, 1996], or ‘sferics’, impulsive ( $\sim 1$  ms) broadband radiation originating from lightning strokes even at global distances from a given receiver. Typical sferic amplitudes are 1–100 picoteslas. Other natural ELF/VLF signals detected on the ground such as chorus [*Gołkowski and Inan*, 2008], hiss [*Hayakawa and Sazhin*, 1992], and whistlers [*Helliwell*, 1965], are often present with substantially smaller amplitudes ( $< 1$  pT). The root-mean-square average spectral density of natural ELF/VLF noise is typically between 1–100

$fT/\sqrt{Hz}$  in this frequency range [Chrissan and Fraser-Smith, 1996]. Signals can also be generated artificially via High Frequency (HF, 3-10 MHz) heating of the auroral lower ionosphere, with amplitudes as strong as several pT [Cohen *et al.*, 2008a] or greater.

The electromagnetic interference from power lines, or ‘hum’, can often be significantly stronger. Power transmission lines are the primary method of delivering power from electric generation facilities to cities, buildings, and homes, and can be routed overhead or underground. Underground power lines generally emit weaker electromagnetic fields, since the individual wires can be placed closer together, but are typically only used in densely populated areas due to higher costs of installation and maintenance. The voltage of power transmission lines vary from a few hundred volts to hundreds of kV, depending on the age of the line and the amount of power being carried, and the voltages typically alternated at 50 Hz or 60 Hz. The non-monochromatic nature of these signals generate harmonics of this fundamental which can extend to many kHz.

The UK National Grid EMF Information site <http://www.emfs.info> has made available quantitative measurements of both electric and magnetic fields for a wide variety of different power lines as far as 100-m distance. For instance, even a low-power 11-kV line (generally used for <500 Amp or <5.5 MW), will typically generate ‘hum’ magnetic fields at 100-m distance of between 2000 and 90,000 pT, depending on the structure and loading of the line, i.e., orders of magnitude stronger than typical natural ELF/VLF signals. Being dominated by near-field energy from power lines, these fields may attenuate with distance as  $\frac{1}{r^n}$  (where  $n$  lies between 1 and 3 depending on the type of line and the conductivity of the ground). Assuming  $1/r^3$  attenuation, the 2000 pT magnetic field value at 100 m distance would be 2 pT at 1 km distance, so even low-power lines at km distances can represent a very substantial source of interference when compared to typical natural ELF/VLF sources.

Even though most of the power in the ‘hum’ may be at the fundamental frequency, for ELF/VLF radio science applications we must take into account the higher harmonics, which have varying relative amplitudes and phases and interfere with natural

signals in the ELF/VLF frequency range. The time-varying nature of the fundamental frequency is also very important. Drifts in the fundamental frequency are part of generator and power plant design, effectively acting as a feedback mechanism for multiple generators to be connected to the same power grid, and for those generators to respond to changing loads on the power line. These drifts can be very significant. For instance, a drift of  $\pm 0.1$  Hz in the fundamental frequency (a reasonable amount, as will be shown later) implies that the 100th harmonic (at  $\sim 6000$  Hz) changes by  $\pm 10$  Hz. A static notch filter at 6000 Hz would therefore require at least  $\pm 10$ -Hz bandwidth to consistently remove the 100th harmonic. A series of notch filters, with  $\pm 10$ -Hz bandwidth could be used, but when these filters are spaced out by 60 Hz, a substantial fraction (at best  $1/3$ ) of the total power is removed, and the natural ELF/VLF signal is therefore distorted. Additionally, coherent subtraction of a constant-frequency sinusoid would be less accurate, as the interference signal effectively has a finite bandwidth due to the frequency drift, which cannot be captured by a sinusoid. Adaptive response to changing power-line characteristics may be particularly important for ELF/VLF magnetic field measurements, since the magnetic field interference may vary substantially as the load (and thus the current) in the power-line changes (whereas the electric field interference may be more steady since the voltage on the power line is more or less constant). It may also be more important for smaller power grids (like more remote areas), for which fewer loads are present on the power line at a given time, and fluctuations may be quicker and more pronounced.

Let us assume that the ELF/VLF data record,  $x$ , is at least several power line periods long, and the power-line interference is quasi-periodic nature, i.e., consisting of a fundamental frequency with harmonics at exactly integer multiples at any given time. The filtering is achieved by subtracting a reconstructed version of the interference signal from the original signal, i.e.,

$$x_{filtered}(t) = x_{raw}(t) - p(t) \quad (\text{D.1})$$

where  $p(t)$  is the reconstructed power-line interference signal. Our task in mitigation

of the power line signal is to estimate  $p(t)$  accurately and with computational efficiency. In this appendix, we describe two particular techniques for mitigating 50/60 Hz (and higher harmonics) interference from power lines. We discuss two techniques, one in which an adaptive filter is utilized to track the power line interference, and a second in which least squares estimation is utilized to estimate the power line signal. The former technique provides good computational efficiency and is currently capable of being implemented in a real time system (such as live spectrogram generation), whereas the latter provides slightly more accurate results and may therefore be preferred for more limited power processing applications. These techniques are also described by *Said* [2009, ch.3].

While the techniques discussed here do not diminish the benefit of a remotely located ELF/VLF antenna (where power-line interference is weak to begin with), they can greatly aid in removing moderate levels of power-line interference.

## D.1 Adaptive filtering

Adaptive filters have been used for removal of power-line interference, both for geophysical applications, and in other fields of study. As noted by *Butler and Russell* [1993], these techniques tend to fall into two categories: sinusoidal subtraction and block averaging. The first simply involves estimating the amplitude and phase of a sinusoid (at the power-line frequency), which is then subtracted from the signal. *Widrow* [1975] review adaptive noise canceling and describe a wide variety of applications, most notably, a 60-Hz subtraction algorithm designed to remove interference from electrocardiogram (ECG) signals in this manner. This algorithm noticeably reduces the interference but only at the fundamental frequency.

The so-called 'block subtraction' technique involves isolating a power-line period where only the interference is present, and subsequently subtracting this waveform repeatedly from the ensuing signal, for instance in *Furno and Tompkins* [1983], *Reising* [1998, pg.41] and *Cummer* [1997, pg.85]. Although this technique intrinsically adapts to the complete harmonic structure of the 60-Hz interference, it relies on manually finding a suitable 'interference-only' power-line period, and still assumes that the



power-line signal does not change noticeably in time. However, in using only one block to estimate this power-line signal, it is invariably susceptible to noise (impulsive and Gaussian) being copied over with every block subtraction. On the other hand, block subtraction requires very simple computations.

An adaptive filter can also be achieved with hardware. For instance, *E. W. Paschal* and *M. Trimpi* are known to have designed and implemented a hardware-based system in which a periodically-averaged 60-Hz waveform is built and then subtracted from the incoming signal as it arrives into the input of an ELF/VLF receiver. A variable delay in the phasing of the subtraction also accounts to some extent for drifting of the fundamental frequency [*E. W. Paschal*, personal communication]. This latter design bears several similarities with the techniques described here, in that it is also able to track and subtract the complete harmonic content of the power-line interference.

### D.1.1 Theory

Under the adaptive filtering approach,  $p(t)$  is calculated via a convolution of the input signal with an impulse train, i.e.,

$$p(t) = x_{in}(t) * I(t) \quad (\text{D.2})$$

We note that depending on the characteristics of the power-line interference,  $x_{in}$  may be the same as  $x_{raw}(t)$ , or may be after subjecting the signal to low-pass-filtering, as will be described later.  $I(t)$  is an impulse train computed as follows

$$I(t) = \frac{\sum_{m=1}^{\infty} e^{-\frac{m}{af_o}} \left( \delta\left(t - \frac{m}{f_o(t)}\right) + \delta\left(t + \frac{m}{f_o(t)}\right) \right)}{2 \sum_{m=1}^{\infty} e^{-\frac{m}{af_o(t)}}} \quad (\text{D.3})$$

We note the important fact that  $f_o$  is a function of time. The impulses in  $I(t)$  are time-separated by the time-varying fundamental ‘hum’ period and weighted with exponentially decreasing values as  $e^{-|t|/a}$ , where  $a$  is a characteristic adaptation time discussed below. Hence, the epochs further away from  $t$  become exponentially less valuable in terms of reconstructing the power-line harmonic signal. There is no impulse at  $t = 0$ , but the impulses exist for both positive and negative values of  $t$ .

Although this filter is noncausal, which implies a post-processing application, the filter could be rewritten in causal form (for application to real-time processing) by removing the second term in the numerator, and eliminating the factor of 2 in the denominator. The denominator is simply a normalization term, referred to later as  $C_1$ . Though this Equation intrinsically applies an exponential window to the data, the technique would also work with other windows (i.e., Gaussian, Hamming, etc). The frequency spectrum of  $I(t)$  can be written as

$$I(f) = \frac{1}{C_1} \sum_{m=1}^{\infty} \frac{2a}{a^2 + (2\pi a(f - mf_o))^2} \quad (\text{D.4})$$

where  $C_1$  is the normalization term equal to the denominator of Equation D.3. The impulse train therefore effectively defines a series of notch filters at harmonic multiples of the fundamental period  $1/f_o$ . The depth and bandwidth characteristics of these filters are a function of  $a$ . Equations D.2 and D.3 can be combined as follows

$$p(t) = \frac{1}{C_1} \sum_{m=1}^{\infty} e^{-m/af_o} (x_{in}(t - m/f_o) + x_{in}(t + m/f_o)) \quad (\text{D.5})$$

In practice, since the summations in Equations (D.4) and (D.5) cannot be computed up to infinity, the summation index  $m$  is limited by a value  $M$  such that  $e^{-\frac{M}{af_o}}$  is sufficiently small (e.g. 10%) for the limited summation to approximate the infinite sum closely enough.

The fundamental frequency,  $f_o$ , may significantly vary on time scales of seconds, and must therefore be explicitly calculated as follows.

$$\Phi_k(t) = \text{arc}([x_{in}(t)e^{-j2\pi kf_{nom}t}] * w(-t)) \quad (\text{D.6})$$

We first demodulate the signal with a series of complex exponentials, with frequencies at several integer multiples  $k$  of the nominal power-line frequency  $f_{nom}$  (either 50 or 60 Hz). The values of  $k$  are chosen empirically and discussed in the next section. After multiplying the data with a chosen function  $w(t)$ , the time-varying argument (or phase) for each  $k$  value is calculated. For each phase signal  $\Phi_k(t)$  calculated at separate harmonics, the estimated fundamental frequency (relative to 50 or 60 Hz)

as a function of time is then simply the derivative of this phase with respect to time.

$$f_{o_k}(t) = \frac{1}{k} \frac{d\Phi_k(t)}{dt} + f_{nom} \quad (\text{D.7})$$

Each phase signal  $\Phi_k(t)$  yields an independent estimate of the frequency variations. These separate estimates, each of which are affected by the noise content, are then linearly combined, but must be weighted so that the noisier signals have less influence on the final frequency estimate.

$$f_{est}(t) = \frac{\sum_k \frac{f_{o_k}(t)}{W_k}}{\sum_k W_k} \quad (\text{D.8})$$

The weights are determined by

$$W_k(t) = \left( \sum_t (f_{o_k}(t) - \overline{f_{o_k}}(t))^2 \right)^{-1} \quad (\text{D.9})$$

i.e., inverse of the standard deviation of each estimate with respect to the unweighted mean of the estimates  $f_{o_k}(t)$ . Finally, the frequency estimate is then convolved with an exponential function with characteristic decay time  $b$  in order to remove rapid variations in the frequency estimate which result from lower signal-to-noise ratio (such as what may occur in the presence of a strong sferic):

$$f_o(t) = f_{est}(t) * e^{-\frac{|t|}{b}} \quad (\text{D.10})$$

We note that this last Equation applies an exponential window to the data, though the technique would also work with other types of windows (i.e., Gaussian, Hamming, etc). The estimated frequency signal  $f_o(t)$  is then used for the adaptive filtering described above, in Equation D.3.

### D.1.2 Implementation

We now describe the implementation of this adaptive 60-Hz (or equivalently 50-Hz) filtering technique and discuss its applications, with the following steps:

- (1) Step through the raw data in overlapping segments (in this case, 50% overlap is

used), applying Equation D.6 to each step, and then calculating the frequency of each segment from Equation D.7. Values of  $k$  are chosen here to be 1,3,5,7,9,11,13, since the first seven odd harmonics of 60 Hz are found empirically to show the highest signal-to-noise ratio (even harmonics are typically much weaker), though different power-line or receiver characteristics may require different choices of  $k$ . For this step,  $w(t)$  is chosen to be a Hamming function. The applied discrete-time version of the Equation D.6 can be thought of as a downsampled version of a short time Fourier transform or time-dependent Fourier transform [Oppenheim *et al.*, 1990, pg.714] filterbank technique.

(2) Combine the various frequency estimates utilizing Equation D.8, and then apply Equation D.10 utilizing a suitable selection of  $b$ , i.e., of a timescale sufficiently fast so that variations in the fundamental frequency can be effectively included.

(3) Apply Equation D.10 to the result of step (2).

(4) The reconstructed signal in Equation D.2 is determined from the filter in Equation D.3, taking  $t = 0$  to be the center of the segment, and frequency  $f_o$  inferred from interpolation of  $f_o$  (so that each segment may be of varying length based on the calculated time-varying frequency).

(5) The reconstructed interference signal is then subtracted from the signal as per Equation D.1.

We note that the impulse separation length that would be needed for Step 3 is in general not an integer number of samples. For sampling frequencies  $f_s$  substantially higher than the highest ‘hum’ harmonic, however, the segment length  $f_s/f_o(t)$  can be rounded to the nearest integer and the resulting error is found not to impact the results substantially for the examples shown in this paper (where  $f_s=100$  kHz, and the power-line harmonics are confined below  $\sim 10$  kHz). For sampling frequencies not substantially higher than the maximum power-line harmonic, interpolation may be required so that this rounding error does not significantly impact the results.

The characteristic adaptation times  $a$  and  $b$  account for the variation in the power-line harmonic content and power-line fundamental frequency, respectively, which can occur in particular as the loading on the power lines changes. Smaller lines with less stable loading would likely require shorter adaptation times, allowing the filter to adapt more quickly. On the other hand, shorter adaptation times decrease the

number of epochs effectively included in Equation D.3, thereby increasing the bandwidth of signal that is subtracted and possibly including portions of ‘real’ ELF/VLF data. Shorter adaptation times also intrinsically introduce more uncertainty into the frequency calculation, which can adversely affect the quality of the subtraction technique.

Figure D.1 illustrates the method of frequency tracking and the proper selection of  $b$ . Utilizing the phase-demodulation step, the frequency of the first seven odd harmonics of 60 Hz are separately tracked, each of which shows a similar frequency-time pattern superposed onto noise. The frequency variation of each harmonic implies a variation in the fundamental frequency (after simply dividing by the harmonic number), so in essence we have seven separate estimates of the time-varying fundamental frequency. Using Equation D.8, these observations are linearly averaged to form the best estimate of the power-line frequency. In this case, the 7th and 11th harmonics can be observed to have the cleanest measurements of the frequency, and therefore are more heavily weighted. The lower right plot of Figure D.1 shows the linear sum, which has remarkably low variability despite having excellent (60-Hz) time resolution. In this particular case, the power-line harmonic can be seen to vary by as much as  $\sim 0.2$  Hz on time scales of several seconds, so a value of  $b$  below  $\sim 1$  s will be necessary to achieve adequate frequency tracking.

Figure D.2 shows an example of the effect on the post-filtered spectrum by the selection of  $a$  and  $b$ . Shown are the 42nd and 43rd harmonics of 60-Hz, for each of two selections of  $a$  and  $b$ . The red curves indicate the raw (unfiltered) spectrum (estimated using Welch’s method), with the blue curves showing the result after subtraction. For the case  $b = \infty$ , the fundamental frequency is forced to be a constant in time. By comparing the two left-hand plots to the two right-hand plots, it can be clearly seen that the quality of the subtraction dramatically improves when the frequency tracking is utilized rather than when the subtraction is carried out simply with a constant value for the ‘hum’ frequency. In addition, comparing the two right-hand plots (where the frequency-tracking is adequately employed), we see that the choice of  $a$  too high leaves a significant amount of ‘hum’ interference present, whereas a choice of  $a$  too low in fact subtracts too much of the power content, leading to a ‘well’ (i.e., a depression)

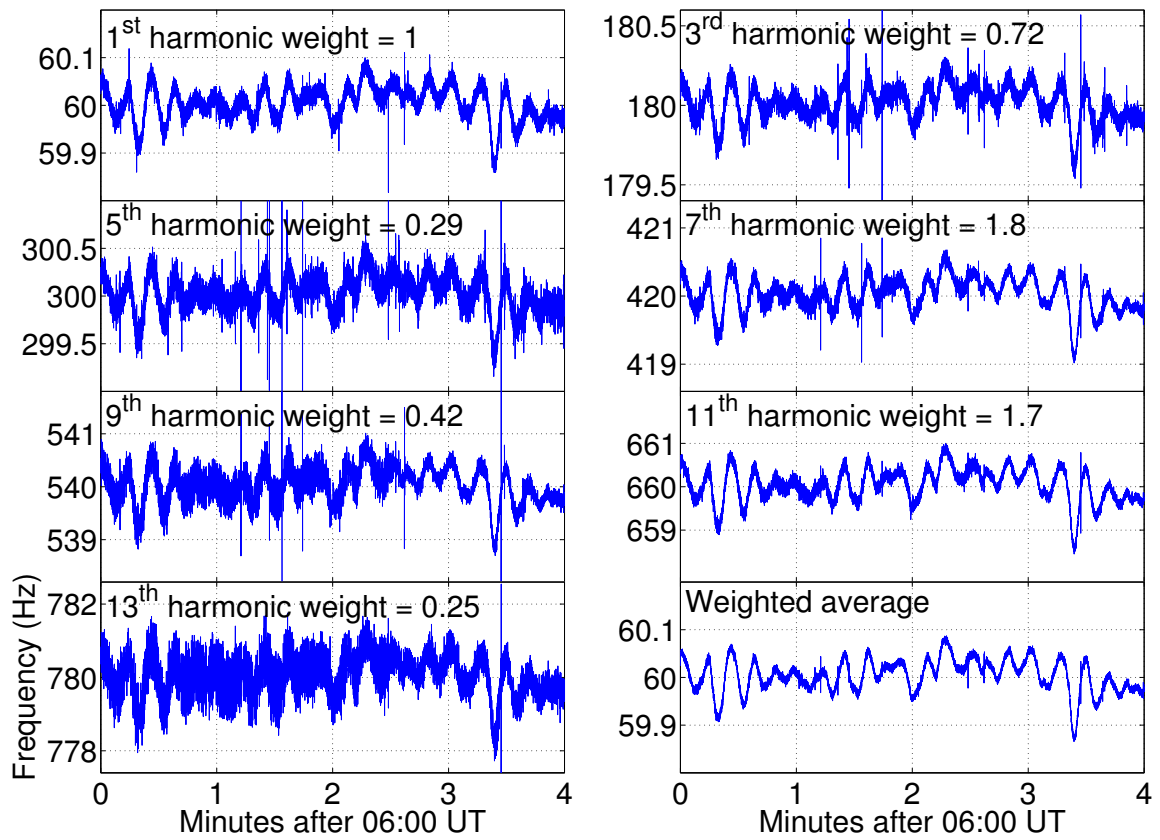


Figure D.1: Power-line frequency tracking

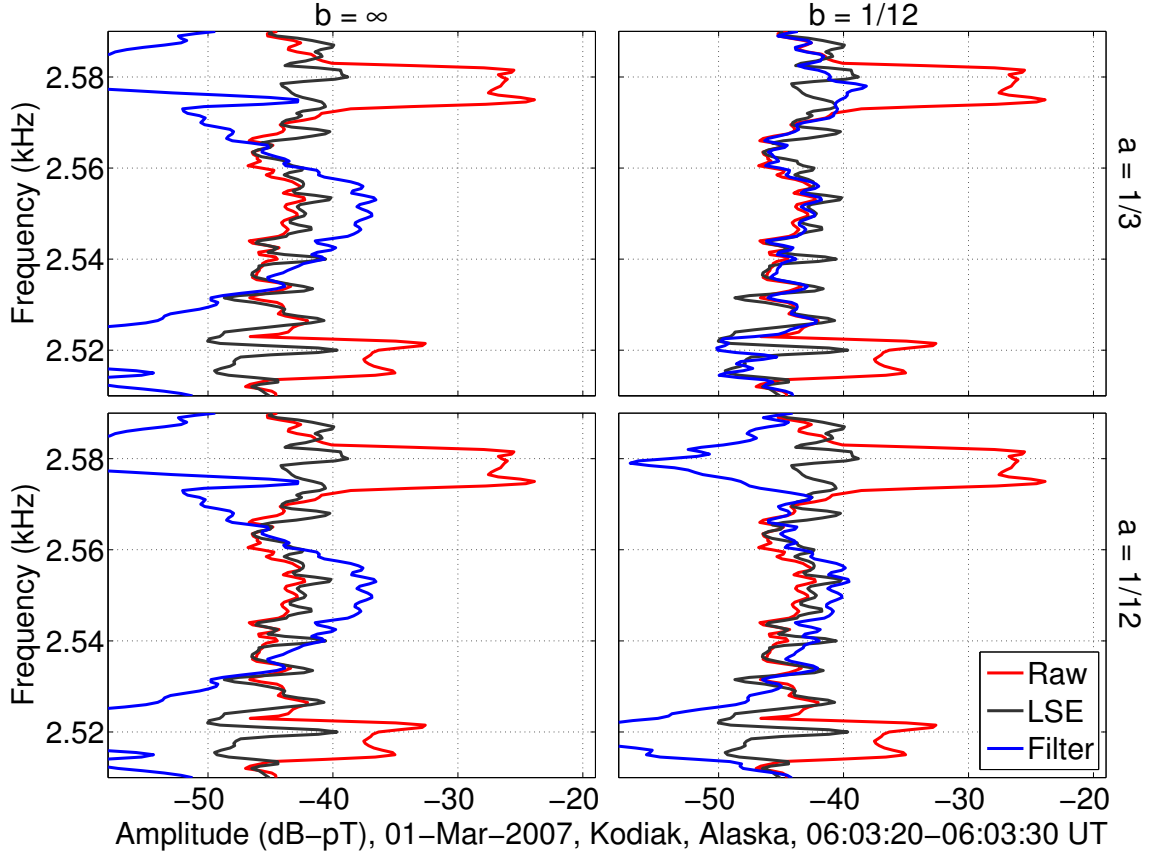
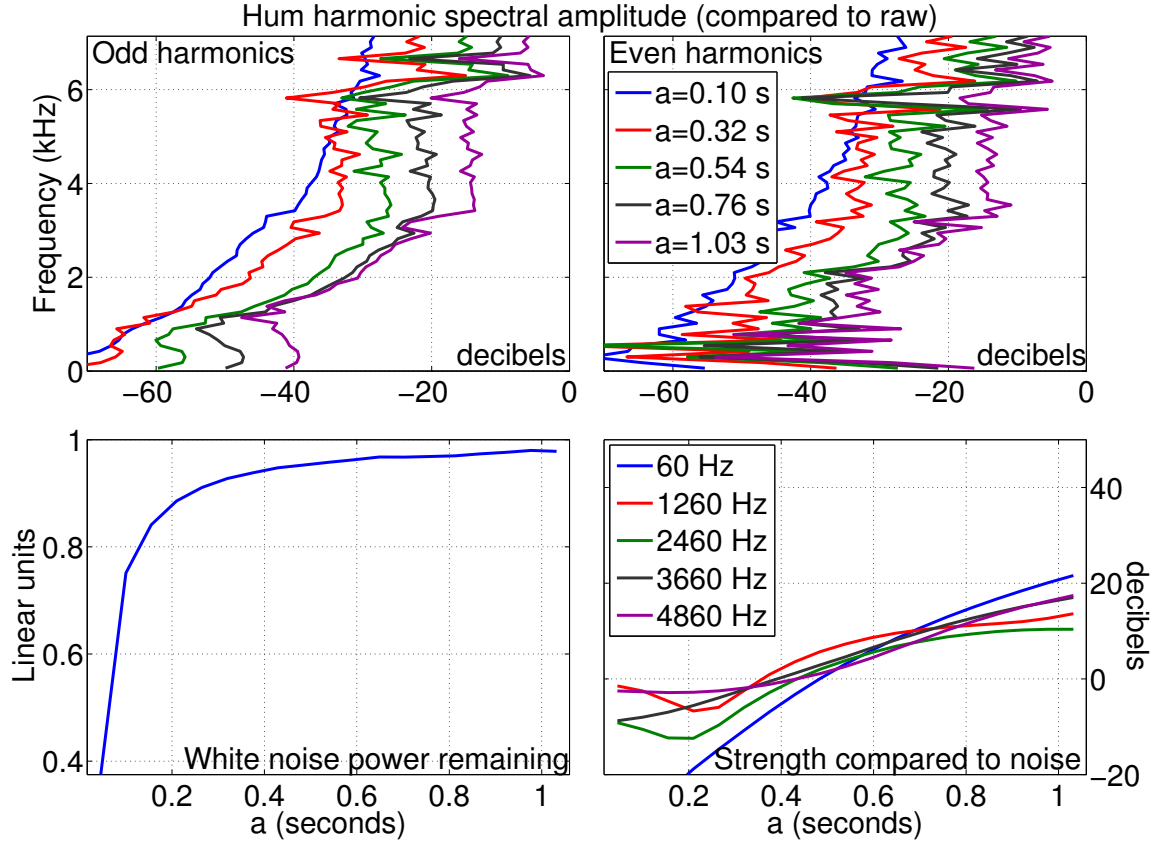


Figure D.2: Spectrum of ELF/VLF data as  $a$  and  $b$  parameters are varied

in the spectrum. The well is particularly strong on the 42nd harmonic, which is  $\sim 10$  dB weaker than the 43rd harmonic.

The varying characteristics of the filtered data as a function of  $a$  (given a sufficiently low value of  $b = 1$  second) are shown in Figure D.3. The top two plots show a measure of the strength of the harmonics after subtraction, compared to the strength of the harmonic in the raw data, as a function also of frequency. The two plots show the even and odd harmonics separately, since the odd harmonics are in general much stronger. In these plots, 0-dB indicates that the subtraction algorithm has not reduced the strength of the ‘hum’ harmonic at that frequency. Both plots show that as the  $a$  parameter is reduced, the magnitude of the spectrum begins to drop further below the magnitudes in the raw data. In particular, the lower values

Figure D.3: Variations of  $a$  parameter

of  $a$  have a particularly dramatic effect on the highest harmonics, whereas removal of the lowest harmonics is comparatively easier, and can be achieved with larger values of  $a$ . The same effect can be seen for both the odd and even harmonics, although the threshold value of  $a$  where the subtraction is adequately effective appears to be different for the two, since the even harmonics are  $\sim 10$  dB weaker.

As shown by the ‘well’ in Figure D.2, a choice of  $a$  too low removes too much power, thereby introducing too much distortion into real ELF/VLF data. To illustrate this effect, the same filter used to derive the subtraction in the upper plots is also applied to white noise, and the amount of power remaining, as a function of  $a$ , is shown in the bottom left panel of Figure D.3. For instance, for  $a = 0.1$  seconds,  $\sim 20\%$  of the power in the entire spectrum is removed, indicating that the real power of ELF/VLF



content is correspondingly reduced.

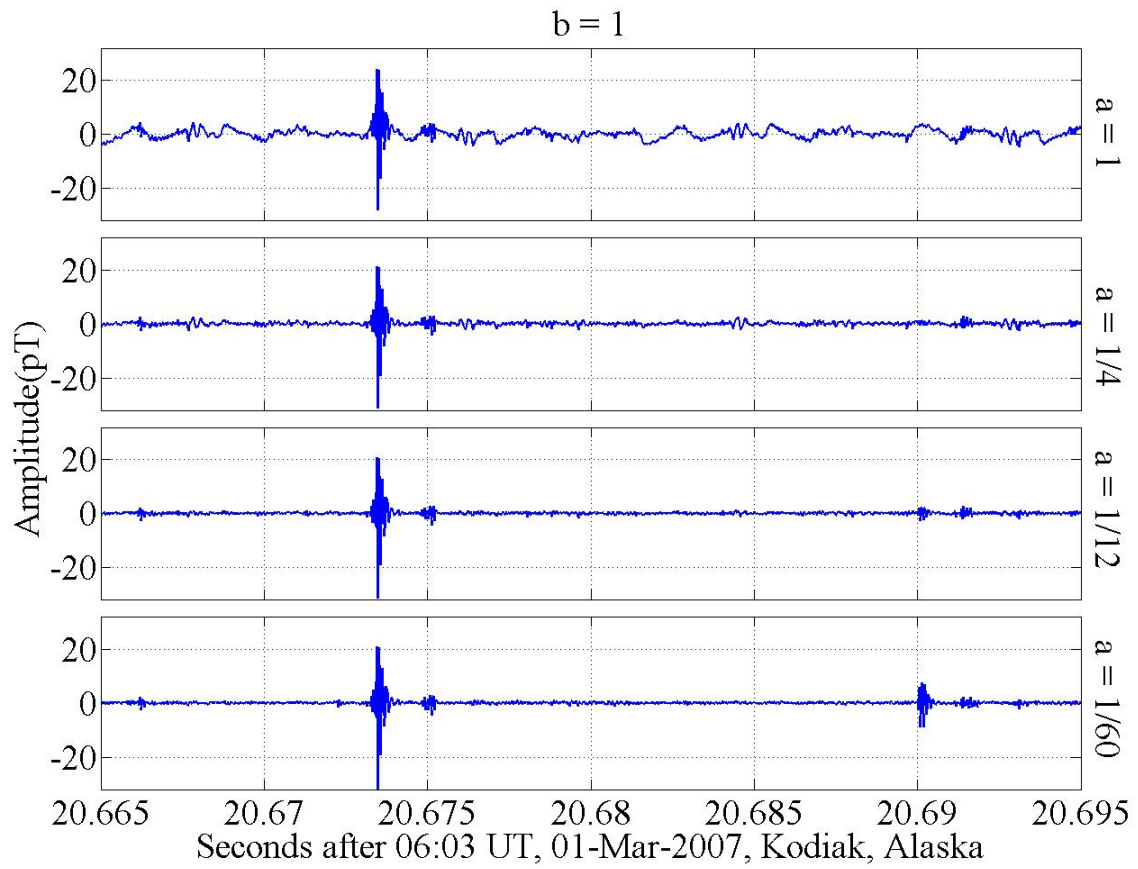
Figure D.3, bottom right panel, shows the strength of four chosen power-line harmonics compared to an estimate of the noise floor, again as a function of  $a$ . An ideal choice of  $a$  would subtract sufficiently from the power-line spectrum so as to reduce the harmonic amplitudes approximately to the noise floor, or 0 dB. For this particular case, values of  $a$  in the 0.2–0.4 s range appear to be most appropriate. It is also apparent that the differing harmonics exhibit different characteristics as the value of  $a$  varies, so that the choice of  $a$  may also be dependent on frequency.

In addition, a choice of  $a$  too low creates parasitic repetitions of various features in the data, since the number of periods effectively included in the averaging (reflected by  $C_1$ ) becomes very small. In Figure D.4, a small 30-ms segment of data is shown from Kodiak, Alaska, in which a radio atmospheric is clearly present at  $\sim 06:03:20.674$ . A parasitic sferic can be seen to appear at  $\sim 20.691$  seconds, for  $a = 1/12$ , stronger still for  $a = \frac{1}{60}$ . This parasitic signal is simply a repetition of the larger sferic, but occurs  $\sim 17$  ms (or one period of 60 Hz) later, as a result of the subtraction. This effect can be mitigated by applying a zero-phase low-pass filter to  $x_{raw}$  in order to form  $x_{in}$ . If the power-line harmonics only contain significant power up to a frequency  $f_1$ , then only the frequency content below  $f_1$  needs to be included in the reconstruction. The reconstructed signal with only frequency content below  $f_1$  can still be coherently subtracted from the unfiltered raw signal if a zero-phase low-pass filter had been employed.

Utilizing the aforementioned methods, it may also be possible to determine  $a$  and  $b$  automatically and dynamically, so that this filtering technique can be very generally applied in a real-time system, or also without a-priori investigation or assessment of the power-line characteristics. Computation time for this algorithm is determined to be easily short enough for real-time operation.

## D.2 Least squares estimation

A second possible method of estimating the power-line interference comes from least-squares estimation. Assume that for a given length of data, the power line frequency

Figure D.4: Time series data for varying values of  $a$

$f_o$  is constant. In this case, the interference signal  $p(t)$  can be written in terms of a sum of individual harmonic components, from the following equation

$$p(t) = \sum_K^{k=1} (A_k \cos(2\pi f_o kt) B_k \sin(2\pi f_o kt)) \quad (\text{D.11})$$

where  $A_k$  and  $B_k$  are real coefficients which indicate the sin and cosine components of the power line interference at the  $k$ th harmonic, assuming the power line signal has  $K$  harmonics that need to be subtracted.

To setup our least squares problem, we rewrite D.11 as a matrix equation, or

$$p(t) = PY(t) \quad (\text{D.12})$$

where  $P$  is a  $2K \times 1$  matrix, containing the sine and cosine coefficients, as follows

$$P = \begin{bmatrix} A_1 \\ A_2 \\ \vdots \\ A_K \\ B_1 \\ B_2 \\ \vdots \\ B_K \end{bmatrix} \quad (\text{D.13})$$

and  $Y(t)$  is a  $K \times T$  matrix (where  $T$  is the length of data being estimated) defined with rows containing sine and cosine functions, as follows

$$Y(t) = \begin{bmatrix} \cos(2\pi f_o t) \\ \cos(4\pi f_o t) \\ \vdots \\ \cos(2K\pi f_o t) \\ \sin(2\pi f_o t) \\ \sin(4\pi f_o t) \\ \vdots \\ \sin(2K\pi f_o t) \end{bmatrix} \quad (\text{D.14})$$

We can now rewrite our ELF/VLF data as

$$x(t) = PY(t) + n(t) \quad (\text{D.15})$$

where  $n(t)$  includes everything else in the ELF/VLF data (natural ELF/VLF signals, VLF transmitters, and other local interference sources) which, for the purposes of this estimation problem, is noise. Our task is estimating  $Y(t)$  given knowledge of  $x(t)$ , a linear operator, and additive noise. For cases where  $n(t)$  is white Gaussian, the optimal mathematical solution is well known, and is given by

$$Y_{\text{est}} = (P^T P)^{-1} P^T x \quad (\text{D.16})$$

Unfortunately, Equation D.16 is really a nonlinear matrix equation, because  $f_o$  is not immediately known. So we apply Equation D.16 and search for a value of  $f_o$  which minimizes the residual error, or

$$E_{\text{Res}} = (Y_{\text{est}} - Y)(Y_{\text{est}} - Y)^T \quad (\text{D.17})$$

Once the value of  $f_o$  which minimizes  $E_{\text{Res}}$  is found, the solution of  $Y_{\text{est}}$  is considered optimal, and  $p(t)$  is now fully specified.

The number of harmonics  $K$  can be arbitrarily specified, they need not be a consecutive series of integers, but they can simply contain the strongest harmonics of the power line. For instance, in the presence of natural noise which obscures the

power line signals below  $\sim 1$  kHz, the values of  $k$  can be chosen to include only higher-order harmonics of 50/60 Hz, those above 1 kHz.

Due to the fact that nonlinear estimation via least squares requires a matrix inversion, as well as repetition of the linear optimization to find the correct frequency, this technique is in practice much more computationally intensive, and cannot in its current form be used for real-time data processing.

### D.3 Examples

Figure D.5 shows the results of the two subtraction algorithms applied to a 10-second record of ELF/VLF data taken from Valdez, Alaska ( $61.06^\circ$  N,  $146.02^\circ$  W). In both panels, the first 10-second period show unfiltered data, the second 10-second period shows data after adaptive filtering (with  $a = b = 1/3$  s), and the third 10-second period shows data after least-squares power-line estimation.

The left hand panels shows an example of chorus emissions, which can be seen as a series of brief  $\sim 1$  second long rising emissions. Although the chorus elements are barely visible in the raw data, they are seen to be much clearer in the post-processed data, both using the adaptive filter approach and the least-squares estimation approach. The right hand panels shows an example of ELF/VLF radiation generated with High Frequency heating of the auroral electrojet (a particular instance presented by *Cohen et al.* [2008]), utilizing the HAARP facility near Gakona, Alaska. The generated signal consists of constant-frequency tones at 2375 Hz (3 seconds), 2875 Hz (1 second), and 2175 Hz (1 second), followed by a ramp from 500 Hz to 3 kHz (5 seconds). The signal-to-noise ratio of both tones and ramps is much larger for the post-processed cases.

The top two panels show the effect of each technique in a visual spectrogram. In this presentation, the difference between the adaptive filter technique and the least-squares estimation technique is barely noticable, as both seem to do an adequate job at removing the power-line interference.

However, close examination of the spectrum begins to indicate some discernable differences between the two techniques. The bottom panels show 10-second long

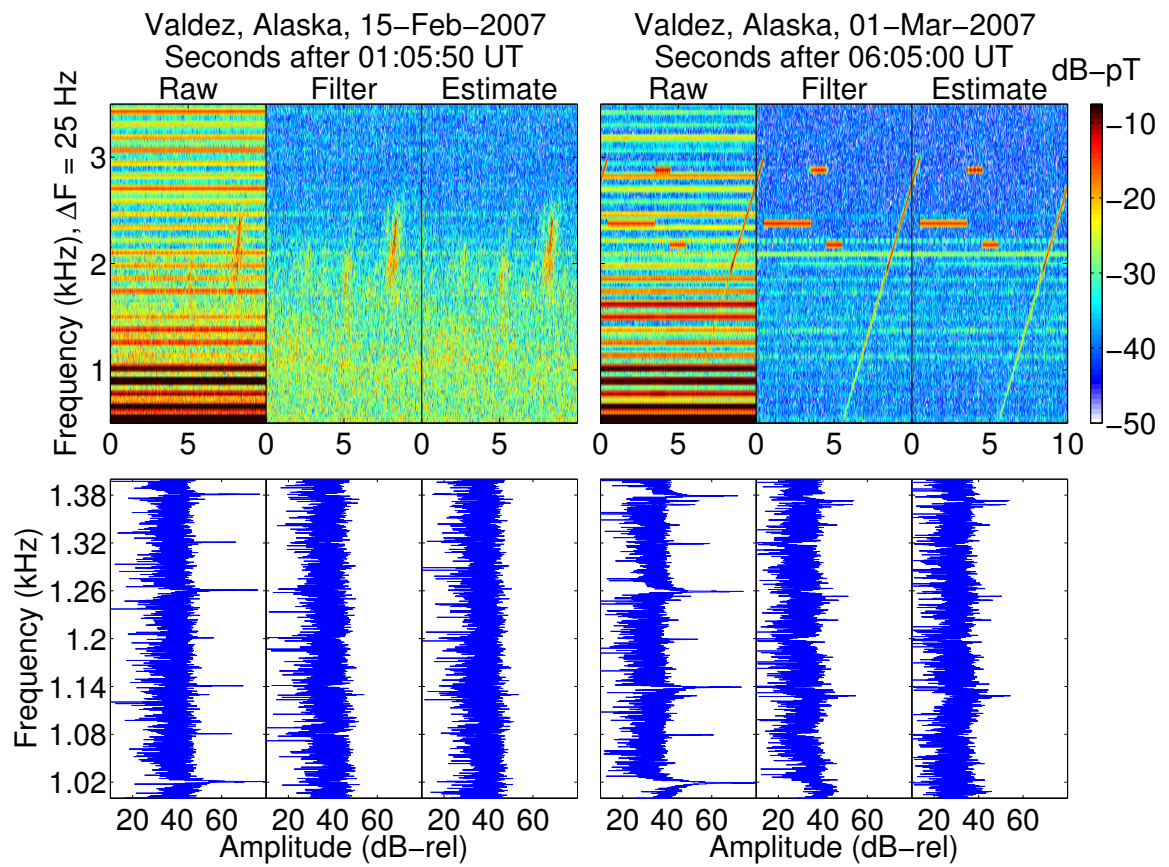


Figure D.5: Examples of power-line filtered data

Fourier transforms of the same data records in the above spectrograms, but here it is visible that the adaptive filtering technique adds some degree of a ‘well’ at the frequencies corresponding to the even harmonics of 60 Hz. On the other hand, the least-squares estimation technique does not leave such an artifact in the data, because the amplitudes of the harmonics are individually calculated.

The presence of the ramp enables us to evaluate the degree to which the subtraction algorithm removes the actual frequency content of the ramp, in essence subtracting real data long with the power line interference. In particular, if the subtraction algorithm removed substantial power from the HAARP signal, the ramp would be seen to have its frequency content modulated at frequency intervals of  $\sim 60$  Hz. However, the ramp in Figure D.5 does not demonstrate such a deleterious effect for the least-squares estimation technique, while the adaptive filter technique does generate some amount of 60 Hz modulation on top of the ramp, due to more imperfect subtraction.

It should be noted that the least squares technique shown here takes 10–100 times longer to compute, depending on the parameters chosen for the least-squares harmonic (and the number of harmonics used to estimate the frequency). Currently, a standard computer processes a minute of data using the adaptive filter technique in approximately 1s, whereas the least squares technique takes on the order of a minute. So although the advantage of the least-squares technique is visible for long integrations or very careful examinations of the frequency content of a given ELF/VLF record, it is likely not worth the benefit for any low-resolution plotting, such as spectrograms. This fact makes the adaptive filter sufficiently useful for live data processing, such as line spectrogram generation which occurs during many particular times of experimentation with HAARP.

# Appendix E

## ON/OFF Duty Cycle Observations

In Chapter 5, we discussed the role of duty cycle (percentage of time during which heating occurs, as opposed to recovery) in the HF heating experiments described in Chapter 3. In the duty cycle discussion, we focused in particular on the strength of the fundamental frequency as the duty cycle is varied, since this is the quantity that can be directly compared to our observations of geometric modulation and beam painting.

However, some additional information on the nature of the generation process can be derived by looking at the higher harmonics of the signal. Harmonic content of generated ELF/VLF signals from HF heating has been discussed by a number of workers, as is detailed in Chapter 1. However, it is worth highlighting that *Barr et al.* [1999] found that different harmonics (particularly, the odd and even ones) are sourced at different altitudes. It is also worth noting that for square wave amplitude modulation as is utilized here, the HAARP-generated HF signal has harmonic content at every odd number, so that the third harmonic signal received is in part from the component of the HAARP HF signal at the third harmonic of the fundamental frequency. On the other hand, the second harmonic of the fundamental frequency is almost entirely ionospherically generated, resulting from the nonlinear conversion from HF power modulation envelope to ionospheric conductivity modulation (although the HAARP HF signal is not a perfect square wave, so it does contain some small second harmonic content).



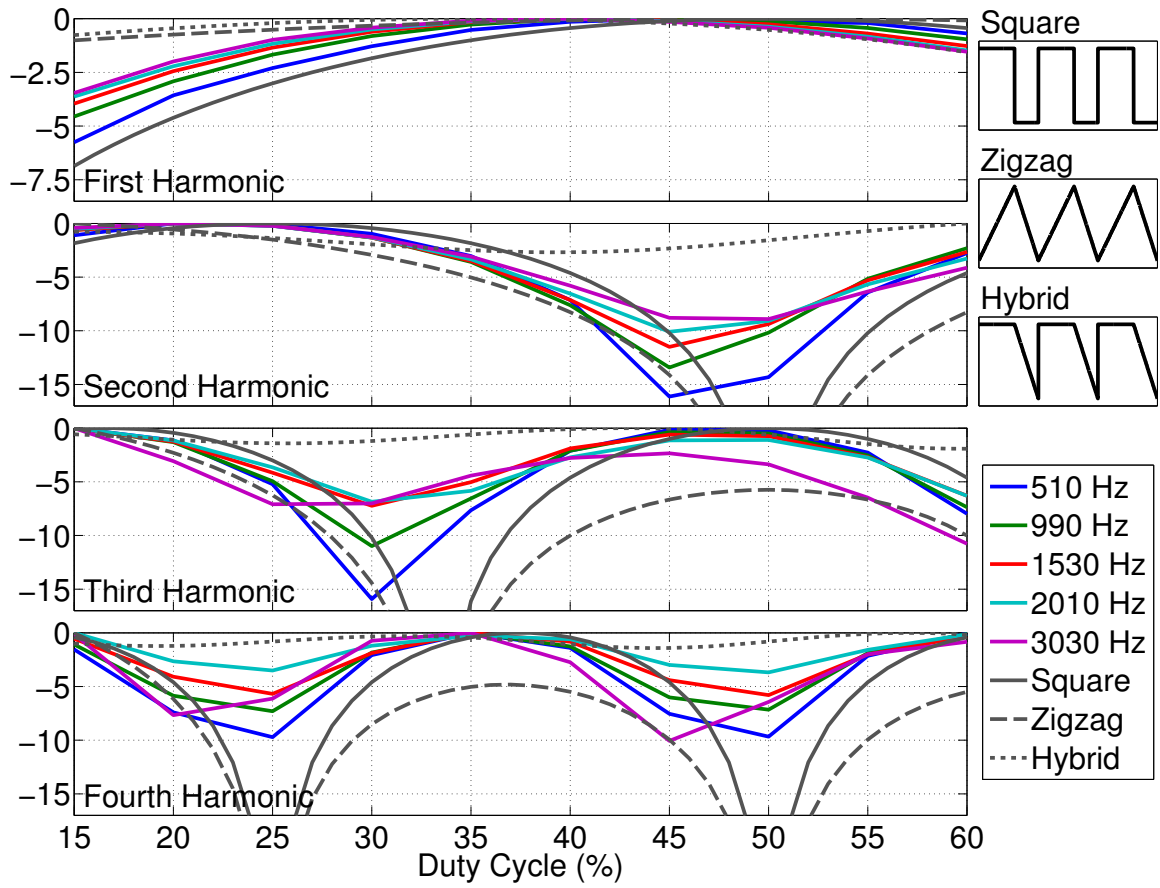


Figure E.1: Amplitudes of generated ELF waves as a function of duty cycle

Figure E.1 shows the amplitude of the first four harmonics received at Chistochina, as a function of square wave duty cycle, for the same duty experiment discussed in Chapter 5 (so the top plot is a reproduction of the top panel of Figure 5.3). The higher harmonics are not reliably detected at Kodiak or Juneau, so we show here only data from the nearby receiver.

In addition to the experimental data, the analytical harmonic content of three generic waveforms are shown with the gray lines. The top right corner of Figure E.1 shows schematically the shape of these waveforms. The square wave has an instantaneous change between 0 and 1 at both the OFF-ON and ON-OFF transitions. This waveform would more represent the conductivity modulation in the ionosphere if both the heating rate and cooling rate were significantly faster than the time scale of the modulation frequency (like, for instance, low  $D$  region altitudes). The zigzag wave assumes a linear variation between 0 and 1, rising at a constant rate during the ON portion, and falling at a constant (but separate) rate during the OFF portion. This waveform is appropriate if the heating and cooling rates are significantly slower than the time scale of the modulation frequency, such as is the case at the high  $D$  region altitudes considered here. Finally, the hybrid wave implies an instantaneous rise, but a linear-rate fall, which would be most representative of conductivity changes when the heating rate occurs much faster than the modulation frequency, but the cooling rate occurs much slower, such as for very high-ERP heating at medium  $D$  region altitudes. Comparing the observed variations to the analytical curves may therefore yield some additional information about the source region.

It is straightforward to convert the received amplitudes at Chistochina to an efficiency measure, since the HF power utilized by HAARP is proportional to the duty cycle. These results are shown in Figure E.2.

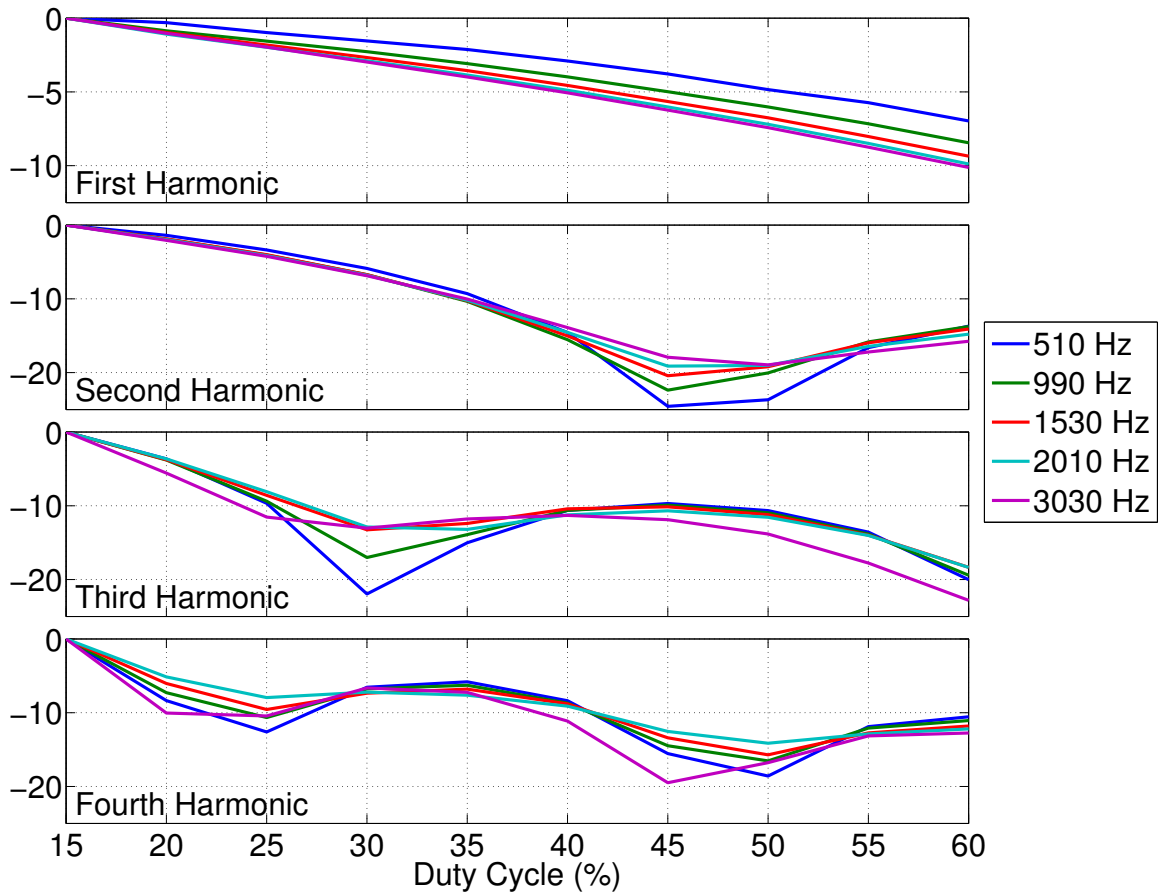


Figure E.2: Efficiency of generated ELF waves as a function of duty cycle

# Bibliography

- Banks, P., Collision frequencies and energy transfer: electrons, *Planet. Space Sci.*, *14*, 1085–1103, 1966.
- Barr, R., and P. Stubbe, ELF and VLF radiation from the ‘polar electrojet antenna’, *Radio Sci.*, *19*(4), 1111–1122, 1984.
- Barr, R., and P. Stubbe, ELF radiation from the Tromsø “super heater” facility, *Geophys. Res. Lett.*, *18*(6), 1035–1038, 1991a.
- Barr, R., and P. Stubbe, On the ELF generation efficiency of the Tromsø “super heater” facility, *Geophys. Res. Lett.*, *18*(11), 1971–1974, 1991b.
- Barr, R., and P. Stubbe, ELF harmonic radiation from the Tromsø heating facility, *Geophys. Res. Lett.*, *20*(20), 2243–2246, 1993.
- Barr, R., and P. Stubbe, ELF and VLF wave generation by HF heating: A comparison of AM and CW techniques, *J. Atmos. Sol. Terr. Phys.*, *18*(58), 2265–2279, 1997.
- Barr, R., M. T. Rietveld, H. Kopka, P. Stubbe, and E. Nielsen, Extra-low-frequency radiation from the polar electrojet antenna, *Nature*, *317*(12), 155–157, 1985a.
- Barr, R., M. T. Rietveld, P. Stubbe, and H. Kopka, The diffraction of VLF radio waves by a patch of ionosphere illuminated by a powerful HF transmitter, *J. Geophys. Res.*, *90*(A3), 2861–2875, 1985b.
- Barr, R., P. Stubbe, M. T. Rietveld, and H. Kopka, ELF and VLF signals radiated by the ‘polar electrojet antenna’: Experimental results, *J. Geophys. Res.*, *91*(A4), 4451–4459, 1986.

- Barr, R., M. T. Rietveld, P. Stubbe, and H. Kopka, Ionospheric heater beam scanning: A mobile source of ELF/VLF radiation, *Radio Sci.*, 22(6), 1076–1083, 1987.
- Barr, R., M. T. Rietveld, P. Stubbe, and H. Kopka, Ionospheric heater beam scanning: A realistic model of this mobile source of ELF/VLF radiation, *Radio Sci.*, 23(3), 379–388, 1988.
- Barr, R., P. Stubbe, and H. Kopka, Long-range detection of VLF radiation produced by heating the auroral electrojet, *Radio Sci.*, 24(4), 871–879, 1991.
- Barr, R., W. Ireland, and M. J. Smith, ELF, VLF, and LF radiation from a very large loop antenna with a mountain core, *Proc. H of IEE*, 140, 129–134, 1993.
- Barr, R., P. Stubbe, and M. T. Rietveld, ELF wave generation in the ionosphere using pulse modulated HF heating: initial tests of a technique for increasing ELF wave generation efficiency, *Ann. Geophysicae*, 17, 759–769, 1999.
- Barr, R., D. Llanwyn Jones, and C. J. Rodger, ELF and VLF radio waves, *J. Atmos. Sol. Terr. Phys.*, 62, 1689–1718, 2000.
- Baumjohann, W., Ionospheric and field-aligned current systems in the auroral zone: A concise review, *Adv. Space. Res.*, 10(2), 55–62, 1983.
- Belyaev, P. P., D. S. Kotik, S. N. Mityakov, S. V. Polyakov, V. O. Rapoport, and V. Y. Trakhtengerts, Generation of electromagnetic signals at combination frequencies in the ionosphere, *Radiophysics and Quantum Electronics*, 30(2), 189–206, 1987.
- Bittencourt, J., *Fundamentals of plasma physics*, third ed., Bittencourt, J.A., 2003.
- Booker, H. . G., Propagation of wave-packets incident obliquely upon a stratified doubly refracting ionosphere, *Phil. Trans. R. Soc. Lon, Ser. A*, 237(781), 411–451, 1938.
- Borisov, M., A. Gurevich, and K. Papadopoulos, Direct Cerenkov excitation of waveguide modes by a mobile ionospheric heater, *Radio Sci.*, 31(4), 859–867, 1996.
- Budden, K., *The Wave-guide Mode Theory of Wave Propagation*, Logos Press, 1961a.

- Budden, K. G., The numerical solution of differential equations governing reflexion of long radio waves from the ionosphere, *Proc. Roy. Soc.*, *A227*, 516–537, 1955.
- Budden, K. G., *Radio Waves in the Ionosphere*, Cambridge University Press, 1961b.
- Budden, K. G., *The propagation of radio waves: the theory of radio waves of low power in the ionosphere and magnetosphere*, Cambridge University Press, 1985.
- Budilin, L. V., et al., Localization of height of nonlinear currents responsible for low-frequency radiation in the ionosphere, *Scientific-Research Institute of Radio-physics*, *20* (Translated from Izvestiya Vysshikh Uchebnykh Zavedenii Radiofizika), 83–86, 1977.
- Butler, K. E., and R. D. Russell, Subtraction of powerline harmonics from geophysical records, *Geo-physics*, *58*(6), 898–903, 1993.
- Carroll, J. C., E. J. Violette, and W. F. Utlaut, The Platteville high power facility, *Radio Sci.*, *11*(11), 889–894, 1974.
- Carroll, K. J., and A. J. Ferraro, Computer simulation of ELF injection in the Earth-ionosphere waveguide, *Radio Sci.*, *25*(6), 1363–1367, 1990.
- Chevalier, M. W., W. B. Peter, U. S. Inan, T. F. Bell, and Spasojevic, Remote sensing of ionospheric disturbances associated with energetic particle precipitation using the South Pole VLF beacon, *J. Geophys. Res.*, *112*(A11306), doi:10.1029/2007JA012,425, 2007.
- Chrissan, D. A., and A. C. Fraser-Smith, Seasonal variations of globally measured ELF/VLF radio noise, *Radio Sci.*, *31*(5), 1141–1152, 1996.
- Cohen, M. B., U. S. Inan, and G. R. Fishman, Terrestrial gamma ray flashes observed aboard Compton Gamma Ray Observatory/Burst And Transient Source Experiment and ELF/VLF radio atmospheric, *J. Geophys. Res.*, *111*(D24109), doi:10.1029/2005JD006,987, 2006.

- Cohen, M. B., M. Gołkowski, and U. S. Inan, Orientation of the HAARP ELF ionospheric dipole and the auroral electrojet, *Geophys. Res. Lett.*, *35*(L02806), doi:10.1029/2007GL032,424, 2008a.
- Cohen, M. B., U. S. Inan, and M. Gołkowski, Geometric modulation: A more effective method of steerable ELF/VLF wave generation with continuous HF heating of the lower ionosphere, *Geophys. Res. Lett.*, *35*(L12101), doi:10.1029/2008GL034,061, 2008b.
- Cohen, M. B., U. S. Inan, and M. Gołkowski, Reply to Comment by R. C. Moore and M. T. Rietveld on "Geometric modulation: A more effective method of steerable ELF/VLF wave generation with continuous HF heating of the lower ionosphere", *Geophys. Res. Lett.*, *36*(L04102), doi:10.1029/2008GL036,519, 2009a.
- Cohen, M. B., U. S. Inan, and E. P. Paschal, Sensitive broadband ELF/VLF radio reception with the AWESOME instrument, *IEEE Trans. Geosc. Remote Sensing*, *47*(manuscript in press), 10.1109/TGRS.2009.2028,334, 2009b.
- Cohen, M. B., U. S. Inan, M. Gołkowski, and M. J. McCarrick, ELF/VLF wave generation via ionospheric HF heating: Experimental comparison of amplitude modulation, beam painting, and geometric modulation, *J. Geophys. Res.*, p. doi:10.1.1029/2009JA014410, 2009, in press.
- Cummer, S. A., Lightning and ionospheric remote sensing using VLF/ELF radio atmospherics, Ph.D. thesis, Stanford University, 1997.
- Cummer, S. A., and U. S. Inan, Measurement of charge transfer in sprite-producing lightning using ELF radio atmospherics, *Geophys. Res. Lett.*, *24*(14), 1731–1734, 1997.
- Cummer, S. A., T. F. Bell, U. S. Inan, and D. L. Chenette, VLF remote sensing of high-energy auroral particle precipitation, *J. Geophys. Res.*, *102*(A4), 7477–7484, 1997.

- Cummer, S. A., U. S. Inan, and T. Bell, Ionospheric D region remote sensing using VLF radio atmospherics, *Radio Sci.*, *33*(6), 1781–1792, 1998.
- Dalgarno, A., M. B. McElroy, M. H. Rees, and J. C. G. Walker, The effect of oxygen cooling on ionospheric electron temperatures, *Planet. Space Sci.*, *16*, 1371–1380, 1968.
- Davies, K., *Ionospheric Radio*, Institute of Engineering and Technology, 1990.
- Dazey, M. H., and H. C. Koons, Characteristics of a power line used as a vlf antenna, *Radio Sci.*, *17*(3), 589–597, 1982.
- Ferraro, A. J., H. S. Lee, R. Allshouse, K. Carroll, A. A. Tomko, F. J. Kelly, and R. G. Joiner, VLF/ELF radiation from the ionospheric dynamo current system, modulated by powerful HF signals, *J. Atmos. Terr. Phys.*, *44*(12), 1113–1122, 1982.
- Ferraro, A. J., H. S. Lee, R. Allshouse, K. Carrol, R. Lunnen, and T. Collins, Characteristics of ionospheric ELF radiation generated by HF heating, *J. Atmos. Terr. Phys.*, *46*(10), 855–865, 1984.
- Ferraro, A. J., H. S. Lee, T. W. Collins, M. Baker, D. Werner, F. M. Zain, and P. Li, Measurements of extremely low frequency signals from modulation of the polar electrojet above Fairbanks, Alaska, *IEEE Trans. Ant. Prop.*, *37*, 6, 1989.
- Field, E. C., L. R. Kiws, P. R. Bannister, R. F. Ingram, W. D. Hopkins, and M. A. Roberts, An aerostat-supported ELF/VLF transmitter, *Radio Sci.*, *24*, 235–246, 1989.
- Fishman, G. J., and U. S. Inan, Observation of an ionospheric disturbance caused by a gamma-ray burst, *Nature*, *331*, 418–420, 1988.
- Frank, R. L., Current developments in Loran-C, *Proc. IEEE*, *71*(10), 1127–1142, 1983.



- Furno, G. S., and W. J. Tompkins, A learning filter for removing noise interference, *IEEE Trans. Biomed. Eng., BME-30*(4), 234–235, 1983.
- Galejs, J., Excitation of slots in a conducting screen above a lossy dielectric half space, *IRE Trans. Ant. and Prop., AP-11*(3), 296–305, 1962.
- Getmantsev, C. G., N. A. Zuikov, D. S. Kotik, N. A. Mironenko, V. O. Mityakov, Y. A. Rapoport, V. Y. Sazanov, V. Y. Trakhtengerts, and V. Y. Eidman, Combination frequencies in the interaction between high-power short-wave radiation and ionospheric plasma, *JETP*, 20, 101–102, 1974.
- Gibby, A. R., U. S. Inan, and T. F. Bell, Saturation effects in the VLF triggered emission process, *J. Geophys. Res.*, 113(A11215), doi:10.1029/2008JA013,233, 2008.
- Ginzburg, V. L., and A. V. Gurevich, Nonlinear phenomena in a plasma located in an alternating electromagnetic field, *Sov. Phys. Usp.*, 3, 115–146, 1960.
- Gołkowski, M., and U. S. Inan, Multistation observations of ELF/VLF whistler mode chorus, *J. Geophys. Res.*, 113(A08210), doi:10.1029/2007JA012,977, 2008.
- Gołkowski, M., U. S. Inan, A. R. Gibby, and M. B. Cohen, Magnetospheric amplification and emission triggering by ELF/VLF waves injected by the 3.6 MW HAARP ionospheric heater, *J. Geophys. Res.*, 113(A10201), doi:10.1029/2008JA013,157, 2008.
- Gołkowski, M., U. S. Inan, and M. B. Cohen, Cross modulation of whistler mode and hf waves above the haarp ionospheric heater, *Geophys. Res. Lett.*, 36(L15103), doi:10.1029/2009GL039,669, 2009.
- Gould, R. N., Some preliminary experimental tests of a novel method of radiating very low frequencies, *Nature*, 190(4773), 332–222, 1961.
- Griffiths, D. J., *Introduction to Electrodynamics: Third Edition*, Prentice Hall, 1999.
- Harriman, S. K., E. W. Paschal, and U. S. Inan, Magnetic sensor design for femto-tesla low-frequency signals, *IEEE Trans. Geosc. Remote Sensing*, p. Paper in press, 2009.

- Hayakawa, M., and S. S. Sazhin, Mid-latitude and plasmaspheric hiss: A review, *Planetary Space Science*, 40(10), 1325–1338, 1992.
- Helliwell, R. A., *Whistlers and related ionospheric phenomena*, Dover Publications, 1965.
- Helliwell, R. A., and J. P. Katsufakis, VLF wave injection into the magnetosphere from Siple Station, Antarctica, *J. Geophys. Res.*, 79(16), 2511–2518, 1974.
- Huxley, L. G. H., and R. W. Crompton, *Atomic and Molecular Processes*, chap. 10, The Motion of Slow Electrons in Gases, pp. 336–374, Academic Press, 1962, edited by Bates, D. R.
- Inan, U. S., VLF heating of the lower ionosphere, *Geophys. Res. Lett.*, 17(6), 729–732, 1990.
- Inan, U. S., and A. S. Inan, *Electromagnetic waves*, Prentice Hall, 2000.
- Inan, U. S., H. C. Chang, and R. A. Helliwell, Electron precipitation zones around major ground-based VLF signal sources, *J. Geophys. Res.*, 89(A5), 2891–2906, 1984.
- Inan, U. S., J. V. Rodriguez, and V. P. Idone, VLF signatures of lightning-induced heating and ionization of the nighttime D-region, *Geophys. Res. Lett.*, 20(21), 2355–2358, 1993.
- Inan, U. S., M. B. Cohen, R. K. Said, D. M. Smith, and L. I. Lopez, Terrestrial gamma ray flashes and lightning discharges, *Geophys. Res. Lett.*, 33(L18802), doi:10.1029/2006GL027,085, 2006.
- Inan, U. S., M. Golkowski, M. K. Casey, W. Moore, R. C. and Peter, P. Kulkarni, P. Kossey, E. Kennedy, S. Z. Meth, and P. Smit, Subionospheric VLF observations of transmitter-induced precipitation of inner radiation belt electrons, *Geophys. Res. Lett.*, 34(L02106), doi:10.1029/2006GL028,494, 2007a.

- Inan, U. S., N. G. Lehtinen, R. C. Moore, K. Hurley, S. Boggs, D. M. Smith, and G. J. Fishman, Massive disturbance of the daytime lower ionosphere by the giant gamma-ray flare from magnetar SGR 1806-20, *Geophys. Res. Lett.*, *34*(L02103), doi:10.1029/2006GL029,145, 2007b.
- Inan, U. S., D. Piddychiy, W. B. Peter, J. A. Sauvaud, and M. Parrot, DEMETER satellite observations of lightning-induced electron precipitation, *Geophys. Res. Lett.*, *34*(L02103), doi:10.1029/2006GL029,238, 2007c.
- Inan, U. S., et al., Multi-hop whistler-mode ELF/VLF signals and triggered emissions excited by the HAARP HF heater, *Geophys. Res. Lett.*, *31*(L24805), doi:10.1029/2004GL021,647, 2004.
- James, H., The ELF spectrum of artificially modulated D/E-region conductivity, *J. Atmos. Terr. Phys.*, *47*(11), 1129–1142, 1985.
- James, H., U. S. Inan, and M. T. Rietveld, Observations on the DE-1 spacecraft of ELF/VLF waves generated by an ionospheric heater, *J. Geophys. Res.*, *95*(A8), 12,187–12,195, 1990.
- James, H. G., R. L. Dowden, M. T. Rietveld, and H. Stubbe, P. and Kopka, Simultaneous observations of ELF waves from an artificially modulated auroral electrojet in space and on the ground, *J. Geophys. Res.*, *89*(A3), 1655–1666, 1984.
- Jin, G., M. Spasojevic, and U. S. Inan, Relationship between electrojet current strength and ELF signal intensity in modulated heating experiments, *J. Geophys. Res.*, *114*(A08301), doi:10.1029/2009JA014,122, 2009.
- Jones, D. L., ELF radio in: 100 years of radio, *IEE Conference Publications*, *141*, 121–106, 1995.
- Jones, T. B., K. Davies, and B. Wieder, Observations of D-region modifications and low and very low frequencies, *Nature*, *238*, 33–34, 1972.
- Kapustin, I. N., R. A. Pertsovskii, A. N. Vasil'ev, V. S. Smirnov, O. M. Raspopov, L. E. Solov'ev, A. A. Ul'yachenko, A. A. Arykov, and N. V. Galakhova, Generation

- of radiation at combination frequencies in the region of the auroral electric jet, *JETP Letters*, 25(5), 228–231, 1977.
- Kimura, I., P. Stubbe, M. T. Rietveld, R. Barr, K. Ishida, Y. Kasahara, S. Yagitani, and I. Nagano, Collaborative experiments by Akebono satellite, Tromsø ionospheric heater, and European incoherent scatter radar, *Radio Sci.*, 29(1), 23–37, 1994.
- Kimura, I., et al., Satellite and ground observations of HIPAS VLF modulations, *Geophys. Res. Lett.*, 18(2), 309–312, 1991.
- Koons, H. C., and M. H. Dazey, High-power VLF transmitter facility utilizing a balloon lofted antenna, *IEEE Trans. Ant. Prop.*, AP-31(2), 243–248, 1983.
- Kotik, D. S., and V. Y. Trakhtengerts, Mechanism of excitation of combination frequencies in ionospheric plasma, *Soviet Physics. JETP Letters (English translation)*, 21(2), 51–52, 1975.
- Kuo, S. P., J. Faith, M. C. Lee, and P. Kossey, Numerical comparison of two schemes for the generation of ELF and VLF waves in the HF heater-modulated polar electrojet, *J. Geophys. Res.*, 103(A3), 4063–4069, 1998.
- Lee, H. S., A. J. Ferraro, and J. C. Olson, Detection and characterization of geomagnetic pulsations using HF ionospheric heating, *Radio Sci.*, 25(6), 1429–1439, 1990.
- Lefeuvre, J. F., F. and Rauch, et al., Detection from Aureol-3 of the modulation of auroral electrojet by HF heating from ELF signals in the upper ionosphere above Tromsø, *Results of the Arcad 3 Project and of the Recent Programmes in Magnetospheric and Ionospheric Physics, Cepedues-Editions*(Toulouse), 609–616, 1985.
- Lehtinen, N. G., and U. S. Inan, Radiation of ELF/VLF waves by harmonically varying currents into a stratified ionosphere with application to radiation by a modulated electrojet, *J. Geophys. Res.*, 113(A06301), doi:10.1029/2007JA012,911, 2008.

- Lehtinen, N. G., and U. S. Inan, Full-wave modeling of transionospheric propagation of VLF waves, *Geophys. Res. Lett.*, *36*(L03104), doi:10.1029/2008GL036,535., 2009.
- Li, P. J., and A. J. Ferraro, Determination of D region electron densities from ELF frequency stepping experiment, *Radio Sci.*, *25*(6), 1387–1395, 1990.
- Lunnen, R. J., H. S. Lee, A. J. Ferraro, T. W. Collins, and R. F. Woodman, Detection of radiation from a heated and modulated equatorial electrojet current system, *Nature*, *311*(13), 134–135, 1984.
- McCarrick, M. J., D. D. Sentman, A. Y. Wong, R. F. Wuerker, and B. Chouinard, Excitation of ELF waves in the schumann resonance range by modulated HF heating of the polar electrojet, *Radio Sci.*, *25*(6), 1291–1298, 1990.
- McNeil, J. D., and V. F. Labson, Geological mapping using VLF radio field; chapter 7 in, *Electromagnetic Methods in Applied Geophysics*, *2*(Society of Exploration Geophysicists), 1991.
- Mentzoni, M. H., and R. V. Row, Rotational excitation and electron relaxation in nitrogen, *Phys. Rev.*, *130*, 2312–2316, 1963.
- Milikh, G. M., and K. Papadopoulos, Enhanced ionospheric ELF/VLF generation efficiency by multiple timescale modulated heating, *Geophys. Res. Lett.*, *34*(L20804), doi:10.1029/2007GL031,518., 2007.
- Milikh, G. M., M. J. Freeman, and L. M. Duncan, First estimates of HF-induced modifications of the D region by the HF Active Auroral Research Program facility, *Radio Sci.*, *29*(5), 1355–1362, 1994.
- Milikh, G. M., K. Papadopoulos, M. McCarrick, and J. Preston, ELF emission generated by the HAARP HF-heater using varying frequency and polarization, *Izvestiya Vysshikh Uchebnykh Zavedenii, Radiofizika*, *42*(8), 728–735, 1999.
- Mitra, A. P., *Ionospheric Effects of Solar Flares*, Reidel, Dordrecht, Netherlands, 1974.

- Molchanov, O. A., and M. Hayakawa, Subionospheric VLF signal perturbations possibly related to earthquakes, *J. Geophys. Res.*, *103*, 17,489–17,504, 1999.
- Moore, R. C., ELF/VLF wave generation by modulated HF heating of the auroral electrojet, Ph.D. thesis, Stanford University, 2007.
- Moore, R. C., and M. T. Rietveld, Comment on “Geometric modulation: A more effective method of steerable ELF/VLF wave generation with continuous hf heating of the lower ionosphere” by M. B. Cohen, U. S. Inan, and M. A. Golkowski, *Geophys. Res. Lett.*, *36*(L04101), doi:10.1029/2008GL036,002, 2009.
- Moore, R. C., U. S. Inan, and T. F. Bell, Observations of amplitude saturation in ELF/VLF wave generation by modulated HF heating of the auroral electrojet, *Geophys. Res. Lett.*, *33*(L12106), doi:10.1029/2006GL025,934, 2006.
- Moore, R. C., U. S. Inan, T. F. Bell, and E. J. Kennedy, ELF waves generated by modulated HF heating of the auroral electrojet and observed at a ground distance of  $\sim 4400$  km, *J. Geophys. Res.*, *112*(A05309), doi:10.1029/2006JA012,063, 2007.
- Nagano, I., K. Miyamura, S. Yahitani, I. Kimura, T. Okada, K. Hashimoto, and A. Y. Wong, Full wave calculation method of VLF wave radiated from a dipole antenna in the ionosphere - analysis of joint experiment by HIPAS and Akebono satellite, *Electronics and Communications in Hapan, Part 1*, *77*(11), 615–624, 1994.
- Oikarinen, A., J. Manninen, J. Kulitima, and T. Turunen, Observations of intensity variations and harmonics of heater induced VLF waves, *Journal of Atmospheric and Solar-Terrestrial Physics*, *59*(18), 2351–2360, 1997.
- Oppenheim, A. V., R. W. Schaffer, and J. R. Buck, *Discrete Time Signal Processing: Second edition*, Prentice Hall, 1990.
- Papadopoulos, K., A. S. Sharma, and C. L. Chang, On the efficient operation of a plasma ELF antenna driven by modulation of ionospheric currents, *Comments Plasma Phys. Controlled Fusion*, *13*(1), 1–17, 1989.

- Papadopoulos, K., C. Chang, P. Vitello, and A. Drobot, On the efficiency of ionospheric ELF generation, *Radio Sci.*, *25*, 1131–1320, 1990.
- Papadopoulos, K., H. B. Zhou, and C. L. Chang, Cerenkov excitation of whistler/helicon waves by ionospheric HF heating, *Geophys. Res. Lett.*, *21*(17), 1767–1770, 1994.
- Papadopoulos, K., T. Wallace, G. M. Milikh, W. Peter, and M. McCarrick, The magnetic response of the ionosphere to pulsed HF heating, *Geophys. Res. Lett.*, *32*(L13101), doi:10.1029/2005GL023,185, 2005.
- Parrot, M., The micro-satellite DEMETER, *J. Geodynamics*, *33*, 535–541, 2002.
- Parrot, M., U. S. Inan, and N. G. Lehtinen, V-shaped VLF streaks recorded on DEMETER above powerful thunderstorms, *J. Geophys. Res.*, *113*(A10310), doi:10.1029/2008JA013,336., 2008.
- Paschal, E. W., The design of broad-band VLF receivers with air-core loop antennas, *Tech. rep.*, STARLab, Stanford University, 1980.
- Pashin, A. B., and W. B. Lyatsky, On spectra of ionospheric conductivity variations during a heating experiment, *Radio Sci.*, *32*(4), 1513–1522, 1997.
- Payne, J. A., Spatial structure of very low frequency modulated ionospheric currents, Ph.D. thesis, Stanford University, 2007.
- Payne, J. A., U. S. Inan, F. R. Foust, T. W. Chevalier, and T. F. Bell, HF modulated ionospheric currents, *Geophys. Res. Lett.*, *34*(L23101), doi:10.1029/2007GL031,724, 2007.
- Peter, W. B., and U. S. Inan, Perturbations of midlatitude subionospheric VLF signals associated with lower ionospheric disturbances during major geomagnetic storms, *J. Geophys. Res.*, *111*(A03301), doi:10.1029/2005JA011,346, 2006.
- Peter, W. B., and U. S. Inan, A quantitative comparison of lightning-induced electron precipitation and VLF signal perturbations, *J. Geophys. Res.*, *112*(A12212), doi:10.1029/2006JA012,165, 2007.

- Piddyachiy, D., U. S. Inan, and T. F. Bell, DEMETER observations of an intense upgoing column of ELF/VLF radiation excited by the HAARP HF, *Geophys. Res. Lett.*, *113*(A10308), doi:10.1029/2008JA013,208, 2008.
- Platino, M., U. S. Inan, T. F. Bell, J. S. Pickett, E. J. Kennedy, J. G. Trotignon, R. J. L., and P. Canu, Cluster observations of ELF/VLF signals generated by modulated heating of the lower ionosphere with the HAARP HF transmitter, *Ann. Geophysicae*, *22*, 2643, 2004.
- Platino, M., U. S. Inan, T. F. Bell, M. Parrot, and E. J. Kennedy, DEMETER observations of ELF waves injected with the HAARP HF transmitter, *Geophys. Res. Lett.*, *33*(L16101), doi:10.1029/2006GL026,462., 2006.
- Potemra, T., Heating of the electrons in the F region of the ionosphere, *Tech. Rep. Technical Report 63-036 to Advanced Research Projects Agency*, Radioscience Laboratory, Stanford University, 1963.
- Raghuram, R., R. L. Smith, and T. F. Bell, VLF antarctic antenna: impedance and efficiency, *IEEE Trans. Ant. and Prop.*, *AP-22*, 334, 1974.
- Ratcliffe, J. A., *The Magneto-ionic Theory and its Applications to the Ionosphere*, Cambridge University Press, Cambridge, 1959.
- Reising, S. C., Remote sensing of the electrodynamic coupling between thunderstorm systems and the mesosphere/lower ionosphere, Ph.D. thesis, Stanford University, 1998.
- Reising, S. C., U. S. Inan, T. F. Bell, and W. A. Lyons, Evidence for continuing currents in sprite-producing cloud-to-ground lightning, *Geophys. Res. Lett.*, *23*(24), 3639–3642, 1996.
- Rietveld, M. T., and P. Stubbe, Ionospheric demodulation by powerful pulsed radio waves: A potential new diagnostic for radars suggested by Tromsø heater results, *Radio. Sci.*, *22*(6), 1084–1090, 1987.



- Rietveld, M. T., H. Kopka, E. Nielsen, P. Stubbe, and R. L. Dowden, Ionospheric electric pulsations: A comparison between VLF results from an ionospheric heating experiment and STARE, *J. Geophys. Res.*, *88*(A3), 2140–2146, 1983.
- Rietveld, M. T., R. Barr, H. Kopka, E. Nielsen, P. Stubbe, and R. L. Dowden, Ionospheric heater beam scanning: A new technique for ELF studies of the auroral ionosphere, *Radio Sci.*, *19*(4), 1069–1077, 1984.
- Rietveld, M. T., H. Kopka, and P. Stubbe, D-region characteristics deduced from pulsed ionospheric heating under auroral electrojet conditions, *J. Atmos. Terr. Phys.*, *48*(4), 311–326, 1986.
- Rietveld, M. T., H. P. Mauelshagen, P. Stubbe, H. Kopka, and E. Nielsen, The characteristics of ionospheric heating-produced ELF/VLF waves over 32 hours, *J. Geophys. Res.*, *92*(A8), 8707–8722, 1987.
- Rietveld, M. T., P. Stubbe, and H. Kopka, On the frequency dependence of ELF/VLF waves produced by modulated ionospheric heating, *Radio Sci.*, *24*(3), 270–278, 1989.
- Rodger, C. J., et al., Radiation belt electron precipitation into the atmosphere: Recovery from a geomagnetic storm, *J. Geophys. Res.*, *112*(A11307), doi:10.1029/2007JA012,383, 2007.
- Rodriguez, J. V., Modification of the earth’s ionosphere by very low frequency transmitters, Ph.D. thesis, Stanford University, 1994.
- Rodriguez, J. V., and U. S. Inan, Electron density changes in the nighttime D region due to heating by very-low-frequency transmitters, *Geophys. Res. Lett.*, *21*(2), 93–96, 1994.
- Rowland, H. L., M. J. Keskinen, J. S. Villaseñor, and A. Y. Wong, Observations and simulations of VLF harmonic generation with the High-power Auroral Simulation array, *J. Geophys. Res.*, *101*(A12), 27,027–27,033, 1996.

- Said, R. K., Accurate and efficient long-range lightning geo-location using a VLF radio atmospheric waveform bank, Ph.D. thesis, Stanford University, 2009.
- Sazhin, S. S., and M. Hayakawa, Magnetospheric chorus emissions: A review, *Planet. Space. Sci.*, 40(5), 681–697, 1992.
- Scherrer, D., M. Cohen, T. Hoeksema, U. Inan, R. Mitchell, and P. Scherrer, Distributing space weather monitoring instruments and educational materials worldwide for IHY 2007: The AWESOME and SID project, *Adv. Space Res.*, 42, 1777–1785, 2008.
- Sen, H. K., and A. A. Wyller, On the generalization of the Appleton-Hartree magnetoionic formulas, *J. Geophys. Res.*, 65, 3931–3950, 1960.
- Starks, M. J., R. A. Quinn, G. P. Ginet, J. M. Albert, G. S. Sales, B. W. Reinisch, and P. Song, Illumination of the plasmasphere by terrestrial very low frequency transmitters: Model validation, *J. Geophys. Res.*, 113(A09320), doi:10.1029/2008JA013,112., 2008.
- Stubbe, P., and H. Kopka, Modulation of the polar electrojet by powerful HF waves, *J. Geophys. Res.*, 82(16), 2319–2325, 1977.
- Stubbe, P., and W. S. Varnum, Electron energy transfer rates in the ionosphere, *Planet. Space Sci.*, 20, 1121–1126, 1972.
- Stubbe, P., H. Kopka, and R. L. Dowden, Generation of ELF and VLF waves by polar electrojet modulation: Experimental results, *J. Geophys. Res.*, 86(A11), 9073–9078, 1981.
- Stutzman, W. L., and G. A. Thiele, *Antenna Theory and Design*, Wiley Publishing, 1998.
- Swanson, E. R., Omega, *Proceedings of the IEEE*, 71(10), 1140–1155, 1983.
- Taranenko, Y. N., U. S. Inan, and T. F. Bell, Interaction with the lower ionosphere of electromagnetic pulses from lightning: Heating, attachment, and ionization, *Geophys. Res. Lett.*, 20(15), 1539–1542, 1993.

- Tascione, T. F., *Introduction to the Space Environment: Second Edition*, Krieger Publishing Company, 1994.
- Thompson, B. J., N. Gopalswamy, J. M. Davila, and H. J. Haubold, *Putting the "I" in IHY*, SpringerWien, 2009.
- Thomson, N. R., Experimental daytime VLF ionospheric parameters, *J. Atmos. Terr. Phys.*, 55, 831–834, 1993.
- Thomson, N. R., M. A. Clilverd, and W. M. McRae, Nighttime ionospheric D region parameters from VLF phase and amplitude, *J. Geophys. Res.*, 112(A07304), doi:10.1029/2007JA012,271, 2007.
- Tomko, A. A., Nonlinear phenomena arising from radio wave heating of the lower ionosphere, Ph.D. thesis, The Pennsylvania State University, 1981.
- Uman, M. A., *The Lightning Discharge*, Dover Publications, 1987.
- United States Coast Guard, LORAN-C user's handbook, *Tech. Rep. COMDTINST M16562.3*, United States Department of Transportation, 1980.
- Utlaut, W. F., Radio-wave modification of the ionosphere, *J. Geophys. Res.*, 75(31), 6402–6405, 1970.
- Utlaut, W. F., and R. Cohen, Modifying the ionosphere with intense radio waves, *Science*, 174, 245–254, 1971.
- Villaseñor, J., A. Y. Wong, B. Song, J. Pau, M. McCarrick, and D. Sentman, Comparison of ELF/VLF generation modes in the ionosphere by the HIPAS heater array, *Radio Sci.*, 31(1), 211–226, 1996.
- Wait, J. R., *Electromagnetic waves in stratified media*, Pergamon Press, 1962.
- Wait, J. R., and K. P. Spites, Characteristics of the Earth-ionosphere waveguide for VLF waves, *Tech. Rep. 300*, National Bureau of Standards, Boulder, Colorado, 1964.

- Watt, A. D., *VLF Radio Engineering*, Pergamon Press, 1967.
- Werner, D. H., and A. J. Ferraro, Steerable ELF/VLF radiation produced by an array of ionospheric dipoles generated from HF heating, *IEEE Trans. Ant. and Prop.*, *AP-35*(9), 1022–1030, 1987.
- Widrow, e., B., Adaptive noise cancelling: Principles and applications 1716., *Proc. IEEE*, *63*(12), 1692–1716, 1975.
- Wolf, T. G., and U. S. Inan, Path-dependent properties of subionospheric VLF amplitude and phase perturbations associated with lightning, *J. Geophys. Res.*, *95*(A12), 20,997–21,005, 1990.
- Wong, A. Y., et al., High-power radiating facility at the HIPAS observatory, *Radio Sci.*, *25*(6), 1269–1282, 1990.
- Wood, T. G., and U. S. Inan, Long-range tracking of thunderstorms using sferic measurements, *J. Geophys. Res.*, *107*(D21), 4553, 2002.
- Yagitani, S., I. Nagano, K. Miyamura, and I. Kimura, Full wave calculation of ELF/VLF propagation from a dipole source located in the lower ionosphere, *Radio Sci.*, *29*(1), 39–54, 1994.